IMAGING THE SPATIAL-TEMPORAL NEURONAL DYNAMICS USING DYNAMIC CAUSAL MODELLING

Chun-Chuan Chen

Wellcome Department of Imaging Neuroscience

Institute of Neurology

A thesis submitted for the degree of Doctor of Philosophy

University College London

May, 2009

Primary supervisor: Dr. Nick S Ward

Secondary supervisor: Professor Karl J Friston

Declaration

I, Chun-Chuan Chen, confirm that the work presented in this thesis is my own. Where information has been derived from other sources, I confirm that this has been indicated in the thesis.

Abstract

Oscillatory brain activity is a ubiquitous feature of neuronal dynamics and the synchronous discharge of neurons is believed to facilitate integration both within functionally segregated brain areas and between areas engaged by the same task. There is growing interest in investigating the neural oscillatory networks in vivo. The aims of this thesis are to (1) develop an advanced method, Dynamic Causal Modelling for Induced Responses (DCM for IR), for modelling the brain network functions and (2) apply it to exploit the nonlinear coupling in the motor system during hand grips and the functional asymmetries during face perception.

DCM for IR models the time-varying power over a range of frequencies of coupled electromagnetic sources. The model parameters encode coupling strength among areas and allows the differentiations between linear (within frequency) and nonlinear (between-frequency) coupling. I applied DCM for IR to show that, during hand grips, the nonlinear interactions among neuronal sources in motor system are essential while intrinsic coupling (within source) is very likely to be linear. Furthermore, the normal aging process alters both the network architecture and the frequency contents in the motor network.

I then use the bilinear form of DCM for IR to model the experimental manipulations as the modulatory effects. I use MEG data to demonstrate functional asymmetries between forward and backward connections during face perception: Specifically, high (gamma) frequencies in higher cortical areas suppressed low (alpha) frequencies in lower areas. This finding provides direct evidence for functional asymmetries that is consistent with anatomical and physiological evidence from animal studies. Lastly, I generalize the bilinear form

of DCM for IR to dissociate the induced responses from evoked ones in terms of their functional role. The backward modulatory effect is expressed as induced, but not evoked responses.

Acknowledgments

I would like to express my sincere gratitude to my supervisors, Nick Ward and Karl Friston. They have been so supportive and dedicated their time to guide me through the journey of exploring the brain during my four years in FIL. I deeply appreciate their vast knowledge and very insightful comments and encouragement, plus a great sense of humour. Without them, this thesis would not be possible. My warmest thanks go to James Kilner and Stefan Kiebel for their sharing of expertise and valuable advice and help. I would like to thank Klaas Stephan and Rik Henson for their very constructive suggestions and discussions and essential support on the face paper. I would like to thank Rohit. Jolly for his help in experiment setup and data acquisition. I also thank Eric Featherstone and Peter Aston for the design and programming involved in creating the hand grip manipulandum and Vladimir Litvak for comments on the presentation of the motor paper and technical support. I thank all my colleagues in FIL, past or present, in particular, the theoretical neurobiology group. They have made my life here colourful and joyful.

Many thanks to the subjects for their time and cooperation in this work.

Finally, I thank my family and friends for their love and care and support.

During my days in London, I was supported by National Science Council of Taiwan (Taiwan Merit Scholarship; TMS-94-1-A-037; 2005-2008), Wellcome trust and Institute of Neurology, UCL

Table of Contents

Chapter 3 Nonlinear motor networks during hand gripping tasks

List of Tables

List of Figures

Abbreviations

AR	Autoregressive
BG	Basal Ganglia
DCM for IR	Dynamic Causal Modelling for Induced Responses
ECD	Equivalent Current Dipoles
EEG	Electroencephalography
EMG	Electromyogram
ERD	Event Related Desynchronization
ERS	Event Related Synchronization
FFA	Fusiform Face Area
GC	Granger Causality
GLM	General Linear Model
HAROLD	Hemispheric Asymmetry Reduction in Older Adults
ICA	Independent Component Analysis
IHI	InterHemispheric Inhibition
ISOs	Infra-Slow Oscillations
LFPs	Local Field Potentials
M1	Primary Sensorimotor Area
MEG	Magneto-Encephalography
MVC	Maximum Voluntary Contraction
OFA	Occipital Face Area
PCA	Principal Component Analysis
PM	Premotor Area
SEMs	Structural Equation Models
SMA	Supplementary Motor Area
SNR	Signal to Noise Ratio
SVD	Singular Value Decomposition
TMS	Transcranial Magnetic Stimulation
TRPow	Task-Related Power

Publications arising from work in this thesis

Published papers

- **C.C. Chen** , S. Kiebel, KJ Friston , Dynamic causal modelling of induced responses. *NeuroImage*, 2008; (41):1293-1312.

- **C.C. Chen**, R.N. Henson, K.E. Stephan, J.M. Kilner, and K.J. Friston1. Forward and backward connections in the brain: A DCM study of functional asymmetries in face processing. *NeuroImage*, 2009 Apr 1;45(2):453-62

- Stefan J. Kiebel, Marta I. Garrido, Rosalyn Moran, **Chun-Chuan Chen**, and Karl J. Friston, Dynamic causal modeling for M/EEG, *Human Brain Mapping*, 2009; 30(6):1866-1876

- **C.C. Chen**, J.M. Kilner, K.J. Friston, S. Kiebel, R. Jolly, N. Ward. Nonlinear coupling in the motor system. Journal of Neuroscience. Submitted.

In Preparation

- **C.C. Chen**, J.M. Kilner, K.J. Friston, S. Kiebel, R. Jolly, N. Ward, Age-dependent changes in the motor networks during hand grips.

- **C.C. Chen**, J.M. Kilner, N. S. Ward, S. Kiebel, K.E. Stephan, K.J. Friston, Backward connections mediate the induced modulatory effects

Abstracts

- **C.C. Chen** J.M. Kilner, N.S. Ward, K.J. Friston. A neural code of motor programmes during hand gripping tasks: A DCM study.. Human Brain Mapping Conference, Melbourn, Australia.2008.

- **C.C. Chen** J.M. Kilner, N.S. Ward, K.J. Friston. A neural code of motor programmes during hand gripping tasks: A DCM study. International workshop of NeuroMath, Rome, Italy.2007..

- **C.C. Chen** J.M. Kilner, A.C. Marreiros, N.S. Ward, K.J. Friston,. Dynamic causal modelling of induced responses. Human Brain Mapping Conference, Florence, Italy.2006.

- A.C. Marreiros, S.J. Kiebel, K.E. Stephan, **C.C. Chen**, L.M. Harrison, K.J. Friston. Dynamic causal modelling of fMRI with neural mass models. Human Brain Mapping Conference, Florence, Italy. 2006.

- **C.C. Chen**,J.M. Kilner, N.S. Ward, K.J. Friston. Dynamic causal modelling of induced responses: Face validation. Biomag 2006 – 15th International Conference on Biomagnetism, Vancouver, Canada.2006.

CHAPTER 1

INTRODUCTION

1.1 Oscillatory activities in the brain

Neurologists should take brain rhythms seriously.
Simon F. Farmer, Brain (2002)

Oscillatory activity in the brain is ubiquitous and a hallmark of many neuronal systems. Rhythmic neuronal oscillations were first observed in rabbit brains in 1890 by Beck (see Swartz B.E. and Goldensohn E.S., 1998 for a review of EEG-related history) (Swartz and Goldensohn, 1998). Since then oscillatory activity in human brains has been seen consistently across different spatial scales, from single unit recordings, through local field potential (LFPs) recordings, to macroscopic measures such as electroencephalogram (EEG) or magnetoencephalogram (MEG) (Crone et al., 1998a; Crone et al., 1998b; Kilner et al., 2003; Leocani et al., 1997). Furthermore, several different cortical regions have been shown to be involved, predominantly in the vicinity of the primary motor, sensory, visual and auditory cortices as well as subcortical structures such as the thalami and basal ganglia (BG) (Gray et al., 1989; Tiitinen et al 1993; Tass et al 1998; Singer, 1999; Tallon-Baudry and Bertrand, 1999; Varela et al, 2001;

Singh et al 2002, Brown, 2007; Priori et al., 2004). In addition, neurons can exhibit a broad range of oscillations from theta to gamma-band oscillations (~4-70 Hz) as well as high gamma (~80-150 Hz). Brain rhythms are of interest in neuroscience because of the idea that oscillations might facilitate integration both within functionally segregated brain areas (i.e. small-scale circuits) and between areas engaged by the same task (large-scale networks) (Singer and Gray, 1995; Kahana et al., 1999; Rodriguez et al., 1999; Engel et al., 1991; Gray et al., 1992; Gray and Viana Di Prisco, 1997 ; Konig et al., 1995; Murthy and Fetz, 1992; Sanes and Donoghue, 1993; Singer, 1969; Steriade et al., 1996). In short, neuronal oscillations exhibit a variety of spatial distributions, frequencies and are associated with several brain network functions.

Electromagnetic waves are defined by their frequency contents (i.e. spectrum) and this principle applies also to brain rhythms. In general, brain rhythms can be divided into theta (4-8 Hz), alpha (8-15 Hz), beta (15-30), gamma (30-80) and more recent, high gamma (80-150 Hz) bands according to their frequency span. Depending on the brain region or the underlying task they might have a different name or frequency content. For example, mu (10- and 20- Hz) rhythms are seen in sensori-motor regions during the resting condition and Piper (40- Hz) electromyogram (EMG) rhythms (Salmelin and Hari 1994; Brown et. al., 1998). In this thesis, I will focus on the oscillations between 4 and 48 Hz in the motor system (Murthy & Fetz, 1992, 1996a, b; Sanes & Donoghue, 1993; Baker, Olivier & Lemon, 1997) and in the "core system" for face processing identified by Haxby

and colleagues (Haxby et al., 2000). In the following section, the recognized functional roles of brain rhythms in terms of frequency and phase are reviewed.

1.1.1 Frequency aspects of neuronal rhythms

Dynamic modulation of oscillatory power at 10- , 20- and 30- Hz in primary motor cortex (M1), supplementary motor area (SMA) and premotor cortex (PM) has been examined intensively in numerous studies. In general, alpha and beta power in M1, SMA and PM are suppressed before movement emerges and rebound after the end of movement. These changes are known as event-related desynchronization (ERD) and event-related synchronization (ERS) respectively, and are sometimes accompanied by transient gamma ERS (Andrew and Pfurtscheller, 1996; Crone et al., 1998a; Crone et al., 1998b; Leocani et al., 1997; Pfurtscheller and Lopes da Silva, 1999; Pfurtscheller et al., 1998; Toro et al., 1994; Wheaton et al., 2008). According to their topographical patterns, alpha, beta and gamma activities exhibit a somatotopic representation in M1 and are believed to be associated with the control of movement (Pfurtscheller, 2003; Salmelin and Hari, 1994). Studies of corticomuscular coherence and transcranial magnetic stimulation (TMS) further verify that beta and gamma range (15 - 40) oscillations originating from M1 contribute to motor control by driving the spinal motorneurons via the corticospinal tract (Darling et al., 2006; Mima and Hallett, 1999; Thut and Miniussi, 2009; Grosse et al., 2002). In addition, corticomuscular coherence and spectral densities can be modulated by movement kinematics, such as movement speed and movement type (Kilner et al., 2002; Kilner et al., 2003;

Leocani et al., 1997; Manganotti 1998; Muller-Putz et al., 2007; Muller et al., 2003; Neuper and Pfurtscheller, 2001; Patino et al., 2008; Pfurtscheller, 1992; Rau et al., 2003; Omlor et al., 2007). In particular, mu (8-13) rhythm power fluctuation can also be seen during observing action execution and is believed to play a role in the 'mirror neuron' system (Oberman et al., 2005; Ulloa and Pineda, 2007). In relation to the time course of alpha, beta and gamma power dynamics, it was suggested that changes in these oscillations are also associated with motor preparation/planning in addition to motor execution (Ohara et al., 2000; Rektor et al., 2006). Sensory feedback is also clearly important for optimal motor control, and studies of deafferented subjects have shown that the power of 15-30 Hz neuronal oscillations and 15- to 30-Hz coherence between EMG activity in hand muscles significantly decrease compared to that of control subjects. This suggests that proprioceptive information contributes to the modulation of 15- to 30-Hz oscillations in the motor system (Kilner et al., 2004; Patino et al., 2008). In other pathological states, those oscillatory activities are especially interesting and can be used to address questions about the underlying mechanisms as an index of functional deficits (Czigler et al., 2007; Patino et al., 2006; Raethjen et al., 2007). For example, in Parkinson's patients, the substantial synchronization at 4~6 Hz between the contralateral primary motor cortex and forearm muscles is thought to contribute to resting tremors, while the excessive synchrony at 10- to 35 Hz in basal ganglia (BG) and subthalamic nucleus is likely to contribute to bradykinesia (for review, Brown, 2007).

There is growing interest in the functional significance of oscillations in 'non-motor' areas, e.g. face perception. Multiple oscillations are engaged in face processing, including delta (0.5-4 Hz), theta, alpha, beta, and gamma oscillations (see Basar et al., 2006 for review). Perception of faces can induce changes in the coherence of broadband (4-45 Hz) power between the fusiform gyrus and temporal, parietal, and frontal cortices (Klopp et al. 1999; Klopp et al. 2000). Specifically, the perception of a known picture (for instance, grandmother's face) compared to unknown elderly faces induced greater theta oscillations in the frontal area (Basar et al., 2006). Moreover, the emotional facial expression induced greater theta oscillation in the right temporal-occipital locations than that in right central areas (Balconi and Pozzoli, 2008; Guntekin and Basar, 2007; Ozgoren et al., 2005).

1.1.2 Evoked and induced activities

Operationally speaking, cortical oscillatory activity can be divided into (i) ongoing (or spontaneous), (ii) evoked and (iii) induced components (Galambos, 1992; Tallon-Baudry and Bertrand, 1999). Evoked and induced activities are event-related and elicited by the changes of the environment, either internally (e.g. a thought) or externally (e.g. electrical stimulus) or both, whereas ongoing components are not associated with the processing of a stimulus or the occurrence of specific events. The work in this thesis focuses on event-related evoked and induced responses. The difference between evoked and induced responses is their phase-relationship to the stimulus. Specifically, evoked components are phase-

locked to the stimulus, whereas induced responses are not. Conventionally, in order to extract the evoked activities from unwanted disturbance (mainly non-phase locked signals including measurement noise and induced activities) an averaging technique is employed. Averaging the E/MEG signals across trials eliminates the non-stationary components and yields the evoked potentials/fields with enhanced signal-to-noise ratio (proportional to $N^{1/2}$ where N = the number of averaged trials). Evoked spectral properties can be obtained subsequently via Fourier or wavelet transform. In contrast, induced responses can only be derived in the time-frequency domain because the non-phase locked property will lead to their cancellation when averaging (Figure 1.1 left). The extraction of induced responses comprises two steps: In the first, each trial is projected into the time–frequency domain to obtain the spectral densities without the cancellation effect. These are then averaged across trials to obtain the total power (Figure 1.1 right). In the second step, the power of evoked and background components are subtracted from this total power to obtain the induced power. In short, evoked responses are the power of the average; while induced responses are the average power without the power of the average. The functional role of induced responses has been described as mediating 'top-down' modulation through backward connections in cognitive studies of attention, learning and face perception; as opposed to the bottom-up driving process that may be more manifest evoked components, which are considered to be mediated mainly via feed-forward projections (Tallon-Baudry and Bertrand, 1999). The implication is that the evoked and induced activities may reflect different neuronal processes and mechanisms.

However, a recent study using simulated data has reported that the evoked and induced responses may “share” common generating mechanisms up to certain level (David et.al, 2006). In the work of David and colleagues, the authors propose two generating mechanisms for neuronal processes: dynamic and structural; both dynamic and structural mechanisms can mediate induced responses (see David et.al, 2006 for details). For example, if the transfer functions of the system change, reflecting changes in the systems coupling parameters, the input power will be expressed differently in the induced power. These are structural effects. On the other hand, if there are amplitude variations in stimulus-locked inputs, the evoked power will be recapitulated in the induced power as the variance of the amplitude increases, although the evoked responses in time domain remains the same. These are dynamic causes. One possible explanation of these amplitude variations (gain effects) is the effect of attention (McAdams and Maunsell, 1999; Treue and Martinez-Trujillo, 1999). In the work of David and colleagues’, the authors propose two generating mechanisms for neuronal processes: dynamic and structural; Dynamic mechanisms express the changes of the inputs as part of the perturbation to the system while structural mechanisms reflect the changes in the responses resulted from the perturbation. Both dynamic and structural mechanisms can mediate the induced responses (see David et.al, 2006 for details). For example, if the transfer functions of the system change at time t, reflecting the changes of systems coupling parameters, the input power will be expressed as the induced power. This is the structural effects. On the other hand, if there are amplitude variations in stimulus-locked inputs, the evoked power will be recapitulated in the induced power as the variance of the

amplitude increases, although the evoked responses in time domain remains the same. This is the dynamic causes. One possible explanation of these amplitude variations (gain effects) is the effect of attention (McAdams and Maunsell, 1999; Treue and Martinez-Trujillo, 1999). Figure 1.2 (adapted from David et al. 2006) illustrates the concept of this many-to-many mapping between evoked and induced activities and the underlying mechanisms. Therefore, a generative model which can account for the 'shared' generating mechanisms is needed when studying the underlying neuronal processing. Indeed, the conventional way of separating evoked and induced responses posits an assumption that they are linearly related but this may not hold when modelling the oscillatory networks with respect to their generating mechanisms. In this thesis, I propose a generative model that models the average of total power, i.e. both the evoked and induced components, termed Dynamic Causal Modelling for induced responses (DCM for IR). Thus the term 'induced responses' in DCM for IR refers to *both* the evoked and induced responses which is different from the conventional definition of induced responses. In chapter 2, I will describe DCM for IR in detail, and in chapter 6, I will further exploit/disassociate the relationship of evoked and induced responses in terms of the generating mechanisms using a generative dynamic causal model.

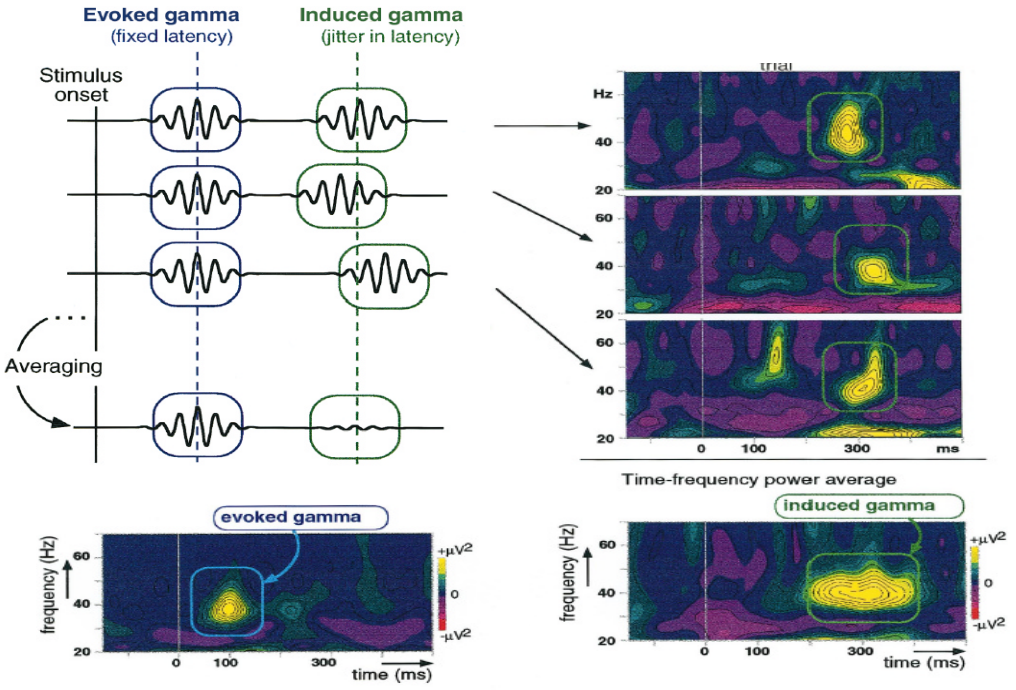

Figure 1.1 Schematic illustration of obtaining evoked and induced responses (adapted from Tallon-Baudry and Bertrand, 1999). Left : the evoked components can be derived from the average of trials in time domain. Right : the induced responses are averaged in the time- frequency domain, preserving non-phase locked components.

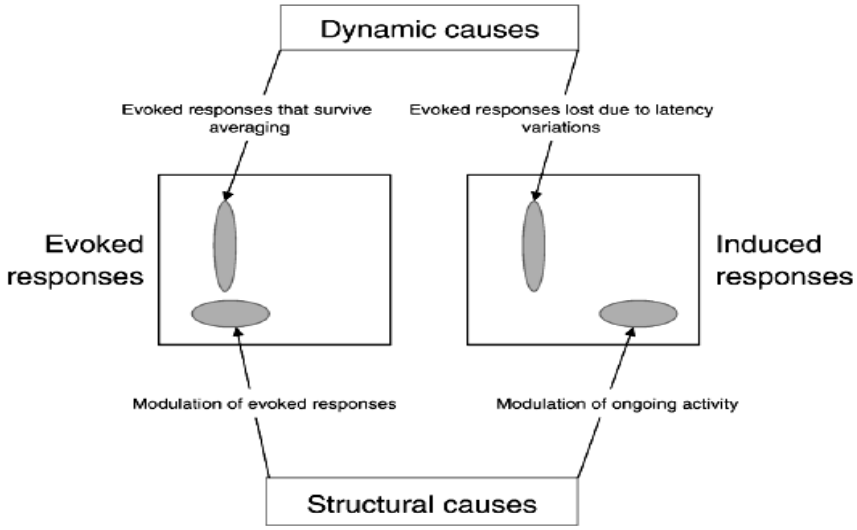

Figure 1.2 Schematic illustration of the relations between dynamic v.s. structural causes and evoked and induced responses (from David et al, 2006)

1.2 Measuring the brainweb: methodological considerations

No man is an island, entire of itself.
John Donne (1572-1631)

The human brain has more than one hundred billion neurons (of the order of 10^{11}) and those neurons work together in 'distributed networks' (Jacobs and Scheibel, 1993; Kandel, 2000). The concept of neural assemblies inspires the analysis of functional neuronal networks. One of the first attempts was to use neuroanatomical maps of cytoarchiteacture that define the connection between brain regions to understand functional networks (Brodmann, 1909). The advent of modern brain mapping techniques has made it possible to investigate cerebral functions in the intact human brain, non-invasively. In particular, the rich and versatile information embedded in EEG/MEG signals together with high temporal resolution offers a good opportunity to understand the dynamics of complex brain functions. However, given the fact that neuronal processing is complex and nonlinear in nature, it is difficult to decipher the neural code completely and the need for development of new modelling methods is growing. In the following section, several methodological issues in studying neural networks are briefly introduced, including linear and nonlinear methods, univariate and multivariate approaches, inferential and non-inferential modelling, and power modulation and phase-synchrony. More comprehensive discussion of the methodological and functional relevance to the specific aims of this thesis work will be provided in chapters 2 to 6.

1.2.1 Linear versus Nonlinear methods

In mathematics, a function f of a set of independent variables $X = \{x_1, x_2 \ldots x_n\} \in R^n$ is linear if it can be written as $f(X) = AX + B$ whilst a nonlinear function is a function that cannot be written in that form, for instance $f(X) = AX^2 + BX + C$ where the matrices A, B and C contain arbitrary constants. The key feature of a linear function is that it satisfies the principle of superposition : $f(aX_1 + bX_2) = af(X_1) + bf(X_2)$. In the field of signal processing and control theory, the characteristics of a system can be described entirely by a fundamental function (Oppenheim, 1999; Stark H., 1994; Moon, 2000). A system is a set of multiple interconnected functional components, comprising three elements: the input X(t), the output Y(t) and the system function *f*(t) (also called impulse response function in the time domain or transfer function in the frequency domain). The system function provides a transformation from the input to the output. A system can be represented mathematically: $Y(t)=f(t) \otimes X(t)$ ($\otimes$ is the convolution operator) and is linear if and only if this system function *f*(t) is linear. This notation enables the effective estimation of neural systems (i.e. coupling) by characterizing the system function. Linear methods use a linear system function to measure dependencies between or among variables whereas nonlinear approaches have a nonlinear system function. In other words, linear analysis engages only the first-order transfer function, which is easy to solve while non-linear methods have the high-order, generalised transfer functions and are capable of catching subtle yet important brain dynamics; in addition to linear features (in some cases, without linear features, for example,

bispectral analysis; see Appendix B for mathematical description). Specifically, in the frequency domain, this speaks to the fact that cross-frequency interactions must be nonlinear because different frequencies can only be coupled through high-order transfer functions (Friston et al 2001). Linear methods can measure only the within frequency coupling using a first order transfer function. This notion is central to my thesis and I will elaborate this point in more detail in chapter 2, along with an exploratory simulation using a neural mass model.

Linear approaches such as coherence and correlation have been used intensively to study oscillatory neuronal activity (Gerloff and Hallett, 1999, Gerloff et al., 1998 and Manganotti et al., 1998; Andrew and Pfurtscheller, 1996; Babiloni et al., 2004; Gross et al., 2001; Kilner et al., 2004; Serrien et al., 2005). Linear methods can extract the most significant features of the data and provide a means of summarizing the system characteristics. However, a linear approximation may not be able to represent all the properties of brain signals accurately (Micheloyannis et al., 2003) as evidence has emerged that nonlinearity is a crucial aspect of brain function (for review, see Stam, 2005). Importantly, nonlinear approaches have been applied widely to study inter-areal communication in the expression of cross-frequency coupling in spectral characterisations of the time-series (Breakspear, 2002; Chen et al., 2009; Jensen and Colgin, 2007; Tallon-Baudry and Bertrand, 1999; Varela et al., 2001; von Stein and Sarnthein, 2000). At the microscopic scale, nonlinear interactions at synaptic connections are believed to have a modulatory effect on generating the post-synaptic responses (Kandel, 2000; see also chapter 5 for examples). However, at the macroscopic scale, the functional role of nonlinear coupling is yet

to be determined (Breakspear, 2002; Robinson et al., 2003; Wright et al., 2001). In animal studies, it has been reported that hippocampal neurons in rats exhibit nested oscillations, where the phase of theta rhythms (~8 Hz) is coupled to the amplitude of a high rhythm at gamma (~40 Hz) frequencies during active exploration. The network of interneurons targeting fast and slow r-aminobutyric acid (GABA) type A receptors is thought to provide substrate for these rhythms and nonlinear coupling (nested oscillation) is believed to associate with declarative memory (White et al., 2000). Nevertheless, evidence is emerging to suggest that nonlinear coupling may mediate the modulatory effects reflecting top-down processing (Friston 2003; von Stein and Sarnthein, 2000a; von Stein et al., 2000b; Breakspear, 2002). This may be important as a behavioural goal can be achieved successfully when the higher areas of the cortical hierarchy predict incoming sensory information and can pass it to lower levels to explain away bottom-up inputs; This is known as predictive coding (Rao and Ballard 1999; Friston 2005). Moreover, nonlinear coupling mechanisms seem to play a critical role in pathological states. From work in patients with Parkinson's disease it has been shown that in the absence of dopamine treatment, the low-beta rhythms (13-20 Hz) in subthalamic nucleus are nonlinearly correlated with the high-beta rhythms (20-35 Hz), as revealed by bispectral analysis (Marceglia et al., 2006) and nonlinear properties of multichannel EEG are manifest (Pezard et al., 2001). In contrast, under the same pathological conditions (symptomatic), cortico-cortical coherence in the motor system is diminished (i.e. decreases of linear relationship) (Cassidy and Brown, 2001) despite the fact that oscillations tend to become synchronized (Brown, 2007). It seems that linear and nonlinear interactions are a

pair of complementary functions of neuronal networks that are dynamically engaged in different brain states and can be differentially modulated in health and disease.

In short, linear measures of the statistical dependency between two time-series are very useful for quantifying long-range interactions using EEG (Bressler, 1995; Gross et al., 2001; Nunez et al., 1997) while nonlinear methods account for the additional coupling among different frequencies. As suggested by Pereda et al, linear and non-linear approaches may assess different parts of the interdependency between signals and one should not be biased by nonlinear methods when choosing analysis strategies (Pereda et al., 2005).

1.2.2 Univariate versus Multivariate approaches

In mathematics, the difference between univariate and multivariate approaches relates to the number of variables being studied. Univariate methods characterize the features of only one variable, whereas multivariate methods deal with more than one variable. Univariate methods provide the estimates of parameters controlling the local fluctuations of neuronal activities at one point (e.g. one MEG channel), whilst multivariate approaches allow the assessment of dependence between signals taking into account the large-scale interactions among distributed network elements. For example, the univariate analyses, such as task-related power (TRPow) or ERD/ERS (Andrew and Pfurtscheller, 1996; Babiloni et al., 2004; Gerloff et al., 1998; Klimesch et al., 1996; Leocani et al., 1997; Manganotti et al., 1998; Oishi et al., 2007; Toro et al., 1994) or correlation

dimension (D2) (Grassberger and Procaccia, 1983; Pritchard and Duke, 1995; Molnár, 1999;Müller et al., 2001) are applied to single time-series and activity in relation to the task manipulation, such as task complexity (the higher the task loading, the greater the D2 value is). Conversely, multivariate methods like Coherence (Andrew and Pfurtscheller, 1996; Babiloni et al., 2004; Kilner et al., 2004; Kilner et al., 2000), Granger Causality (GC) (Granger, 1969 and Granger 1980; see Appendix A for mathematical description) and DCM (Chen et al., 2008; Chen et al., 2009; Friston et al., 2003; Garrido et al., 2007) analyze two or more time-series and provide an estimate of neuronal connectivity, which describes the underlying network functions. Generally speaking, univariate methods are easy to implement and tractable, whereas multivariate approaches involve the estimation of covariance among random fluctuations in different time-series; which is often complicated and difficult without certain assumptions. For example, by assuming the observation errors are independent (or not correlated), the estimate of error covariance becomes simpler since the error covariance matrix becomes a diagonal matrix (Penny et. al. 2004). Perceptions, actions or thoughts, rely upon the integration of functionally specialized brain areas; therefore the multivariate methods seem to be a more appropriate approach when it comes to study brain function as a whole. Although univariate and multivariate analyses address distinct features of the neurophysiological systems, they are not mutually independent of each other. For example, the dimensional complexity of systems described by D2 values (a univariate measurement) decreases as the connectivity of neuronal networks (a multivariate characteristic) increases (Friston 1997b).

1.2.3 Inferential versus Non-inferential modelling

Neuroscience provides abundant data, which call for the development of inferential methods for studying the functional organization of brain. Inferential methods can incorporate prior knowledge into data analysis as deterministic or probabilistic models using Bayes' theorem (Stark H., 1994). Evaluating the posterior distribution on model parameters allows one to make inferences about the underlying model. Non-inferential (or model-free; data-driven) methods, such as independent component analysis (ICA), characterize sources of variation without an explicit model and can be useful in examining properties of dataset and in outlier detection (Jung et al., 2000a; Jung et al., 2000b). When measuring brain network function, non-inferential methods are closely related to descriptive approaches that detect functional connectivity (e.g., correlation or coherence), while inferential methods are required to estimate effective connectivity (see chapter 2 for the distinction between functional and effective connectivity). Importantly, inferential and non-inferential methods differ in the philosophy of analysis strategy: Inferential methods, such as the General linear model (GLM) and Dynamic causal modeling (DCM) (Chen et al., 2008; Chen et al., 2009; Friston et al., 2003), posit certain assumptions about the underlying model and formulate a framework. The analysis and inference that follows focuses on the parameters of the model being tested. In contrast, non-inferential modelling, such as principal component analysis (PCA) or ICA (Dien et al., 2007; Friston et al., 1999; Friston et al., 2000; Jung et al., 2001; Makeig et al., 2004) explores the data and reveals the most likely structure or model suggested by the data. Since non-

inferential modelling requires no priors or formal model specification, it is usually easy to apply but very often difficult to interpret the results. Figure 1.3 summarizes the differences between inferential and non-inferential approaches.

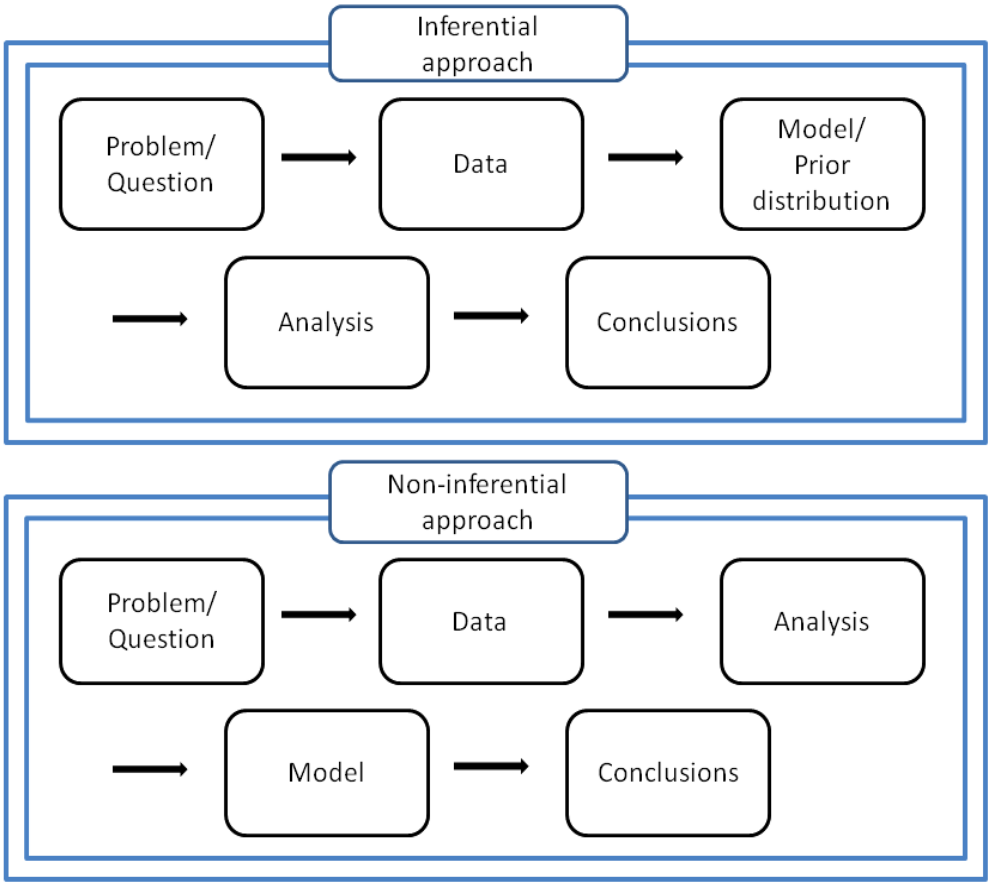

Figure 1.3 The flowchart of data analysis steps with respect to inferential and non-inferential approaches

1.2.4 Power modulation versus Phase synchronization

Oscillatory activity can be projected into two dimensional (time-frequency) space using Fourier or wavelet transforms. This is based on Fourier's discovery 200 years ago that time series (here, the oscillatory activity) are a weighted sum of

basis functions at different frequencies. If the basis functions are known, then the weighting at different frequencies w and time bin t of the time series, i.e. spectrum W(w,t), can be estimated by a convolution procedure (a convolution of the time signal x(t) with a basis function $j(t)$) : $W(w,t) = \int x(t) \cdot \overline{j(l-t)} dl$. The basis functions are a sinusoidal and morlet wavelet for Fourier and morlet wavelet transforms, respectively. As the basis functions in both transforms are complex, so are the spectrum. Therefore, the spectrum comprises two components: the frequency-specific amplitudes (i.e. the power), the squared magnitude of the real part of complex numbers and the instantaneous phase $q(w,t)$, derived from the imaginary part of complex numbers using $q(w,t) = a\tan(im(w(w,t)), re(w(w,t)))$. Neuroscience studies in animals suggest that the synchronous discharge of certain neuronal assemblies reflects an underlying interaction among neurons/areas mediating the functional organizations in the brain, i.e. the binding hypothesis (Singer and Gray 1995). ….For example, one functional role of neural synchrony is apparent in sensorimotor integration. Synchronization of neural responses is observed between visual and parietal areas; as well as between parietal and motor cortices, when awake behaving and well-trained cats process visual information attentively to direct motor responses. Synchrony patterns vary with behavioural situation. This suggests that synchronization may serve for the integration of sensory and motor aspects of behaviour (Roelfsema et al., 1996; Roelfsema et al. 1996 1997). Similar results have been found in monkey studies (Murthy and Fetz, 1992, 1996 a, b; see also the review paper by Engel et al, 1999). This synchronization of neuronal discharges results in the increase of signal power and

constant phase relation between neurons. This phenomenon can be modulated internally or externally before, during or after an event. In other words, "… *this modulation is context dependent, occurs over different time scales and can be transient (e.g., changes of connectivity due to attention modulation) or enduring (e.g., somatotopic reorganisation due to limb amputation)*" (David et al., 2004) and lead to the dynamic fluctuation of the spectral densities (Kilner et al., 2003; Pfurtscheller 1999) and partial phase resetting/shifting over multiple frequencies (Breakspear, 2002; Makeig et al., 2002; Penny et al., 2008; Penny et al., 2002). The dynamic spectral changes of neuronal activity can be considered as the changes of the parameters (for example, coupling strength) that control oscillations in neuronal networks (Pfurtscheller and Lopes da Silva, 1999) where high phase synchronization may reveal the intrinsic firing properties of neurons (Varela et al., 2001). Although phase and power appear to be two different phenomena, they must of course be related by some common generative model (see discussion in chapter 7). Indeed, they could serve as complementary characterizations. Studying the characteristics of oscillatory activity in terms of power modulation and phase synchronization can be a tool to access the functional relations among cortical areas, such as resolving the ‘’binding problem’’ (Gray et al., 1989; Singer 1999; Engel et al., 2001).

In summary, the complex nature of brain function makes it difficult to unravel the information processing in neuronal networks and leads to a debate on the best method to analyze neurobiological data (David et al., 2004). The choice of an appropriate method is dependent on the quality and characteristics of the data and the interpretation of the analytic results is restricted by the methods

employed. Table 1.1 summarizes the main characteristics of the methods discussed above.

Table 1.1 Summary of the main characteristics of mentioned methods

	Linear	Non-linear	Univariate	Multivariate	Inferential	Non-inferential	Power	Phase
Task-related Power (TRPow)	v		v			v	v	
Correlation Dimension (D2)		v	v			v	v	
Coherence	v			v		v		v
Granger Causality (GC)	v	v[+]		v		v	v	
Principal Component Analysis (PCA) / Independent Component Analysis (ICA)		v		v		v	v	
Phase synchrony		v		v		v		v
General Linear Model (GLM)	v			v	v		v	
Dynamic Causal Modelling for Induced responses (DCM for IR)	v	v*		v	v		v	

[+] GC can be extended to measure the nonlinear coupling

* DCM for IR can measure the cross-frequency coupling, i.e. nonlinear interactions, though it uses only the linear/bilinear form to approximate the differential state equations (linearization of the state equations) (see chapter 2 for details).

1.3 Experimental techniques: MEG and EEG

In this thesis, MEG and EEG will be used to measure oscillatory activity in the brain. According to Maxwell's equations, any changes of electrical field will induce an orthogonally oriented magnetic field and vice-versa. In neuronal systems, electric currents flow in the intra- and extracellular space to propagate messages among neurons and their compartments. MEG and EEG provide a measurement that is directly related to electric currents in neurons (Cohen, 1972; Hamalainen, 1992) (Figure 1.4 A). Both MEG and EEG have excellent temporal resolution on a millisecond scale and are particularly suitable for measuring dynamic neural activation. The important distinctions between MEG and EEG are summarized below:

(1) First, the *origins of EEG/ MEG signals* are different. Signals in MEG and EEG derive from the net effect of ionic currents flowing in the dendrites of neurons during synaptic transmission. EEG is sensitive to extracellular volume currents produced by postsynaptic potentials, MEG primarily detects intracellular currents associated with these synaptic potentials because the field components generated by volume currents tend to cancel out in a spherical volume conductor (Hamalainen, 1992). Action potentials are not usually detectable, mainly because the currents associated with action potentials flow in opposite directions and yield zero net magnetic field and very transient time constant (~1ms).

(2) Second, the *detection sensitivity of signal direction*. According to the right-hand rule in electromagnetic theory, the propagation direction of electric

waves is perpendicular to that of magnetic waves (Figure 1.4 B). Therefore, MEG is mainly sensitive to the activity arising from neurons in sulci, which generate currents tangentially with respect to the surface of the head (tangential dipoles) whereas EEG can detect primarily radial sources located in the cortical gyri and those tangential sources secondly (Figure 1.4 C).

(3) Third, the *volume conduction effect*. EEG signal is the result of distortion when electric currents pass through different tissues, as the resistivity is tissue-dependent (such as skull, scalp and cerebrospinal fluid), but not the permeability. So the brain is transparent to MEG resulting in a higher spatial resolution in MEG.

(4) Finally, MEG needs no reference channel which contrasts with EEG, where an active reference can lead to difficulties in the interpretation of the data.

In summary, both MEG and EEG have excellent temporal resolution and are able to follow neural dynamics on a millisecond scale. Although the origins of EEG and MEG signals are different, they can be considered as the complementary device to each other.

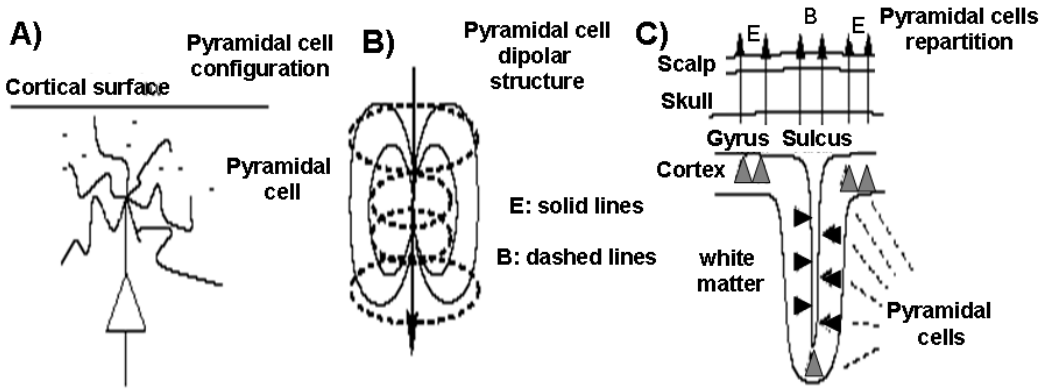

Figure 1.4 The neuronal origins of EEG/MEG signals. A) Pyramidal cells in the cortex . B) The directed electric field (E) and magnetic field (B). C) The difference of directional sensitivity in MEG and EEG. (adapted from a report of The EEG and MEG inverse problems: The adjoint state approach I: The continuous case [1])

1.4 Aims of this thesis

The work in this thesis aims to characterize spatiotemporal dynamics of neural and functional connectivity in human brains. It comprises four main components, covering the development of the methodology followed by scientific applications. Specifically, the aims of this thesis are to:

I. **Chapter 2** : Develop an advanced method, Dynamic Causal Modelling for Induced responses ; DCM for IR, for studying brain networks

[1] This report can be found at http://hal.inria.fr/view_by_stamp.php?label=INRIARRRT&halsid=emgvuuhekiv98jn3b55511nk14&action_todo=view&id=inria-00077112&version=1

II. **Chapter 3 and 4**: Explore nonlinear coupling in the motor system (chapter 3) and address the age-dependent changes in the motor networks (chapter 4) using a simple linear form of DCM

III. **Chapter 5**: Test whether there are functional asymmetries during face perception using a bilinear form of DCM

IV. **Chapter 6**: Dissociate the evoked and induced responses in terms of their generating mechanisms.

CHAPTER 2

DYNAMIC CAUSAL MODELLING OF INDUCED RESPONSES : THE METHOD

2.1 Introduction

The aim of this chapter is to describe a dynamic causal model for induced or spectral responses (DCM for IR) measured with EEG and MEG. The importance and functional roles of induced oscillations have been described in chapter 1 and it is that which motivated this work. The purpose of this chapter is to establish a phenomenological model of how induced responses are caused, and how they evolve dynamically, in a distributed system of coupled electromagnetic sources. This work represents a further extension of dynamic causal modelling to cover spectral responses as measured by the EEG or MEG (David et al 2006a; Kiebel et al 2006, Moran et al., 2007). Inversion of this model, given empirical data, furnishes inferences about different models and the parameters of a particular model. This allows one to disambiguate between different connectivity architectures that may underlie induced responses and to make quantitative

inferences about the coupling among distributed cortical regions. Furthermore, one can assess changes in coupling that result from experimental manipulations or pathophysiology. Critically, this model allows one to distinguish between changes in linear and nonlinear coupling in the brain. The machinery presented here contributes to this endeavour by allowing one to make inferences and quantify changes in either linear or nonlinear coupling, induced experimentally or associated with pathophysiology. I will demonstrate this in the next three chapters to ask whether there is a difference in the relative contribution of linear and nonlinear mechanisms between intrinsic (within-area) and extrinsic (between-area) coupling (chapter 3) and age-dependent changes in the motor networks (chapter 4) and whether backward connections exert greater nonlinear influences than forward connections in visual processing hierarchies (chapter 5). These sorts of questions are central to understanding the nature of neuronal computations and how they are implemented in the brain. In a future work, I will apply this method to assess coupling in the motor system, during recovery from stroke.

There are many approaches to detecting and estimating neuronal coupling using frequency-based analyses of electrophysiological recordings. These can be divided into descriptive and mechanistic; a distinction that is closely related to the difference between functional and effective connectivity. In the following, I discuss various approaches to motivate the present model. In contrast to dynamic causal modelling, the majority of current approaches are descriptive in nature:

2.1.1 Descriptive approaches: detecting functional connectivity

Functional connectivity has been defined as the statistical dependence among remote neurophysiological time-series. To establish functional connectivity one has to show that the statistical dependencies are significant. This entails, in its most general formulation, measuring the mutual information among two or more time-series (Roulston, 1999; Quian Quiroga et al., 2002). There are several approaches to assessing mutual information, which divide broadly into linear and non-linear. The most common approach uses linear systems theory and measures the correlation or coherence between two time-series. It has been shown repeatedly that these measures (the information in the cross-correlation function and coherence is identical) are very useful for quantifying long-range interactions using EEG (Bressler, 1995; Gross et al., 2001; Nunez et al., 1997). Measures of linear dependencies can be generalised to multivariate time-series to furnish interesting formulations in terms of directed transfer functions and Granger causality (Brovelli et al., 2004; Bernasconi et al., 1999).

Nonlinear methods

In terms of non-linear approaches; the most general approach relies upon the notion of generalised synchrony (Rulkov et al., 1995; Schiff et al., 1996), which posits a mapping between the manifolds containing the state-space trajectories of two time-series. These time series may not be correlated or indeed have any obvious formal similarity in their periodic structure. These techniques

usually rely upon some form of temporal embedding or attractor reconstruction. An attractor is a set that describes how a dynamic system will evolve after a long period of time. An attractor could be a point, a torus or have a fractal structure (stranger attractor; examples of which can be found in chaotic dynamics theory). One benefit of reconstructing an attractor for a dynamic system is that one can reduce the dimensionality of a system. For example, for an oscillatory dynamic system, the state-space of the system may be high, but the system can be projected onto a lower dimension space, uniquely determined by its phase. Examples can be found in Penny et al, 2009 and Breakspear and Terry, 2002. Generalised synchronisation exists between two dynamical systems when the state of the response system is a function of the state of the driving system. If this function is continuous, two neighbouring points on the attractor of one system should correspond to two nearby points on the attractor of the other. This correspondence is used to see if the evolution of neighbouring trajectories in one attractor can be used to predict the evolution of a point on the other attractor (see Breakspear and Terry, 2002 for an example). Usually, generalised synchrony is used to detect nonlinear coupling by comparing the mutual predictability (information) between time series before and after destroying their nonlinear dependencies (by randomising their phase relationships). A special case of generalised synchrony is phase-synchrony.

Phase-synchronisation, between two oscillators, is a ubiquitous phenomenon, which appears when they are coupled in a broad range of structures, including EEG sources (Pikovsky et al., 2001). Time-frequency analysis of phase-

synchronisation is popular in current research on cortical networks (David et al., 2003; Engel et al., 2001; Varela et al., 2001). Establishing phase-synchronisation proceeds in two steps; estimation of instantaneous phase and the quantification of the phase-locking. This quantification uses the distribution of phase differences to establish significant mutual information between the two time-series. Both generalised and phase-synchrony can be expressed between coupled systems that show autonomous or indeed chaotic dynamics.

Another approach to detecting nonlinear coupling is based on nonlinear system identification theory for controllable systems. This approach formulates dependencies in terms of generalised or nonlinear transfer functions that are estimated using generalised or poly-spectral analysis. Bispectral measures such as bicoherence (Dumermuth et al., 1971) have been used to detect nonlinear coupling in human EEG (Jeffrey and Chamoun, 1994; Shils et al., 1996). The key thing about nonlinear coupling is that it induces dependencies among different frequencies. I will exploit this below (see also Friston 2000). The same nonlinear cross-frequency coupling is seen in phase-synchrony; two principal forms of cross-frequency phase interactions are recognized (Palva et al, 2005): *n:m* phase-synchrony, which indicates amplitude-independent phase locking of *n* cycles of one oscillation to *m* cycles of another (Tass et al., 1998), and nested oscillations, which reflect the locking of the amplitude fluctuations of faster oscillations to the phase of a slower oscillation (Vanhatalo et al., 2004). These forms of phase synchronisation can be used to disclose non-linear coupling, in which a slower frequency comes to entrain or be entrained by a faster frequency.

In summary, there are several ways to establish the statistical dependencies between two measured time-series (see David et al 2004 for a comparison of these approaches and Pereda et al 2005 for a comprehensive overview of nonlinear methods). However, they are all concerned principally with detecting functional connectivity; they are not concerned with the mechanisms or causes that underlie these dependencies.

2.1.2 Modelling approaches: estimation of effective connectivity

Effective connectivity is defined as the influence that one neural system exerts over another. Critically, this definition posits a causal mechanism for the dependencies described above. In a time-series setting, these models are usually dynamic and rest on differential equations that are causal in a control theory sense. I refer to these models as Dynamic Causal Models (Friston 2003; David et al 2006b). The idea behind Dynamic Causal Modelling is to explain observed responses in terms of a dynamic system that is perturbed by exogenous inputs that are either known or unknown. The model is defined by the form and parameters of differential equations that describe the evolution of the system states. Inversion of these models allows one to make inferences about the models and their parameters. Critically, this allows one to compare different models and quantify them in terms of the conditional density over both models and parameters. These models are based on specific hypotheses about putative sources and their assumed connectivity. This is a fundamental departure from descriptive approaches to

functional connectivity because it allows one to answer questions about the mechanisms and functional architectures that cause observed responses. These questions are posed in terms of competing models, which are evaluated in relation to each other; clearly, the answers that obtain are conditional on the models considered.

In contrast to the descriptive approaches, there are relatively few causal models of spectral responses. Those that do exist can, again, be divided into linear and non-linear. Linear models are normally derived by linearising a neurobiologically informed nonlinear model of neuronal dynamics (e.g., a mean-field or neural mass model) and evaluating the spectral response under some assumptions about the spectral composition of exogenous input (Wright and Liley 1994). Steady-state spectral measurements can then be used to invert the model and infer on important biophysical parameters such as rate constants or coupling parameters (Rowe et al, 2005; Moran et al 2007). In the non-linear and dynamic domain there are even fewer models. An important class are models that are based upon loosely coupled oscillators:

Models of spectral dynamics

The theory of coupled phase oscillators has found many applications to biological, chemical and physical phenomenon (Kuramoto, 1984; Kopell and Ermentrout, 1986). Under certain assumptions, the behaviour of networks of neurons with largely oscillatory output can be approximated by a system of

equations that govern the phases of each oscillator (Ermentrout and Kleinfeld 2001)

$$\dot{y}_i = w + \sum_j f(y_i - y_j) \qquad 1$$

Here y_i is the instantaneous phase of the *i*-th unit or population; $w = 2pv$, where v is the intrinsic frequency of the oscillators and $f(y_i - y_j)$ is the effective coupling, which is a non-linear [periodic] function of the phase-difference between two oscillators. The sum runs over all units that are connected. In these models, it is assumed that the amplitude of the oscillations is unimportant and the key dynamics are narrow-band. This equation recently has been used recently as the basis of a dynamic causal model for phase coupling (Penny et al, 2009).

The model above speaks to a specific class of DCMs: DCMs can be phenomenological or biophysical. Biophysical DCMs are constrained by the known physical or biological processes generating the observed signals. In contrast, phenomenological DCMs describe the causal dynamics in a purely formal fashion. Equation 1 is an example of this, where the form of the effective coupling can be motivated using neurobiological constraints (see Ermentrout and Kleinfeld 2001) but is not formulated explicitly in terms of neuronal processes. The DCM described in this chapter is phenomenological and complements models based on instantaneous phase by modelling the evolution of instantaneous power:

$$\dot{g}(w)_i = \sum_j f(g(w)_i, g(w)_j) \qquad 2$$

Here, $g(w)_i$ is the spectral density, over frequency w, of the i-th unit. In this model, temporal changes of power in a source are explained as a network function of power in all sources. This sort of model can deal with situations in which oscillations in one area become amplitude modulated by oscillations in another band in the same or another areas; e.g. theta-band modulation of gamma activity (e.g., Guderian and Düzel 2005). Here, high levels of theta activity would engender increases in gamma.

This model is phenomenological in the sense I make no attempt to motivate the form of effective coupling, $f(g_i, g_j)$ but simply use the coefficients of its Taylor expansion as parameters (see below). Note that it is possible to model the nested rhythms (see chapter 1 for the definition and chapter 7 for examples), but it is beyond the scope of this thesis. This is exactly the same device used in bilinear DCMs for functional magnetic resonance imaging (fMRI) time-series (Friston et al, 2003) and is recapitulated here for spectral responses as measured with EEG or MEG. The ensuing simple form for the DCM is particularly useful because it allows us to partition the effective coupling between regions at the same frequency and between regions across frequencies. This is important because, as noted above, within-frequency coupling is generally mediated by linear mechanisms, whereas cross-frequency coupling rests on non-linear mechanisms. This is pertinent to neuronal dynamics, where nonlinear mechanisms may predominate in functional integration.

In summary, the DCM elaborated below describes the phenomenological evolution of spectral densities in multivariate time-series; it is formulated to model coupling within and between frequencies that are associated with linear and non-linear mechanisms respectively. This is similar to the bilinear form adopted for fMRI, which distinguishes between task or stimulus-invariant coupling (linear) and context-sensitive (nonlinear or bilinear) changes in that coupling.

2.1.3 Overview

This chapter comprises four sections. In the first, I reprise, briefly, a generalised convolution model of neuronal coupling (Friston 2000) to demonstrate the link between cross-frequency coupling and nonlinear mechanisms. I illustrate these phenomena using a neural-mass model that is the basis of biophysical DCMs for ERPs (David et al 2006b). In the second section, I describe a DCM for induced responses and relate its parameterisation to the generalised convolution models of the first section. The model provides the likelihood function of a generative model, which is inverted using standard variational techniques. This inversion is summarized briefly in the last part of this section. In the third section, I try to establish the face validity of the model using synthetic data, where the true inputs and architecture are known. I generated synthetic data and compared linear and nonlinear models to identify the veridical model. This enabled us to establish face validity and see how the inversion behaves under different noise levels. The fourth section provides a demonstration of the model and its inversion using real EEG data acquired during face perception.

2.2 Nonlinear and cross-frequency coupling

In this section, I show why nonlinear mechanisms are mandatory for coupling across frequencies. I have dealt with this issue in a series of papers on the theoretical neurobiology of functional integration (e.g. Friston 2000; 2001) and summarize the main points here. The results in this section are not necessary to derive the DCM of the next section; they are used to highlight the sorts of behaviours that this model has to accommodate.

2.2.1 Generalised convolution models

In what follows, I treat any neuronal system or electromagnetic source as an input-state-output system. I will show that if this neuronal system is nonlinear, the energy at one frequency in the inputs (from other sources) manifests at different frequencies in the outputs. This induces cross-frequency coupling between any two sources, when the output of one serves as the input the other. The Fliess fundamental formula (Fliess *et al* 1983) describes the causal relationship between system outputs and the history of its inputs. This relationship conforms to a Volterra series, which expresses the output as a generalised convolution of the input, critically without reference to any hidden states. This series is a functional Taylor expansion of the outputs, $y(t)$ with respect to the inputs $u(t)$ (Bendat

1990). The reason it is a *functional* expansion is that the inputs are a function of time[1].

$$y(t) = \sum_i \int \ldots \int k_i(s_1,\ldots,s_i)u(t-s_1),\ldots,u(t-s_i)ds_1,\ldots,ds_i$$
$$k_i(s_1,\ldots,s_i) = \frac{\partial^i y(t)}{\partial u(t-s_1),\ldots,\partial u(t-s_i)} \qquad 3$$

where $k_i(s_1,\ldots s_i)$ is the *i*-th order kernel. The integrals are over the past or history of the inputs, which renders the system causal. Introducing the spectral representation in terms of the unitary Fourier transform pair[2]

$$u(t) = \int s_u(w)e^{jwt}dw$$
$$s_u(w) = \int u(t)e^{-jwt}dt \qquad 4$$

where, $g_u(w) = \langle s_u(w), s_u(-w) \rangle$ is spectral density; I can rewrite the Volterra expansion and it transform as

$$y(t) = \sum_i \int_{-p}^{p} \ldots \int_{-p}^{p} e^{j(w_1+,\ldots,+w_i)t}\Gamma_i(w_1,\ldots,w_i)s_u(w_1),\ldots,s_u(w_i)dw_1,\ldots,dw_i$$
$$s_y(w) = \sum_i \int_{-p}^{p} \ldots \int_{-p}^{p} \Gamma_i(w_1,\ldots,w_i)s_u(w_1),\ldots,s_u(w-w_1\ldots-w_i)dw_1,\ldots,dw_{i-1} \qquad 5$$

where the functions

[1] For simplicity, I will deal with a single input and a single output
[2] Omitting constants of proportionality for clarity

$$\Gamma_1(w_1) = \int_0^\infty e^{-jw_1 s_1} k_1(s_1) ds_1$$

$$\Gamma_2(w_1, w_2) = \int_0^\infty \int_0^\infty e^{-j(w_1 s_1 + w_2 s_2)} k_2(s_1, s_2) ds_1 ds_2$$

$$\dots$$

are the Fourier transforms of the kernels. These functions are called *generalised transfer functions* and mediate the expression of frequencies in the output given those in the input. Critically, the influence of higher order kernels, or equivalently generalised transfer functions means that a given frequency in the input can induce a *different* frequency in the output. A simple example of this would be squaring a sine wave input to produce an output of twice the frequency (Friston 2001). Generalised transfer functions are usually estimated through estimates of polyspectra. For example, the spectral form of Equation 5 and its high-order counterparts are[3]

$$\begin{aligned} g_{uy}(-w_1) &= \Gamma_1(w_1) g_u(w_1) \\ g_{uuy}(-w_1, -w_2) &= 2\Gamma_2(w_1, w_2) g_u(w_1) g_u(w_2) \\ &\vdots \\ g_{u\dots y}(-w_1, \dots, -w_n) &= n! \Gamma_n(w_1, \dots, w_n) g_u(w_1) \dots g_u(w_n) \end{aligned} \qquad 6$$

Coherence (sometimes called coherency), $g_{uy}(w)$ is simply the second-order cross-spectrum between the input and output and is related to first-order

[3] These equalities hold only when the Volterra expansion contains just the *n*-th order term and are a generalisation of the classical results for the transfer function of a linear system.

effects (*i.e.* the first-order kernel or transfer function). Coherence is therefore a surrogate for first-order or linear connectivity. Bicoherence or the cross-bi-spectrum $g_{uuy}(w_1,w_2)$ is the third-order cross-poly-spectrum and implies a non-zero second-order kernel or transfer function. See Friston (2000), Jeffrey and Chamoun (1994) and Shils et al (1996) for examples of detecting nonlinear coupling with bi-spectral analyses and Priestley (1988) for the mathematical background.

In the present context, the thing I need to take from this formulation is that the only way one frequency in the input can modulate another frequency in the output is through second or higher-order kernels. This means that dependencies between different frequencies are mediated by non-linear coupling. I can express this in terms of the changes in the spectral density of the response, induced by changes in the input; where, under linear coupling

$$\frac{\partial g_y(w_1)}{\partial g_u(w_2)} = \begin{cases} |\Gamma_1(w_1)|^2 & w_1 = w_2 \\ 0 & w_1 \neq w_2 \end{cases} \qquad 7$$

2.2.2 An illustration using a nonlinear neural-mass model

To illustrate the induction of responses across different frequency bands, I evaluated the time-frequency power of the input and response of a nonlinear neural-mass model of electromagnetic sources. The neural mass model is the

same model used in David et al (2006b) and is used in DCM for event-related potentials.

Briefly, the model is based on linear post-synaptic responses to pre-synaptic input. Three different populations are coupled using their mean firing rates, which are a static nonlinear function of voltage as shown in Figure 2.1. The dynamics of each neuronal subpopulation *i* are governed by second-order differential equations in voltage of the form

$$\ddot{V}_i + 2k_i\dot{V}_i + k_i^2 V_i = k_i H_i \sum_j g_{ij} S(V_j) \qquad 8$$

The form of the implicit response kernel and nonlinear voltage-firing curve, $S(V_j)$ are shown in Figure 2.2. The three subpopulations correspond roughly to the supragranular, infragranular and granular layers of cortex and are interconnected (with coupling parameters, g_{ij}) according to known connectivity rules. The nonlinearity in Equation 8 makes this a useful model of weak nonlinear coupling among neuronal sources. Figures 2.3 and 2.4 such show the results of perturbing this model of neural masses; the time-frequency profile of the input and responses show how nonlinear transformations induce frequencies not present in the input:

The top panels of Figure 2.3 show the input (left) and output (right) in the time-domain and the lower panels show the same data in time-frequency format.

The response at each time and frequency was estimated using a Fourier transform with a sliding Gaussian window

$$g_y(w,t) = \left| \int y(s-t)\exp(-s^2/2s^2)e^{-jws}ds \right|^2 \qquad 9$$

where $s = 256$ ms specifies the width of the window. The input was a four second box-car function plus random fluctuations, sampled from a Gaussian density with a standard deviation of one sixteenth of the box-cars amplitude. It can be seen that the response has a very different spectral profile to the input, with marked power in the 10 – 20 Hz range. However, this response could be meditated by linear effects and represent a filtering of the broad band input. To illustrate nonlinearity, I repeated the simulation but using a four second pure sine-wave input at 16Hz. The left-hand panels of Figure 2.4 show clearly that this single frequency induces structured responses at much higher frequencies. To ensure this cross-frequency induction was mediated by nonlinear mechanisms, I repeated the simulation but scaled the input down by a factor of 128; this keeps neuronal states within the linear regime of the models depolarisation-firing curve and suppresses nonlinearity (see Figure 2.2, right). Following this single change, the spectral output is now a quasi-copy of the input (see right-hand panels). It is this sort of linear and nonlinear neuronal coupling, among neuronal populations, I want to model and make inferences about.

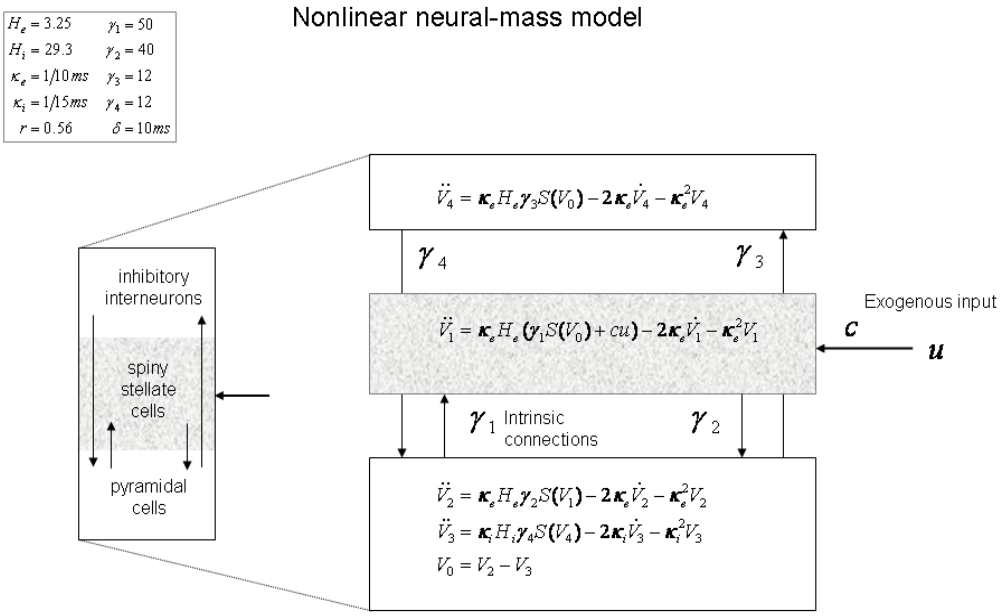

Figure 2.1 Nonlinear neural-mass model used to illustrate non-linear transformations (see David et al. 2003 for details). This model comprises three interconnected subpopulations. The model uses a transmembrane potential state-space model at the synaptic level and a nonlinear sigmoid transformation $S(V)$ at the soma of neurons to model spike rates.

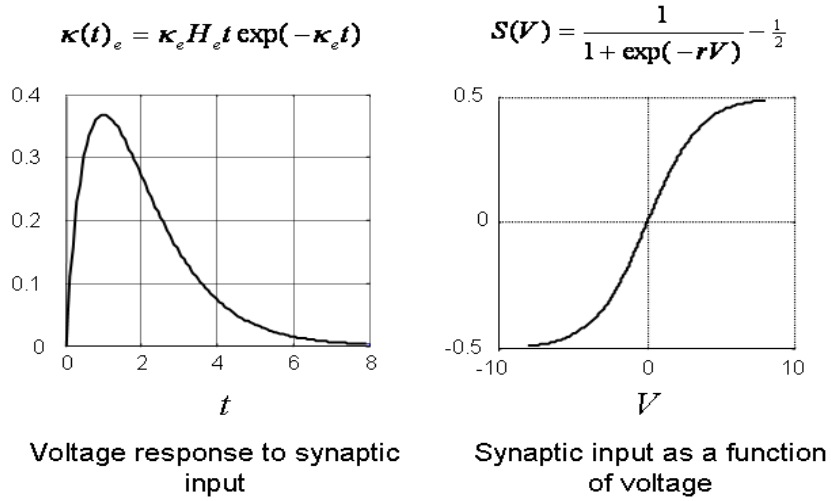

Figure 2.2 The implicit form of the linear impulse response function of transmembrane potential (left) and the sigmoid firing-input curve $S(V)$ (right).

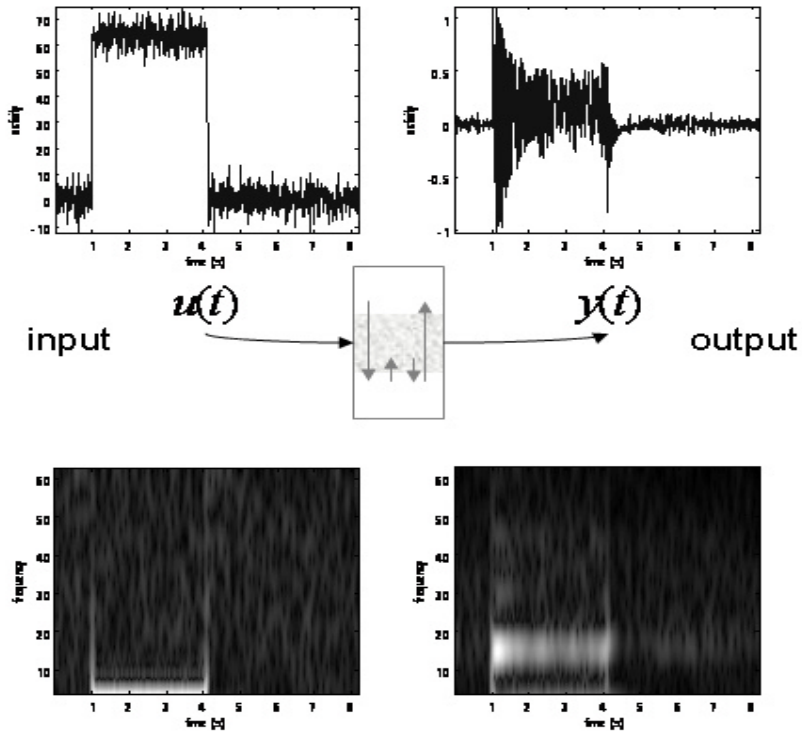

Figure 2.3 The input-output relation of the neural mass model (Figure 2.1) in the time-frequency domain. Left: deterministic input comprising a four second box-car function plus random fluctuations (top) and its spectral profile (bottom). Right: response time course (top) and its spectral profile (bottom).

In the next section, I describe DCM for induced responses, where the states of each neuronal source are summarised in terms of their spectral profiles. I will see that a simple parameterisation of this model allows for a partitioning of within and between frequency coupling and, implicitly, a partitioning into dynamics that can be attributed to linear and nonlinear effects.

High amplitude inputs (nonlinear)

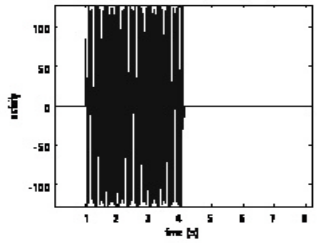

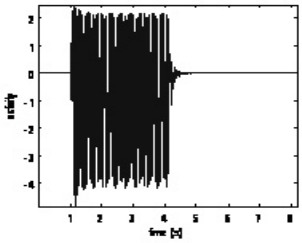

input output

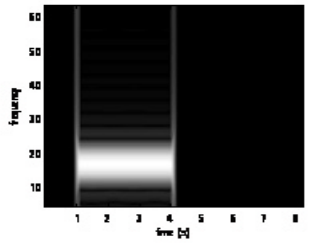

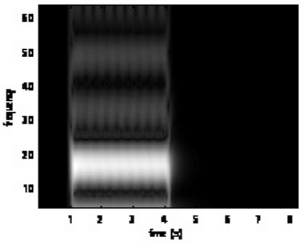

Low amplitude inputs (linear)

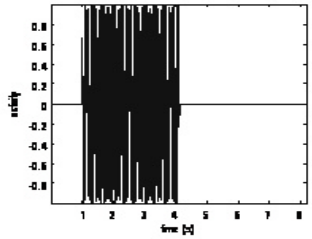

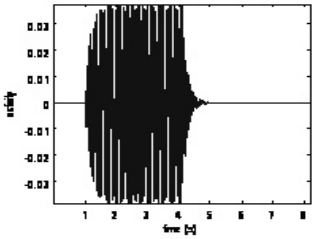

input output

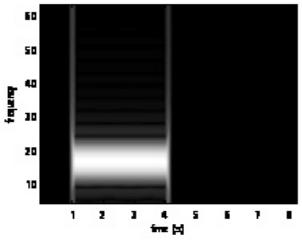

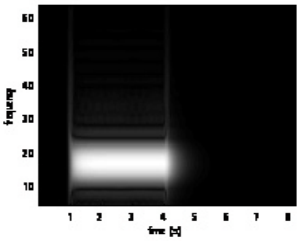

Figure 2.4 The time-frequency profiles of inputs and responses of the neural mass model in previous figures, showing nonlinear and linear effects. Upper panel: High input amplitude engages the nonlinear regime of the neuronal mass model, such that narrow-band input induces structured responses at higher frequencies. Lower panel: after scaling the input down by 128, the system operates in the linear regime and the spectral output is a simple copy of the input.

2.3 Dynamic causal model

This section describes the dynamic causal model, which I will invert in subsequent sections to make inferences about synthetic and real data. Probabilistic model inversion requires a generative model. A probabilistic generative model requires the specification of a *likelihood model* and its *priors*. The likelihood model simply describes the probability of obtaining some data features (in this case spectra) given a model and its parameters, while the priors place constraints on the parameters.

2.3.1 A model for spectral features

The generalised convolution model of the previous section assumes neuronal dynamics are stationary; i.e., they express the same power over time. This model is fine for continuous steady-state electrophysiological recordings and

has been used as a DCM for steady-state local field potential recordings (Moran et al 2007). However, evoked brain dynamics are non-stationary and evolve over peristimulus time. This means I need a DCM of time-dependent changes in spectral energy. The model described below assumes that the spectral energy at one frequency in a source causes changes in the same (linear coupling) or different (nonlinear coupling) frequencies, in other sources. It is fairly simple to show that, under a linear state-space model of these changes in spectral density, the coupling between changes in frequency determines the coupling between frequencies at steady-state. This means that between-frequency coupling in the DCM must be mediated by nonlinear mechanisms (by Equation 7 of the previous section).

Consider J sources in the brain, each described by a state vector, $g_j(w,t) \in \Re^{K\times 1}$ of spectral densities at K frequencies

$$g_j(w,t) = \begin{bmatrix} g_j(w_1,t) \\ \vdots \\ g_j(w_K,t) \end{bmatrix} \qquad 10$$

I will treat these spectral states as perturbations around their expected levels, in the absence of exogenous input. I can model the dynamics of these spectral states using a first-order Taylor expansion of Eq. 2 to give

$$t\dot{g}(t) = t\begin{bmatrix} \dot{g}_1 \\ \vdots \\ \dot{g}_J \end{bmatrix} = \begin{bmatrix} A_{11} & \cdots & A_{1J} \\ \vdots & \ddots & \vdots \\ A_{J1} & \ldots & A_{JJ} \end{bmatrix} g(t) + \begin{bmatrix} C_1 \\ \vdots \\ C_J \end{bmatrix} u(t) \qquad 11$$

Where the matrices A and C contain coupling parameters that control changes in spectral activity induced by other sources and exogenous (*e.g.*, stimulus) inputs, $u(t)$

$$A_{ij} = \begin{bmatrix} a_{ij}^{11} & \cdots & a_{ij}^{1K} \\ \vdots & \ddots & \vdots \\ a_{ij}^{K1} & \ldots & a_{ij}^{KK} \end{bmatrix} \quad C_i = \begin{bmatrix} c_i^1 \\ \vdots \\ c_i^K \end{bmatrix} \qquad 12$$

Under this model, the scalar a_{ij}^{kl} encodes how changes in the *k*-th frequency in the *i*-th source depend on the *l*-th frequency in the *j*-th source. The leading diagonal elements are $a_{ii}^{kk} = -1$; this means that each frequency has an intrinsic tendency to decay or dissipate. Similarly, c_i^k controls the frequency-specific influence of exogenous inputs on the *k*-th frequency in the *i*-th source. This enables within and between-frequency coupling within and between sources. In later work, I will generalise the above model, $t\dot{g} = Ag + Cu$ to a bilinear approximation, in which experimental effects, v (*e.g.*, condition or trial-type under which the responses were elicited) can change the coupling. This involves the inclusion of a bilinear term in Equation 11 to give

$$t\dot{g} = (A + \sum_j v_j B^j)g + Cu \qquad 13$$

In this chapter I will focus on the modelling of induced responses for a single trial type and ignore trial-specific influences.

Steady-states responses

This simple first-order DCM can be related to the spectral representation of input-output systems of the preceding section by considering its equilibrium solution; in other words, the states to which the DCM converges. Under these steady-state conditions, $\dot{g} = 0$ and $Ag = -Cu$. Recall that $a_{ii}^{kk} = -1$; this means that when the DCM is at equilibrium, the within-frequency coupling a_{ij}^{kk} between sources plays the same role as the first-order transfer function of the previous section (*c.f.*, Eq. 5).

$$\begin{aligned} \dot{g}_i(w_k) &= 0 \\ &= \sum_{j,l} a_{ij}^{kl} g_j(w_l) + c_i^k u \Rightarrow \\ g_i(w_k) &= \sum_{j,l \neq i,k} a_{ij}^{kl} g_j(w_l) + c_i^k u \end{aligned} \qquad 14$$

$$\Rightarrow \frac{\partial g_i(w_k)}{\partial g_j(w_l)} = \begin{cases} a_{ij}^{kk} & w_k = w_l \\ a_{ij}^{kl} & w_k \neq w_l \end{cases}$$

Equation 14 says that if the inputs are changing slowly (and I can assume $\dot{g} \approx 0$), I would see that long-term fluctuations in the k-th frequency in the i-th source scale with fluctuations in the l-th frequency of the j-th source in proportion to a_{ij}^{kl}. However, I know from the previous section that any dependencies among frequencies are mediated by nonlinear mechanisms. This means that, under linear coupling, all the cross-frequency coupling parameters must be zero; $\forall i \neq j : a_{ij}^{kl} = 0$. If any are not; $\exists i \neq j : a_{ij}^{kl} \neq 0$, I can infer a nonlinear coupling between sources i and j. Clearly, I am not suggesting that steady-state is actually attained by the brain; but I can assume convergence, following perturbation, is fast relative to changes in exogenous input. In other words, I can integrate the differential state questions by linearising the dynamics with respect to their fixed points, under the assumption that the changes in spectral dynamics are sufficiently slow, with respect to the changes in exogenous input (i.e. steady state). The fixed points (or equilibrium points) can be found when the changes of spectral densities are close enough to zero and this is governed by the (unknown) convergence rate parameter t in Eq. 11, estimated from the data. Tau can be regarded as a global (lumped) time-constant that reflects the characteristic time-constant of the underlying population dynamics.

In summary, if I discount all the between-frequency couplings and consider the equilibrium solution of spectral dynamics (*i.e.*, when the rate of change frequency is zero): the spectral power at a given frequency in one region is determined by the power at the same frequency in other regions. This is the sort

of coupling that would be expected under linear mechanisms. Conversely, between-frequency coupling can be attributed to nonlinear coupling.

The spectral dynamics of sources

Having established a model of spectral responses of the sources it is now necessary to specify how these responses are expressed in measurement space. In some instances this would not be necessary; for example, in local field potential or intracranial recordings obtained directly from each source. However, I will assume the measurements have been obtained non-invasively using EEG or MEG. Consider the conventional linear forward model for electromagnetic sources $x(t) = [x_1(t), \ldots x_J(t)]^T$ and the corresponding lead-field matrix L for multi-channel of data, $d(t)$. The observed response is a mixture of activity over all sources

$$\begin{aligned} d(t) &= Lx(t) \Rightarrow \\ s_d(w) &= Ls(w) \\ g_d(w) &= L\left\langle s(w)s(-w)^T \right\rangle L^T \end{aligned} \qquad 15$$

This means spectral responses in channel space are a mixture of the inner product of Fourier coefficients. Unfortunately, this DCM does not model these coefficients; this would require modelling both the power and phase of source activity, so that the coherence among sources $\left\langle s(w)s(-w)^T \right\rangle$ could be generated.

To circumnavigate this problem, I project the data from channel space to the sources and then compute the spectral density

$$x(t) = L^{-} d(t)$$
$$\tilde{g}_i(w,t) = \left| \int x_i(s-t) \exp(-s^2/2s^2) e^{-jws} ds \right|^2 \qquad 16$$

where $\tilde{g}(w,t)$ are the spectral responses modelled by the DCM and L^{-} is the generalised inverse of the lead-field matrix for the chosen sources. Eq.16 is formally equivalent to a Morlet wavelet transform, where the window width scales inversely with the frequency. In this work I use $s = kw^{-1}$, which covers about k cycles. In theory, this k parameter allows a trade-off between time and frequency resolution. A larger parameter results in a smoother spectral density estimate and loss of temporal resolution. Usually, this parameter must be greater than 5 to give an efficient estimate of spectrum (Lachaux et al., 2002), because of spectral leakage (as the window becomes small, in relation to wavelength). In this thesis, 7 was chosen based on prior knowledge (the characteristic time-constants of event-related spectral responses).

The inversion of the electromagnetic part here can be seen as feature selection, in the sense that Eq. 16 is a deterministic nonlinear function of channel data that returns spectral features associated with specific source locations. The advantage is that there is a unique solution for the features because the prior specification of source locations means the inverse problem is not ill-posed;

provided the number of (equivalent current dipoles ; ECD) sources is small relative to the number of channels. Note that the generalised inverse of the lead-field in Eq. 16 is one of many inversion schemes that one can use to project data from channel to source space (Darvas et al., 2004; Friston et al., 2008; Kiebel et al., 2007; Michel et al., 2004). The generalised inverse is an appropriate projector if one knows a priori where the sources are located. In other words, when there is no source localization problem. Once these locations have been established, the generalised inverse of the associated lead-field matrix furnishes a near-optimum ECD summary of activity that avoids suppression of local correlated activity. In this model, I assume the source locations are specified and leave optimization of these spatial parameters to another study.

Note that the model generates time-varying power at each source, whereas the spectral features I extract in Eq.16 have three moments. It would be simple to include free parameters that map the predicted source power to these three moments but these parameters are of no interest. Therefore, I simply add the power over the moments and estimate a single free parameter, G_i, which scales the power of underlying neuronal dynamics to give the observed mixture $\tilde{g}_i(w,t)$.

2.3.2 The probabilistic model

I now have, under Gaussian assumptions about observation error, e , a likelihood model for observed spectral activity in sources $\tilde{g}_i(w_j, t_k)$ that can be expressed as a mixture of predicted activity $g_i(w_j, t_k)$, baseline power and random fluctuations:

$$\tilde{g}_i(w_j, t_k) = G_i g_i(w_j, t_k) + r_{ij} + e_{ijk} \quad \Leftrightarrow \quad p(\tilde{g}_i^j(t_k) \mid q) = N(G_i g_i^j(t_k) + r_{ij}, l^{-1}V) \quad 17$$

The predicted activity obtains by integrating Eq.11, given the parameters, $q \supset t, A, C, G$ and input $u(t)$. The scalar r_{ij} models baseline power over time at the *i*-th source and *j*-th frequency[4]. A likelihood model furnishes a way of measuring the likelihood of observed data; put simply, one generates a prediction using the model parameters and input. The probability of getting the observed data-features is then specified by the amplitude of the prediction errors, relative to the precision (inverse variance) of the random fluctuations. l is the precision of this measurement noise in feature-space (power over sources and frequency) and is estimated as a free parameter. This scale parameter scales a temporal correlation matrix V encoding serial correlations among the observation noise. Because the time-frequency analysis necessarily smoothes random effects, I made V a Gaussian autocorrelation matrix, with a standard deviation of 32ms. The standard deviation of the noise autocorrelation $s_V > s$ is bound by the window-width, s in the time-frequency analysis in Eq.16. This window imposes serial correlations on spectral data-features and implicitly any random fluctuations. I chose a value

[4] In practice, I estimate the baseline power as the frequency at the first time-bin.

that corresponds to the correlations induced by evaluating frequencies at $f \approx s_V^{-1} \approx 30\,\text{Hz}$.

In this work, the priors $p(q)$ on the model parameters were Gaussian shrinkage priors. Table 2.1 lists their prior densities and Figure 2.5 provides a graphical summary of the ensuing model. Note that non-negative scale parameters have log-normal priors[5].

Table 2.1 Priors on model parameters

Parameter q	Description	Prior density $p(q)$
$a = q_m^2/q_s$ $b = q_m/q_s$ $q_m = 80\exp(q_1)$ $q_s = 1024\exp(q_2)$	*input (Gamma) parameter*	$p(q_1) = N(0, \frac{1}{16})$ $p(q_2) = N(0, \frac{1}{16})$
$t = 1/16\exp(k)$	*Convergence time*	$p(k) = N(0, \frac{1}{4})$
A_{ij}^{kl}	*Internal coupling*	$p(A_{ij}^{kl}) = \begin{cases} N(0,1) & \textit{present} \\ N(0,0) & \textit{absent} \\ N(-1,0) & i = j \wedge k = l \end{cases}$
C_i^k	*External coupling*	$p(C_i^k) = \begin{cases} N(0, \frac{1}{16}) & i = \textit{input} \\ N(0,0) & i \neq \textit{input} \end{cases}$
$G_i = \exp(q_i^G)$	*Power scaling*	$p(q_i^G) = N(0, \frac{1}{512})$

[5] I also used weakly informative log-normal hyperpriors on the precision hyperparameter.

Exogenous input

The predicted power obtains by integrating Eq. 11. This requires the stimulus input to be specified. This exogenous input causes a burst of power in the network of sources. The frequency selectivity of this perturbation is encoded by the free parameters C above. This input models changes in source activity, caused by putative subcortical afferents whose activities are time-locked to stimuli. The frequencies induced depend on the model's free parameters, which are optimised during inversion. From the point of view of each source, there is no real difference between the effects of exogenous input and input from other sources (see Eq. 11).Typically, only a few sources are allowed to receive exogenous input, which can have an arbitrary and source-specific frequency profile. Sources that do not receive input have their input parameters 'switched off' by priors that are precisely zero. The temporal form of the input is not known and has to be estimated. In this study, I use a simple parameterisation, which assumes the spectral perturbation has the form of a gamma distribution.

$$u(t) = \frac{b^{a} t^{a-1} e^{-bt}}{\Gamma(a)} \qquad 18$$

where $\Gamma(a)$ is the gamma function and priors on the input parameters, a, b are chosen such that the peak of the input is at about 80ms, with a dispersion of about 32ms (see Table 2.1). The free parameters now comprise,

$q \supseteq a, b, t, A, C, G$. Note that the C parameter encodes the frequency-selective responses to the exogenous input (see Figure 2.8 b for example); and will have zero mean and zero variance for areas that do not receive any exogenous inputs (see Table 2.1). Gi scales the output of the dynamic system (i.e. caused by exogenous input and input from other areas, through non-zero coupling) to give the observed spectrum. Gi is area-dependent but not frequency-dependent.

The choice of 80ms as the prior latency of the input is motivated by known latencies from single-unit electrode recording studies of visual and inferotemporal cortex (*e.g.*, Hirsch et al 2002). It takes this amount of time for visual input to reach secondary and higher visual areas. This is also the time when evoked sensory potentials start to express themselves in cortical sources (i.e., the N1 component). Note that the latency is a free parameter, so that suboptimal priors (within some reasonable bound), will be corrected during model inversion. In addition, relatively informative priors were placed on uninteresting free parameters to allow for small variations; these include the input parameter (gamma function), convergence time (tau), external coupling (C) and the power scaling (Gi). These weakly informative priors, come from an earlier study (Friston et al, 2003), while the internal coupling parameters (A and B) have essentially non-informative priors (variance of one) as we aim to infer on these.

Frequency bands and modes

Hitherto, I have considered the states as spectral densities at a discrete number of frequencies or frequency bands. These states can be regarded as the coefficients of narrow-band spectral basis functions or frequency-modes. In practice, I actually use the orthonormal principal modes of the source data, $U = [U_1, \ldots, U_K]$, obtained by a singular value decomposition (SVD) of the spectral responses over time and sources, where $\tilde{g} = U\Lambda V^T$ and Λ is a leading diagonal matrix of singular values. This means that instead of working with K' frequencies, I can reduce the problem to modelling the coupling among $K < K'$ modes that cover all frequencies in different proportions.

In this context, the states g_i^k represent the contribution of the *k*-th frequency-mode, $U_k(w)$ to the spectral dynamics of the *i*-th region. I can project the predicted spectral dynamics in the state-space of frequency modes to frequency space using, $g_i(w) = Ug_i$. Similarly, one can characterise the coupling as functions of frequency; *i.e.*, $A_{ij}(w_k, w_l) = UA_{ij}U^T$ and $C_i(w) = UC_i$. These projections are possible because the frequency modes are orthonormal and I am using a linear DCM. I typically use between two and four modes, which account for about ninety percent of the observed variance in spectral responses. I have specified the likelihood and priors of this generative model and can now turn to model inversion and comparison.

2.3.3 Bayesian inversion of DCMs

In this section, I review briefly model inversion and selection. For a given DCM, say model *m*; parameter estimation corresponds to approximating the moments of the conditional or posterior distribution given by Bayes rule

$$p(q \mid \tilde{g}, m) = \frac{p(\tilde{g} \mid q, m)\, p(q, m)}{p(\tilde{g} \mid m)} \qquad 19$$

The estimation procedure employed in DCM is described in Friston *et al* (2006). The posterior moments (conditional mean m and covariance Σ) are updated iteratively using Variational Bayes under a fixed-form Laplace (*i.e.*, Gaussian) approximation to the conditional density $q(q) = N(m, \Sigma)$. This is equivalent to Expectation-Maximization (**EM**) that employs a local linearization of the predicted responses about the current conditional expectation of the parameters. The **E**-step conforms to a Fisher-scoring scheme that optimises the variational free energy $F(q, l, m)$ with respect to the conditional moments. In the **M**-step, the precision parameters l are updated in exactly the same way to provide their maximum likelihood estimates. The estimation scheme can be summarized as follows:

$$\begin{aligned} \mathbf{E}-\text{step} \quad & q \leftarrow \max_{q} F(q, l, m) \\ \mathbf{M}-\text{step} \quad & l \leftarrow \max_{l} F(q, l, m) \end{aligned}$$

20

$$\begin{aligned} F(q, l, m) &= \left\langle \ln p(\tilde{g} \mid q, l) + \ln p(q) - \ln q(q) \right\rangle_q \\ &= \ln p(\tilde{g} \mid l) - D(q \,\|\, p(q \mid \tilde{g}, l)) \end{aligned}$$

The free energy is simply a function of the log-likelihood and the log-prior and $q(q)$, which is an approximation to the posterior density $p(q \mid \tilde{g}, l, m)$ I require. The last line of Equation 20 shows that the free energy is the log-evidence or marginal likelihood minus the Kullback-Leibler divergence between the real and approximate conditional density. This means that the variational parameters (conditional moments and precision) maximize the log-evidence, while minimising the discrepancy between the true and approximate conditional density. This scheme is identical to that employed by DCM for fMRI and ERP.

2.3.4 Model comparison and selection

Inference on the parameters of a particular model uses the conditional density, $q(q)$. Usually, this involves specifying a parameter or compound of parameters as a contrast, $c^T m$. Inferences about this contrast are made using its conditional covariance, $c^T \Sigma(l) c$. For example, one can compute the probability that a contrast is greater than zero. This inference is conditioned on the particular

model specified. However, in many situations one wants to compare different models, for example models with and without particular connections. This entails Bayesian model comparison. Different models are compared using their evidence (Penny *et al*. 2004). The model evidence or marginal likelihood is

$$p(\tilde{g} \mid m) = \int p(\tilde{g} \mid q, m)\, p(q \mid m) dq \ . \qquad 21$$

This is the normalization term of equation (19). By using the Laplace approximation (see Penny et al., 2004 for the details of this Laplace approximation), the log model evidence can be expressed as

$$\begin{aligned} &\log P(\tilde{g} \mid m)_L = Accuracy(m) - Complexity(m) \\ &where \\ &Accuracy(m) = -\frac{1}{2}\log|C_e| - \frac{1}{2} r(q)^T C_e^{-1} r(q) \\ &Complexity(m) = \frac{1}{2}\log\left|C_p - \frac{1}{2}\log|\Sigma|\right| + \frac{1}{2} e|q|^T C_p^{-1} e|q| \end{aligned} \qquad 22$$

The evidence can be decomposed into two components: an accuracy term and a complexity term. The accuracy term is simply the log-likelihood of the data expected under the conditional density and the complexity term is the Kullback-Leibler divergence between the approximating posterior and prior density. Clearly, for two models with identical accuracy, the model with the simpler network architecture will win; as the complexity term decreases the model evidence. A detailed description of the optimization procedure and Bayesian model selection

employed in this thesis can be found in Friston, 2002, Friston et al., 2003 and Penny et al., 2004.

In the following, I approximate the model evidence for model m, with its free energy bound. After convergence, the divergence above is minimized and this bound becomes tight such that

$$\ln p(\tilde{g} \mid m) \approx F(m) \qquad 23$$

The most likely model is the one with the largest log-evidence. This enables Bayesian model selection. Model comparison rests on the likelihood ratio of the evidence for two models. This ratio is the Bayes factor B_{ij}. For models i and j

$$\ln B_{ij} = \ln \frac{p(\tilde{g} \mid m = i)}{p(\tilde{g} \mid m = j)} = F(m = i) - F(m = j) \qquad 24$$

Conventionally, strong evidence in favour of one model requires the difference in log-evidence to be about three or more (*i.e.* a relative probability of about twenty). In what follows, I will use model comparison to compare models with and without various sorts of connections. By assuming uniform priors on the models I can convert the model evidence into a conditional probability over models by normalising the evidences so that they sum to one. Under this assumption, two models with a log-evidence of three imply that I can be 95% confident that the better model is more likely, given the data features.

2.3.5 Summary

Figure 2.5 summarises DCM for induced responses, which entails two steps. The first is to specify the model; *i.e*. the source locations and the network, based on prior knowledge or beliefs about the functional anatomy of the paradigm. For source locations, one can employ conventional source reconstruction methods; for example, source imaging (Mattout *et al*. 2006) or equivalent current dipoles (ECD) models (Kiebel *et al*., 2007; Kiebel *et al*., 2006). In terms of the network architecture, one needs to specify whether directed connections exist and whether they are linear or nonlinear (*i.e*., whether the cross-frequency terms in *A* are, *a priori* precisely zero or not).

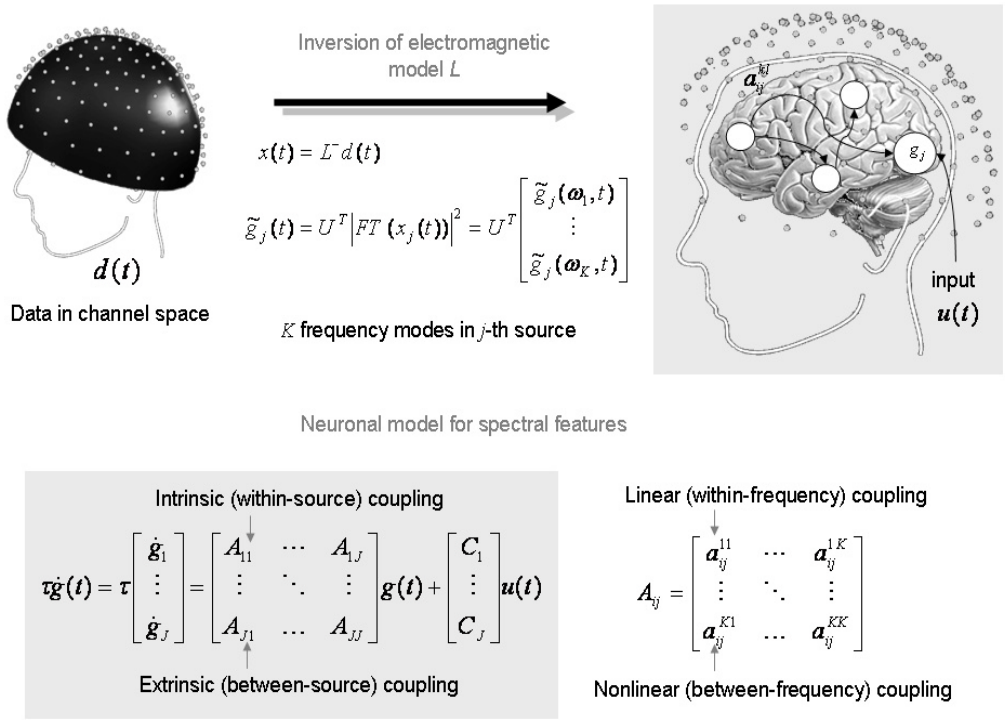

Figure 2.5 Schematic illustration of the analysis procedure. Upper panel: The spectral dynamics in the sources, $\tilde{g}_j(t)$, are first evaluated from observations in

sensor space; They are projected onto source space using the pseudo-inverse of the lead-field, L^{-}. The spectral densities obtain by squaring the absolute values after Morlet wavelet transform. Lower panel: the linear form of state equations. At the neuronal level, the DCM comprises a vector of states for each electromagnetic source, allowing for linear and nonlinear coupling.

The second step is to invert the model given some observed spectral features. The source spectra obtain by projecting the channel data, $d(t)$, to source space and evaluating the spectral density over K' frequency bins using Eq. 16. These spectral features are reduced in number, using orthonormal frequency modes $U = [U_1, \ldots, U_K]$ to encode spectral dynamics. These dynamics are modelled using linear state equations (Eq. 14), where the elements of the coupling matrix a_{ij}^{kl} comprises the within $(i = j)$ and between $(i \neq j)$ source coupling parameters, which can be either within $(k = l)$ or between $(k \neq l)$ frequencies. The coupling between two regions can then be characterised as a function of source and target frequencies; $A_{ij}(w_k, w_l) = UA_{ij}U^T$ and displayed as a matrix or image. Linear coupling matrices have strong coupling among the same frequencies so that large coupling values are deployed along the leading diagonal. Conversely, nonlinear coupling entails between frequency effects with large off-diagonal terms (see Figure 2.6). Because I use a small number of frequency modes, these coupling matrices encode broad-band coupling among the modes. This means that linear coupling can 'diffuse' away from the leading diagonal but retains its symmetrical form.

The above procedure can be repeated for several models or hypotheses about the underling architecture generating induced activity and the competing models compared using their differences in log-evidence.

I have now covered the specification, estimation and comparison of DCMs for induced responses. In the next section I try to establish their validity using synthetic data.

2.4 Face validity: Simulations

This section addresses the face validity of the DCM described in the previous section. First I generated synthetic data to show that, using model comparison, the scheme can disambiguate competing models correctly. I use a very simple example to demonstrate the basic features of model selection. In the second simulations I used a more realistic model (based on the analysis of real data in the next section) to establish the identifiability of various parameters and ensure they can be estimated accurately under typical levels of noise. In all simulations, data were generated by integrating Eq.11 given known model parameters (which also specify exogenous input). I then added noise to create synthetic data that were generated by a known architecture and known parameters. Critically, I used parameters that were based on the estimates from the analysis of real EEG data. This ensured that the simulations were biologically plausible.

$$UA_{ij}U^T = \sum_k \sum_l a_{ij}^{kl} U_k U_l^T$$

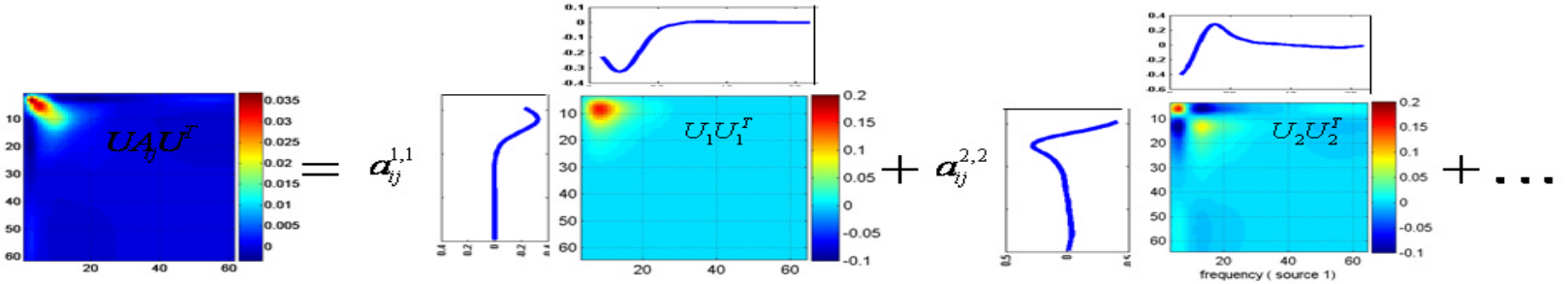

An example of linear (within-mode) coupling

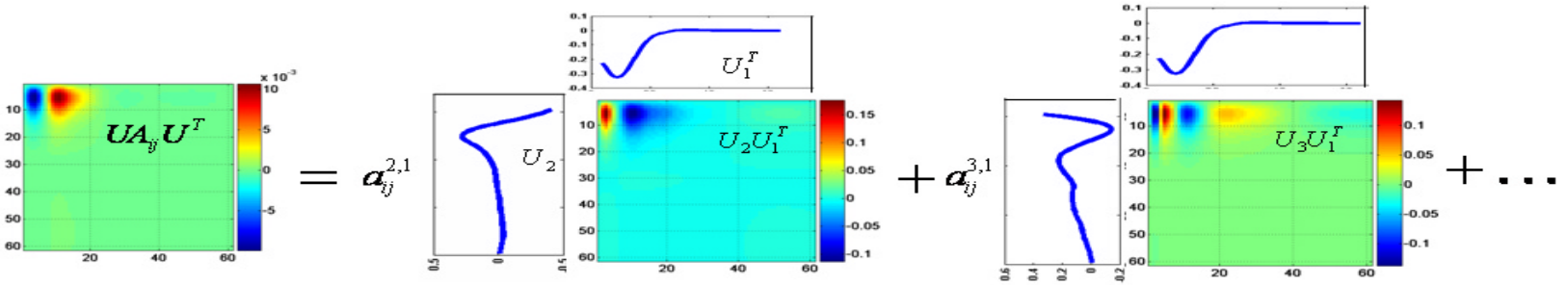

An example of nonlinear (between-mode) coupling

Figure 2.6 Visualizing the estimated coupling parameters. These images represent the coupling strength between different frequencies and obtain by projecting the coupling matrices in mode-space to frequency space. Upper panels: linear components; lower panel: non-linear components; I will use this form in subsequent figures.

Observation noise was created by evaluating the time-frequency power of a white noise process, using the same wavelet-transform employed in the empirical analyses. This ensured the serial correlations in the noise matched those observed empirically. Simulated noise processes were scaled and mixed with synthetic signal to give the desired signal to noise ratio (SNR).

2.4.1 Model selection: distinguishing between linear and nonlinear coupling

In these simulations, I generated data using a very simple DCM under linear and nonlinear coupling, with a SNR of 19.46 dB. The model comprised two sources with two frequency modes in each source, where the first source projected to the second. See Table 2 for of the values of the coupling parameters used (other parameters were set to their prior expectations in Table 1). The input to the system was a bump function that elicited responses in both modes in, and only in, the first region. The first DCM modelled all the connections as linear. The second used the same coupling parameters but allowed for fairly weak nonlinear coupling from the second to the first frequency mode. I used two DCMs to invert these two data sets: The first modelled linear coupling only and the second allowed for nonlinear coupling between the two sources. The model parameters and results of Bayesian inversion of these two simulated datasets are summarized in Table 2. For nonlinear data, the nonlinear DCM had a greater model evidence than the linear DCM ($\ln B_{21} = 126$) and *vice versa*, for linear data, where the linear DCM

has the higher model evidence ($\ln B_{12} = 66$). When data are generated under a nonlinear model, the linear model simply cannot explain them, which is reflected in the relatively large difference in log-model evidences. For linear data, this difference is much smaller ($\ln B_{12} = 66$), because the nonlinear fit to the data is as good as the linear one. However, the nonlinear model has more parameters, which decrease the model evidence relative to the linear model, rendering it a less likely model. The agreement between the true and conditional estimates of coupling is self-evident and, under this level of noise, I would be very confident that this coupling was not zero.

2.4.2 Model inversion under different levels of noise

In these simulations, I use the posterior expectations computed for real EEG data set as generating model parameters. The architecture was based on the model used to analyse the data in the next section obtained during a face-presentation paradigm. This model comprised two pairs of homologous regions in the right and left hemispheres, corresponding to early visual and fusiform sources. The sources within each hemisphere were connected reciprocally, whereas only the fusiform sources were connected between hemispheres. The spectral activity in each source was expressed in four frequency modes (identified by a singular value decomposition of the real EEG data; see Figure 2.7). The input enters bilaterally at the visual sources. This exogenous input introduces a burst of power that perturbs the network at a time corresponding roughly to the arrival of subcortical input

conveying sensory information (about 60ms after stimulus onset). The responses were generated as described above by integrating Eq.11 to gives, for each source, dynamics in the state-space of frequency modes

To produce observation noise at the source level I generated sensor level white noise at four different variances. I then projected these random effects to source space using the pseudo-inverse of the lead-field and finally transformed it into the time-frequency domain (c.f., Eq.16). After projection onto the frequency modes I added the resulting noise spectra to the simulated source spectra. I quantified the resulting noise levels, in source space, in terms of signal to noise ratio (SNR) at 20.38, 14.8, 10.83, and 4.54 dB; where I take 14.8 dB as representative of typical data. For example, real EEG data had an estimated SNR of 19.74 dB. Table 2.3 summarizes the results of model inversion in terms of (i) selected posterior expectations and (ii) average errors on the linear and nonlinear coupling parameters (i.e., differences between the true values and conditional expectations). These results suggest that, when the SNR is greater than 15 dB, the connection strengths are estimated with a high degree of accuracy. As anticipated, the errors increase with noise. When the SNR is too low, inference can change in a qualitative sense. For example, at 4.54 dB, I found that one non-linear coupling was a posteriori very likely to be present ($p > 0.95$), although the true parameter was zero. This may be because as the noise variance increases, the optimization scheme gets trapped in the local minimum; however, a more likely explanation is due to the conditional dependencies among the estimates, where one parameter is over-estimated at the expense of another being under-estimated: At high noise

levels in this simulation, there is an underestimate of one coupling parameter at 10.83dB. This coupling parameter should be significant but Bayesian inversion fails to show this. Note that these dependencies are accommodated in Bayesian model selection (which integrates over the parameters). In conclusion, a typical SNR of 20 to 15dB gives veridical estimates, whereas higher noise levels (i.e., SNR of 10 to 5) can lead to inappropriate inferences (as indicated by the starred entries, with a posterior inference that the coupling parameter was greater or less than zero).

Table 2.2 First simulations: results of inverting a linear and nonlinear model using linear and nonlinear data (SNR = 19.46 dB). p(A) indicates the conditional probability that the coupling parameter is greater than zero. *F* is the log-evidence of each model and data pair. The winning model for each data set is indicated by a grey box.

	Nonlinear data	**Linear data**
True Parameter	$A^{1,1}_{2,1}$ = 0.72 $A^{2,2}_{2,1}$ = - 0.45 $A^{2,1}_{2,1}$ = 0.24	$A^{1,1}_{2,1}$ = 0.72 $A^{2,2}_{2,1}$ = - 0.45
Non-linear DCM	$A^{1,1}_{2,1}$ = 0.82 p = 0.99 $A^{2,2}_{2,1}$ = - 0.45 p = 0.99 $A^{2,1}_{2,1}$ = 0.32 p = 0.99 **F = -2561**	$A^{1,1}_{2,1}$ = 0.72 p = 0.99 $A^{2,2}_{2,1}$ = - 0.64 p = 0.99 $A^{2,1}_{2,1}$ = 0.03 p = 0.96 **F = -4420**
Linear DCM	$A^{1,1}_{2,1}$ = 1.3 p = 0.79 $A^{2,2}_{2,1}$ = - 0.19 p = 0.99 **F = -2687**	$A^{1,1}_{2,1}$ = 0.76 p = 1.00 $A^{2,2}_{2,1}$ = - 0.29 p = 0.99 **F = -4354**

Table 2.3 Second simulations: The impact of noise level on estimation accuracy of the parameters. The first column displays the true parameters for a selected subset of linear and non-linear parameters. Each subsequent column shows their posterior mean for decreasing signal-to-noise ratios (SNR). The last three rows display the errors of the linear and non-linear parameters, averaged over connections and expressed as a percent.

Non-linear DCM	SNR (dB)			
	20.38	14.80	10.83	4.54
$A^{3,1}_{1,1} = 1.89$	1.89	1.89	1.84	1.75
$A^{4,2}_{1,1} = 2.05$	2.05	2.05	2.00	1.94
$A^{3,4}_{1,1} = -1.05$	-1.05	-1.05	-1.03	-1.19
$A^{3,1}_{2,1} = -1.62$	-1.62	-1.62	-1.60	-1.49
$A^{4,2}_{1,3} = 0.10$	0.10	0.10	0.08	0.09
$A^{3,4}_{1,2} = 0.65$	0.62	0.65	0.62	0.64
$A^{4,3}_{2,1} = -1.75$	-1.75	-1.75	-1.76	-1.70
$A^{2,4}_{2,1} = -0.97$	-0.97	-0.97	-0.88* p<0.95	-0.94
$A^{4,3}_{1,2} = 0$	0.00	0.00	0 .00	0.48* p >0.95
Average error for linear coupling parameters (%)	<0.1 %	<0.1 %	2.33 %	8.60 %
Average error for non-linear coupling parameters (%)	<0.1 %	<0.1 %	25.3 %	20.9 %
Average error for all parameters (%)	<0.1 %	<0.1 %	13.8%	14.8%

2.5 Analyses of real EEG data

In this section, I demonstrate DCM for induced responses using EEG data. The data represents a single-subject data set from a study by Henson *et al.* (2003)[6]. The subject performed a judgement task on faces and scrambled faces. The data were sampled at 200 Hz using a whole-head, 128-channel ActiveTwo system. Bipolar horizontal and vertical electro-oculograms (EOG) were obtained using electrodes placed at the bilateral outer canthi and the left eye respectively to exclude trials with an EOG artefact. The data used here comprise time-frequency responses averaged over 86 trials.

The lead-field or gain matrix was computed for a canonical mesh (Mattout et al 2007) and co-registered channel locations, using a three-sphere head model as encoded in BrainStorm (http://neuroimage.usc.edu/brainstorm/). The co-registration and forward model was computed within SPM5 (http://www.fil.ion.ucl.ac.uk/spm).

2.5.1 Exemplar analysis using DCM

Note that this single-subject analysis is used only to illustrate DCM for induced responses; I will not attempt a neurobiological interpretation of these results. Furthermore, face-perception is not necessarily the most interesting

[6] These data are available from http://www.fil.ion.ucl.ac.uk/spm/data/mmfaces.html

paradigm, in terms of induced responses. I used these data because they are easily available (from http://www.fil.ion.ucl.ac.uk/spm), which means other people can reproduce the analysis reported below.

The specification of a DCM, *i.e.*, the network and source locations, is a critical step. I envisage that, for a given study, there would be several competing models that one might want to test. In the current framework, one does this by specifying models in terms of their connections and whether these connections are linear or nonlinear. Model comparison[7] can then be used to select the best model and inferences about the parameters of the selected model can proceed using the conditional mean and covariance of the coupling parameters. Here, I will simply test two models to illustrate model specification, comparison, and inference. I used prior knowledge about sources in visual and fusiform cortices and employed source reconstruction implemented in SPM5 to localize four sources from a conventional ERP analysis of the data (Friston *et al*. in press). These source comprised the left and right visual cortex (**LV** and **RV**), and left and right fusiform area (**LF** and **RF**). The locations of these sources are provided in Figure 2.7a, in canonical space. For these sources, spectral changes, in several frequency bands, have been found during face processing (Klopp *et al.*, 1999). Spectra were constructed from -100ms to 400ms. I used a Morlet wavelet transform with a coefficient, $k = 7$, over 4 to 64 Hz. The resulting spectra were de-trended and reduced using four principal modes as described above (see Figure 2.7b). In the

[7] Note that due to the feature selection (Eq. 16) one cannot compare models based on different lead-fields. In other words, models can only be compared if they include the same sources.

first (nonlinear) DCM, I allowed bi-directional cross-frequency coupling between source pairs **LF**-**RF**, **LV**-**LF**, and **RV**-**RF**. In the second (linear) model, I allowed only within-frequency interactions among these sources. I use two exogenous inputs to **LV** and **RV**. The (estimated) temporal dynamics and spectral effects of these inputs on both visual sources are shown in Fig.2.8.

2.5.2 Results

Figure 2.9 summarizes the results based on the nonlinear DCM. The arrows indicate directed connections. Coupling strengths are represented as functions of source and target frequency (*c.f.*, Figure 2.6). I only show coupling matrices for which one or more of the underlying coupling parameters was greater than zero, with 95% confidence or more. These matrices encode the coupling among frequencies; for example, there are several cross-frequency influences in the forward connection from **RV** to **RF,** in which alpha (8-12Hz) in the fusiform source is induced by alpha in the visual source. However, the same alpha suppresses beta (16Hz), while increasing fusiform gamma power. These changes recapitulate the simulations in Figure 2.4, where low frequencies in the input produce high frequency responses.

Figure 2.10 shows the equivalent results for the linear DCM. In this case, only the forward connections and one transcallosal connection contained parameters that were greater then zero (at 95% confidence). This model is largely

constrained to predicting the dynamics of alpha power and is unable to account for any cross-frequency effects.

Bayesian model comparison clearly favoured the nonlinear model with a log-Bayes factor of 392. Figure 2.11 shows the observed and predicted spectral densities of the selected (nonlinear) model. Using these spectral densities, I estimated the SNR to be 19.74 dB. Interestingly, the coupling strengths in the right hemisphere were stronger than those in the left. Previous studies have found a right lateralization for face processing (Kanwisher and Yovel, 2006). One can directly test this with DCM, using contrasts; for example, I found that the difference between the left and right (right minus left), averaged over all cross-frequency coupling parameters, is greater than zero, with a posterior confidence of 99%. In summary, using DCM and model comparison I find strong evidence for right-lateralised nonlinear coupling among early visual and fusiform sources.

a

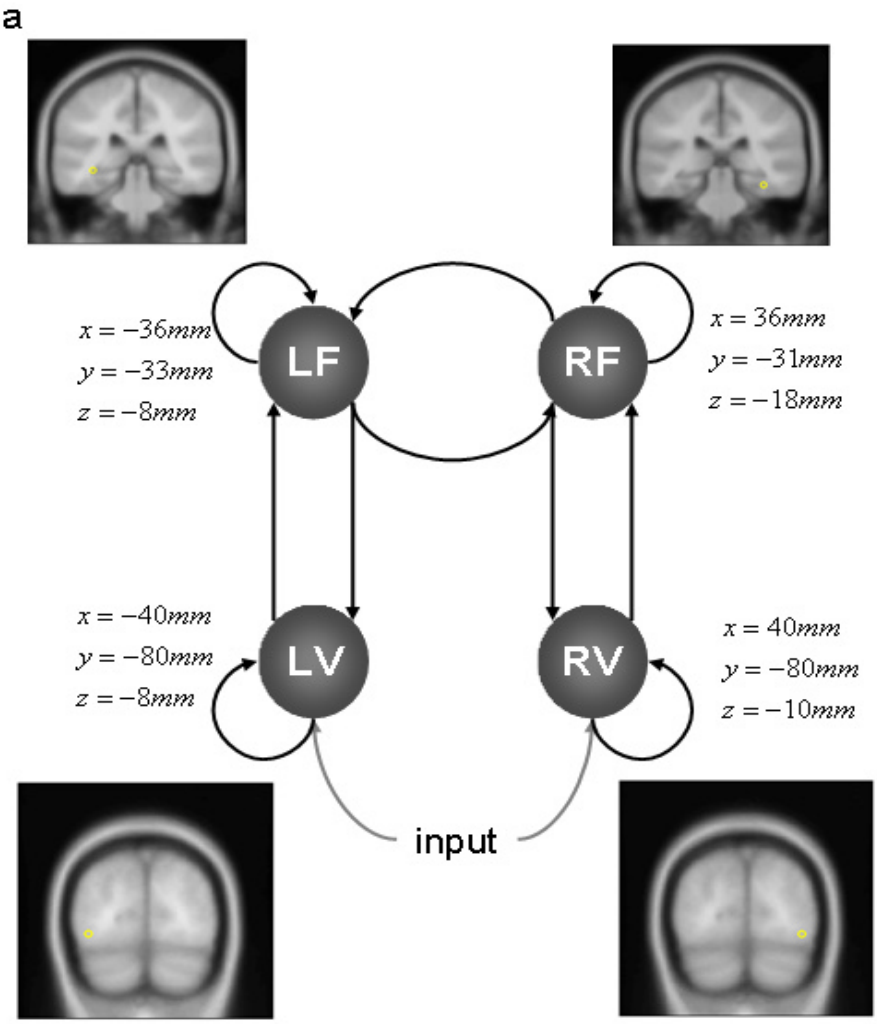
x = −36mm
y = −33mm
z = −8mm
LF
RF
x = 36mm
y = −31mm
z = −18mm
x = −40mm
y = −80mm
z = −8mm
LV
RV
x = 40mm
y = −80mm
z = −10mm
input

b

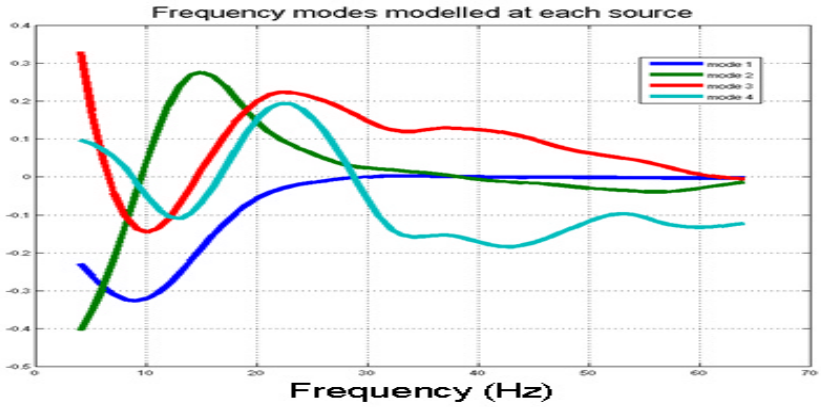
Frequency modes modelled at each source
mode 1
mode 2
mode 3
mode 4
Frequency (Hz)

Figure 2.7 Real EEG data analysis. Left (a): System or graph underlying the DCM (RV – right visual; RF – right fusiform; LV – left visual; RF - right fusiform). Right (**b**): the frequency modes, $U_i(w)$, identified using singular value decomposition of spectral dynamics in source space (over time and sources).

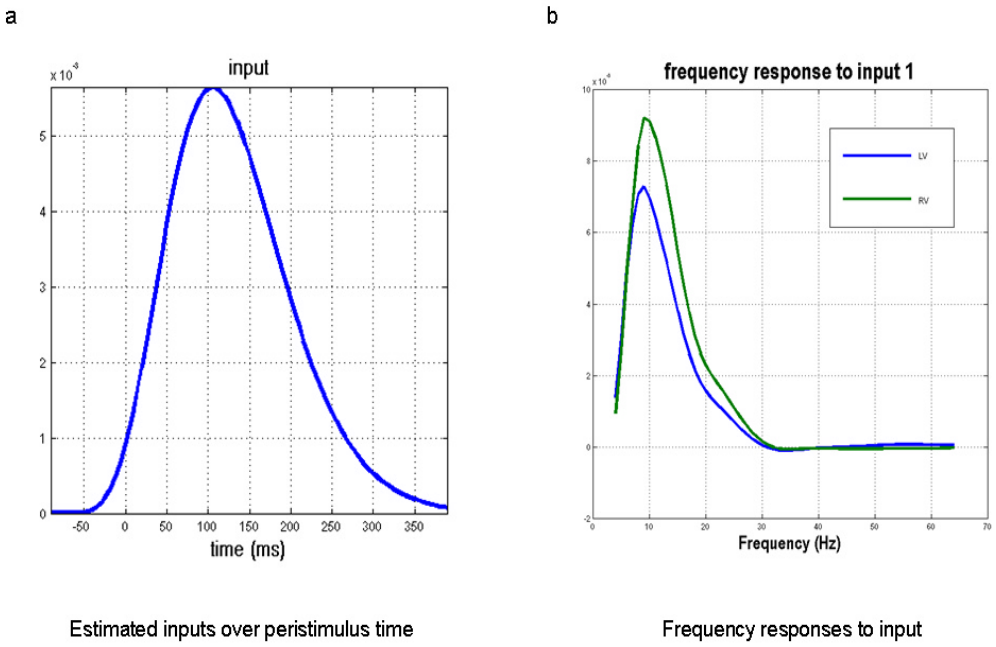

Figure 2.8 Inputs to the DCM of real EEG data: (a): estimated time course of inputs to RV and LV based on the conditional means of the input function (Eq.18). (b). spectral response to input in the same areas. These profiles correspond to UC_i.

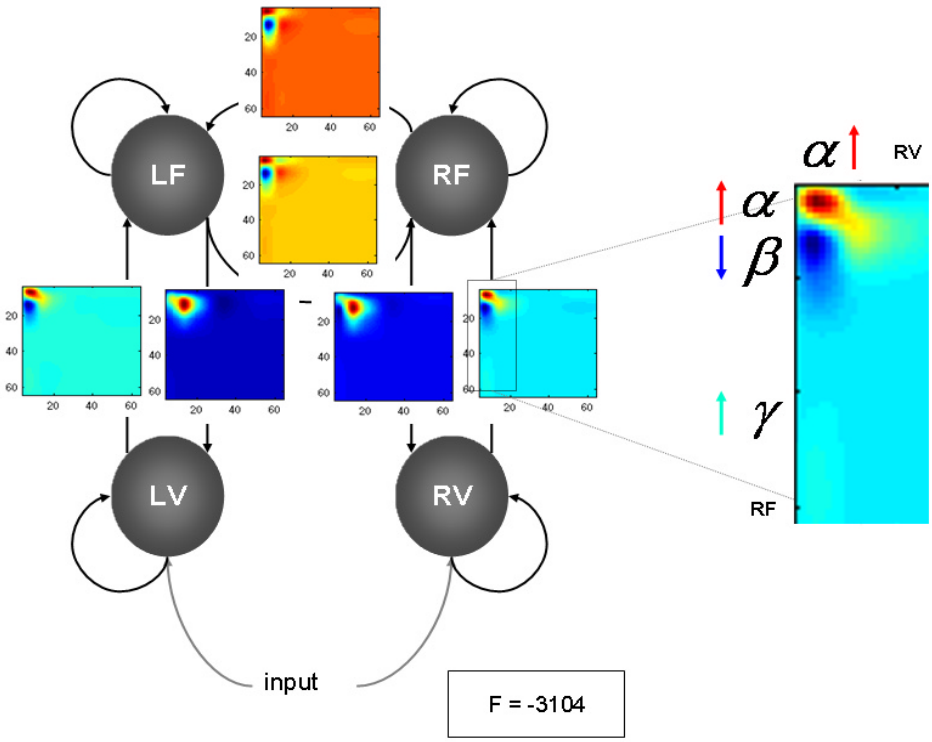

Figure 2.9 Results for non-linear DCM of real EEG data: The arrows show the directed connections from one source to another. The coupling strengths are represented as coupling functions of frequency, which show the effects the spectral density in one source has on the density in another. The source names are as in Figure 2.7.

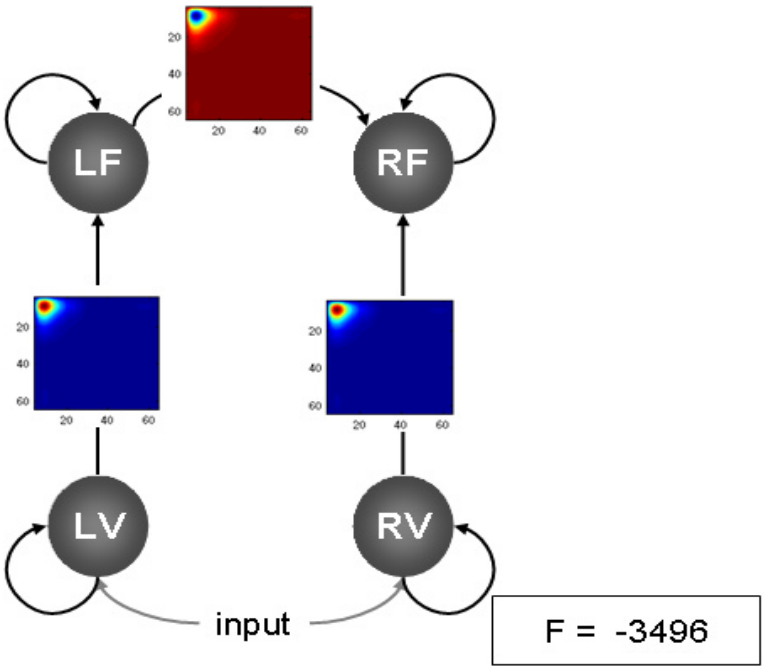

Figure 2.10 Results for linear DCM of real EEG data: As for Figure 2.8 but for a reduced linear model. The source names are as in Figure 2.7.

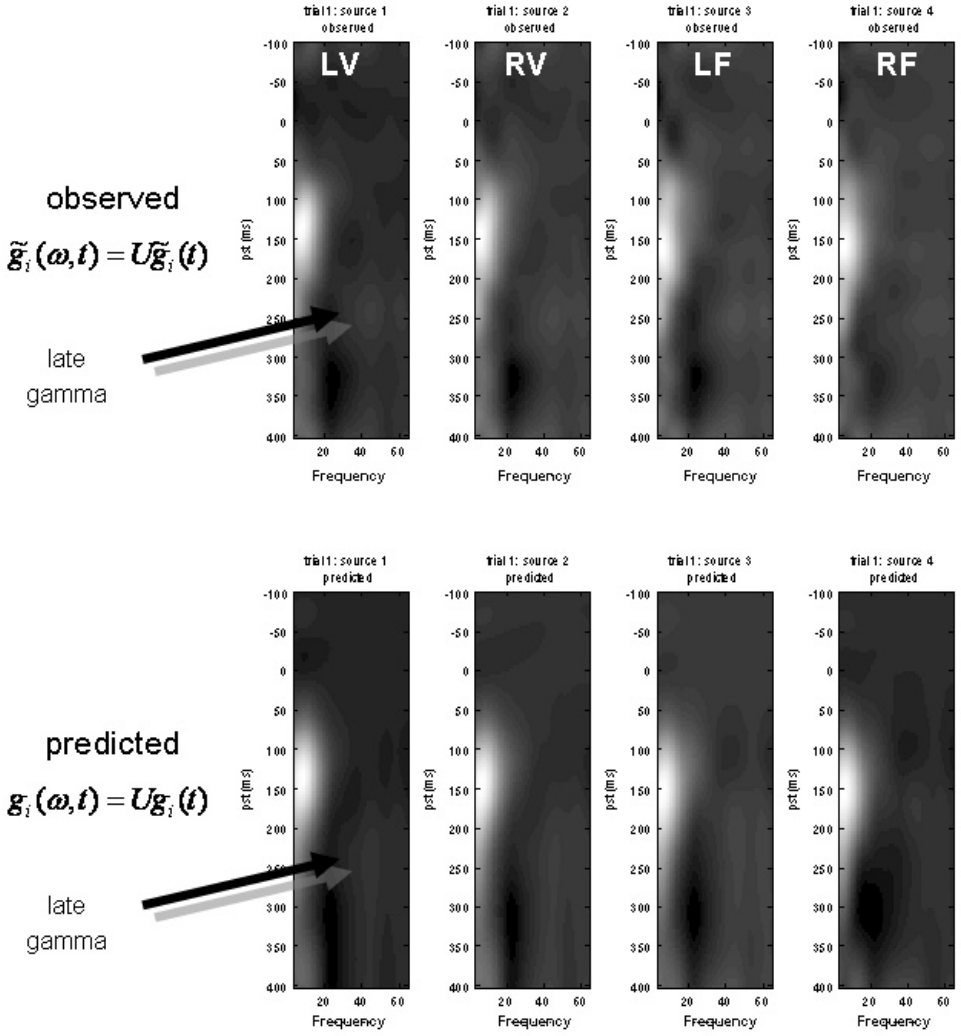

Figure 2.11 The observed and predicted spectral densities of the selected (nonlinear) model. Upper panels: Observed EEG time-frequency power data for all four sources. Lower Panels: Fitted data. It can be seen that the model captures the main spectral dynamics fairly well. There is pronounced alpha activity around 140ms with a partial return to pre-stimulus levels by 260ms. This corresponds largely to the evoked components. Although not very easy to see, there is also a late increase in gamma power that starts around 250ms (arrow). The images correspond to the observed and predicted quantities $U\tilde{g}_i(t)$ and $Ug_i(t)$ respectively.

2.6 Discussion

Nonlinearities in neuronal activity are an important aspect of processing in large-scale neuronal networks and have led to many different proposals of how to best to characterise them given some data (*e.g.*, David et al., 2004). As I have illustrated above, linear coupling is mediated by first-order transfer functions that transfer energy in the source to the target, while non-linear mechanisms express themselves as cross-frequency interactions, through high-order, generalised transfer functions. A simple example of this is frequency doubling when one squares a sinusoid; *i.e.*, $\exp(jwt)^2 = \exp(j2wt)$ (see Friston 2001). Biological evidence speaks to the prevalence of nonlinear interactions among cortical areas during cognitive tasks (*e.g.*, Bullock *et al.*, 1997; Schack *et al.*, 2002). I have shown that second-order features of the data (*i.e.*, the spectrum) can be modelled by DCM for induced responses in a way that can disambiguate between linear and non-linear coupling. DCM is not for a surrogate for widely used linear models (*e.g.*, coherence, correlations) but represents a complementary approach to disclose cross-frequency interactions among areas (see also Pereda *et al.* 2005).

In this study, I have assumed that the locations of the sources are known. This means there is no source-reconstruction problem and no spatial parameters to optimise. The specification of source locations is itself a large area both in terms of evoked (Baillet and Garnero 1997) and induced responses (Singh et al 2003). In this work, the source locations were based on previous analyses of the data used

using multiple sparse priors on distributed forward models (Friston et al 2008). I would advocate that whatever source reconstruction technique is used, only the locations should be retained and used to re-estimate source-activity using the forward model provided by ensuing the ECD forward model. This is because the assumptions implicit in distributed forward models can introduce (e.g., though smoothness constraints) or remove (e.g. through beam-forming assumptions; Singh et al 2003) correlations among neighbouring sources. Inverting a simple ECD forward model also ensures the DCM is insensitive to the reconstruction scheme used to define the ECD locations.

This model furnishes a framework within which one can make inferences about causal coupling. Note that model-free approaches cannot be used to make causal inferences in a control theory sense. For example, coherence and mutual information measure interdependency between time series obtained from two sources but provide no information about directionality. Despite their names, extensions of these methods, such as Granger causality and transfer entropy, do not provide evidence for causality in a formal sense because they are based on multivariate autoregressive models, which may be causal or acausal. However, an advantage of model-free approaches[8] is that they can usually be applied in an exploratory fashion. Hypotheses about coupling, generated by these analyses, can then be tested formally using a DCM.

[8] By model-free I mean any technique based on simply on probability distributions; noting that these distributions may be parameterised with a model (*e.g.,* autoregressive models).

An important feature of DCM for induced responses is that it models the full time-frequency spectrum. This differs from typical approaches, which select a-priori a few specific frequency bands. I model spectral dynamics in terms of a mixture of frequency modes (obtained with singular value decomposition). The dynamics of each mode are encoded by the evolution of a state. It is this multi-state vector, for each source, that captures how the energy in different frequencies interacts, either linearly or nonlinearly, among sources. A critical issue is whether inferences differ with the number of frequency modes per source. In Fig. 2.12, I show that the exact number does not seem to have an effect on inference. Using a synthetic dataset (the second set of simulations with an SNR of 15), generated with three modes, I find that the nonlinear DCM is always the best model for different numbers of modes. In principle, choosing too many modes should not affect inference (as shown above), because parameters that relate to superfluous states will not explain data but only decrease the evidence of the model. In practice, I suggest people use as many modes as necessary to represent 90 % of the data variance. The obvious minimum to model interesting dynamics is two modes. Note that one cannot compare models with different number of modes (because the log-evidence is a function of the data features, which are defined in terms of modes).

2.7 Conclusion

Nonlinear interactions are an important phenomenon in the brain and are expressed as cross-frequency coupling in spectral characterisations of EEG and

MEG time-series. Dynamic Causal Modelling for induced responses exploits this to model dynamic broad-band power changes as a consequence of linear and non-linear coupling among brain sources. The ensuing scheme might be useful when trying to disambiguate linear and nonlinear contributions to distributed processing in a network of electromagnetic sources. In the next three chapters (chapter 3-5), I will apply this method to empirical datasets measured during motor tasks and face perceptions and in chapter 6, I will generalize this dynamic causal model to address the relation between evoked and induced activities in terms of their generating mechanisms.

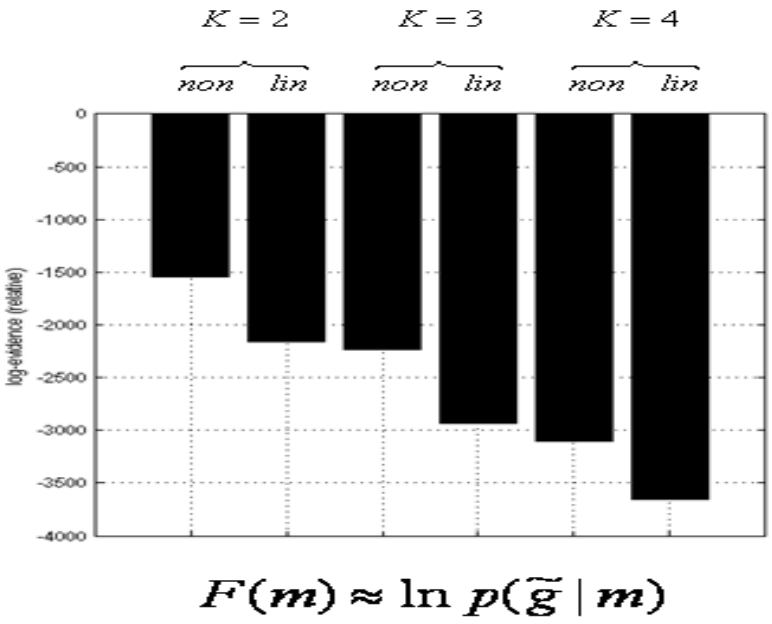

Figure 2.12: Model comparison: The effect of using a different number of modes on the log-evidences for the linear and non-linear DCM. Importantly, the relative log-evidences remain stable when I change the number of modes.

CHAPTER 3

NONLINEAR COUPLING IN THE HUMAN MOTOR SYSTEM

3.1 Introduction and specific aims

The aim of this chapter is to characterise the modulation of frequency-dependent coupling among neuronal sources during action execution using MEG and a simple linear form of DCM for IR (see Chapter 2; Chen et al. 2008). Hand movements have been shown to modulate oscillatory power in motor system at different frequencies, such as alpha ERD and beta ERS in brain areas engaged by action execution; e.g., M1, SMA and PM (Pfurtscheller and Andrew, 1999). Given that oscillations facilitate integration both within functionally segregated brain areas and between areas engaged by the same task (Singer and Gray, 1995; Kahana et al., 1999; Rodriguez et al., 1999), many studies investigating oscillatory activity have focussed on (linear) coupling between nodes of a network at the same frequency (Andrew and Pfurtscheller, 1996; Gerloff et al., 1998; Gross et al., 2001; Serrien et al., 2005). More recently, evidence has emerged that suggests (nonlinear) coupling among different frequencies may play an equally important role in inter-areal communication (Breakspear, 2002; Chen et al., 2009; Jensen and

Colgin, 2007; Tallon-Baudry and Bertrand, 1999; Varela et al., 2001; von Stein and Sarnthein, 2000). In view of the finding that action execution induces changes in different oscillatory frequencies within connected brain regions, in this chapter I wanted to model how these oscillations are orchestrated during motor control. It is important to consider the nature of this frequency-specific coupling given that excessive synchronization at distinct frequencies is seen in some pathological conditions. For example, in Parkinson's patients, synchronization between the contralateral primary motor cortex and forearm muscles at 4~6 Hz is thought to contribute to resting tremors, while excessive synchrony in the basal ganglia and subthalamic nucleus at 10 to 35 Hz is associated with bradykinesia (for review, see Brown, 2007). The motivation for the work reported here was to establish a reference point for future clinical studies, using normal subjects and a simple established paradigm. This normative reference might help pinpoint where abnormal modulations of specific frequencies arise.

The aim of this chapter was to model modulations of frequency-specific oscillations in the motor network induced by an established handgrip task (Ward et al., 2008). I modelled these modulations in terms of coupling between electromagnetic sources, where power in one source causes changes in the power expressed in others. Critically, I distinguished between within-frequency (linear coupling) and between-frequency (nonlinear) coupling. Specifically, I asked whether there is a difference in the relative contribution of linear and nonlinear mechanisms between intrinsic (within-area) and extrinsic (between-area) coupling. The results suggest that extrinsic connectivity is best characterised as nonlinear

(between-frequency) coupling, whereas intrinsic connections are best modelled with linear (within-frequency) coupling.

3.2 Material and Methods

3.2.1 Experimental design

Nine healthy, right-handed subjects (20~32 years of age, 5 males and 4 females) were recruited. Written consent was obtained from all subjects, in accordance with the Declaration of Helsinki. The study was approved by the Joint Ethics Committee of the Institute of Neurology, UCL and National Hospital for Neurology and Neurosurgery, UCL Hospitals NHS Foundation Trust, London.

Subjects were instructed to perform a visually cued ballistic isometric grip, using their dominant hand with an inter-trial interval of 7±2 secs. Prior to scanning, subjects were asked to grip the manipulandum to generate a maximum voluntary contraction (MVC). The target force was set at 45% of MVC. Subjects were trained to approximate the target force with visual feedback prior to scanning. However, no visual feedback was provided during scanning, in order to minimise activity in occipital and parietal sources. Force output was recorded using a MEG-compatible gripper and used to identify the movement onset (i.e. the reaction time, from the onset of the visual cue until the onset of the ballistic grip), the grip duration and force level.

MEG signals were measured continuously at 240 Hz during task performance using a whole-head CTF Omega 275 MEG system. At the beginning

and end of each measurement, the positions of three anatomical landmarks (bilateral pre-auricular points and nasion) were recorded to exclude excessive head movement (maximal translation < 1.3 cm ; 2.68~12.68 mm).

The MEG data were pre-processed offline using SPM8 (SPM8, Wellcome Trust Centre for Neuroimaging, http://www.fil.ion.ucl.ac.uk/spm/). The data were epoched from -500 to +1000 ms, where time zero indicates movement onset. Poorly performed (reaction times of more than one sec) and artefact contaminated (MEG amplitude > 500 fT) trials were excluded from further analysis; resulting in 88-98 artefact-free epochs per subject (88 98 90 98 94 96 90 93 95) with 642.66±54.92 ms mean reaction time and 639.45±54.48 ms grip duration. The mean force level was 45±25 % of subject-specific MVC. These artefact-free epochs were projected from channel space to the sources using the generalised inverse of the lead-field matrix for the chosen sources (see Model specification below). The spectral density from 4-48Hz at each source was computed over peri-stimulus time using a time-frequency Morlet wavelet transform (wavelet number: 7). The absolute value of the resulting time-frequency responses were averaged over trials and baseline-corrected by subtracting the frequency-specific power of the first time-bin. For computational expediency, I reduced the dimensionality of spectra into four principal frequency components derived from a SVD of the spectra (see chapter 2 for details). This preserved over 93 % of the spectral variance in all subjects (range 93% ~ 97%). The resulting spectral dynamics enter DCM as the observations that the model attempts to explain.

3.2.2 DCM specification (sources and coupling)

The source locations were taken from the group results of an fMRI study using the identical task (Figure 3.1), where five subjects performed 25 ballistic isometric hand grips to 45% of MVC. Imaging data were analysed using SPM5 as described elsewhere (Ward et al., 2008). The localisations were taken as the peak coordinate in Montreal Neurological Institute (MNI) space within each significant cluster (voxels significant at $p < 0.05$, corrected for multiple comparisons across the whole brain). Peak increases in activity were seen in left M1, bilateral PM and SMA. In addition, right M1 was included because of significant task-related deactivation during hand grip secondary to transcallosal interhemispheric inhibition (Ward et al., 2008) (Figure 3.1).

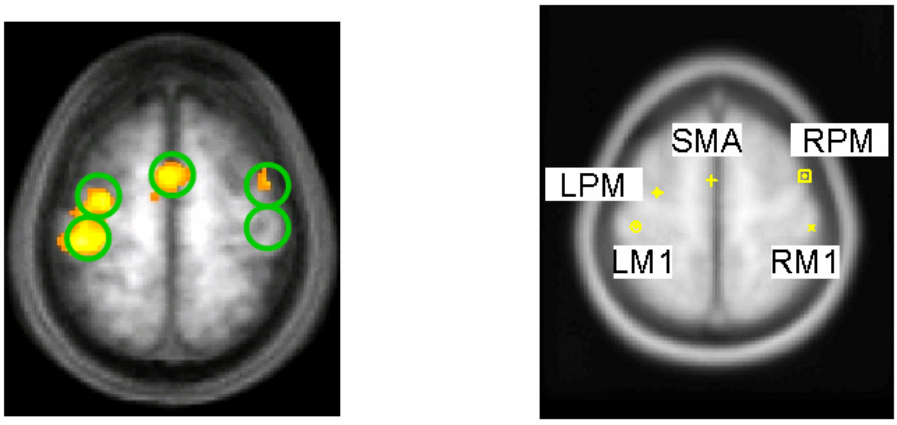

Figure 3.1 Location of the four sources extracted from a parallel fMRI study (left) and shown on a template MRI image (right).

Using these five sources I then specified 12 different connectivity models as shown in Figure 3.2. This model space was constructed using three model

attributes. First, whether intrinsic (I) connections are linear (L) or non-linear (N) and second, whether extrinsic (E) connections are linear or non-linear. This results in four sorts of models. The third attribute was the lateralization of cross-hemispheric coupling between PM and M1. I modelled three levels of this lateralisation: right PM to left M1 (r-), or left PM to right M1 (l-) or both (b-). This gave a total of 12 models, as shown in Figure 3.3. I use the designation r-ILEL to mean a right-lateralised architecture, where Intrinsic connections are Linear and Extrinsic connections are Linear. The exogenous inputs go to the bilateral M1s and SMA.

3.2.3 Inference on models: Bayesian Model Selection (BMS)

At a single subject level, I compared the difference in log model evidence or marginal likelihoods between models, i.e. log Bayes factor (Penny et al. 2004) to identify the best among the models tested. To identify the model with the most evidence at the group level, I added the log-evidences from each subject, under the assumption that each subject's data are conditionally independent of each other. In other words, the log-evidences from each subject were summed under a fixed-effects assumption on model space (i.e., there is one model that is the best for all subjects).

$$\ln p(y_1, y_2, ...y_n \mid m_i) = \ln \prod_{j=1}^{n} p(y_j \mid m_i) = \sum_{j=1}^{n} \ln p(y_j \mid m_i)$$

to obtain the log-evidence for the i-th model across all n subjects. For any given pair of models, a Bayes factor of about twenty (i.e a difference of three or more in log space) is usually considered as "strong" evidence in favour of one model

relative to another (Penny et al. 2004). To ensure differences in log-evidence were consistent across subjects, the log-evidences for each model, over the nine subjects, were entered into a repeated-measures analysis of variance (ANOVA) with two within subject factors (nonlinearity with four levels and laterality with three levels – corresponding to the columns and rows of Figure 3.2 respectively).

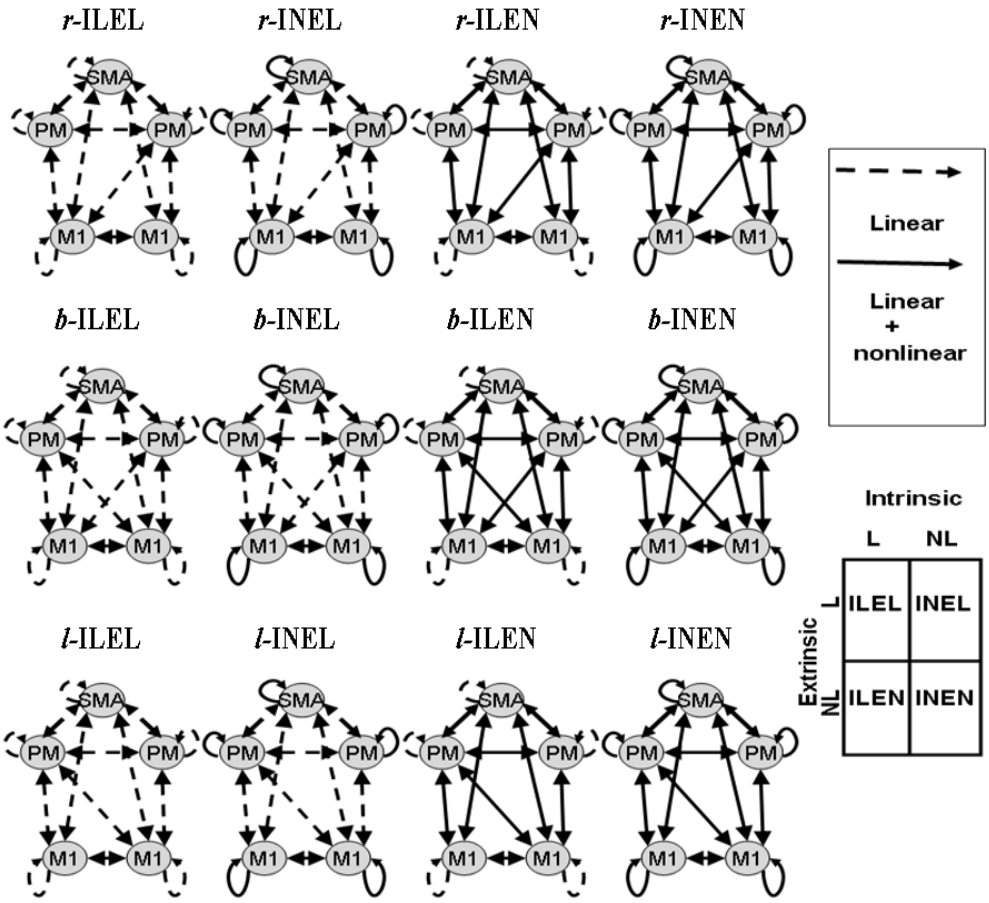

Figure 3.2 The connectivity architecture for all the models considered. The upper panel shows the symmetric models differed according to whether the linear or nonlinear connections are intrinsic or extrinsic. The lower panel represents the asymmetric DCMs. The solid and dashed lines indicate the effect of nonlinearity

and linearity, respectively. N: nonlinear coupling; L: linear coupling; I: Intrinsic connection; E: Extrinsic connection.

3.2.4 Model parameters: Visualization of coupling matrices

To quantify the coupling under the best model, for each intrinsic or extrinsic connection the (frequency to frequency) matrices of subject-specific estimates were smoothed (to account for inter-subject variability in frequency-to-frequency coupling using a Gaussian kernel with FWHM 8 Hz). These were then averaged by entering them into a conventional SPM analysis to identify reliable frequency-specific connectivity. I report the average coupling strengths in, and only in, non-zero frequency bins (at $p<0.005$ uncorrected).

3.3 Results

3.3.1 Time-frequency responses at source level

The estimated event-related spectral responses at the source level of a representative subject are shown in Figure 3.3 (upper panel), where the alpha[1] power decreases bilaterally in M1 from movement onset to 300 ms. This pattern was observed consistently across all subjects. Transient beta power increases were seen in bilateral M1, SMA and left PM (6 out of 9 subjects), and enhanced gamma was seen in SMA and PM bilaterally (8 out of 9). I also observed transient

[1] I refer to the conventional classification of frequency bands into theta (4-8 Hz), alpha (8-15 Hz), beta (15-30 Hz), and gamma (>30 Hz).

bilaterally M1 beta power decreases in some subjects (5 out of 9). Taken together, these time-frequency responses are in line with previous findings (Crone et al., 1998a; Crone et al., 1998b; Kilner et al., 2003; Leocani et al., 1997). The lower panel in Figure 3.3 shows the predicted spectral responses, at the source level, by the best (**l-ILEN**) model (see 'Inference on models' for details). Note that the spectra are normalized individually with respect to their maximum.

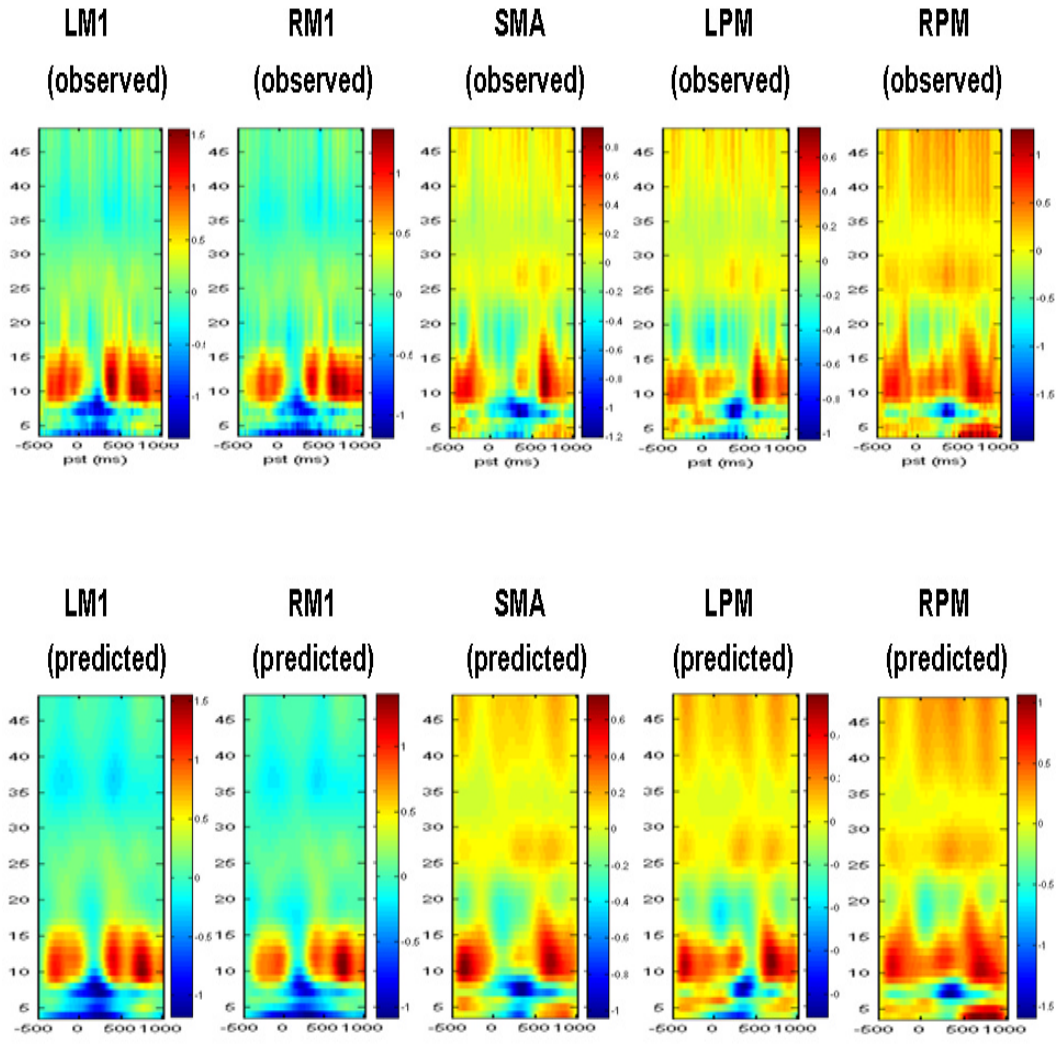

Figure 3.3 The observed (upper panel) and predicted (lower panel) spectral responses for a representative subject under the best mode (**l-ILEN**) from the Bayesian model comparison.

3.3.2 Inference on models: Nonlinear effect and motor networks

Figure 3.4 summarizes the results of the model comparison. It is immediately obvious that the models which fit the data best are those with nonlinear extrinsic coupling (Figure. 3.4). Models with one or more nonlinear connection were consistently better than purely linear models in every subject (Figure. 3.4). An ILEN model was the best in six out of nine subjects and four out of those six subjects have the l-ILEN model as the best at the single subject level. At the group level, the l-ILEN model was the best model amongst those tested. Note that the BMS results are conditional on the assumption of fixed effects. The random effects assumption can be employed to account for the between subject variability in model space. (i.e. the group heterogeneity) or outliers in the model-evidences (see Stephan et al, 2009 for details and chapter 6 for example). In addition, it is also important to note that the most complex model (b-INEN) is not necessarily the best (only one subject had this model as the best). This is because the log-evidence includes a penalty term for complexity. The two-way ANOVA confirms the strong evidence for nonlinearity (levels: **ILEL**, **INEL**, **ILEN**, and **INEN**; $F(1.70,13.63)=15.483$, $p<0.0001$) in terms of its consistency over subjects. However, there was no effect of laterality (levels: right, bilateral and left lateralized models; $F(1.03,8.27)=0.744$, $p=0.417$) nor any interaction ($F(1.34,10.70)=1.026$, $p=0.359$).

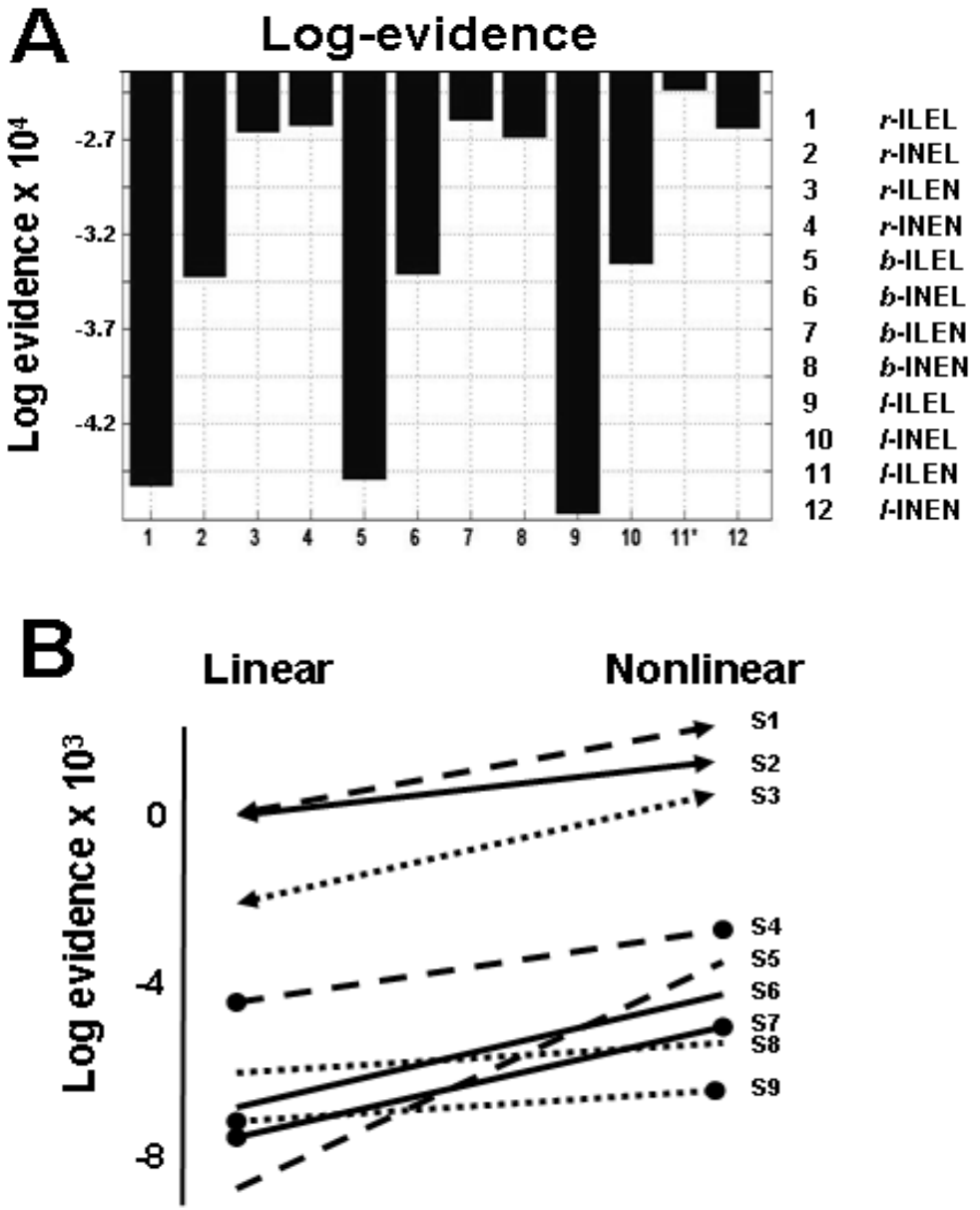

Figure 3.4 Results of Bayesian Model Selection. (A) Pooled log-evidences of the twelve DCMs tested). It can be seen that the best model is **l-ILEN** (log-evidence = -24297) and the next best is **b-ILEN** (log-evidence = -25880). **(B)**: Comparison of the average log-evidences for the three purely linear (**ILEL**) models and the remaining nonlinear models; shown for each subject. The positive slopes over all subjects indicate that the nonlinear coupling is essential as the nonlinear models are always better than the linear ones.

In summary, in normal subjects, I found very strong evidence for nonlinear coupling between areas but no evidence for nonlinear interactions within areas. Furthermore, this evidence was expressed consistently in subject-specific responses. In addition, there is evidence for an asymmetry of interhemispheric interactions in the right hand movement task I used; although this was less consistent over subjects.

3.3.3 Coupling parameters

The coupling parameter matrices of all subjects under the **l-ILEN** model, where each matrix represents the frequency-to-frequency coupling of one connection enter the statistic test and the corresponding SPMs of the T-statistic (thresholded at $p<0.005$ uncorrected) are shown for 'excitatory' (positive; Figure 3.5A) and 'inhibitory' (negative; Figure 3.5B) effects respectively. As seen in Figure 3.5, I found several instances of consistent nonlinear (between-frequency) interactions. These seem to be more profound when the coupling is negative. For instance, several consistent regions of negative coupling are found far from the (within-frequency), leading diagonal compared to the positive coupling SPMs. When considering reciprocal connections, the frequencies entailed by nonlinear coupling appear asymmetric. For example, in Figure 4B (arrows), the negative coupling from LPM to RM1 involves alpha-gamma coupling, while the reciprocal RM1 to LPM connection shows significant gamma-theta coupling. In the same vein, theta oscillations in SMA suppress gamma oscillations in LM1 but, from LM1 to SMA, the negative coupling was between gamma and alpha. A summary

of these T-test results is provided in Table 3.1. The more quantitative characterisations of the nonlinear coupling identified by Bayesian model comparison speak to the complicated nature of nonlinear interactions in the brain, even when modelled as simply as with DCM for induced responses.

Table 3.1 Summary of the SPM analysis of the coupling parameters (+ denotes positive and - denotes negative coupling)

	LM1	***RM1***	***SMA***	***LPM***	***RPM***
LM1		theta-theta (+) alpha/beta-beta (+)	theta-theta(+) theta-gamma(-) alpha-alpha (-)	beta-theta(+) alpha-alpha(-)	
RM1	beta-beta (+) gamma-gamma (+)		beta-beta(+) gamma-gamma(+)	gamma-alpha (-)	gamma-beta(+) gamma-theta(+) theta-alpha(-) alpha-gamma (-)
SMA	gamma-alpha (-)	alpha- alpha(+) gamma- alpha (-)		alpha-alpha (+) beta-beta(+) gamma-gamma (+) alpha-alpha(-)	theta-alpha(+) beta-beta(+) gamma-gamma(+) beta-gamma(-) gamma-beta(-)
LPM	theta-alpha(-) alpha-theta(-) beta- alpha (-)	beta-alpha(+) gamma-beta(+) theta-alpha(-) gamma-theta(-)	beta-gamma(+) gamma-gamma(+) theta-alpha(-) alpha-gamma (-) gamma-theta/alpha (-) gamma-gamma(-)		alpha-gamma (-) beta-alpha(-)
RPM		gamma-gamma (+) beta-alpha(-)	alpha-theta(+) alpha-beta(+) gamma-gamma (+) beta-gamma(-)	alpha-alpha(+) alpha-beta(-) beta-gamma(-) gamma-alpha (-)	

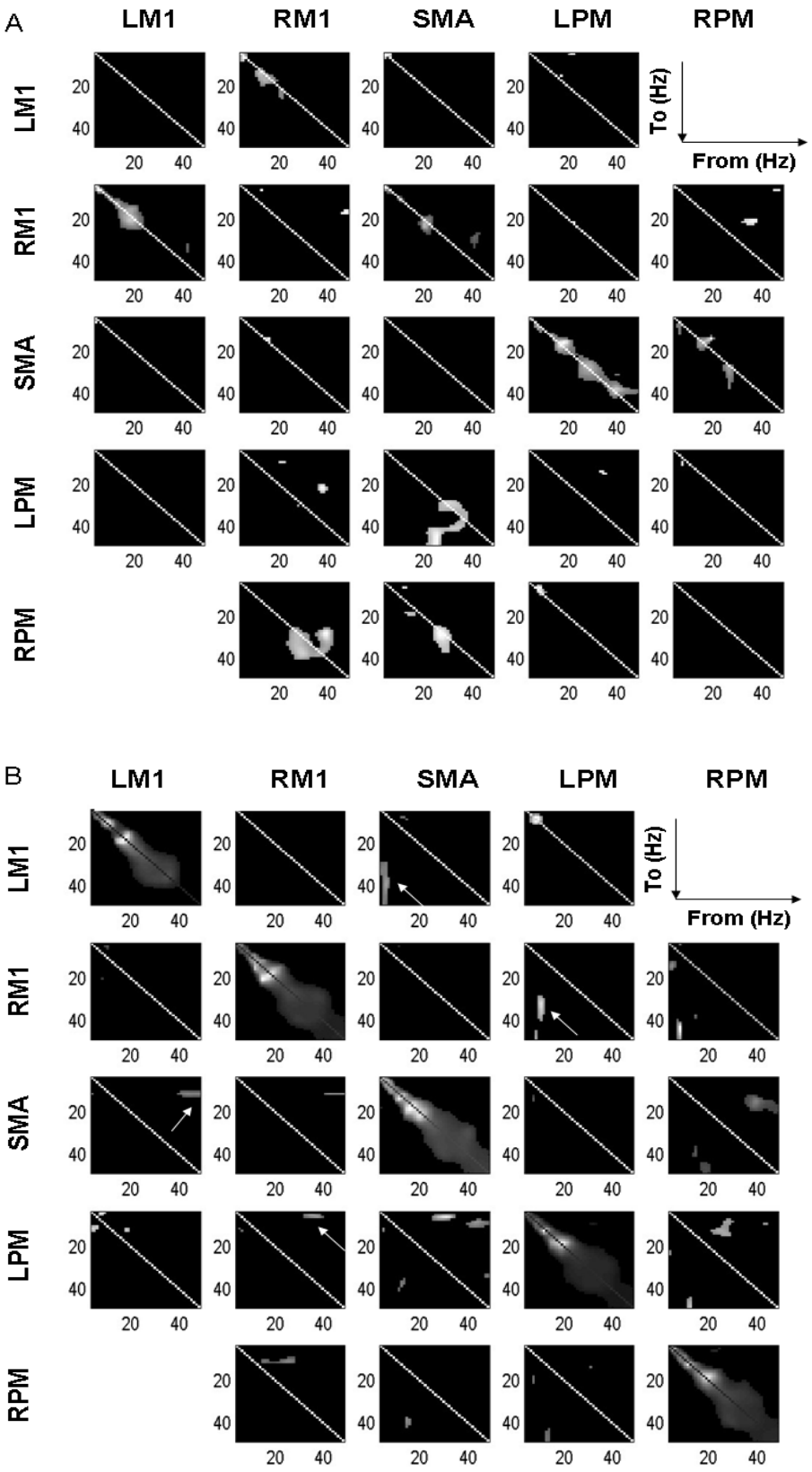
A
LM1
RM1
SMA
LPM
RPM
To (Hz)
From (Hz)
20
40
B
LM1
RM1
SMA
LPM
RPM
To (Hz)
From (Hz)
20
40

Figure 3.5 Statistical results of coupling parameters. (**A**) SPM of the positive coupling strengths (one-tailed), thresholded at $p<0.005$ uncorrected. This shows regions of frequency-frequency space, where the average coupling was great than zero. (**B**) SPM of negative coupling parameters. The arrows indicate functional asymmetries in terms of frequency-specific coupling. The significance of the linear (within-frequency) intrinsic coupling is partly due to prior constraints on the parameters that ensure the system is dissipative.

3.4 Discussion

In this work, I provide empirical evidence for nonlinear coupling among distributed neuronal sources in the motor system. Furthermore, these data support the idea that nonlinear coupling plays an important role in modulating spectral responses under normal conditions. Interestingly, I found no evidence for nonlinear or between-frequency coupling intrinsic to each source, suggesting that linear or driving mechanisms may provide a sufficient account of the interactions among local neuronal populations. In addition, I found evidence for an asymmetric inter-hemispheric interaction involving right PM in this right-hand movement task. A quantitative examination of the extrinsic or long-range coupling parameters, showed some interesting asymmetries in frequency space and that this coupling was predominantly negative or suppressive.

3.4.1 Intrinsic (local) linear and extrinsic (global) nonlinear effects

A recent pharmacological study in rat brains has shown that co-application of kainic acid and carbachol to layer V in M1 can reliably induce synchronous oscillatory activity in the beta frequency band in layer II to VI (Yamawaki et al., 2008). These results imply that inter-laminar influences may be mediated by driving or linear effects because they induce distributed oscillations at the same frequency. Furthermore, it has been shown that in pathological conditions such as Parkinsonism, abnormal oscillatory synchronization of neuronal populations in cortex, subthalamic nucleus and basal ganglia can lead to movement impairment (Brown, 2007; Levy et al., 2002; Marceglia et al., 2006; Priori et al., 2004). The findings suggest that the local interactions may be predominantly linear under normal conditions. Other studies have demonstrated nonlinear coupling in EEG/MEG signals in a variety of tasks, systems and pathological conditions (Breakspear, 2002;Antoniou et al., 2004; Breakspear, 2002; Chavez et al., 2003; Kotini and Anninos, 2002) leading to suggestions that nonlinear coupling is an important aspect of functional integration (Jensen and Colgin, 2007; Tallon-Baudry and Bertrand, 1999; Varela et al., 2001). I have shown that during the performance of a simple motor task both linear and nonlinear coupling is likely to be present. Specifically, the results demonstrate that local interactions can be explained by linear coupling, but that coupling between regions is nonlinear in nature.

3.4.2 Asymmetry of inter-hemispheric connections

Asymmetry in the human brain architectures has been shown in many studies, both functionally or anatomically (Amunts et al., 1996; Friston, 2005; Rockland and Pandya, 1979; Zeki and Shipp, 1988). In the motor system, handedness and experience-dependent plasticity are thought to be the main factors subtending these asymmetric properties (Haaland et al., 2000; Karni et al., 1995; Kloppel et al., 2007). Moreover, functional lateralization of motor control can be altered by pathological or traumatic changes (Ward et al., 2004). In this study, I was able to quantify task-dependent frequency-specific causal influences mediating the observed spectral responses and characterise functional asymmetry in terms of long-range coupling. Bayesian model comparison suggested that the left lateralised **ILEN** model was superior to the symmetric homologue. The left-lateralised model conforms to the left hemisphere dominance, expressed for example in the asymmetric engagement of premotor cortex during skilled movement in right-handed adults (Pollok et al., 2006).

3.4.3 Asymmetry of hierarchical connections

In addition to hemispheric asymmetries, frequency-specific coupling was distinct in forward and backward connections, especially between the SMA and premotor sources. Furthermore, predominant positive and negative couplings are located in different frequency bands in most connections. For example, the gamma

rhythm in left M1 inhibits the alpha activity in SMA but no consistent positive connection was found.

It is important to establish the normal pattern of the frequency-specific interactions in the motor system because several movement disorders show frequency-related abnormalities, such as resting tremors (4~6 Hz) and bradykinesia (10- to 35 Hz) (Brown, 2007). However, the details of the underlying mechanisms remain largely unknown. The study provides a qualitative and quantitative characterisation of frequency-specific effects under normal conditions, which I hope will be useful when studying induced responses in patients. To my knowledge, this is the first study of frequency-specific coupling in the motor network under normal conditions. Given that, in the motor system, induced responses depend on the task and show substantial between-subject variability (Aoki et al., 1999; Kilner et al., 2000; Kristeva et al., 2007; Omlor et al., 2007), I do not anticipate these results will generalize to other movement-related networks. Rather, I consider this study as a reference point for similar studies in patients using the same paradigm.

In conclusion, I have established the prevalence of nonlinear or between-frequency coupling among distributed components of the motor system during a simple motor task. These extrinsic nonlinear interactions appear to unfold in the context of local or intrinsic linear coupling within each area. The associated task-dependent motor network has asymmetric features, as reflected in both the deployment of connections and the frequency specificity of reciprocal connections. In chapter 4, I will show how this motor network is affected by healthy aging.

CHAPTER 4

AGE-DEPENDENT CHANGES IN THE MOTOR NETWORKS DURING HAND GRIPS

4.1 Introduction and specific aim

Age-associated changes in the central nervous system have been studied intensively, both functionally and anatomically. In healthy adults, recent neuroimaging studies suggest that changes in activation patterns result from neuro-anatomical and neurochemical abnormalities that occur with aging (Morrison and Hof, 2002; Page et al., 2002; Rowe et al., 2006b; Gruss and Braun, 2004; Sarter and Bruno, 2004). In relation to cognitive deficits, Cabeza and colleagues reported that prefrontal activity is less lateralized in older adults than in younger adults during cognitive tasks; and proposed the HAROLD (hemispheric asymmetry reduction in older adults) model (Cabeza and Nyberg, 2000; Cabeza, 2002a). These age-related hemispheric asymmetry reductions are thought to play a compensatory role in sustaining cognitive performance: the compensatory mechanism appearing only in high-performing but not low-performing old

subjects (Dolcos et al., 2002; Cabeza et al., 2002b). This is similar to observations in the motor system. Loss of fine movement and slowing of movement speed are features of aging (Smith et al., 1999; Krampe, 2002) but compensatory processes in cortical and subcortical systems may allow the maintenance of performance (Ward, 2006). In general, task-related brain activity may be greater in MI, PM and SMA and other regions in older compared to younger subjects, although this depends on the task used (Ward and Frackowiak, 2003; Ward, 2006; Mattay et al., 2002; Labyt et al., 2003; Labyt et al., 2006; Sterr and Dean, 2008). At the level of neuronal processing, these age-related changes may reflect network connectivity (Dolcos et al., 2002; Cabeza et al., 1997; Rowe et al., 2006a; Taniwaki et al., 2007; Gazzaley et al., 2008). However, how neural networks reorganize in response to age-related degenerative changes remains unclear.

Furthermore, changes in oscillatory activity are seen during neuro-development and aging. For example, the posterior 4 Hz rhythm in the first 3 months after birth can be enhanced with eye-closure but fade between 3 and 10 years of age; at this stage there is a maturation of alpha oscillations and the emergence of the typical blocking effect of eye opening. The delta (~4Hz) rhythm is believed to be the precursor of occipital alpha (Niedermeyer, 1999; Pilgreen, 1995). In addition, it has been reported that oscillatory drive to motoneuron pools changes with development: the younger the subjects are, the lower the EMG and EEG-EMG coherence at ~ 20 Hz is (Farmer et al., 2007; James et al., 2008). Taken together, this suggests that the aging alters not only network architecture but also the frequency content of the ensuing dynamics. The aim of this chapter

was to examine age-related network changes in terms of coupling frequencies based on my previous findings in chapter 3.

4.2 Results

4.2.1 Subjects and Behaviour result

Sixteen healthy, right-handed (eight young, mean age 26, range 20~32 years of age and eight old, mean age 66, range 47-76 years) subjects participated in this study. Part of the data (young group) has been reported in chapter 3. The task undertaken and the data analysis procedure are exactly the same as described in chapter 3. The performance of young and old subjects in terms of reaction time (RT) and grip duration (DU) is summarized in Fig 6.1A. There were no significant differences in reaction time ($p=0.70$; mean= 617.64 and 579.84 ms for young and old group, respectively) or duration ($p=0.71$; mean= 614.45 and 596.05 ms for young and old group, respectively) between young and old groups (one-tailed student *t*-test). This suggests that task performance was similar in both groups, although the variances of RT and DT were higher in the young group (Figure 4.1B). In contrast to other studies (Mattay et al., 2002; Smith et al., 1999; Sterr and Dean, 2008), the mean RT of elder subjects was shorter than that of young subjects, although this did not survive our statistical criterion.

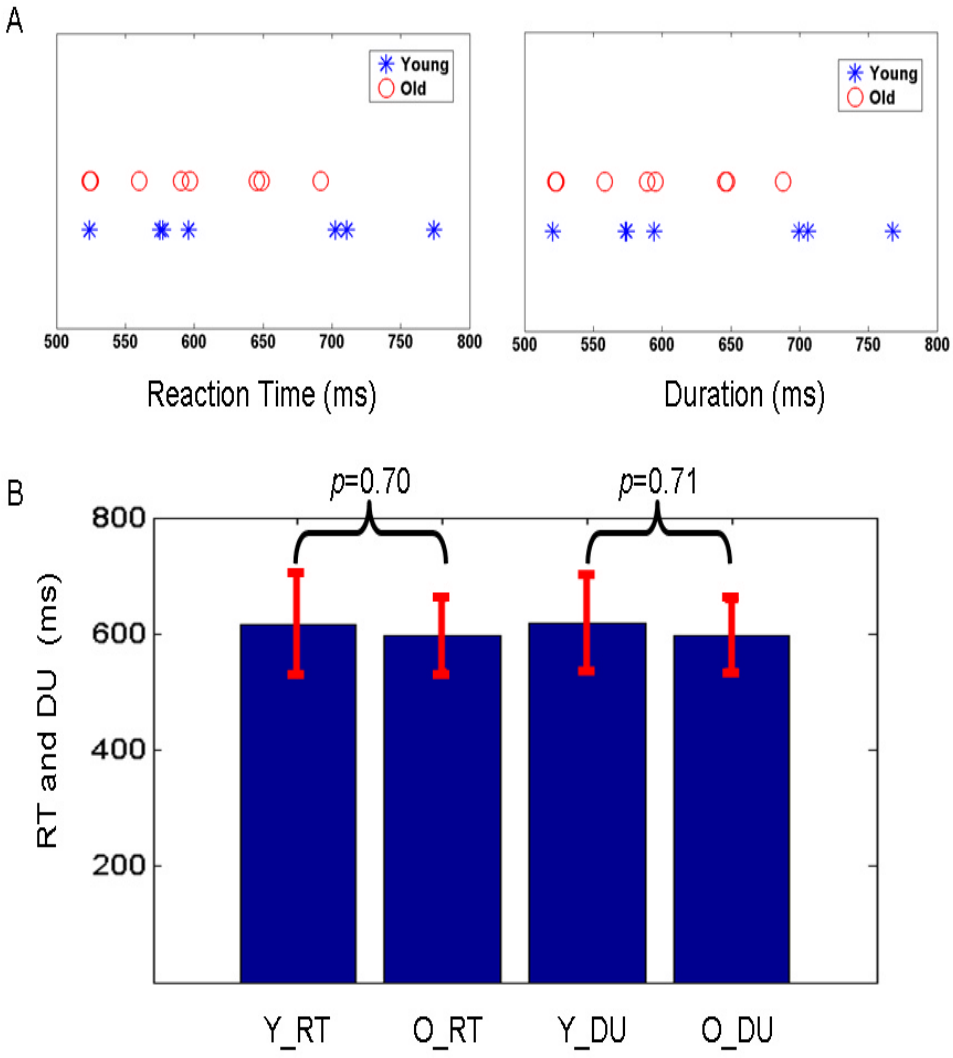

Figure 4.1 Summary of subject performance. A) The RT distribution (left) and the DU (right) data from both groups. B) *P*-values from a two sample *t*-test comparing old and young subjects. Y : young; O : old; RT: reaction time; DU: grip duration.

4.2.2 Inference on model space

Twelve DCMs were inverted for each subject, as shown in Figure 3.2 (chapter 3). The data processing has been described in detail in chapter 3. Figure 4.2 shows the result of Bayesian model selection (BMS) at the group level under fixed-effect assumptions (Penny et al., 2004; Stephan et al., 2009). It is evident that in the old group, the best model is the model with a symmetric connection pattern (sILEN). Critically, the difference between the best models for young and old subjects was the inclusion of RPM-LM1 coupling. This was evident in the old group but absent in the young group. In other words, the left hemispheric dominance in motor control during right hand grip diminished in old subjects. This is in line with Ward and colleagues report of fMRI data (Ward et al., 2008; Talelli et al., 2008a) and the HAROLD model prediction (Dolcos et al., 2002; Cabeza et al., 2002b). To ensure group differences in log-evidence were consistent in relation to inter-subject variability, the log-evidences for each model were entered into a repeated-measures analysis of variance (ANOVA) with 2 by 4 by 3 factors. The ANOVA on log-evidences is effectively a test for differences in log-evidence, which is the same as a test on the evidence ratios (i.e., Bayes-Factors). The advantage of the ANOVA is that one can say the differences are consistently large, in relation to inter-subject variability in log-evidence. This also protects against outlier effects. The group factor has two levels (young and old) and within-subject factors were nonlinearity (four levels) and laterality (three levels – corresponding to the columns and rows of Figure 3.2 respectively). Table 4.1

summarizes the results. These confirm the BMS finding that the two groups differ greatly in laterality (p=0.002); i.e., a group times model interaction.

Table 4.1 Summary of statistical results

Main effect	
Group	F(1.0, 7.0)=0.192, p=0.674
Nonlinearity	F(2.36,16.54)=35.493, p<0.0005*
Laterality	F(1.10,7.70)=20.626, p=0.002*
Interaction	
Group X Nonlinearity	F(1.62,11.32)=4.299, p=0.047*
Group X Laterality	F(1.73,12.12)=11.944,p=0.002*
Nonlinearity X Laterality	F(2.83,19.83)=3.829, p=0.028*
Group X Nonlinearity X Laterality	F(2.40,16.82)=3.179, p=0.060

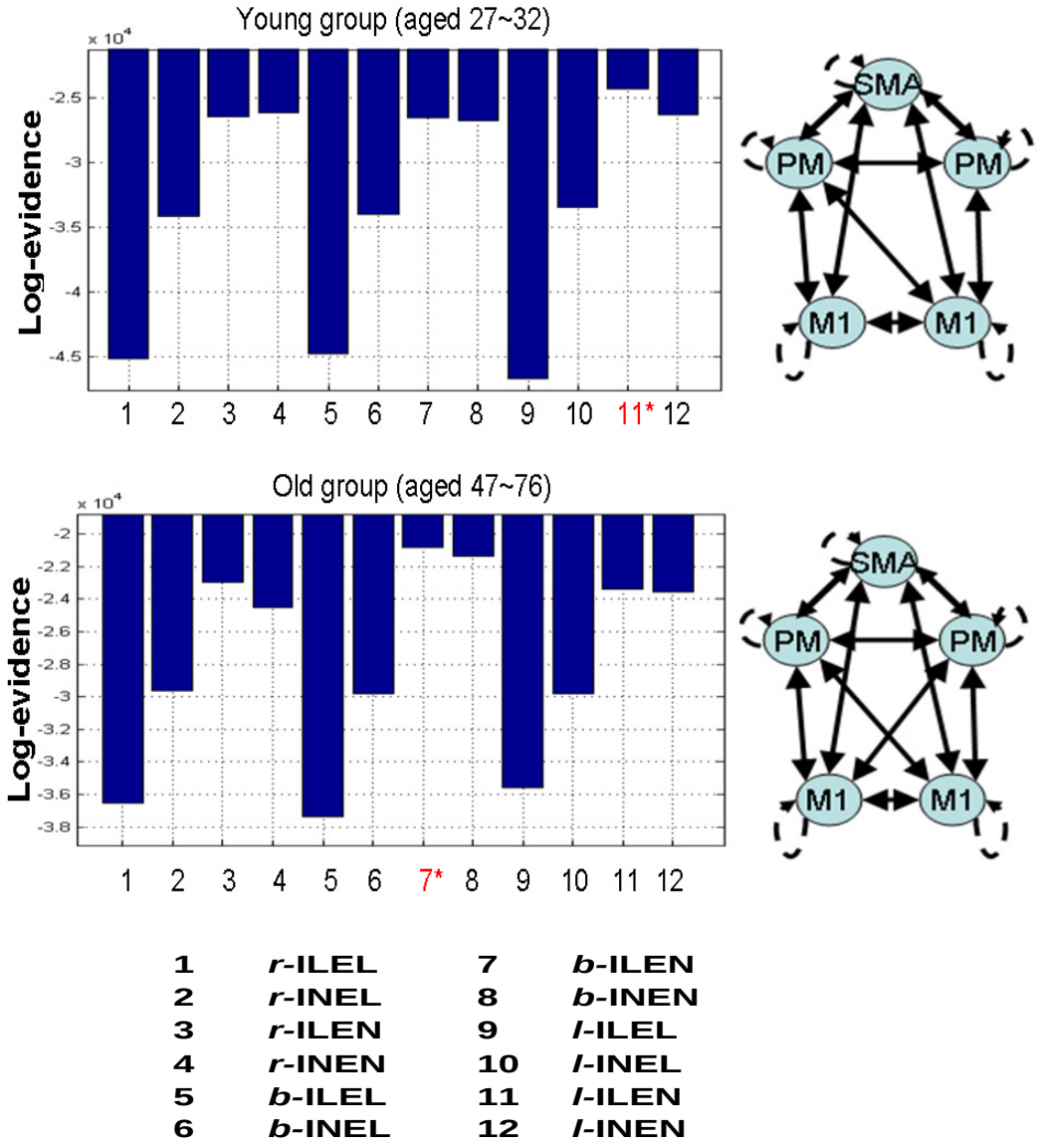

Figure 4.2 BMS results at the group level, under fixed effect assumptions. Upper panel: Summed log-evidences for the twelve DCMs, pooled over young subjects (left) and the network architecture of the best model (right). Lower panel:

Summed log-evidences for the twelve DCMs, pooled over old subjects (left) and the network architecture of the best model (right).

4.2.3 Inference on coupling parameters

The average of the coupling parameters from the group-specific best models, i.e. l-ILEN for young and s-ILEN for old participants are shown in Figure 4.3 (positive) and 4.4, (negative). The coupling strength matrices (the conditional expectations of the coupling matrices) of all subjects were smoothed with a Gaussian Kernel (FWHM = [8 8]) and entered into a conventional SPM analysis to identify the within-group (first-level analysis) significant frequency-specific effective connectivity. Figure 4.5 and 4.6 show the significant 'excitatory' (positive) and 'inhibitory' (negative) effects respectively (shown thresholded at $p<0.005$ uncorrected). The most striking finding is that during right hand grip, the age-dependent RPM –LM1 coupling in old subjects has an inhibitory effect (Figure 4.6B). In addition, there is a tendency in old brains for LM1 to 'talk to' RM1, using higher frequencies compared to the young brains (Figure 4.5; alpha to beta ranges for young and beta to gamma ranges for old subjects). In general, the 'young' motor networks employ more facilitated mechanisms (more distributed positive coupling) whereas the 'old' motor networks show more negative coupling.

To examine the between-group differences, the coupling matrices where compared using a two sample *t*-test. Figure 4.7 shows the results of this analysis, thresholded at $p<0.05$, FWE corrected). I show the increases in positive coupling

and decreases in negative coupling separately. These can be seen in a variety of connections and frequencies. Table 4.2 and 4.3 summarized these significant age-related differences. Interestingly, there was no significant strength decrease in positive coupling (i.e. reduction of excitation), nor a significant strength increase in negative coupling (i.e. reduction of inhibition; for example, the coupling strength rises from -5 to -3) when comparing the parameters of the old group to the young. Note that because there are no RPM-LM1 connections in the motor network of young subjects, the statistical test on these coupling matrices are identical to those in Figure 4.5B and 4.6 B.

4.3 Discussion

In this chapter, I found that the motor network of older subjects has diminished left hemispheric dominance during right hand movement as the older subjects recruit right PM-left M1 connections. In addition, these age-dependent right PM-left M1 connections are inhibitory. Furthermore, the 'old' motor networks have more negative effects in relation to the 'young' motor networks that employ more positive coupling mechanisms.

Inference on model space

Firstly, BMS suggests that there is significant difference in the best model for each group; the symmetric model (s-ILLEN) was the best model for older subjects, as opposed to the asymmetric model (l-ILEN) for younger subjects. This was reflected in a significant model by group interaction, when I performed an ANOVA on the log-evidences (Group x Laterality: $p = 0.002$). Interestingly, there was no main effect of group on the log-evidence, which means most models being tested were as good at explaining both group data.

Possible functional role of inhibition in motor networks of old subjects

A key finding in this chapter is that the older subjects use more inhibitory mechanisms, including the age-dependent right PM-left M1 connections. At a cellular level, inhibitory neurons play an important role in regulating excitatory activity in the cortex and contribute to the generation of gamma oscillations (Chance et al., 2002; Sohal and Huguenard, 2005). For example, in the auditory cortex, cortical inhibition in sound processing can increase its temporal precision (Wehr and Zador, 2003). In somatosensory cortex, inhibition controls the activity of receptive fields as well as their temporal precision (Bruno and Simons, 2002). Furthermore, excitatory and inhibitory neurons are synchronized, when generating sensory-evoked responses (Okun and Lampl, 2008). Moreover, inhibition may play an important role in activity-dependent synaptic plasticity (see Sun 2007 for a review). As the performance of old subjects was not significantly different to that of young subjects, one possible role of enhanced inhibitory coupling may be to

fine-tune the motor system in response to age-related changes; so that performance can be maintained.

In relation to previous fMRI and TMS findings

In fMRI studies of hand-grips, task-related activation is more diffuse and bilateral in older subjects as opposed to the more focused and lateralized responses in young subjects (Ward et al., 2007; Ward et al., 2008). Specifically, age-related signal increases have been seen in ipsilateral M1 and PM; i.e. in older subjects, activations in these areas are greater (Naccarato et al., 2006, Ward, 2006a, Ward et al., 2007; Ward et al., 2008). It is reasonable to assume that neuronal engagement of ipsilateral PM in old subjects may explain the increase of activation in ipsilateral PM seen in fMRI studies; as when the neurons are firing, they consume energy and result in metabolic changes. Interestingly, as PM exhibits an inhibitory effect, our findings might imply that the MEG based characterization (i.e. positive (+) and negative (-) coupling) may not always be in accordance with fMRI (i.e. activation (+) and deactivation (-)). Such a dissociation has been seen in PET (Hershey et al., 2003; see also Buzsaki et al., 2007 for a review on inhibition and brain work) and in EEG-fMRI studies (David et al., 2008) where inhibitory activity was shown to increase the blood flow / BOLD signal.

In terms of the cause of the increased responses in ipsilateral M1, TMS and fMRI studies suggest that the reduction of interhemispheric inhibition (IHI) from left M1 to right M1 might be attributed to the increases of ipsilateral activation during right-hand movement (Talelli et al., 2008a; Talelli et al., 2008b; Ward et al., 2008). This reduction of IHI in advancing age is highly task- and inter-stimulus interval-dependent. At first glance, this TMS result seems to contradict the findings in this chapter as I found no significant reduction of IHI. Instead, there is increase in IHI from left M1 to right M1 (Figure 4.7 lower panel; Table 4.3). However, the two measures are different in many ways. Firstly, the temporal resolution: the estimate of IHI was based on rather transient peripheral signals: a ratio of the conditioned / unconditioned motor evoked potential. This is different to DCM for IR, where the coupling parameters represent the estimated coupling strength over peristimulus time (in this study, -500 ~+1000 ms). Secondly, as IHI uses peripheral signals, it provides indirect and partial measurement of neuronal dynamics. In contrast, DCM for IR models the spectral densities of coupled neuronal sources directly. Further studies using TMS and DCM for IR may help to clarify the functional roles of inhibitory mechanisms in the motor system.

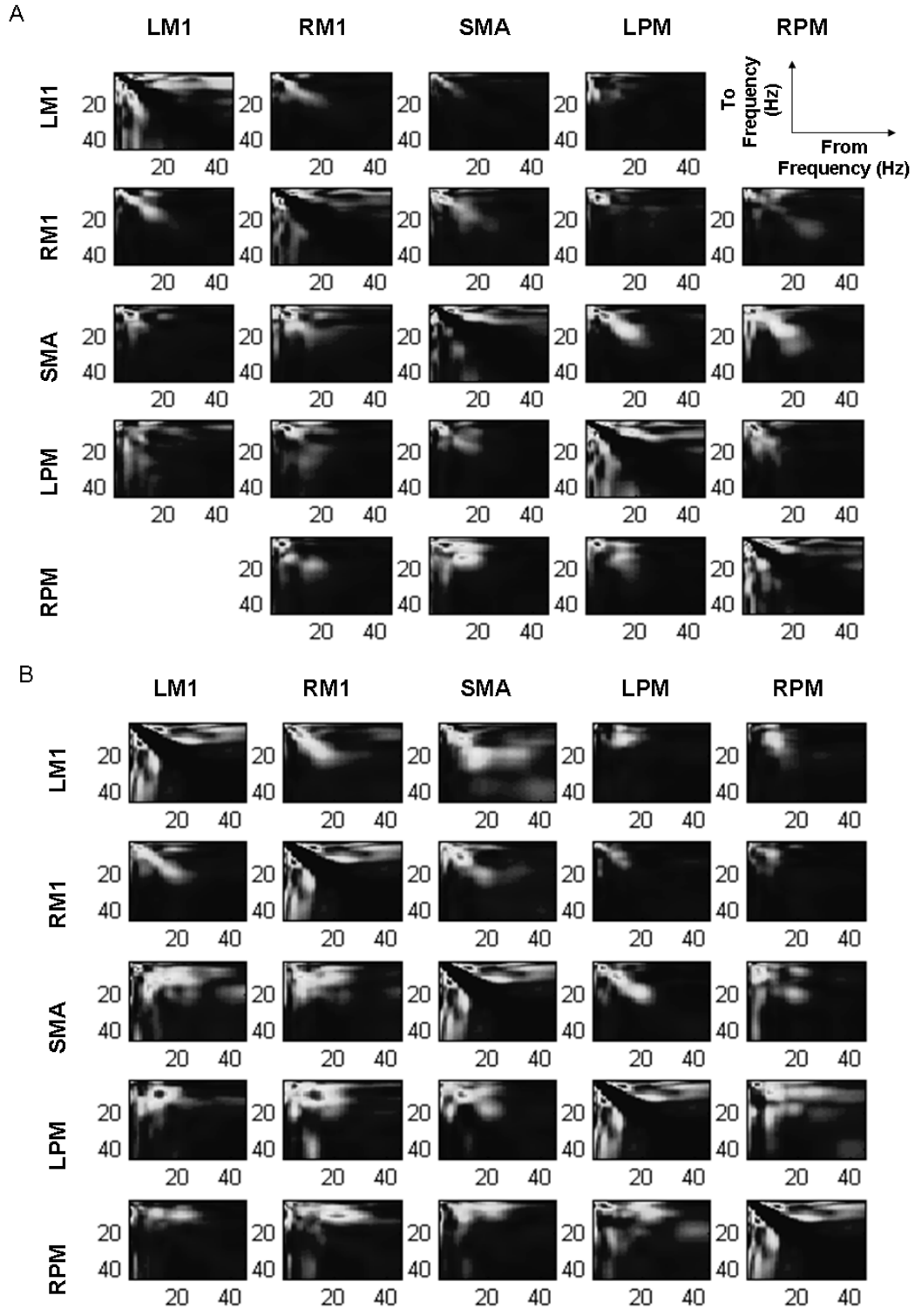

Figure 4.3 Average coupling parameters across young subjects (A) and old subjects (B). Positive are brighter

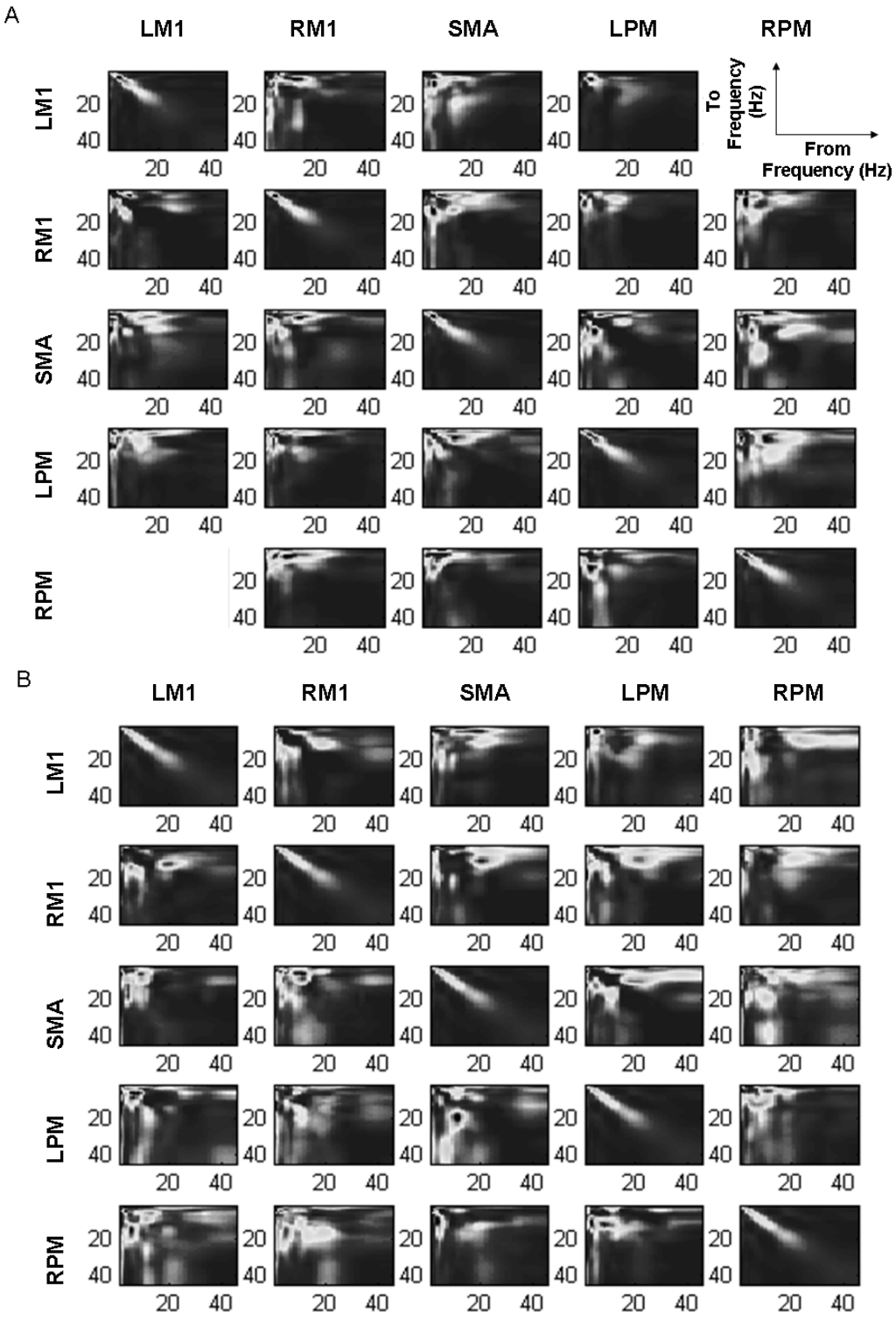

Figure 4.4 Average of coupling parameters across young subjects (A) and old subjects (B). Negative values are brighter.

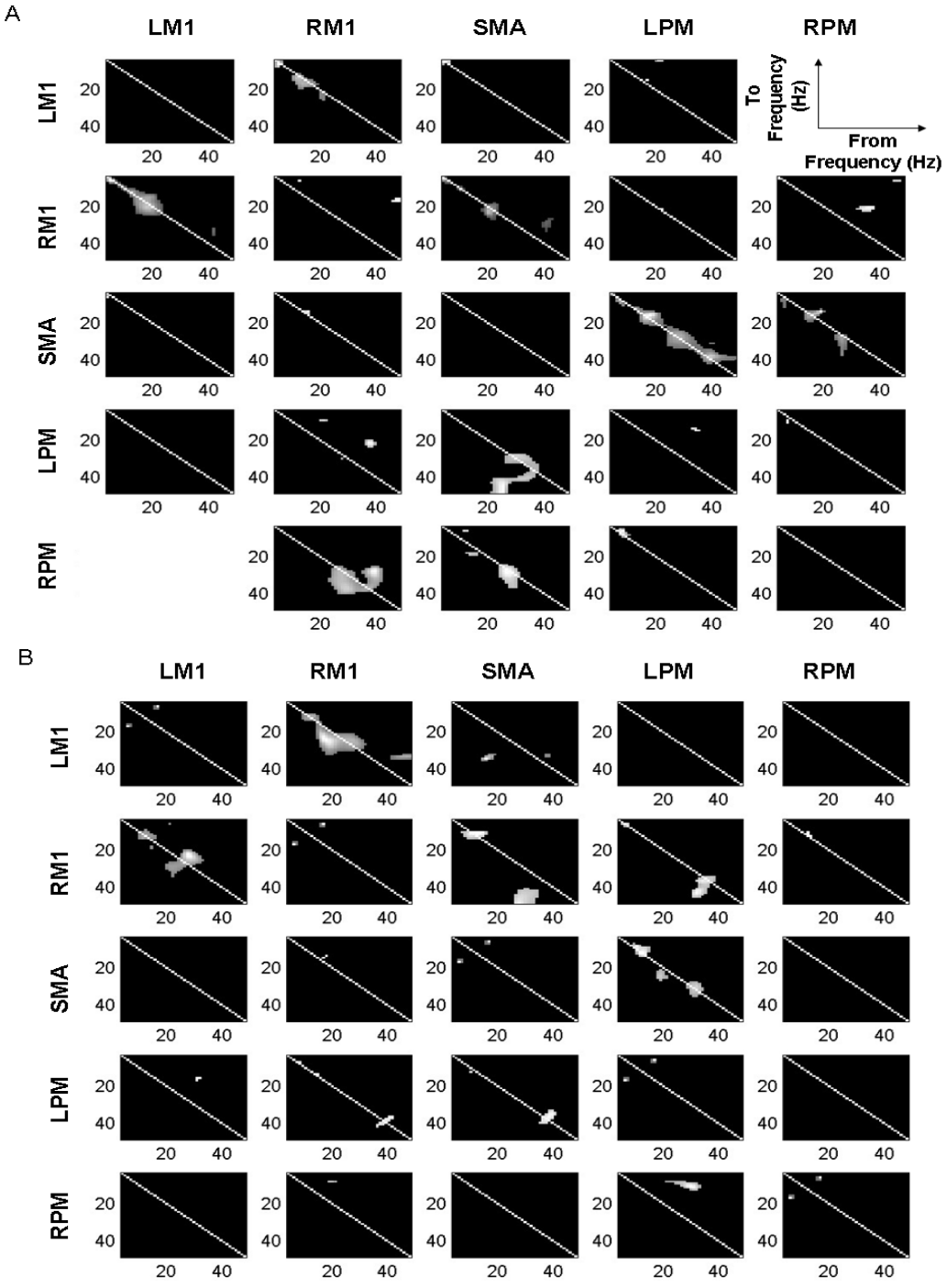

Figure 4.5. SPMs testing for positive coupling parameters (first level analysis: one-tailed t-test thresholded at $p<0.005$ uncorrected). (**A**) SPM{t} of young subjects, (B) SPM{t} of old subjects.

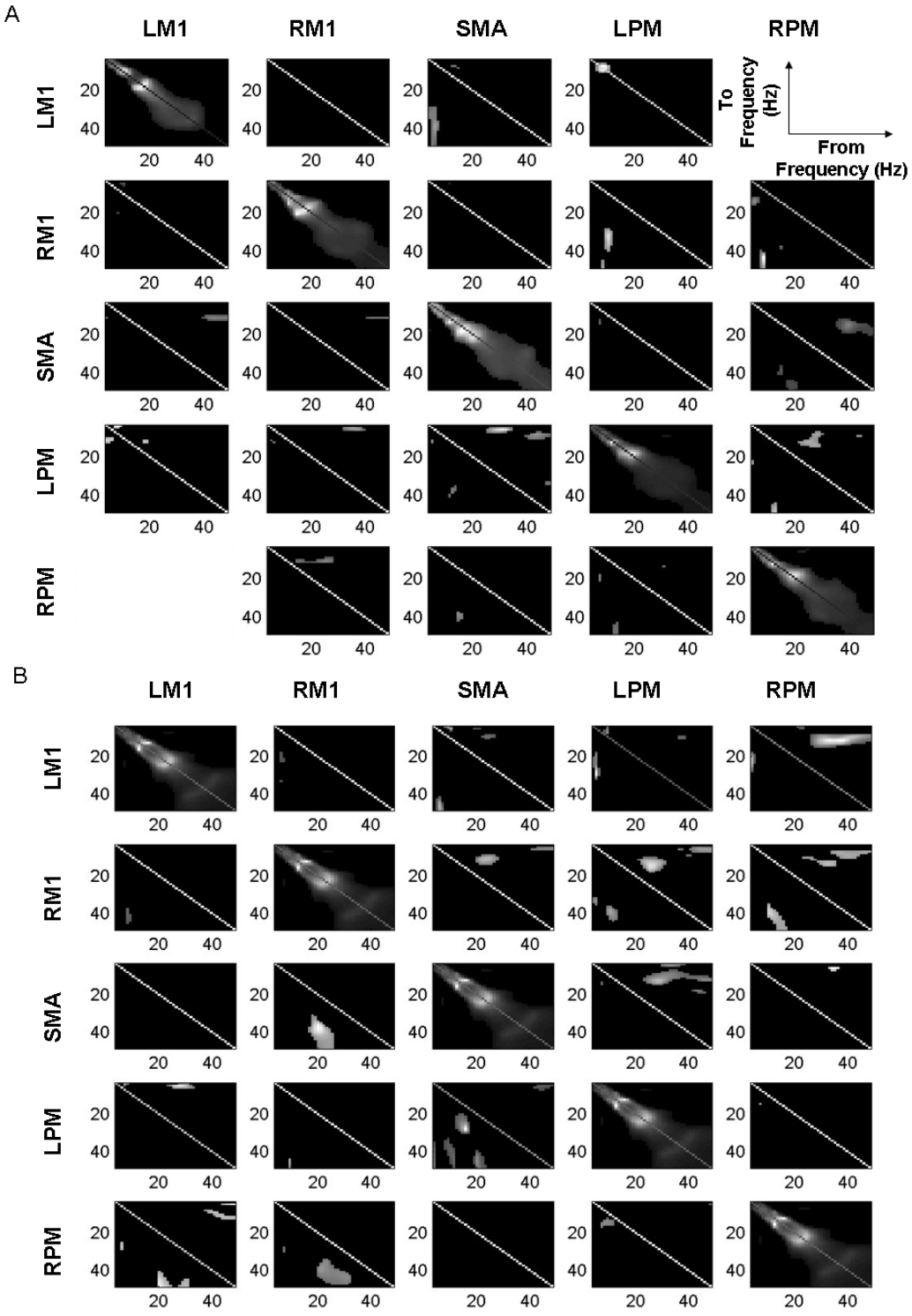

Figure 4.6 SPMs testing for negative coupling parameters (first level analysis: one-tailed t-test, thresholded at $p<0.005$ uncorrected). (**A**) SPM{t} of young subjects, (B) SPM{t} of old subjects

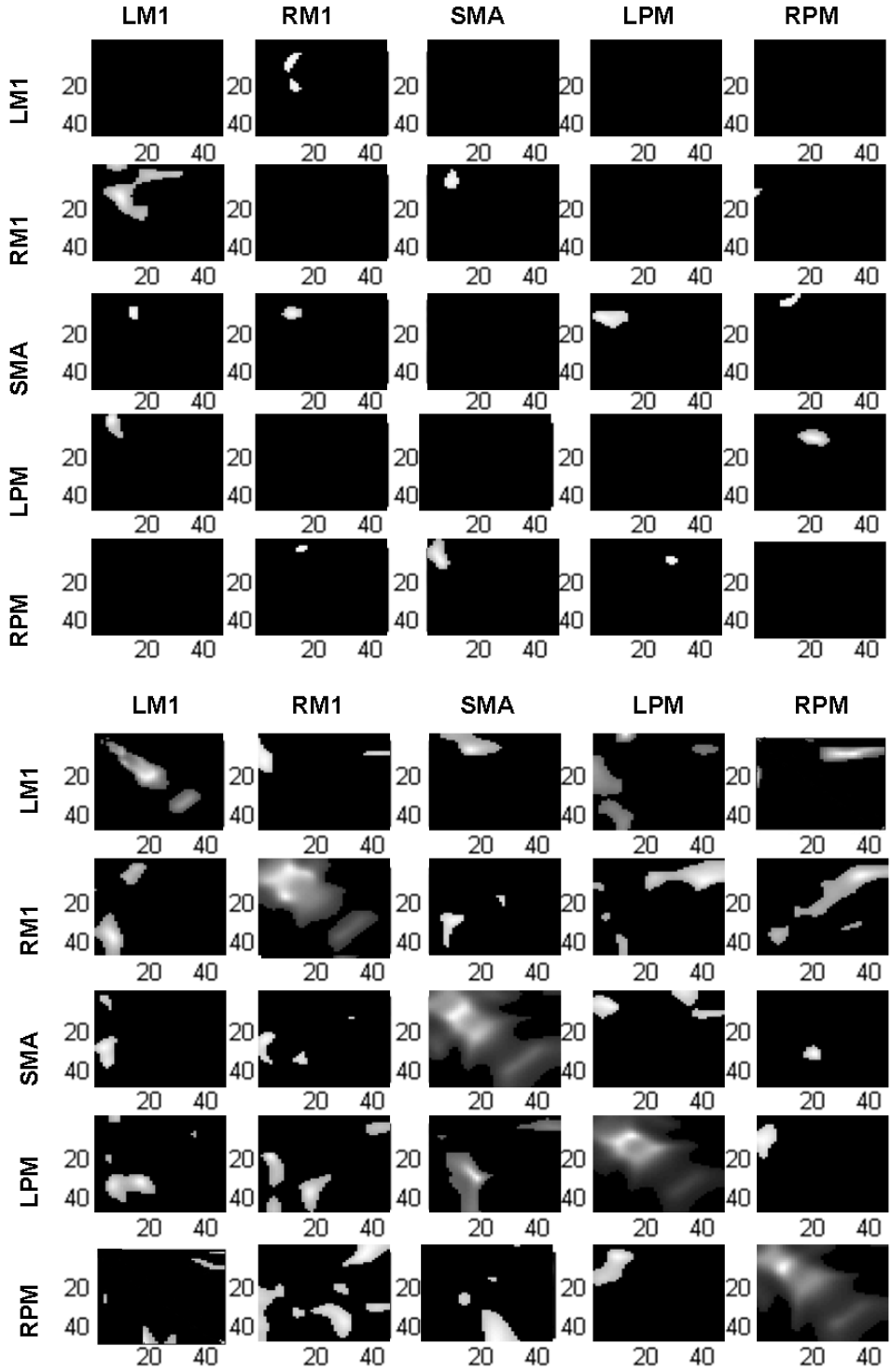

Figure 4.7 Two sample t-test reveals the significant increases in positive coupling (upper panel) and decreases in negative coupling strength (lower panel) in old subjects compared to young subjects ($p<0.05$, FWE corrected).

Table 4.2 Summary of two sample *t*-test on coupling parameters (increases)

	LM1	*RM1*	*SMA*	*LPM*	*RPM*
LM1		Alpha-alpha			
RM1	alpha-theta alpha –beta beta-alpha		Alpha-alpha		Theta-alpha
SMA	Alpha-alpha	Alpha-alpha		Alph-alpha	Alpha-theta/alpha
LPM	Alpha-theta/alpha				Beta-alpha/beta
RPM		Beta-alpha	Alpha-alpha	Gamma-alpha	

Table 4.3 Summary of two sample *t*-test on coupling parameters (decreases)

	LM1	*RM1*	*SMA*	*LPM*	*RPM*
LM1		Alpha-alpha Gamma-alpha	Alpha/beta-theta/alpha	Alpha-beta/gamma Gamma-alpha	Gamma-alpha
RM1	alpha-gamma alpha/beta-alpha		Alpha-gamma	Beta/gamma-alpha	Alpha-gamma Beta-beta Gamma-alpha
SMA	Alpha-alpha Alpha-gamma	Theta-beta Beta-gamma		Alpha-alpha Gamma-alpha	Beta-gamma
LPM	Alpha/beta-gamma	Alpha-beta/gamma Beta-gamma Gamma-alpha	Beta-beta/gamma Gamma-alpha		Alpha-alpha
RPM	Gamma-alpha Beta-gamma	Theta-beta/gamma Beta-gamma Gamma-theta/alpha Gamma-gamma	Beta-beta Gamma-gamma	Alpha-alpha/beta	

CHAPTER 5

FUNCTIONAL ASYMMETRIES IN FORWARD AND BACKWARD CONNECTIONS IN FACE PROCESSING

5.1 Introduction

In previous two chapters, I have shown the DCM results in motor systems using a simple linear form DCM. In this chapter, I aim to show the use of bilinear form of DCM that allows the modelling of experimental manipulations. I tested whether there are functional asymmetries between forward and backward connections in the brain during face perception. The aim of this chapter is to ask if there is an asymmetry in nonlinear or modulatory influences among different levels of a cortical hierarchy. I addressed this asymmetry using MEG data obtained from human subjects during the processing of faces and tried to explain the observed responses using models that do and do not have nonlinear connections. This enabled us to quantify the evidence for nonlinear coupling in qualitative terms, using model comparison. I then compared forward and backward coupling strengths quantitatively, to test for any asymmetries, under the best model.

5.1.1 Hierarchical connections and functional asymmetries

It is now generally accepted that, at least in the sensory cortex, the brain has a hierarchical organisation that is defined largely by asymmetries in extrinsic cortico-cortical connections (Maunsell and van Essen 1983; Zeki and Shipp 1988; Felleman and Van Essen 1991; for motor systems this issue is more controversial, see Shipp 2005). These asymmetries classify a connection as being forward or backward (Rockland and Pandya 1979) and therefore define an implicit (although not necessarily unique; Hilgetag et al 2000) hierarchy of areas. The laminar specificity of forward and backward projections is a key anatomical asymmetry, which may speak to ensuing functional asymmetries (Sandell and Schiller 1982; Murphy and Sillito 1987; Salin and Bullier 1995; Lamme et al. 1998; Angelucci et al. 2002a,b). One of the important aspects of this anatomical asymmetry is that backward connections make synaptic connections predominantly in supra-granular layers, with en-passant connections in infra-granular layers. This is relevant because voltage sensitive (i.e., nonlinear) receptors like NMDA receptors populate, largely, the supra-granular layers (Fox et al. 1989; Rosier et al. 1993), suggesting that backward connections may have preferential access to modulatory, voltage-dependent post-synaptic effects with long time-constants (c.f., Eaton and Salt 1996; Gentet and Ulrich 2004). Similarly, backward connections have also been found to target metabotropic glutamate receptors which, like NMDA receptors, have long time-constants and are thus able to mediate context-sensitive effects (Rivadulla et al. 2002; Salt 2002). The notion that backward connections are more modulatory, in relation to the driving effects of forward connections (Salin and Bullier 1995; Sherman and Guillery 1998), is further supported by the higher degree of divergence that backward connections display and by their ability to transcend more than one cortical level (Zeki and Shipp 1988). In short, most of the evidence from the anatomy of extrinsic (inter-regional) connections, from the spatial distribution of their synaptic connections across cortical layers and from their physiology, points to a functional asymmetry between forward and

backward connections. This asymmetry is consistent with a role for backward connections in modulating, coordinating or providing contextual guidance to bottom-up processing that is driven by forward connections. There are many examples of this ranging from the mediation of extra-classical receptive field effects (Angelucci and Bressloff 2006; Hupe et al. 1998; Lamme and Roelfsema 2000) to the implementation of gain mechanisms that may be involved in attention and biased competition (Larkum et al. 2004). Indeed, direct evidence for the modulatory effect of backward connections has been obtained from reversible deactivation studies in monkeys (Sandell and Schiller 1982; Girard and Bullier 1989; Hupe et al. 1998) and non-invasive fMRI studies of humans (Friston et al 1995; Büchel and Friston 1997; Stephan et al. 2008). However, there have been no direct comparisons of modulatory effects in forward and backward connections in man.

5.1.2 Modulatory effects and nonlinear coupling

The defining characteristics of modulatory pre-synaptic inputs are nonlinear interactions with other pre-synaptic inputs when generating post-synaptic responses. Examples here include the mechanisms of classical neuromodulatory neurotransmitters that, for example, change the conductance of slow potassium channels that mediate after hyper-polarisation (e.g., Metherate et al. 1992; Faber and Sah 2003). These sorts of effects change the response profile of neurons, such that they respond differently to the same driving input. Another key example is the voltage-dependence of NMDA receptor activation, which means that the effect of pre-synaptically released glutamate at these receptors is context-sensitive and nonlinear (e.g., Schiller and Schiller 2001). A third important example of nonlinear interactions relates to action potentials that are back-propagated by means of active conductances throughout the dendritic tree to elicit long-

lasting calcium currents; this means that, depending on the relative timing of synaptic inputs, the propagation of postsynaptic potentials can be facilitated or blocked by preceding synaptic inputs (e.g., Larkum et al. 2004; London and Häusser 2005).

The equivalence between modulatory effects of synaptic connections and nonlinearities in neuronal input-output relations is important because nonlinear effects can be characterised relatively easily using only the observable inputs and outputs of a system. In brief, nonlinear effects induce high-order generalised convolution kernels, in the time domain, or generalised transfer functions in the spectral domain (Friston 2001). These high-order functions couple certain frequencies in the input to different frequencies in the output. A simple example here would be the nonlinear squaring of a sinusoidal wave to double its frequency. This means I can formulate questions about the modulatory effects in terms of coupling between frequencies in spectral responses that are observed in different parts of the brain. This is the basis of a recently developed dynamic causal model (Friston et al. 2003) for EEG and MEG (Chen et al. 2008) that allows one to test various models with and without nonlinear (between-frequency) coupling among specified regions or sources. The study in this chapter is based on this approach.

5.1.3 Nonlinear coupling and generative models in the brain

There are many heuristics that have been used to frame the importance of nonlinear or modulatory coupling in the brain. I focus on a specific but dominant account of functional anatomy, based on hierarchical inference and learning in the brain (Helmholtz 1860; MacKay, 1956; Ballard et al. 1983; Mumford, 1992; Kawato et al. 1993; Dayan et al. 1995; Rao and Ballard 1999; Rao 1999; Friston 2003; Kersten et al. 2004; Friston 2005; 2006). This account suggests that the brain is an inference machine that uses generative models to predict incoming sensory information. In this framework, also

referred to as predictive coding (Rao and Ballard 1999; Friston 2005), perceptual inference corresponds to optimising putative causes of sensory input by minimising prediction error (or, equivalently, variational free-energy). Predictive coding states that brain actively predicts what the sensory input will be, rather than just passively registering it, when trying to represent the environment. Predictive coding is a framework that is equivalent to empirical Bayesian inference in a hierarchical setting (Mumford 1992; Friston et al., 2005; Friston and Kiebel, 2009; Kilner et al., 2007); where the brain tries to infer the causes sensory input. In a biological setting, the minimising of PE can be considered as suppressing the activity of error units using a gradient decent on the variational free-energy associated with the brains internal model of the work and the current sensory input.

This can be achieved simply by generating predictions at higher levels of the cortical hierarchy, which are passed to lower levels to explain away bottom-up inputs. These predictions are updated by prediction errors, conveyed by the forward connections. This scheme entails forward and backward message passing and is formally identical to hierarchical or empirical Bayesian inference (Friston 2003). Critically, because predictions are formed using a generative model of the world, this account predicts that the influence of backward connections is necessarily nonlinear (Friston 2003). A simple example of nonlinearity, in generative models of visual input, would be the occlusion of one object by another. If higher level representations of an object and its occluder are used to provide a prediction of the sensory input, then these top-down effects must interact nonlinearly to encode the occlusion per se. In short, under empirical Bayesian or predictive coding models of perceptual inference, backward connections that convey predictions should suppress activity in lower levels encoding prediction error. Critically, this explaining away of prediction error rests on nonlinear mechanisms. This is

compatible with the physiological evidence, described above, that backward connections mediate modulatory effects.

The functional properties of forward connections are predominantly, but not exclusively, linear; see Friston 2003 and Sherman & Guillery 1998 for a summary of the neurophysiological evidence. However, there is some empirical evidence that forward connections may also exhibit nonlinear properties. For example, transmission of sensory information along forward connections can involve NMDA receptors (Fox *et al.* 1990; Kelly and Zhang 2002; Salt 2002). According to predictive coding theories, forward connections mediate the influence of error units in lower levels on representational units in higher levels, and these bottom-up influences are linear in prediction error (Friston 2003). However, "... although the forward connections mediate linearly separable effects, these connections might be activity- and time-dependent because of their dependence on [higher representations]" Friston (2003). This means the strengths of forward connections may be activity-dependent and therefore appear nonlinear.

In summary, on the basis of the above empirical and theoretical considerations I predicted that coupling between high and low areas would entail cross-frequency or nonlinear coupling. This is because there is substantial evidence that at least one arc (backward connections) of reciprocal self-organising exchanges between visual areas rests on nonlinear synaptic mechanisms. Furthermore, I predicted that backward coupling would suppress neuronal activity in the lowers areas and that this suppression would; (i) be manifest as a significant cross-frequency (nonlinear) suppression (ii) be significantly greater than the equivalent coupling in the forward direction. To test these hypotheses, I used a recently validated dynamic causal model for induced responses measured with M/EEG (Chen *et al.* 2008) to implement different models with and without nonlinear

(between-frequency) coupling among regions involved in visual face processing. Using Bayesian model selection (Penny *et al.* 2004), I compared models in which forward and backward connections could either be linear or nonlinear. I was hoping to show that, qualitatively, nonlinear models were significantly better than their linear homologues. I then examined the coupling estimates from the best model to test the quantitative hypotheses about the suppressive effects of backward connections.

This work comprises three sections. In the first, I briefly summarise dynamic causal modelling for induced responses. This technique is then applied to an MEG study of face perception, as described in the second section. This section describes the factorial construction of four DCMs that were inverted to provide the evidence for each model and subject (*i.e.*, probability of the data given the model). I then identified the best model using Bayesian model comparison and established the consistency of model selection at the between-subject level by analysing the model evidences. In the final section, I present the quantitative characterization of coupling using the conditional parameters estimated of the best model to test for predicted top-down suppression and forward-backward asymmetries.

5.2 Data Acquisition and Analysis

5.2.1 Experimental design and data pre-processing

I analysed spectral responses induced by face processing in ten normal subjects as measured with MEG (Henson *et al.* 2007). Here, I analyse data from a single, eleven minute session, in which subjects saw intact or scrambled faces, subtending visual angles of approximately four degrees. I chose these data because visual processing of face

stimuli *vs*. degraded face stimuli is an example of a perceptual process that has been investigated previously and interpreted in terms of predictive coding principles (*c.f.* Summerfield *et al.* 2006). Scrambled versions of each face were created by phase-shuffling in Fourier space and masking by the outline of the original image. The scrambled faces were therefore matched for spatial frequency power density and size. Subjects made left-right symmetry judgments about each stimulus by pressing one of two keys with either their left or right index finger (range of reaction times was 1031 to 1798 ms). There were 86 intact and 86 scrambled face artefact-free trials as revealed by visual inspection. Ten subjects were tested, five female (young to middle-aged adults). The MEG data were sampled at 625 Hz on a 151-channel axial gradiometer CTF Omega system at the Wellcome Trust Laboratory for MEG Studies, Aston University, England. No subject moved more than 6 mm across the session (median = 1.1 mm, range = 0.2 - 5.6 mm).

The MEG data were pre-processed using SPM5 (Wellcome Trust Centre for Neuroimaging, London). The data were epoched from -600 to +1800 ms, and projected from channel space to source-space using the generalised inverse of the lead-field matrix for the chosen sources (see Model specification below for details). The lead-field (gain matrix) was computed using the coregistered channel locations and a single-sphere forward model computed by Fieldtrip (F.C. Donders Centre for Cognitive Neuroimaging, Nijmegen, as implemented in SPM5). The spectral densities from 4 to 48 Hz at each source were computed using a time-frequency Morlet wavelet transform (Equation 1; wavelet number: 7) between -100 and 600 ms of peristimulus time. The resulting time-frequency responses were first converted to absolute values and averaged over 86 trials for each condition and then baseline-corrected by subtracting the frequency-specific power of the first time-bin. For computational expediency, I reduced the dimensionality

of spectra to four principal frequency components derived from a singular value decomposition (SVD) of the spectra (over conditions and peristimulus time, within subjects). This preserved over 93 % of the spectral variance in all subjects. Note that the generalised inverse of the lead-field described here is one of many inversion schemes that one can use to project data from channel to source space (Darvas et al., 2004; Friston et al., 2008; Kiebel et al., 2007; Michel et al., 2004). The generalised inverse is an appropriate projector if one knows *a priori* where the sources are located. However, the results of any model inversion under these prior assumptions are conditional on the chosen sources being a reasonable summary of the real neuronal sources. If any sources are omitted and misplaced there will be a better model of the data and possibly a different conclusion from model comparison. If one did not know where the spectral signals were coming from, the beam-former method could be one useful strategy that allows one to localize the source positions and estimate spectral features empirically (Singh et al 2003).

5.2.2 Model specification

The anatomical source locations were the maxima of ventral temporal activations in a group SPM analysis of fMRI data from exactly the same paradigm though different subjects (Henson et al. 2003). Those sources have also been reported in MEG face studies (Henson et al. 2007; Itier et al, 2006). Figure 5.1 shows the location of these sources in Montreal Neurological Institute (MNI) coordinates and on a template MRI image in that space. These four sources correspond to the fusiform face area (FFA) and the occipital face area (OFA), bilaterally. The central panel of Figure 5.1 shows the connectivity graph, which served as the basis for constructing alternative DCMs. I assumed reciprocal intra-hemispheric connections between OFA and FFA and reciprocal inter-hemispheric connections between homotopic areas. Additionally, I assumed cross-hemispheric

connections between OFA and contralateral FFA. This connection was added because a previous fMRI study of a prosopagnosic patient with lesions of left FFA and right OFA found normal activation in the right FFA for faces vs. non-faces (Rossion et al. 2003). One possible input to this patient's right FFA is from the intact contralateral OFA. I therefore included forward connections from OFA to contralateral FFA. The connectivity architecture for the models considered in this work is shown in Figure 5.2. All models included reciprocal connections between the visual and fusiform areas within and across the hemispheres. The intrinsic connections were set to be nonlinear because of the highly complex organization of the visual cortices. In mammals, neuroanatomical studies have identified more than 30 functionally distinct cortical areas in extrastriate cortex, for example, with colour- and spatial frequency-sensitive cells (Livingstone and Hubel, 1988; Zeki and Shipp, 1988; Felleman and Van Essen, 1991). Therefore, a specific yet flexible binding mechanism is required in the network that accounts for the integration of distributed activation patterns for information processing and selection in the visual system. In this study, I assumed this binding mechanism to be nonlinear and focussed on the functional asymmetries in forward and backward connections. It is possible that a model with intrinsic linear coupling is a better model and I will address this in future work. Stimuli entered the left and right OFA. I used a factorial approach to specify the models, which systematically varied the form of the A and B matrices in Eq. 2: These models differed according to whether the forward and backward connections, (and implicitly their modulation by face–selective processing) were linear or nonlinear (see upper left panel in Figure 5.2). This resulted in four models (lower panel in Figure 5.2):

- $F_L B_L$: linear forward connections and linear backward connections
- $F_N B_L$: nonlinear forward connections and linear backward connections
- $F_L B_N$: linear forward connections and nonlinear backward connections

- $F_N B_N$: nonlinear forward connections and nonlinear backward connections

I restricted face-selective effects (encoded by the B matrix) to intra-hemispheric forward and backward connections. Clearly, these models are a highly simplified representation of the "core system" for face processing identified by Haxby and colleagues (Haxby et al., 2000; Fairhall and Ishai 2006). However, they are sufficient to address the question, *i.e.* to distinguish between linear and nonlinear coupling in a hierarchical neuronal network.

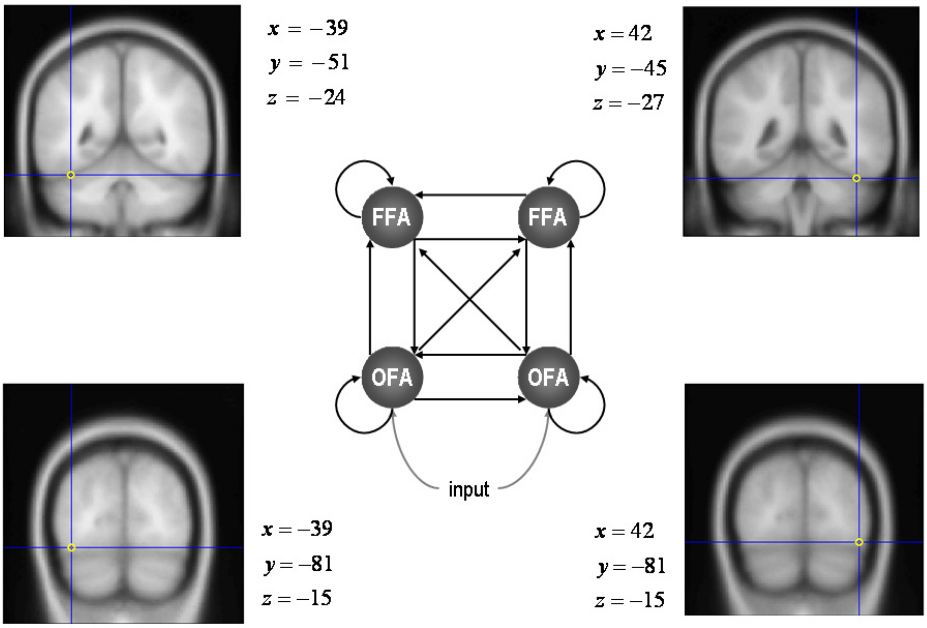

Figure 5.1 Location of the four sources (in MNI coordinates) shown on a template MRI image. The central panel shows the basic connectivity structure of the models, which are presented in more detail in Figure 5.2. OFA: left and right occipital face area; FFA: left and right fusiform face area.

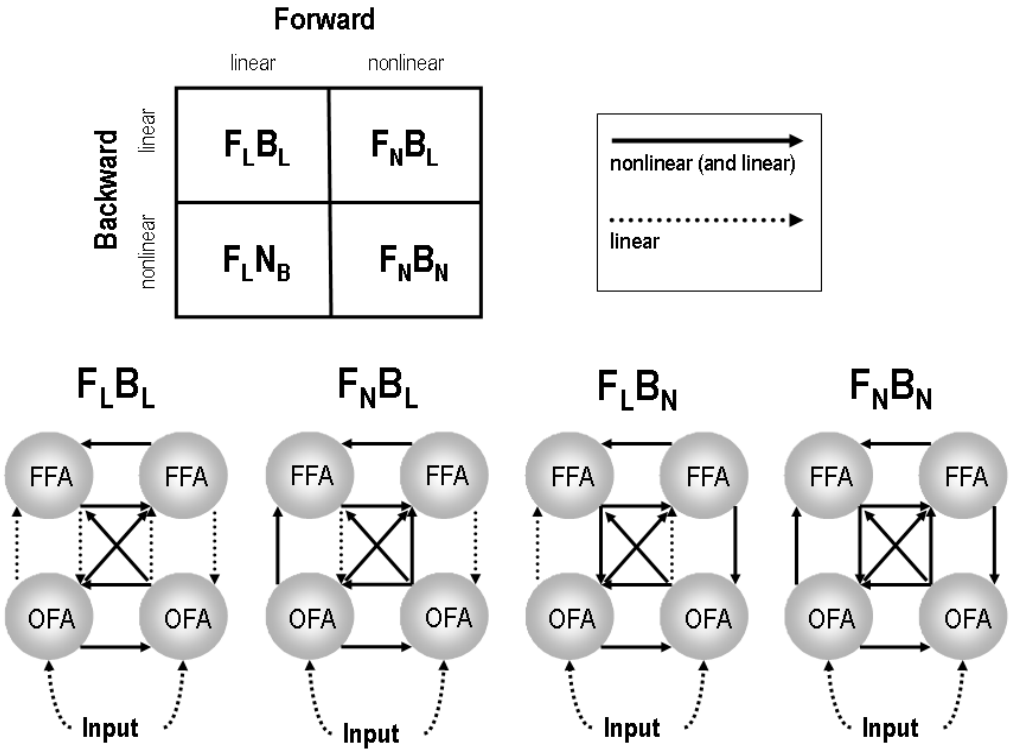

Figure 5.2 The upper panel shows the factorial structure of model space: models differed according to whether the forward and backward connections (and implicitly their modulation by face vs. scrambled face stimuli) were linear or nonlinear. The lower panel shows the connectivity architecture of the ensuing DCMs. The solid and dashed lines indicate nonlinear and linear connections, respectively. N: nonlinear coupling; L: linear coupling; F: forward connection; B: backward connection. For simplicity, the intrinsic (self) connections are omitted. These were nonlinear (see previous figure).

5.2.3 Statistical testing on coupling parameters

To make inferences about the coupling parameters of the best model, the conditional expectations of the forward and backward coupling matrices were entered into a conventional between-subject SPM analysis to identify significant, frequency-specific, differences in effective connectivity. I tested for significant negative or suppressive

effects in backward connections, relative to forward connections for coupling under face processing (*A* plus *B* matrices, see chapter 2 for details). I then repeated this comparison for the face-selective component of coupling (*B* matrix). After performing these *t*-tests I computed an SPM of the *F*-statistic to ensure that the planned comparisons had not missed any other significant differences. The SPM were displayed at $p<0.05$ (uncorrected) and I report maxima at a corrected $p<0.05$ level (Kilner *et al.* 2005).

5.3 Results

5.3.1 Inference on models

Four DCMs were inverted for each subject as described above. The summed log-evidences over subjects are shown in Figure 5.3 (left panel). It can be seen that the best model is F_NB_N (log-evidence sum = -11895), followed by F_LB_N (-16306), F_NB_L (-16308) and F_LB_L (-59890). In other words, the model with nonlinear forward and backward connections was vastly superior to all other models, whereas the model with linear forward and backward connections was clearly the worst. The two 'mixed' models were fairly similar in log-evidence (*i.e.*, positive but not strong evidence for exclusive nonlinear coupling in backward connections relative to forward connections). A repeated-measures ANOVA showed there was a significant interaction ($F = 13.468$; $p = 0.005$; *df* 1,9); suggesting that when backward connections are linear, the log-evidence is greatly affected by whether forward connections are nonlinear; conversely, when backward connections are nonlinear, the log-evidence is much less influenced by the nature of forward connections (see Figure 5.3; right panel). *Post-hoc t*-tests, confirmed that

nonlinear model was significantly better than all other models (F_LB_L: t = 4.473, p = 0.001; F_NB_L: t = 1.908, p = 0.044; F_LB_N: t = 2.306, p = 0.023; df = 9).

To verify that my assumptions about the basic connectivity structure (*c.f.* Figure 5.2) were sound, I created two variants of the F_NB_N model. These included a simplified model (sF_NB_N) that contained no cross-hemispheric OFA-FFA connections and a more complex model (cF_NB_N) that contained reciprocal (as opposed to unidirectional) cross-hemispheric OFA-FFA connections. Bayesian model comparison demonstrated that both were clearly inferior to the nonlinear model. Their summed log-evidences were -17243 (sF_NB_N) and -15638 (cF_NB_N) and paired *t*-tests showed a significant difference in favour of the F_NB_N model (p<0.047 and p<0.008, respectively). The lower log-evidence for the cF_NB_N model provides another interesting demonstration (*c.f.*, Grol *et al.* 2007; Stephan *et al*. 2007a), that increasing the complexity of a model does not necessarily improve it.

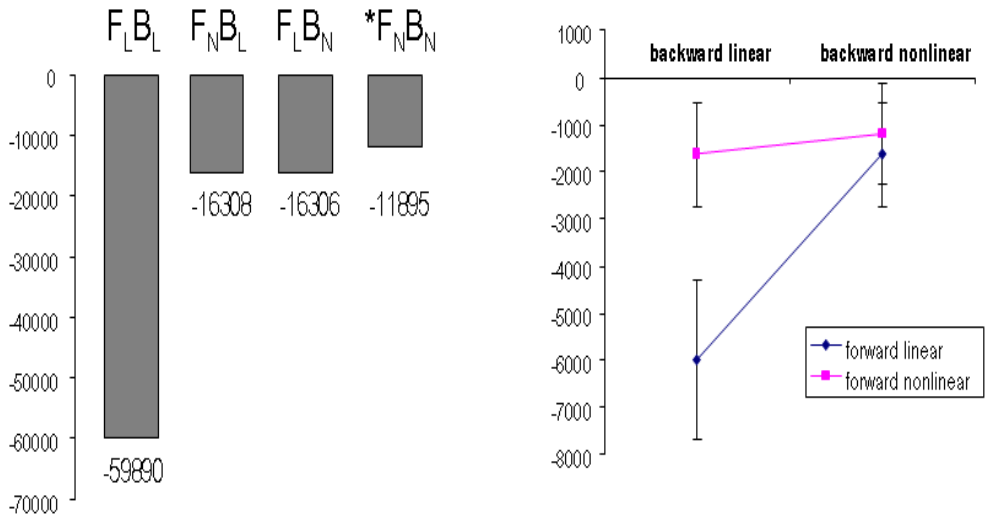

Figure 5.3 **Left panel**: Summed log-evidences for the four DCMs, pooled over subjects. It can be seen that the best model is F_NB_N, followed by F_LB_N, F_NB_L and F_LB_L. **Right panel**: The averaged log-evidence for all four models with standard errors.

In conclusion, I found that the model with nonlinear forward and backward connections was the best model and that the model with nonlinear backward connections came second. Figure 5.4 shows the predicted (under the nonlinear model) and observed spectral responses at the source level, for the two experimental conditions (faces vs. scrambled faces) in a representative subject.

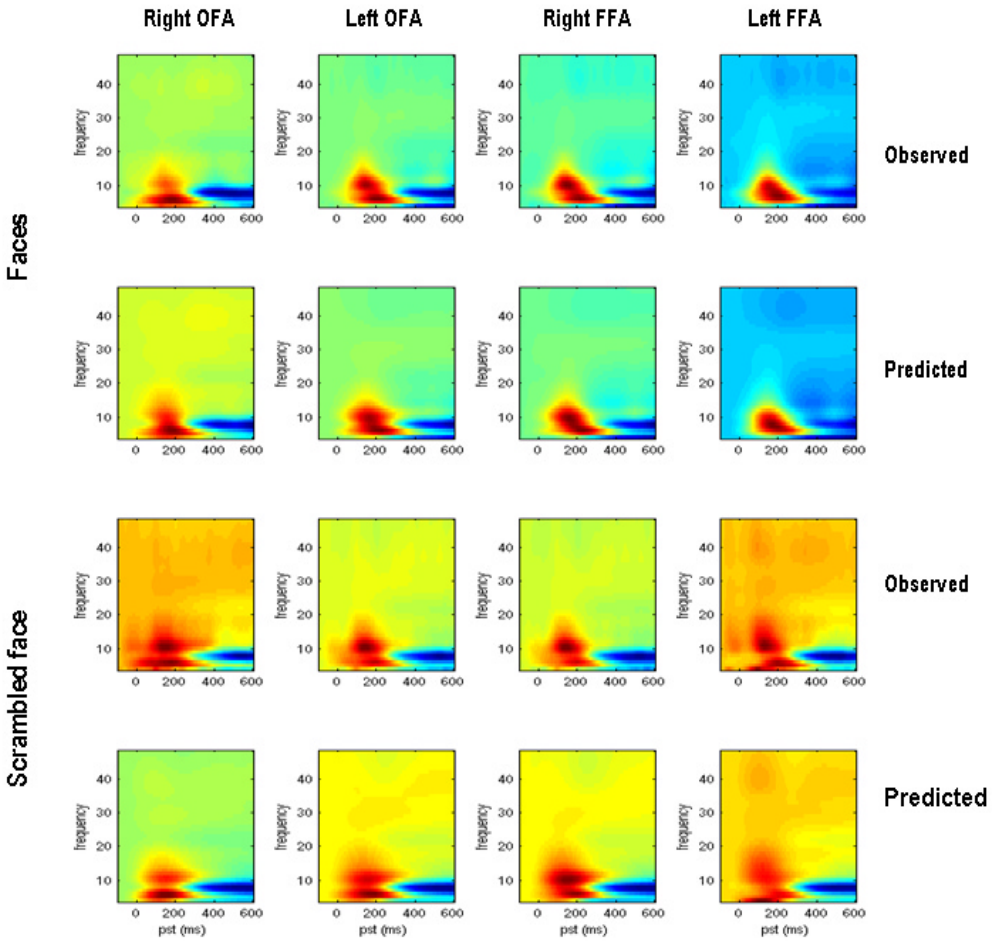

Figure 5.4 This figure shows predicted and observed spectral responses for a representative subject, at the source level, under the best model ($F_N B_N$), for the two experimental conditions (faces *vs*. scrambled faces). The top two rows are the observed and predicted spectra for normal faces; the bottom two rows are the observed and predicted spectra for scrambled faces.

5.3.2 Inference on coupling parameters

Figure 5.5 shows the coupling matrices during face processing for the forward and backward connections in the right and left hemispheres under the nonlinear model. These are the sum of the *A* and *B* matrices, averaged over all subjects). Anecdotally, it can be seen that the forward (upper row) and backward (lower row) connections show profound nonlinear coupling with substantial off-diagonal structure. Furthermore, there are systematic differences between the forward and backward coupling; with the backward coupling showing negative or suppressive cross-frequency effects. Quantitatively, these are most marked in the right hemisphere for low (alpha) to high (gamma), and from gamma to alpha in both hemispheres (red arrows). I tested for these putative asymmetries with planned comparisons.

The SPM testing for a significant suppression in backward, relative to forward connections is displayed by Figure 5.6 (thresholded at $p<0.05$ uncorrected). These comparisons used a stimulus times hemisphere times forward v*s*. backward repeated measures ANOVA with restricted maximum likelihood estimates of non sphericity among the errors. The smoothness of the underlying residual fields was 7.8 x 6.5 Hz resulting in about 32 resolution elements (*i.e.*, effective samples over the frequency x frequency search space of the SPM). This comparison was averaged over hemispheres because I failed to detect a hemisphere times connection interaction. The most (and only) significant difference (red arrow) was in the coupling from high (gamma) frequencies to low (alpha) frequencies. This difference was extremely significant ($t = 4.72$; $p = 0.002$, corrected; $df = 72$). The subject-specific estimates of coupling strength for this cross-frequency coupling are shown in the lower panels for both hemispheres. In the right hemisphere, this difference is due mainly to a suppressive effect of backward

connections; where, remarkably, every subject had a negative connection strength. In the left hemisphere, the difference appeared to be augmented by an activating effect of forward connections.

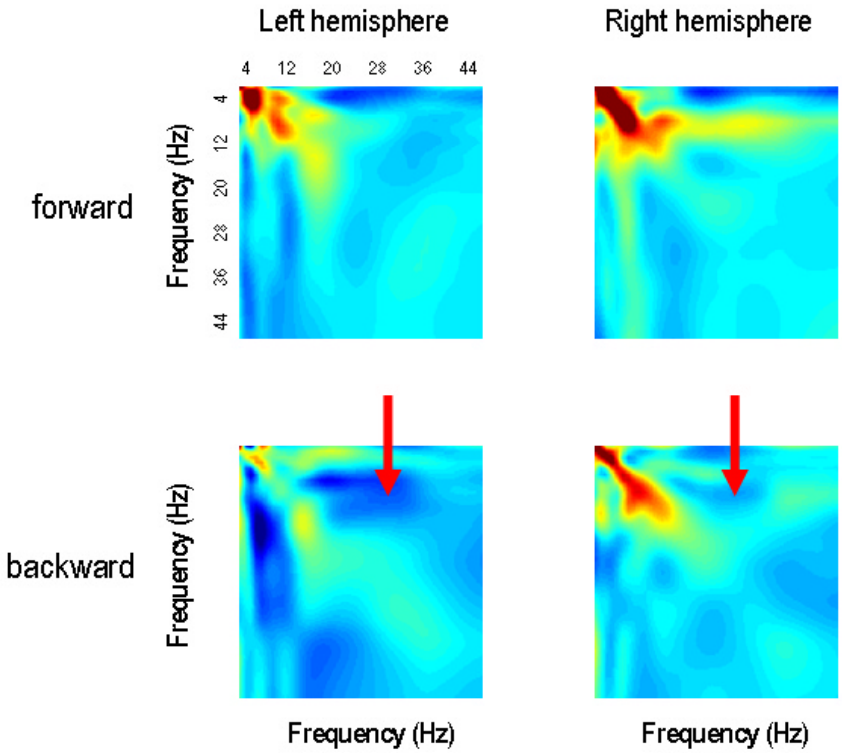

Figure 5.5 Coupling matrices, averaged across subjects, for the coupling strengths of forward and backward connections in the right and left hemispheres of the $F_N B_N$ model.

I then repeated exactly the same analysis but testing for asymmetry in face-selective changes in coupling (*i.e.*, looking just at the *B* matrix). Although this comparison is not orthogonal to the previous comparison, it is reassuring to see exactly the same differences. The only significant difference was again between gamma and alpha frequencies and was even more significant (t = 5.09; p = 0.001 corrected; df =72) than coupling under faces *per se* (Figure 5.7; left panel). Finally, the right panel of Figure 5.7 shows the SPM of the *F*-statistic testing for any differences in coupling over stimuli, hemispheres or connections. There were only three peaks that survived a corrected *p*-

value of 0.05 and only one of these related to nonlinear coupling (F = 5.78; p = 0.006, corrected; df = 8,72). This is exactly the same frequency-specific coupling identified by the planned comparisons. This SPM is shown to illustrate that the planned comparisons did not miss any other significant differences and shows that cross-frequency suppression mediated by backward connections, relative to forward connections, was the most prominent among all differences.

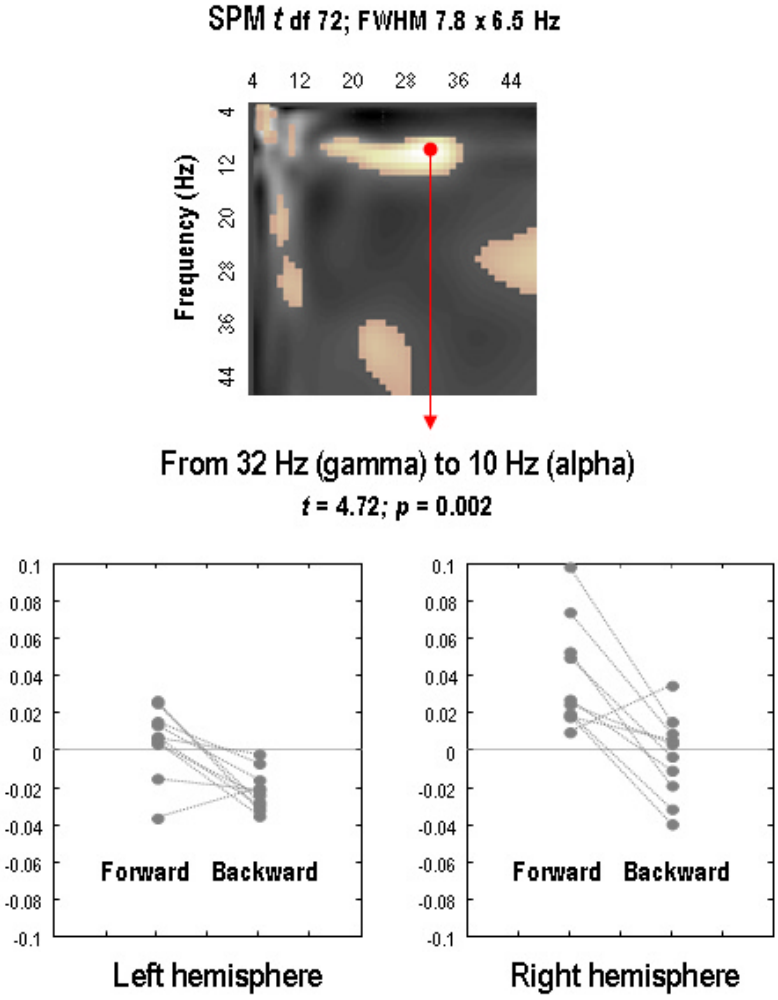

Figure 5.6 **Upper panel**: SPM of the *t*-statistic testing for a greater suppressive effect of backward connections, relative to forward connections. The SPM is thresholded at p<0.05 (uncorrected). **Lower panels:** Subject-specific estimates of the coupling strength at the maximum of the SPM (red arrow) presented for each hemisphere.

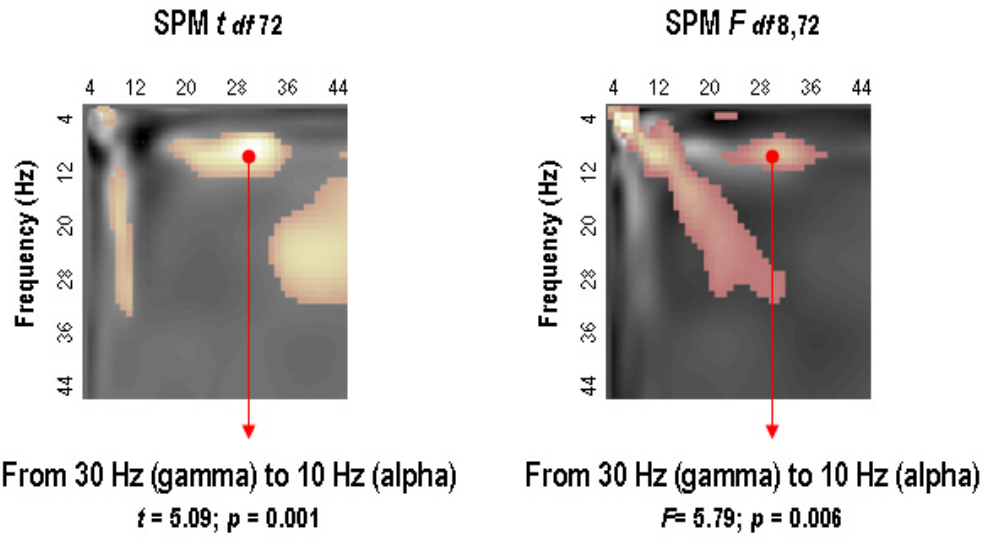

Figure 5.7 **Left panel**: SPM of the *t*-statistic testing for a greater suppressive effect of backward connections, relative to forward connections in the face-selective changes coupling. **Right panel:** SPM of the *F*-statistic testing for any difference in frequency-specific coupling over connections, conditions or hemispheres. Both SPMs are thresholded at p<0.05 (uncorrected). Significant (p<0.05 corrected) peaks are indicated by the red arrows).

5.4 Discussion and conclusions

Coupling between low and high frequency bands has been documented in both animal and human recordings (see Jensen and Colgin (2007) for a review). Canolty *et al.* (2006) demonstrated in humans that the power of high frequency gamma oscillations was modulated by the phase of the low-frequency theta rhythm. The implicit nonlinear coupling between oscillators at different frequencies builds upon previous studies that have identified similar phenomena in both anesthetised (Soltesz & Deschênes 1993) and behaving rats (Bragin et al. 1995). Here, I extend these observations by showing that nonlinear (between-frequency) interactions can be ascribed to specific intracerebral sources and used to disclose asymmetries in directed connections.

Intracranial EEG recordings have shown that faces elicit responses across a number of regions in the ventral temporal visual-processing pathway (Allison *et al.* 1994; Barbeau *et al.* 2008) and furthermore that faces can induce changes in the coherence of broadband (4-45 Hz) power between those regions (Klopp *et al.* 1999; Klopp *et al.* 2000). However, little is known about the functional relevance of this coherence or, in particular, the role of nonlinear (between-frequency) coupling. It has been suggested that nonlinear coupling is a key aspect of functional integration and is an essential aspect of network function (Friston 2001; Jensen and Colgin, 2007; Tallon-Baudry and Bertrand, 1999; Varela *et al.* 2001). To my knowledge, this is the first study to quantify and make inferences about directed nonlinear coupling.

Model selection furnished strong evidence that nonlinear connections are important for explaining the current MEG data: indicating that the best model entailed nonlinearities in both forward and backward connections. The most marked difference in nonlinear coupling between forward and backward connections under this model was an activating effect of high (gamma) frequencies on low (alpha) frequencies in the forward connections and a suppressive effect in backward connections. Not only are these findings consistent with empirical evidence from invasive studies but confirmed theoretical predictions based on Bayesian treatments of perceptual inference. These predictions suggest that backward connections suppress or explain away prediction error as lower levels in cortical hierarchies using nonlinear synaptic mechanisms.

One functional role of backward connections is to mediate the top-down predictions during perceptual inference. In this study, we found that gamma frequencies in the higher level have a suppressive effect on alpha frequencies in the lower level. One

possible explanation is that suppressive backward connections may accelerate the decay of evoked responses in the lower level that encode prediction error (i.e., explain away prediction error). We do not motivate the exact form of the underlying mechanisms in the generative model; rather we model the neuronal dynamics in a phenomenal fashion. Therefore, there may be other explanations for this negative nonlinear backward coupling. However, the phenomenology we observed is consistent with the predictive coding architecture discussed above.

I was a bit surprised to find that high-frequencies affected low-frequencies. I had expected to see the converse given empirical results (e.g., Canolty et al. 2006) and the simulations reported in Friston (2001). However, on reflection, the current results are entirely sensible if one considers that high (gamma) frequencies reflect increased neuronal firing (Chawla et al 1999): Heuristically, this means that gamma activity in low-level areas induces slower dynamics at higher cortical levels as prediction error is accumulated for perceptual synthesis. The concomitant high-level gamma activity (due to intrinsic nonlinear coupling) then accelerates the decay of evoked responses in the lower level that are manifest at, the population level, as damped alpha oscillations. However these mechanistic speculations will need a lot more work to confirm.

In conclusion, using a model-based approach that allows for probabilistic estimates of brain connectivity and its modulation by experimental conditions, this work provides empirical evidence for a functional asymmetry between forward and backward connections in the human brain that is consistent with neuroanatomical and neurophysiological data from animal studies. First, qualitative Bayesian model comparison disclosed overwhelming evidence for nonlinear models, in relation to

formally equivalent models with linear coupling. Secondly, I found a striking quantitative asymmetry between forward and backward connections with regard to stimulus-bound and stimulus-specific (faces relative to scrambled faces) nonlinear coupling. This asymmetry was extremely significant and reproducible over subjects, even under the very conservative SPM procedures for multiple comparisons. This work is a starting point for further investigations of functional asymmetry between forward and backward connections in the human brain. Here, I restricted the models to the bilateral OFA and FFA regions believed to form the core of the visual face-processing system (Haxby *et al.*, 2000). Future modelling studies will include other regions, such as posterior STS, which may also show changes in nonlinear coupling under other stimulus manipulations (e.g., different facial expressions, Winston *et al.* 2004).

CHAPTER 6

BACKWARD CONNECTIONS MEDIATE INDUCED RESPONSES

6.1 Introduction and specific aim

A central focus of the work in this thesis is evoked and induced task-related oscillatory responses. Evoked and induced power can be identified according to their phase relationship to the stimulus: Evoked components are phase locked to the stimulus, whereas induced responses exhibit trial-to-trial jitter in latency. A growing number of studies have demonstrated that induced responses, especially in gamma-band range (30-70 Hz), increase with cognitive demand; such as attention, learning and face perception (Tallon-Baudry and Bertrand, 1999; see Kaiser and Lutzenberger, 2003 and Lee et al., 2003 for comprehensive reviews). Cognitive processing rests on endogenous mechanisms whereby the brain exerts influences over afferent information through top-down effects. Some task-specific induced responses are thought to reflect this top-down effect; whereas evoked responses are thought to be mediated by forward projections (Tallon-Baudry and

Bertrand, 1999; see Kaiser and Lutzenberger, 2003 and Lee et al., 2003 for comprehensive reviews). However, the detection of induced responses relies upon comparisons between carefully matched experimental and control conditions (Kaiser and Lutzenberger, 2003) and the results may be misleading if there are factors that contribute to conditions. In this chapter, I generalize the use of DCM for IR to explain both evoked and induced responses in the same condition, in terms of differences in forward or backward connections. I do this by treating the time-frequency expression of evoked and induced responses as different conditions and comparing models of condition-specific changes in coupling that account for the extra power associated with induced responses.

This approach allows the direct study of the relationship between the evoked and induced neural activity with respect to the underlying mechanisms. In particular, one can ask whether induced responses are mediated by 'top-down' or backward connections. I will illustrate this using the dataset from the hand grip paradigm described in chapter 3. Specifically, I test three models which differ in the connections that change when modeling induced, relative to evoked spectral responses: forward (F), backward (B) and forward-backward (FB) model. In the next section, I briefly reprise the generative model used in this work.

6.2 A generative model of evoked and induced responses

This generative model is exactly the same as the DCM described in chapter 2 (Equation 13) and used in chapter 5; but is recapitulated here to highlight how

we model the difference between evoked and induced responses in terms of their generating mechanisms. I start with the usual bilinear model:

$$t\dot{g} = (A + \sum_{l} v_l B^l)g + Cu$$

where the l indicates condition. The matrices A and C contain coupling parameters that control changes in spectral activity induced by other sources and exogenous (e.g., stimulus) inputs, $u(t)$. The matrices B are introduced to encode the coupling changes induced by the condition effects, v. The v inputs here serve as a contrast weight function that enables selective condition-specific changes in coupling. This selectivity is specified by the B matrix. Here, the first value is zero for the evoked responses and the second value is one for the induced responses. This means the B matrix mediates the changes in coupling for induced response components that are not evident in evoked components. In this application the condition effects represent whether the data features reflect evoked or induced responses, for any particular trial type. This also implies that the evoked and induced data are concatenated along the (area x frequency) dimension. Evoked and induced 'conditions' are created during preprocessing by performing the time-frequency analysis after (evoked) and before (induced) trial averaging. As previously the coupling matrices decompose into:

$$A_{ij} = \begin{bmatrix} a_{ij}^{11} & \cdots & a_{ij}^{1K} \\ \vdots & \ddots & \vdots \\ a_{ij}^{K1} & \cdots & a_{ij}^{KK} \end{bmatrix} \quad B_{ij} = \begin{bmatrix} b_{ij}^{11} & \cdots & b_{ij}^{1K} \\ \vdots & \ddots & \vdots \\ b_{ij}^{K1} & \cdots & b_{ij}^{KK} \end{bmatrix} \quad C_i = \begin{bmatrix} c_i^1 \\ \vdots \\ c_i^K \end{bmatrix}$$

Under this model, the scalar a_{ij}^{kl} encodes how changes in the k-th frequency in the i-th source depend on the *l*-th frequency in the j-th source. The leading diagonal elements are $a_{ii}^{kk} = -1$; this means that each frequency has an intrinsic tendency to decay or dissipate. Similarly, c_i^k controls the frequency-specific influence of exogenous inputs on the k-th frequency in the i-th source. This enables within and between-frequency coupling within and between sources. This generative model uses the *A* matrices to model the 'shared' underlying mechanisms for both the evoked and induced activities and leaves what can not be explained by the shared mechanisms to be modeled by the *B* matrices.

6.3 Data and Model specification

Nine healthy, right-handed (mean age 26, range 20~32 years of age) subjects participated in this study. Part of the data has been reported in chapter 3. Based on the previous result of the best model (Figure 3.4A and summarized in Figure 6.1A), I further tested whether the induced responses are mainly mediated by backward (B) or forward (F) or both (FB) connections in the motor network. To this end, I compared three models that differed in where the modulatory effects take place as shown in Figure 6.1B. I focused on the modulation in the left hemisphere since this is a right hand movement task. In this model, the SMA is assumed to be in the higher level of motor hierarchy than PM and MI as suggested by studies in which the Bereitschaftspotential (BP; or readiness potential/ field) has been measured, and which suggest that SMA is involved in planning and

initiation of movement (Deecke, 1987; Deecke, 1990; Keller and Heckhausen, 1990; Praamstra et al., 1995; Shibasaki and Hallett, 2006).

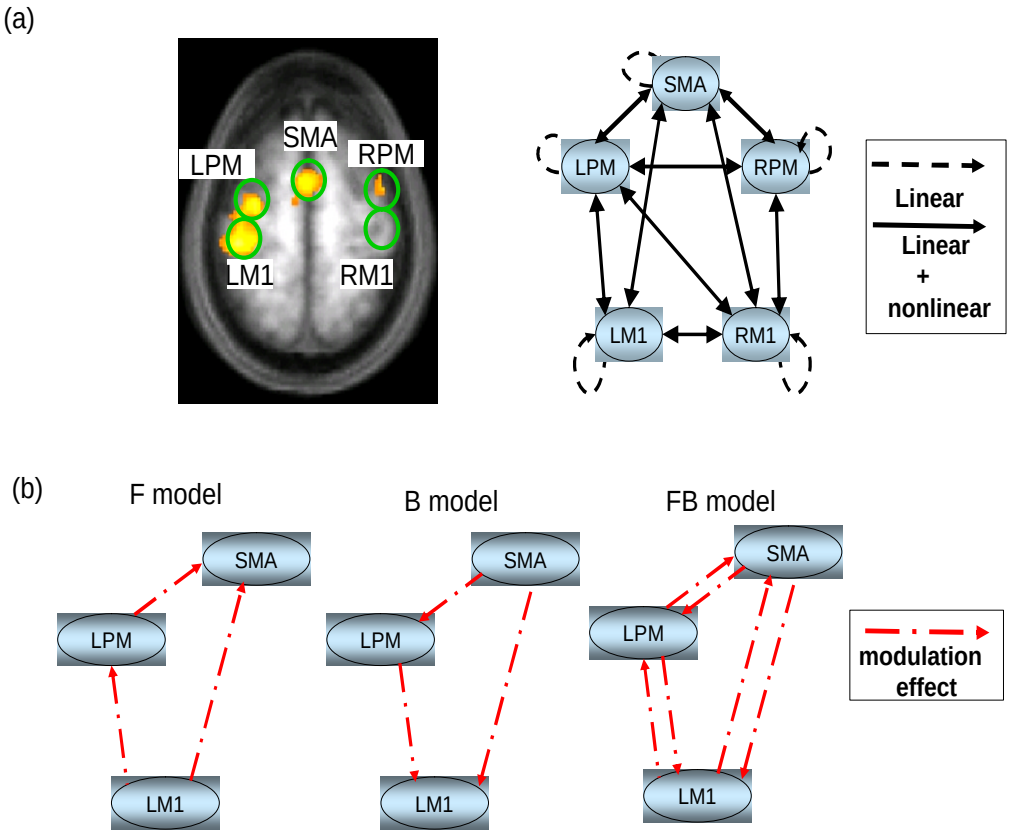

Figure 6.1 Model specifications of Forward (F), Backward (B), and Forward-Backward (FB) models (b) based on the previous results (a). The basic network configuration has the left hemispheric dominance (a; right; see also Figure 3.4A in

chapter 3) and the modulatory effects are allowed in only forward (F model), or backward (B model) or both forward and backward connections (FB model) (b).

6.4 Results

At the single subject level, the data from five out of nine subjects supports the B model while the other four have the F model as the best model. None has the FB model as the best model. This provides the evidence that a more complex model is not always a better model. At the group level, Bayesian Model Selection under both fixed (upper panel) and random effect (lower panel) assumption (Penny et al., 2004; Stephan et al., 2009) identifies the B model as a better model given the data (Figure 6.2). This result provides the direct empirical evidence that backward connections mediate the induced modulatory effects. This finding supports that the role of the induced components is associated with a modulatory effect that could reflect the top-down processing.

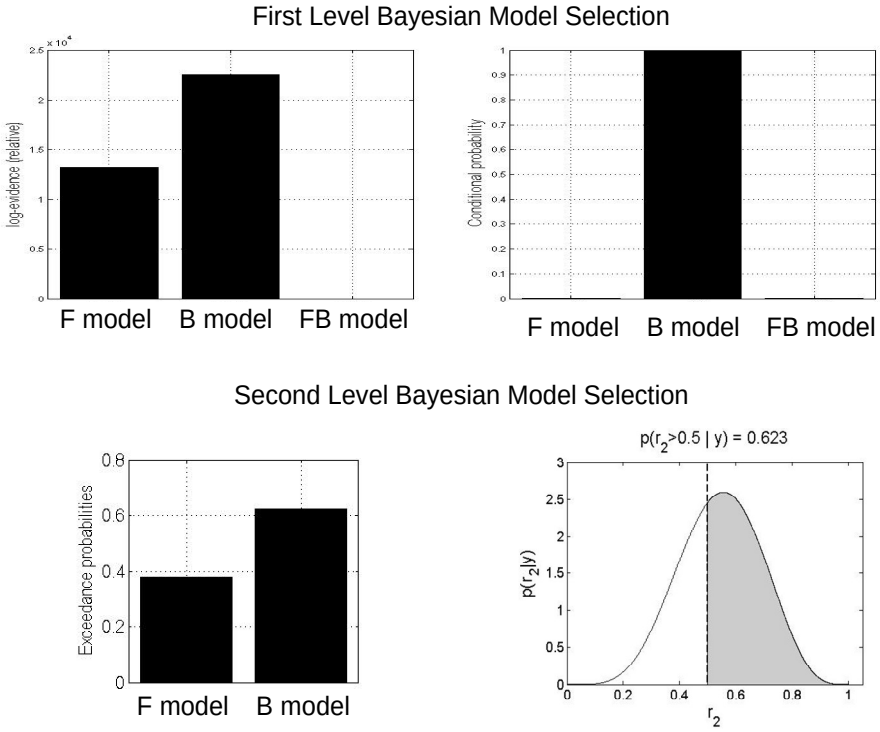

Figure 6.2 Group BMS results of 1st- (upper) and 2nd (lower)- level

6.5 Discussion

A wealth of neuroanatomical evidence suggests that backward connections are more modulatory in relation to the driving effects of forward connections (Sandell and Schiller 1982; Murphy and Sillito 1987; Salin and Bullier 1995; Lamme et al. 1998; Angelucci et al. 2002a,b). Furthermore, the underlying generating mechanisms are very likely to be nonlinear (Salin and Bullier 1995; Sherman and Guillery 1998). Combined with cognitive findings (Galambos, 1992; Tallon-Baudry and Bertrand, 1999), it has further been suggested that induced

responses play an important role in facilitating the top-down modulatory effects through the backward connections. The finding here supports this notion that backward connections from higher areas to lower areas mediated the induced modulatory effects and dissociates the induced activities from the evoked. The backward modulatory effect is expressed as induced activities, but not evoked ones. Importantly, as this task is pre-programmed in the brain through the training phase, this backward modulatory coupling is in agreement with the predictive coding (Rao and Ballard, 1999) that the planned movement representation in the higher level (i.e. SMA and/or PM) inferences the motor commands in the lower level of M1.

The functional role of evoked activities remains ambiguous. The most accepted hypothesis is that evoked responses reflect the bottom-up driving processing mediated by the forward connections and employ mainly linear mechanisms. This had been seen at the mesoscopic scale that the propagation of signals through the cell layers of the cortex is a linear phenomenon (Yamawaki et al., 2008). However, the functional properties of forward connections are predominantly, but not exclusively, linear; see Friston 2003 and Sherman & Guillery 1998 for a summary of the neurophysiological evidence. In chapter 3, 4 and 5, I have shown that nonlinear coupling in forward connections exists both in motor network and in the core system for face perception at the system level. In this chapter, I have found evidence that backward connections mediate the induced responses. In addition, recent studies of event-related potential (i.e. evoked) show evidence that backward connections are essential in explaining the

late ERP components in mismatch negativity studies (Garrido et al., 2007; Garrido et al., 2009). Taken together, both empirical and simulation data (David et al., 2006) suggest that the evoked and induced responses may use certain common mechanisms that generate both components to facilitate the functional integrations between areas. Therefore, evoked and induced components share certain characteristics, but only induced responses covey the backward modulation messages. Further investigation of the frequency contents in forward and backward connections may help to differentiate the functional roles of evoked and induced responses.

CHAPTER 7

CONCLUSIONS AND DISCUSSION

… when you can measure what you are speaking about and express it in numbers, you know something about it…..
William Thompson, Lord Kelvin

In chapter 2, I described DCM for induced responses, a framework for investigating neural connectivity. Subsequently I applied this approach to the analysis and interpretation of real electromagnetic data (chapters 3 to 6). In this chapter, I provide a summary of the work in this thesis, followed by a discussion and future directions.

7.1 Summary and novel contributions of this thesis

The overall goal of this thesis was to further the characterisation of neural network connectivity in human brains. The novel contributions of this thesis can be summarized as follows:

I. Develop a casual modelling scheme for induced responses in electroencephalography and magneto-encephalography, i.e. DCM for IR (chapter 2)

DCM for IR models the time-varying power, over a range of frequencies, as the response of a distributed system of coupled electromagnetic sources to a spectral perturbation. This is an advanced extension of DCM to cover the modelling of components that are not phase-locked to a stimulus (i.e. induced responses). The model parameters encode the frequency response to exogenous input and coupling among sources and different frequencies. The Bayesian inversion of this model enables inferences about the parameters of a particular model and allows one to compare different models, or hypotheses. One key aspect of DCM for IR is that it differentiates between linear and nonlinear coupling; which correspond to within and between-frequency coupling respectively. Synthetic data were used to establish the face validity of this approach and demonstrate: (1) that nonlinear coupling is mediated by cross-frequency interactions; (2) that Bayesian model selection can distinguish between linear and nonlinear coupling and (3) the robustness of model parameter estimation against noise: i.e., a typical signal to noise ratio of 20 to 15dB gives veridical estimates. I then applied this model to EEG data from a face-perception experiment, to ask whether there is evidence for nonlinear coupling between early visual cortex and fusiform areas.

II. Establish nonlinear coupling and age-dependent changes in the motor system during hand grip (chapters 3 and 4)

Having established the reliability of DCM for IR, I then applied it to look for evidence for additional nonlinear (between-frequency) coupling among neuronal sources during hand grip tasks as measured in normal subjects with MEG. I was specifically interested in whether nonlinearities would be found predominantly in connections within areas (intrinsic), between areas (extrinsic) or both. This entailed a comparison of models with and without nonlinear connections under conditions of symmetric and asymmetric interhemispheric connectivity. Bayesian model comparison revealed very strong evidence for nonlinear coupling between sources in this distributed network, but interactions among frequencies, within a source, appeared linear in nature and suggested that the task-dependent motor network was asymmetric during right hand movements. In addition, a quantitative examination of the extrinsic or long-range coupling parameters, showed some interesting asymmetries in frequency space and that this coupling was predominantly negative or suppressive. The results provide empirical evidence for nonlinear coupling among distributed neuronal sources in the motor system and that these play an important role in modulating spectral responses under normal conditions.

In addition, I tested for age-dependent changes in motor networks during hand gripping tasks. I found that the normal aging process alters both the network architecture and cross-frequency coupling in the motor network. Specifically, in

old subjects, the right hemisphere is engaged more in right hand movements, relative to young subjects with the appearance of contralateral premotor to ipsilateral motor inhibitory and coupling, which was markedly nonlinear. In terms of frequency-specific coupling, in old brains, the communication between left and right M1 used higher frequencies compared to the young brains. These findings are important given the pathological modulation of specific frequencies in diseases affecting the motor system such as in Parkinson's disease. These studies provide a qualitative and quantitative characterisation of frequency-specific changes under normal ageing, which I hope will be useful when studying induced responses in patients.

III. Investigate the functional asymmetries in forward and backward connections during face perception (chapter 5)

Furthermore, the bilinear approximation of the neuronal state equations in DCM for IR, like all the other DCMs, allows one to model the experimental manipulations in terms of coupling changes. I demonstrated this by analyzing MEG responses induced by visual processing of normal and scrambled faces and asked if there was evidence for functional asymmetries between forward and backward connections that define hierarchical architectures in the brain. I exploited the fact that modulatory or nonlinear influences (*i.e.*, effective connectivity) entail coupling between different frequencies by comparing models

with and without nonlinear (between-frequency) coupling in both forward and backward connections. A striking asymmetry was found between forward and backward connections; in which high (gamma) frequencies in higher cortical areas (FFAs) suppressed low (alpha) frequencies in lower areas (OFAs). This suppression was significantly greater than the homologous coupling in forward connections. Furthermore, exactly the same asymmetry was observed when we examined face-selective coupling (i.e., coupling under faces minus scrambled faces). These results highlight the importance of nonlinear coupling among brain regions and point to a functional asymmetry between forward and backward connections in the human brain that is consistent with anatomical and physiological evidence from animal studies. This asymmetry is also consistent with functional architectures implied by theories of perceptual inference in the brain, based on hierarchical generative models.

IV Backward connections mediate the induced responses: dissociation of evoked and induced responses in terms of generating mechanisms (chapter 6)

Finally, I used the bilinear form of DCM to model evoked and induced responses and asked whether induced responses were mediated by backward connections. I illustrated this novel application using a gripping task and compared three models which differed in where coupling changes could occur to explain the difference between the time-frequency expression of evoked and

induced responses (evaluated using the same data): Specifically, I looked at forward (F), backward (B)and forward-backward (FB) models. At the group level, Bayesian model selection identified the B model as a better model. This result provides direct empirical evidence that backward connections from higher areas to lower areas mediated induced responses. Importantly, this change in backward nonlinear coupling is in line with the fact that the planned movement representation in the higher level (i.e. SMA and/or PM) mediates motor commands in the lower level of M1.

7.2 Discussion

7.2.1 The question of inter-subject variability

One of the most difficult challenges in studying oscillatory brain activity is how to determinate the frequency bands of interest, as inter-individual variability is large, particularly within the alpha band (Pfurtscheller and Lopes da Silva, 1999). In other words, individuals might have their own preferred frequency band even in a very simple task (Omlor et al., 2007; Aoki et al., 1999; Kilner et al., 2000; Kristeva et al., 2007). One possible solution is just to explore all frequencies, but this can be computational demanding and time consuming. In DCM for IR, SVD is applied to extract subject-specific frequencies of interest. One important benefit of this is data reduction (see chapter 2 for details). The estimated spectral

densities over (frequency x sources x conditions) and time are projected into orthonormal principal frequency modes. In this way, each mode still covers all the frequencies but is in different proportions. This means the subject-specific frequencies can be preserved without bias. I typically used between two and four modes, which account for the majority of the observed variance in spectral responses. The number of modes is usually selected automatically using a modified Kaiser criterion (i.e., the variance explained has to exceed ninety percent).

7.2.2 The question of model specification

Like all the other inferential methods, the analytic results of DCM for IR are conditional on the models considered. Specifically, as part of the DCM approach, the observed MEG data were mapped into the source space by multiplying the generalized inverse lead field matrix given the source locations (cf chapter 2). This generalised inverse of the lead-field is one of many inversion schemes that can be used to project data from channel to source space (Darvas et al., 2004; Friston et al., 2008; Kiebel et al., 2008; Michel et al., 2004). The advantage of this projection is that there is a unique solution for the data features, given the prior specification of source locations. On the other hand, this leads to a valid source spectrum as long as the brain regions considered are the reasonable summary of the real neuronal sources generating the data. In the case that other

sources (but not included in the network) contribute to the MEG field topography; the signals from these un-modeled sources could influence the sources under consideration. Therefore, if any sources are omitted or misplaced, there might be a better model of the data and possibly a different conclusion from model comparison. If one did not know where spectral signals were coming from, the beam-former method could be one useful strategy that allows one to localize the source positions and estimate spectral features empirically (Singh et al 2003). Once these locations have been established, the generalised inverse of the associated lead-field matrix furnishes a near-optimum Equivalent Current Dipoles (ECD) summary of activity that avoids suppression of local correlated activity.

7.2.3 The relationship between power modulation and phase synchronisation

Power and phase are two important data features in spectral analysis. Fluctuations in power and phase synchronization have been shown to be a key aspect of neuronal network dynamics. Mathematically, power and phase could be modulated independently as a spectra X(w,t) can be represented as $X(w,t) = a_w(t)\exp(i j_w(t)t)$ where $a_w(t)$ and $j_w(t)$ control the amplitude and phase modulation, respectively (Varela et al., 2001; Canolty et al. 2006). Importantly, $a_w(t)$ and $j_w(t)$ could be either correlated or independent. These properties have been used in the telecommunication, for example AM (Amplitude

modulation) and FM (Frequency modulation) (Schwartz, 1995). However, in systems neuroscience, their relationship remains unclear. Changes in the synchronous discharge of neuronal assemblies contribute to the increase or decrease of regional power within task-related frequencies (ERS and ERD). Conceptually, increases in regional power (ERS) reflect either increases in population activity or and increase in the phase constancy; whereas decreases in regional power (ERD) may be due to suppression of neuronal activity or loss of phase constancy (reduce phase constancy); or the formation of more anti-phase pairs (induce phase constancy) (Varela et al, 2001). This means there may be a tight coupling between power and phase synchrony. When measured separately, it has been reported that coherence at alpha and beta frequency bands between bilateral primary motor cortex increases during movement preparation and execution; and is accompanied by ERD (Leocani et al., 1997). In addition, Babiloni et al report that significant beta and gamma ERS in the hippocampus and theta ERD in the inferior temporal cortex accompany gamma coherence between hippocampus and inferior-middle temporal cortex during repetitive visuomotor events (Babiloni et al., 2004). Direct detection of phase–power relation is used to address the idea of 'nested rhythms' (Penny et al., 2008; Palva and Palva, 2007). Nested oscillations occur when the phase of low rhythm is coupled with the amplitude of a high rhythm and are observed largely during memory tasks: (theta-gamma) (Lisman and Idiart, 1995), (theta-beta and theta-gamma) (Mormann et al. 2005), (theta-beta/gamma) (Schack et al. 2002) and during sleep (infra-slow oscillations' (ISOs; 0.02 -0.2 Hz) – 1 Hz) (Vanhatalo et al. (2004) and even during the resting state (alpha-high gamma)(Osipova et al. 2007). Taken together, phase

and power are different, complementary phenomena and may share a common generative model.

7.2.4 Measuring Causality

Understanding causality has always been important. In 1620, Francis Bacon published his philosophical work, Novum Organum, in which he proposed to establish the progressive stages of certainty. In neuroscience, we are interested in two aspects of causality: temporal precedence and directional connection: Temporal precedence reflects importance of temporal order by saying the past is causing the present, but not *vice versa*; Directional causality is ascribed to these connections where an arrow from A to B means that A causes B. The most common methods, other than DCM, in measuring temporal and spatial causal relationships are Granger Causality (GC) (see Appendix A for the mathematic description) and Structural Equation Modelling (SEMs; see Penny et. al. 2004a). In general, DCM and GC and SEMs share some common characteristics (see Friston, 2009 for a comparison of DCM and GC for fMRI studies and Penny et. al. 2004a of a comparison of DCM and SEMs for fMRI studies): They (1) are multivariate analyses, (2) can measure the directed coupling, (3) allow one to make inference on models, and (4) rest on temporal causality. However, there are fundamental differences among these approaches. Firstly, in terms of determining coupling directions; GC tries to establish the existence of causal influences with respect to the temporal precedence; so the directed connections are thus inferred

from the data, while SEMs and DCMs (note that this applies to the entire DCM family) pre-specifies the directional relationships in the model a priori (Pearl, 1998; Friston, 2003). DCMs and SEMs are therefore more for making inferences on the models and model parameters. Secondly, stationary assumptions: In both GC and SEMs, it is assumed that when one measures the data, the systems have reached the equilibrium. But in DCMs, the model states evolve with time, so it does not require the underlying processes to be stationary. Note that the stationary assumption is required in one particular DCM: DCM for steady-state responses; see Moran et al., (2009). Thirdly, the nature of exogenous input: DCMs and SEMs have a deterministic and stochastic exogenous input, respectively but no input is considered in GC. Including a deterministic input (for example, the stimulus onset) in a generative model is important because it allows one to model experimental manipulations (Penny et. al. 2004a). Finally, "*...because DCM uses Bayesian model selection, one can compare non-nested network models...*" (Penny et al., 2004a; Penny et al., 2004b). As it is of interest and importance to evaluate the relative measurement efficacy of different approaches, in a future work, I will test the robustness of DCM for IR in terms of *sensitivity* and *specificity* against other approaches (see chapter 7.3).

7.3 Future directions

7.3.1 Construct validity of DCM for induced responses

In chapter 2, I exploited DCM for IR as a novel tool to investigate neural connectivity using electromagnetic signals. It is important that a new method is validated against other approaches. This can be done by evaluating a relative measure of efficacy that could serve as a guideline, when considering appropriate analytic methods for studying neural networks. In future work, I will illustrate the essential detection properties (characteristics) of DCM for IR, including *sensitivity* and *specificity*, which are important for addressing network connectivity (David et. al., 2004). I hope to evaluate the relative measure efficacy for detecting nonlinear neuronal coupling among different methods, including phase synchrony, bispectral analysis and Granger causality (see Appendix A and B for a mathematical descriptions of these methods) in addition to DCM for IR. Instead of performing the different interdependence measures in real data (in which ground truth is unknown), I will use synthetic data that, on the one hand, mimics electromagnetic dynamics in source space, and on the other hand, allows for the manipulation of key parameters, such as, coupling strength. Thus, the sensitivity measurement of every method can be quantified as a function of those parameters. In terms of specificity, surrogate testing could be performed to determine a significant threshold from null data, where the second order moment is preserved but all coupling is destroyed (cf, Theiler, 1994; Theiler et al., 1992). The surrogate data would be used to construct a null distribution of detection measures so that we can assess its statistical properties. The neural mass model could be used to generate neuronally plausible data; it has been shown that the neural mass model is capable of generating complicated activity when assigning different kinetics to different neuronal populations and, in particular, changing the nonlinear coupling

among neuronal populations (David et. al., 2004; Chen et al., 2008; Ursino et al., 2007).

7.3.2 Functional reorganization of motor system after stroke

After focal damage, surviving stroke patients often show motor impairment, commonly hemiparesis. However, after a certain period, some patients show a reduction in this impairment. The recovery processing is thought to be related to reorganization within the central nervous system. But, how the reorganization alters the neural network remains largely unknown. In future studies, I will apply DCM for IR to assess network alternations in the motor system during recovery from stroke, based on my findings in chapter 3 and 4.

Appendix A. Granger Causality

Granger causality measures the causal relation in time, i.e. the temporal order in the events. Granger causality is named after Clive Granger, Noble Prize winning economist, who gave a mathematical formulation to measure GC based on the linear stochastic modeling of time series analysis using autoregressive (AR) model :

$$G_{Y\to x} = \ln(\frac{V_{x|x}}{V_{x|x,y}})$$

where $V_{x|x}$ and $V_{x|x,y}$ are the variances of the prediction errors, e_x and e_{xy} , estimated from

$$x(t) = \sum_{k=1}^{p} a_{xk}\, x(t-k) + e_x(t)$$

$$x(t) = \sum_{k=1}^{p} a_{xy}\, x(t-k) + \sum_{k=1}^{p} b_{xy}\, y(t-k) + e_{xy}(t)$$

$$y(t) = \sum_{k=1}^{p} a_{yx}\, y(t-k) + \sum_{k=1}^{p} b_{yx}\, x(t-k) + e_{yx}(t)$$

where p is the model order, e_{yx} and e_{yx} are the residual noises associated with the model. It's clear that the residual error depends on both the past of x and y. If y is influencing x, then adding past values of y to the regression of x will improve its prediction performance resulting in a higher value of the GC. A comprehensive description can be seen in Granger, 1969 and Granger 1980.

Appendix B. Phase synchrony and Bispectral analysis

Phase synchrony measures the frequency-specific synchronization (i.e., transient phase-locking) between two oscillatory signals :

$$j_{x,y}(t) = \left| f_x(t) - f_y(t) \right|$$

Where $j_{n,m}(t)$ is the instantaneous phase difference between frequency x in area A and frequency y in area B. The phase locking value (PLV) at t is defined as the average value of the phase difference with a reasonable time-resolution (<100 ms) over N trials:

$$PLV(t) = \frac{1}{N} \left| \sum_{n=1}^{N} j_{x,y}(t,n) \right|$$

Inference is made when that synchrony is above the statistical significance, derived from null distribution using surrogate data (see Lachaux, et. al., 1999 for details).

Bi-spectral analysis is the most common tool to investigate quadratic non-linearities of phase coupling between different rhythms within or between different time series (Jeffrey and Chamoun, 1994; Shils et al., 1996). Bispectral analysis is dealing with a special case of phase synchrony where the frequency x is not equal to frequency y and the coupling between two oscillators are stationary. The cross-bicoherence is the normalized bispectrum, range from 0 to 1:

$$\Gamma(f_1, f_2) = \frac{|B(f_1, f_2)|}{\sqrt{\left\langle \cdot |\cdot X(f_1)|^2 \right\rangle \left\langle \cdot |\cdot Y(f_2)|^2 \right\rangle \left\langle \cdot |\cdot Z(f_1 + f_2)|^2 \right\rangle}}$$

Where $B(f_1, f_2) = \left| X(f_1) \cdot Y(f_2) \cdot Z^*(f_1 + f_2) \right|$ is the bispectral density which is the third-order cumulate generating function of Fourier transform

Appendix C. Measuring the power modulation at sensor level based on mutual information

The following document presents a relative method (my previous work) which can measure the nonlinear power modulation at the sensor level.

♦ Human Brain Mapping 29:265–280 (2008) ♦

Mutual-Information-Based Approach for Neural Connectivity During Self-Paced Finger Lifting Task

Chun-Chuan Chen,[1,4] Jen-Chuen Hsieh,[1,2,3,4] Yu-Zu Wu,[1,3,5] Po-Lei Lee,[1,6] Shyan-Shiou Chen,[1] David M. Niddam,[1,4] Tzu-Chen Yeh,[1,2,7] and Yu-Te Wu[1,2,8]*

[1]*Laboratory of Integrated Brain Research, Department of Medical Research and Education, Taipei Veterans General Hospital, Taipei, Taiwan*
[2]*Institute of Brain Science, National Yang-Ming University, Taipei, Taiwan*
[3]*Institute of Neuroscience, School of Life Science, National Yang-Ming University, Taipei, Taiwan*
[4]*Center for Neuroscience, National Yang-Ming University, Taipei, Taiwan*
[5]*Department of Physical Therapy, Tzu-Chi College of Technology, Hualien, Taiwan*
[6]*Department of Electrical Engineering, Nation Central University, Jhongli, Taiwan*
[7]*Faculty of Medicine, School of Medicine, National Yang-Ming University, Taipei, Taiwan*
[8]*Department of Biomedical Imaging and Radiological Sciences, National Yang-Ming University, Taipei, Taiwan*

Abstract: Frequency-dependent modulation between neuronal assemblies may provide insightful mechanisms of functional organization in the context of neural connectivity. We present a conjoined time-frequency cross mutual information (TFCMI) method to explore the subtle brain neural connectivity by magnetoencephalography (MEG) during a self-paced finger lifting task. Surface electromyogram (sEMG) was obtained from the extensor digitorum communis. Both within-modality (MEG-MEG) and between-modality studies (sEMG-MEG) were conducted. The TFCMI method measures both the linear and nonlinear dependencies of the temporal dynamics of signal power within a pre-specified frequency band. Each single trial of MEG across channels and sEMG signals was transformed into time-frequency domain with use of the Morlet wavelet to obtain better temporal spectral (power) information. As compared to coherence approach (linear dependency only) in broadband analysis, the TFCMI method demonstrated advantages in encompassing detection for the mesial frontocentral cortex and bilateral primary sensorimotor areas, clear demarcation of event- and non-event-related regions, and robustness for sEMG - MEG between-modality study, i.e., corticomuscular communication. We conclude that this novel TFCMI method promises a possibility to better unravel the intricate functional organizations of brain in the context of oscillation-coded communication. *Hum Brain Mapp 29:265–280, 2008.* ©2007 Wiley-Liss, Inc.

Key words: time-frequency cross mutual information; TFCMI; functional connectivity; magnetoencephalography; surface electromyogram; coherence; corticomuscular communication

Contract grant sponsors: Taipei Veterans General Hospital (V96 ERI-005), National Science Council. (96-2752-B-075-001-PAE, 96-2752-B-010-006-PAE, 96-2752-B-010-007-PAE).

*Correspondence to: Yu-Te Wu, Associate Professor, Department of Biomedical Imaging and Radiological Sciences, National Yang-Ming University, No. 155, Li-Nong Street, Section 2, Pei-Tou, Taipei 112, Taiwan, Republic of China. E-mail: ytwu@ym.edu.tw

Received for publication 7 September 2006; Revised 9 January 2007; Accepted 27 January 2007
DOI: 10.1002/hbm.20386
Published online 29 March 2007 in Wiley InterScience (www.interscience.wiley.com).

INTRODUCTION

Several populations of human cortical neurons exhibit intrinsic properties of oscillation (~10 and ~20 Hz) in a resting state, predominantly in the vicinity of the primary sensorimotor and visual and auditory cortices, as recorded non-invasively using electroencephalography (EEG) or magnetoencephalography (MEG) [Jasper and Penfield, 1949; Salmelin and Hari, 1994]. The power of oscillation can be modulated dynamically with respect to event occurrence, either decreasing or increasing, a phenomenon termed event-related desynchronization (ERD) or synchronization (ERS) [Andrew and Pfurtscheller 1999]. In the context of movement, it has been suggested that the dynamics of ERD may reflect action planning and execution, while the dynamics of ERS may connote deactivation or inhibition of neural networks during the recovery phase [Lee et al., 2003b; Pfurtscheller et al., 1996]. According to principles of brain organization, the functional integration describes the global influence, which requires the interactions, such as functional connectivity, between large subsets in the nerve system to be coherent; these frequency-dependent regulations make the brain a complex system [Friston, 1997; Tononi et al., 1994]. Several analysis methods have been developed to characterize neuronal couplings, including ERD/ERS quantifying small scale interactions, the coherence method measuring functional connectivity, and the cross mutual information (CMI) method estimating the statistic dependency between spatially separated areas or large scale interactions [Andrew and Pfurtscheller, 1999; David et al., 2004; Grosse et al., 2002].

Quantitative analysis of ERD and ERS around rolandic areas, typically segregated around 10 and 20 Hz, provides a means to understand the dynamics of neuronal populations and can be applied to address questions in physiology and pathophysiology of the human sensorimotor system [Aoki et al., 2001; Crone et al., 1998; Pfurtscheller et al., 1998]. For example, Magnani et al. [2002] evaluated mu ERD onset time in patients with idiopathic Parkinson's disease before and after L-dopa treatment [Magnani et al., 2002]. They concluded that dispersible L-dopa has acute positive effects to improve motor performance and advance the latency of cortical activation during motor programming. The basis of the ERD analysis employed, however, mainly rests on phenomenological description and does not provide insightful mechanisms in the context of functional connectivity.

The coherence method, an approach commonly used to study oscillatory activity, has been exploited to address functional coupling or interaction, information exchange, and temporal coordination between cortical regions [Gerloff et al., 1998; Leocani et al., 1997; Nagamine et al., 1996]. High coherence indicates potentially neuroanatomic or functional connections between cortical areas underlying the sensors, while decreased coherence may denote the disruption of functional couplings [Fein et al., 1988; Leocani and Comi, 1999]. For example, patients with Alzheimer's disease showed significant decrease of α-activity coherence in temporo-parieto-occipital areas [Locatelli et al., 1998]. Patients with severe cognitive impairments display further decreases in coherence. In addition, the coherence method has been adopted to elucidate the oscillatory communication at around 20 Hz between somatomotor cortices and muscles in surface electromyogram-magnetoencephalography (sEMG-MEG) studies [Salenius et al., 1997]. In sEMG-MEG coherence studies, it has been suggested that the transient synchronization of rhythmic activities between sensorimotor areas and muscles can be crucial for motor command [Kilner et al., 1999]. Timmermann et al. [2003] reported that abnormal synchronization at 4–6 Hz between the contralateral primary motor cortex and forearm muscles in Parkinsonian patients may contribute to resting tremors [Timmermann et al., 2003]. The investigation of functional connectivity promises the potential to assess functional derangement within or between modalities [Schnitzler et al., 2000].

The coherence method, however, can be problematic if the signals are contaminated by noise, or the oscillatory frequency band is not carefully defined [Andrew and Pfurtscheller, 1999; Nunez et al., 1997] despite the newly developed time-domain [Jung et al., 2000; Lins et al., 1993; Vorobyov and Cichocki, 2002] or frequency-domain approaches [Mima et al., 2000a; Whitton et al., 1978; Woestenburg et al., 1983]. Theoretically speaking, the coherence method mainly measures linear dependency and is insufficient for the study of complex and nonlinear brain dynamics [Lopes da Silva, 1991; Popivanov and Dushanova, 1999].

Mutual information (MI), which employs the entropy of high-order statistics to estimate uncertainty, is a statistical measure of both linear and nonlinear dependencies between two time sequences [Shannon, 1948]. The cross mutual information (CMI) method in a time-domain has been developed to quantify and assess the functional impairment of information transmission from one area to another in Alzheimer patients [Jeong et al., 2001]. David et al. [2004] used the neural mass model to evaluate the profiles of different dependency measurements in the analysis of functional connectivity [David et al., 2004]. They pointed out that the time-domain CMI method is not reliable enough in broadband analysis, especially when the coupling between the modeled cortical areas is weak. Moreover, the CMI method only analyzes overall signal changes in time domain. The subtle temporal scenario of power changes within a defined frequency band is unfortunately lost; yet this information can be critical for the understanding of pathophysiology of disease condition.

The present study seeks to develop a conjoined time-frequency analytical method for MEG-MEG and sEMG-MEG measurements based on mutual information [Shannon, 1948] for the investigation of functional connectivity. Each single trial of MEG across channels and sEMG signals was transformed into time-frequency domain using the Morlet wavelet to obtain better temporal spectral (power) information [Grossmann and Morlet, 1984]. Time-frequency maps

were averaged across trials and the resulting maps were subsequently averaged over specific frequency bands to yield temporal profiles of power with improved signal-to-noise ratio (SNR). The averages of time series of power were used to compute the CMI across channels. Since MI is computed-based on any two temporal power sequences within a task-specific frequency band, the proposed method can be termed time-frequency cross mutual information (TFCMI) method. This TFCMI method is then applied to within (MEG-MEG) and between (sEMG-MEG) modalities in a self-paced finger lifting task and the results are discussed based on the simulation and the experimental data.

MATERIALS AND METHODS

Subjects and Task

Eight healthy, right-handed subjects (24–32 years of age, gender balanced) were recruited for this study. All subjects gave written informed consent for the experiment with a protocol approved by the institutional review board. They sat comfortably in a magnetically shielded room with forearms relaxed. Subjects were asked to lift their right index fingers once every 8 s (35–40° extension angle) in a self-pacing manner. The protocol in this study is the standard procedure for the Bereitschafts-potential (BP; in EEG) or readiness field (RF; in MEG), as first reported by Kornhuber and Deecke [1965]. Subjects' left hands rested on a pillow in order to avoid contamination of movement-related vibrations in the MEG measurements [Hari and Imada, 1999]. Movement onset was registered using an optical pad (4-D Neuroimaging®, Helsinki, Finland). A trigger pulse was generated at the beginning of each movement taking the interdiction of the laser light from the optical pad as the index of movement onset (zero time). To prevent blinking, subjects were requested to keep their eyes fixed on a cross mark on the center of a back-projection screen 1 m in front of them.

Data Acquisition and Preprocessing

MEG signals were continuously measured at a 1,000-Hz sampling rate during task performance using a whole-head, 204 planar gradiometers (Vectorview®, Neuromag, Helsinki, Finland). This planar type of gradiometer has the advantage of sensitivity of superficial sources, and is particularly suitable for the sensor level analyzing. The sEMG was simultaneously recorded at a 1,000-Hz sampling rate from the extensor digitorum communis to verify movement. The total number of finger movements was about 100 for all subjects. Some of the data had been published to address the issue about cognitive demands on motor tasks [Wu et al., 2006]. All the sEMG data were rectified before subsequent calculation of TFCMI and coherence analysis. Bipolar horizontal and vertical electro-oculograms (EOG) were obtained using electrodes placed at the bilateral outer canthi and the left eye respectively. At the beginning of each measurement, the positions of three anatomical landmarks (bilateral pre-auricular points and nasion) were measured using a 3D magnetic digitizer (Isotrak 3s1002, Polhemus Navigation Science, Colchester, VT) to define a head coordinate system. Four head position indicators (HPIs) were subsequently defined and tracked by the MEG system to ensure no head movement during each measurement (maximal translation <1.5 cm). Individual MRI (T1-weighted, 3D gradient-echo pulse sequence, TR/TE/TI:88.1/4.12/650 (all ms), 128 × 128 × 128 matrix, FOV = 250 mm) were obtained with a 3.0-T Bruker MedSpec S300 system (Bruker, Kalsrube, Germany).

MEG measurements of 204 channels were recorded continuously and termed as a Total Set. Among them, EOG-free measurements (EOG <600 uV) were extracted as an Accepted Set (approximately at least 100 trials should be collected on-line). All MEG measurements in the Total Set were used to evaluate the robustness of the TFCMI method against physiological noise.

Computation of Time-Frequency Maps Using Morlet Wavelet Transformation

Each trial of MEG and sEMG raw data with 4,000 samples (from −2 to +2 s relative to the movement onset time) was processed using the Morlet wavelet transformation to generate the time-frequency representation of signals (Fig. 1a,b). The time window was defined during this period based on the prominent spectral changes of movement-related activities (Fig. 1d), which is in line with previous study of a self-paced finger flexion task [Feige et al., 1996], where the 20-Hz spectral power depress started at about −2.5 s and a power elevation in β frequency range started at about +0.5 s, with fading out at about +2 s. Let $x_{i,k}(t)$ denote the data from the kth trial of ith channel at time instant t, its Morlet wavelet transformation is given by:

$$W_{x_{i,k}}(t,f) = \int x_{i,k}(\lambda) \cdot \overline{\phi_{t,f}(t-\lambda)}\,d\lambda$$

where $W_{x_{i,k}}(t,f)$ represents the energy density in frequency f of the kth trial of the ith channel at time instant t; $\phi_{t,f}(\lambda) = A \cdot e^{i2\pi f(\lambda - t)} e^{\frac{-(\lambda-t)^2}{2\sigma^2}}$ are the Morlet wavelets; their time spread is defined by $\sigma = \frac{8}{2\pi f}$; $A = (\sigma\sqrt{2})^{-1/2}$ is the normalization factor and $\overline{\phi_{t,f}(\lambda)}$ are the complex conjugates of $\phi_{t,f}(\lambda)$.

Time-frequency maps encompassing the α (8–13 Hz) and β (16–25 Hz) activities were created separately by averaging across trials within each subject (Fig. 1c). (Note that only two channels with β activity are shown on the map). They were displayed topographically with colors representing power (see Fig. 2). In the sEMG-MEG study of corticomuscular coupling, only the time-frequency map of the β activities underwent further analysis. Frequency components from 16 to 25 Hz were chosen, based on previous electromangentophysiological studies of weak and moderate tonic contractions [Baker et al., 1997; Conway

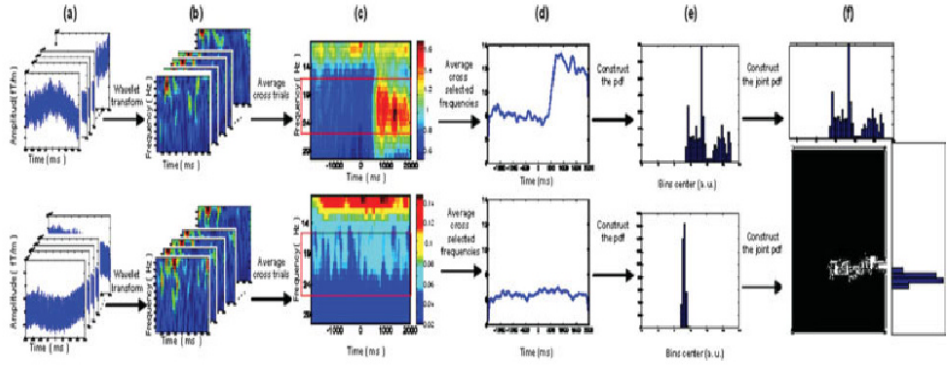

Figure 1.

Schematic diagram of TFCMI computation. Raw MEG measurements from any two planar gradiometers of each trial (a) were processed using the Morlet wavelet transformation to obtain time-frequency maps (b). Colors indicate power amplitude in an arbitrary unit (a.u.). The mean time-frequency map (c) for each channel was created by averaging the individual time-frequency maps across trials. The red rectangle represents the prespecified bandwidth in β band (16–25 Hz). The temporal curves of power changes for each channel (d) were created by averaging over the β band (or α band) in the mean time-frequency map and were used to estimate the probability density function (e) and the joint probability density function (f). [Color figure can be viewed in the online issue, which is available at www.interscience.wiley.com.]

et al., 1995; Halliday et al., 1998; Kilner et al., 1999; Mima and Hallett, 1999; Mima et al., 2000b; Salenius et al., 1997].

Detection of Neural Connectivity Using TFCMI

Power from two averaged time-frequency maps was subsequently separately averaged over selected frequency bands to produce two temporal curves (Fig. 1d). Each curve represents 4,000 samples of a random variable, F_i, at the ith MEG channel. These samples of F_i were used to construct the probability density function (pdf), $p(F_{i,b})$, (Fig. 1e) for the computation of entropy, $H(F_i)$:

$$H(F_i) = -\sum_{b=1}^{64} p(F_{i,b}) \ln p(F_{i,b})$$

where the $b = 1, 2, \ldots, 64$ was the index of sampling bins for the construction of approximated pdf. It is noteworthy that the estimation of pdf and joint pdf from the data histogram is crucial for the computation of mutual information. In order to estimate pdf and joint pdf stably, that is, neither underestimation nor overestimation [Fraser and Swinney, 1986], 64 bins were adopted for 4,000 samples as suggested by Jeong et al. [Jeong et al., 2001].

Entropy is the average amount of information reflecting the measure of uncertainty. Similarly, the joint probability density function (jpdf) between the ith and jth MEG channels can be computed as $p(F_{i,b}, F_{j,b})$ for the estimation of joint entropy, $H(F_i, F_j)$ (Fig. 1f).

$$H(F_i, F_j) = -\sum_{b=1}^{64} p(F_{i,b}, F_{j,b}) \ln p(F_{i,b}, F_{j,b})$$

Then the TFCMI between two random variables F_i and F_j was calculated as follows:

$$\mathrm{TFCMI}(F_i, F_j) = H(F_i) + H(F_j) - H(F_i, F_j) = -\sum_{b=1}^{64} p(F_{i,b}, F_{j,b}) \ln \frac{p(F_{i,b}, F_{j,b})}{p(F_{i,b}) p(F_{j,b})}$$

The TFCMI value is used as an index of functional connectivity. Figure 1 shows the schematic diagram for TFCMI computation.

Determination of the COI

The channel located in the vicinity of the sensorimotor area exhibiting the most prominent β ERD was chosen as the channel of interest (COI) [Pfurtscheller and da Silva, 1999 for the details of β ERD computation; Andrew and Pfurtscheller, 1999; Pfurtscheller and Aranibar, 1979; Pfurtscheller and da Silva, 1999]. TFCMI and coherence were computed between the COI and any other channels. In addition, the COI was replaced by an arbitrary channel (A-COI) unrelated to the motor task to investigate the specificity for regional detection. For the between-modality study, that is, the sEMG-MEG study, the sEMG was used as the COI.

Statistical Threshold

The 95% confidence limit of t-distribution was used as a threshold to determine the regions of significant likelihood associated with the COI in TFCMI and coherence analysis,

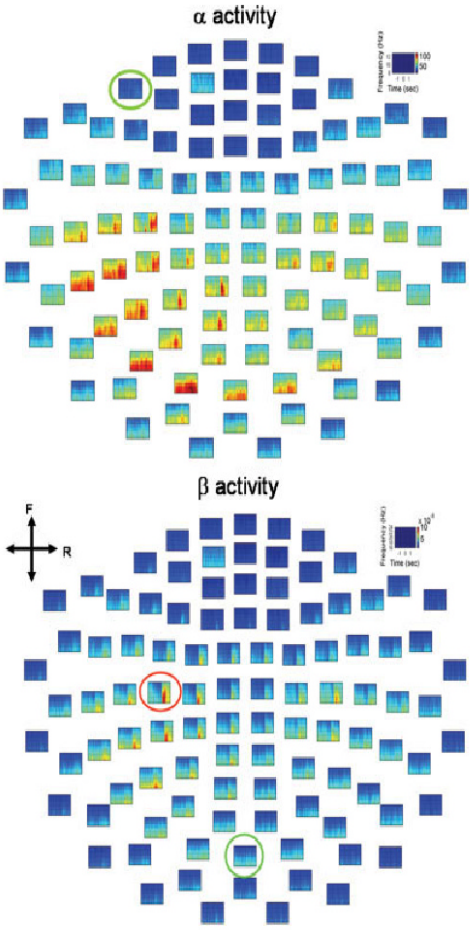

Figure 2.

Mean time-frequency maps of α and β oscillatory activities. The red circle indicates the channel-of-interest (COI) with the strongest β oscillatory activity (lower panel); the chosen COI was also used for analysis of α oscillation. Green circles denote arbitrary COIs (A-COIs), irrelevant to the motor task. Both COI and A-COIs were employed as reference channels in the subsequent analyses (see Figs. 4, 5). Color indicates power amplitude. The maps are shown in top view. F, front; R, right. [Color figure can be viewed in the online issue, which is available at www.interscience.wiley.com.]

respectively. The confidence levels for TFCMI and coherence were computed in different ways fundamentally. For TFCMI method, value of TFCMI between the COI and any other channels was pre-normalized with respect to the maximal value of TFCMI obtained at the COI. Normalized values were between 0 and 1 and were used to construct the t-distribution. The degree of freedom is 1 since we have averaged across trials before TFCMI calculating. In other words, the TFCMI was computed from only one averaged power spectrum. The 95% confidence level was then set at mean +6.314 standard deviation (SD; df = 1, one tailed) to eliminate the bias due to large variation. The conventional coherence method (or magnitude squared coherence) [Zaveri et al., 1999] was also applied to the same data set based on the same COI by using an fast Fourier transform window of 512 points with 256 points overlapping, trial by trial. This allows no overlapping of each epoch signals and makes the spectral resolution (Δf) of this coherence estimate to be 0.25 Hz, the inverse of the epoch length, 1/4 sec ^{1} [Zaveri et al., 1999]. Before averaging across trials, an arc-hyperbolic tangent transform are applied to the coherence values, as described by Rosenberg et al. [1989], so that the coherence values have a normal distribution [Rosenberg et al., 1989]. The significant threshold of 95% confidence limit was then given by mean +1.65SD (df = 100, one tailed) [Halliday et al., 1995]. For the purpose of presentation, coherence values between 0 and 1 were rescaled to the maximal coherence value. Only values of TFCMI and coherence above the significant thresholds were cataloged as significant interactions and were represented topographically as maps with colors indicating the relative coupling level above significance.

Visualization of TFCMI maps

To better visualize the resolved coupled areas of each subject, the TFCMI maps were superimposed on top of each individual cortical surface. The procedure was described in following steps. First, the positions of four HPIs were used to calculate the relative rotation and translation between the sensor coordinate system and the head coordinate system. This allowed the sensor array positions to be transformed into the head coordinate system. Second, three anatomical landmarks (bilateral pre-auricular points and nasion) on individual MRI were identified and aligned with head coordinate. The sensor array positions were subsequently transformed into the MRI coordinate system. Third, the cortex was segmented from each individual MRI and reconstructed using ASA® (A.N.T. software BV, The Netherlands). Fourth, a sphere was fitted to the transformed sensor array positions using the least squares technique and rescaled to make the sensors abut to the reconstructed cortical surface. Finally, the TFCMI results in the form of contour maps were projected onto the transformed sensor arrays overlaid on top of cortical surface.

It should be noted that the correspondence between the position of the MEG gradiometers and the underlying sources cannot be precisely determined without a proper source analysis. Nevertheless, the MEG gradiometer is designed to detect the largest signal right above the current source and suppressing ambient noise, suggesting that the gradiometer with the maximum current flux may ascribe to currents mainly from the directly beneath cortical area and partly from several surrounding cortical regions. In this article, the word "regions," referring to

"regions directly beneath MEG sensors and possibly surrounding regions," is used loosely henceforth for the purpose of simplicity. Though the minor contribution from surrounding regions was not taken into account in this study, it will be exploited on the source space in future work.

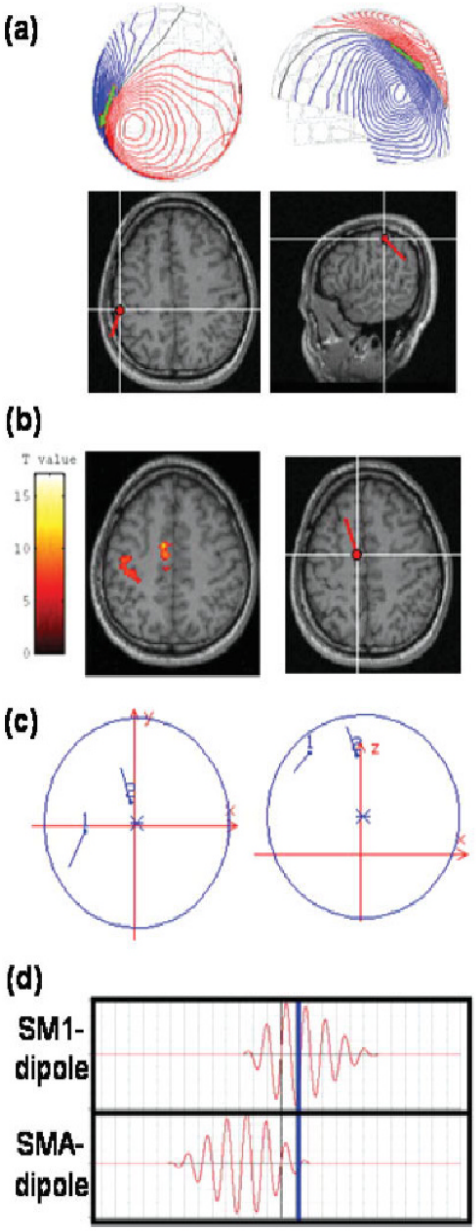

Simulation of Coupling Between Two Regions

Two simulations (Simulation, Neuromag® system software) were conducted to establish the face validation of the TFCMI method in terms of the detection efficacy. Simulation 1 examined the ability of TFCMI to reject false coupling caused by noise when there were no actual coupled sources. Simulation 2 attempted to clarify the detection efficacy of TFCMI with regards to low SNR under the circumstance that the neuromagnetic signals received by planar MEG from the bilateral SMAs can be drastically attenuated due to anatomical architecture [Joliot et al., 1998; Lang et al., 1991].

In Simulation 1, one oscillatory dipole (23 Hz) was placed in the left SM1 (SM1-dipole) of a chosen subject to synthesize magnetic fields on the sensor array. Position and moment of the SM1-dipole were taken from the equivalent current dipole (ECD) fit [Hamalainen et al., 1993] to the movement evoked field I (MEFI) of the specific subject (Fig. 3a). The time point of the fit was 14 ms post movement. In Simulation 2, an additional dipole (23 Hz) (SMA-dipole) was placed at a mesial region in the vicinity of SMA and pointed anteriorly based on the literature [Erdler et al., 2000; Lang et al., 1991]. The anatomical seeding of the SMA-dipole was adopted from the same subject's results in a parallel functional MRI (fMRI) experiment using similar task (repetitive index finger movement; T2*-weighted gradient-echo echo planar imaging sequence, TR/TE/flip angle = 2000/50 ms/90°, 64 × 64 × 20 matrix, FOV = 192 mm) (Fig. 3b). The distance between the SM1- and SMA-dipole was 55.07 mm (Fig. 3c). The oscillating source of the SMA-dipole preceded that of the SM1-dipole by 600 msec (Fig. 3d) [Erdler et al., 2000; Lang et al., 1991]. It is noteworthy that this design aims to emulate the spa-

Figure 3.

SM1- and SMA-dipole allocation in simulation studies. (a) SM1-dipole position and moment. The SM1-dipole placement in the left SM1 was based on the equivalent current dipole (ECD) fit to movement evoked field I. Upper panel displays the isocontour maps of the recorded neuromagnetic signals and the dipole (in green). The SM1-dipole was rendered onto the subject's own MRIs in axial view (lower panel; subject's right hemisphere to the right of the image). Anatomically, this SM1-dipole was located slightly posterior to the contralateral central sulcus. (b) SMA-dipole position and moment. The SMA-dipole was seeded in the left SMA (right panel) close to the midline with coordinates adopted from a parallel fMRI experiment conducted by the same subject (left panel). (c) Spatial relationship between SM1- and SMA-dipoles. Left, axial view; right, sagittal view. (d) Time courses of SM1-dipole (upper panel) and SMA-dipole (lower panel). In this simulation, the time course of the SMA-dipole preceded that of SM1-dipole by 600 m (Erdler et al., 2000; Lang et al., 1991). The blue line denotes the time-point for the ECD fit in the subsequent analysis (see Fig. 7a). [Color figure can be viewed in the online issue, which is available at www.interscience.wiley.com.]

tially distributed connections in low SNR circumstance, rather than to link this simulation to the underlying functional connections during movements. Accordingly, the strength of the SMA-dipole activity used in Simulation 2 was manipulated with a range of 0.5 to 1 times of SM1 dipole to modulate SNR [Chen et al., 1991; Erdler et al., 2000; Joliot et al., 1998]. Random noise was added onto each sensor measurement. Both TFCMI and coherence analysis were performed on the synthetic data. Moreover, conventional ECDs were fitted on the synthetic data to estimate the locations of neural generators, which were used as comparisons to TFCMI results.

RESULTS

Motor Task Performance

All subjects followed the instructions and performed the task well. The average number of trials in Accepted Sets among subjects was 98 epochs. Intervals between successive movements (intermovement interval, IMI) of Accepted Sets among subjects were between 7.968 and 15.162 seconds (mean, 13.124 s) and there was no feedback to cue subjects' movements. EOG ratio (the ratio of EOG sets to Total Sets) varied from 1.9% to 35.29%. Table I shows task performance and compositions of MEG test data for Accepted Set, IMI, EOG trials, Total Set and EOG ratio.

Neural Correlates of Event-Related α and β Oscillatory Activities: Within Modality

The resultant spatial distributions of neural connectivity for α and β activities, respectively, were represented by maps with colors representing the values, that is, the strengths of neural connectivity of α and β activities (Fig. 4a). TFCMI maps, both show strong connectivity within the contralateral sensorimotor region. The strengths of connectivity above threshold (95% confidence limit) can be alternatively displayed using colored lines, linking significant regions and the COI (Fig. 4b). Under the assumption that the gradiometer MEG sensors represent the major cortical oscillatory activity of underlying cortical tissues, contour maps projected on the reconstructed cortical surface reveal the regions coupled with the COI, including the mesial frontocentral cortex (termed the supplementary motor area, SMA, due to the anatomical correspondence; see simulation and discussion), bilateral primary sensorimotor areas (SM1), and contralateral premotor area (PM) (Fig. 4c). Table II lists neural correlates revealed by TFCMI and coherence methods. In MEG-MEG studies, TFCMI results for all subjects ($n = 8$) show encompassing of bilateral SM1s, SMA, and contralateral PM in both α and β activities. The coherence results for β activity show encompassing of bilateral SM1s ($n = 2$), SMA ($n = 3$), and contralateral PM ($n = 6$) in some subjects. For α activity, contralateral SM1 was engaged in all subjects ($n = 8$). Two of the subjects had additional SMA encompassing, and four showed contralateral PM encompassing.

Impact of COI on TFCMI and Coherence Analysis

Figure 5 shows the COI-specific results obtained from TFCMI method and coherence method. The TFCMI method resolved more neural connections than coherence method, such as ipsilateral SM1, when task-related COI was chosen (Fig. 5, upper panel; Table II). When the task-related COI was replaced by an A-COI irrelevant to the motor task, the A-COI TFCMI result demonstrated a highly focal encompassing centered at A-COI area (exclusively within), while the A-COI coherence result showed a rather dispersed neural connection with A-COI, incongruent with the known anatomy (Fig. 5, lower panel).

Between- and Within-Modality Analysis: sEMG-MEG and MEG-MEG

Figure 6 gives analytical results for TFCMI and coherence around beta band (16–25 Hz) for between- and within-modality signals, (sEMG-MEG and MEG-MEG studies) for subject 8. Simultaneous recording of sEMG for both right and left hands precluded mirror movement in the left hand (Fig. 6a). Both TFCMI and coherence results exhibited remarkable corticomuscular coupling over con-

TABLE I. Motor task performance and MEG test data

Subject index	Accepted set	IMI (mean ± SD; ms)	EOG Set	Total set	EOG ratio (%)
1	105	15,162 ± 6,969	27	132	20.45
2	93	14,571 ± 3,612	38	131	29.01
3	104	14,476 ± 3,774	41	145	28.27
4	91	13,867 ± 3,891	16	107	14.95
5	88	13,760 ± 7,589	48	136	35.29
6	103	14,302 ± 7,237	2	105	1.90
7	100	7,968 ± 1,573	8	108	7.40
8	98	14,968 ± 3,807	3	101	2.97
Average	98		22	120	

IMI, inter-movement interval; SD, standard deviation; EOG, electro-oculogram.

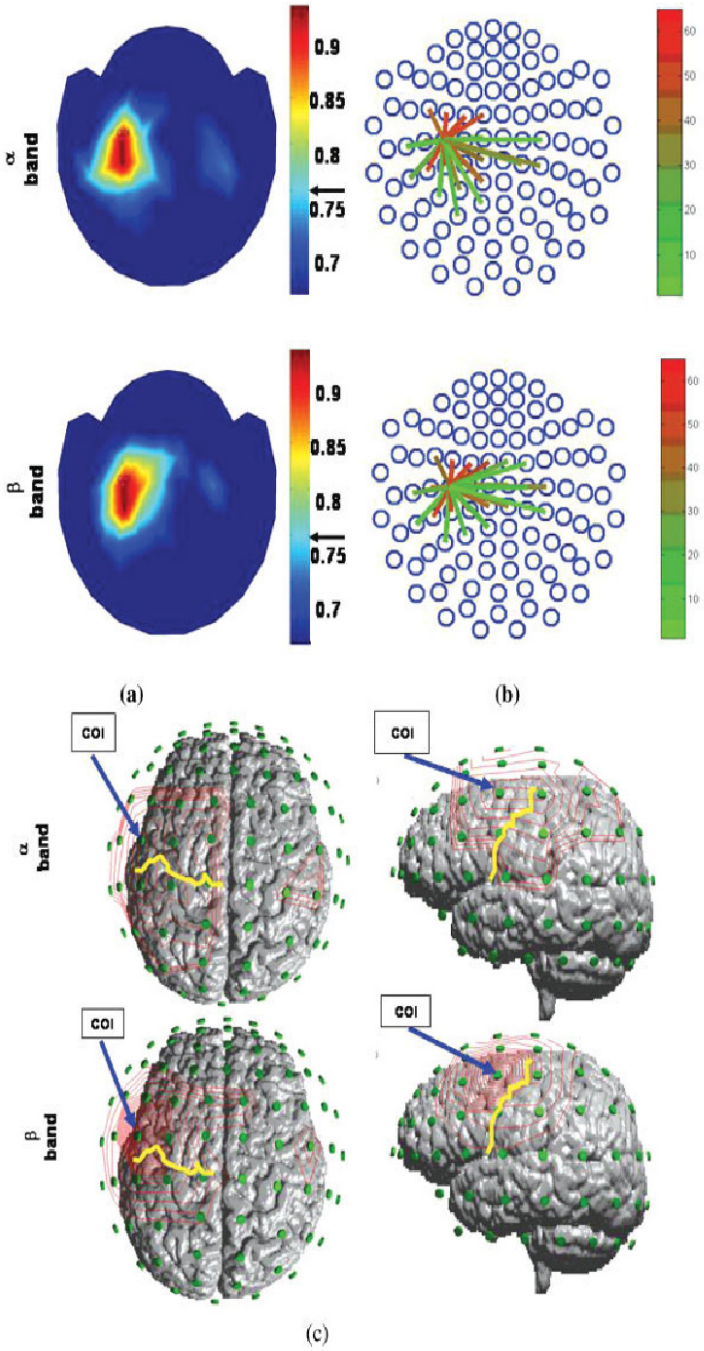

Figure 4.
Event-related α and β oscillatory activities networks (TFCMI). Individual data set. (a) Topographic maps of the spatial distribution of significant TFCMI values between COI and other MEG channels for α and β oscillatory activities. Color indicates the strength of connectivity. The arrows besides the color bar indicate the significant threshold. (b) An alternative display of the strengths of connectivity above the significant threshold. Regions of significant communications with the chosen COI were marked by links emanating from the COI. (c) TFCMI values in contour maps. The maps were projected onto the rescaled sensor array and the individual MRI to better the anatomical visualization of the coupled regions. Areas engaged included SMAs, bilateral SM1s, and contralateral PM. Yellow curves are the central sulcus; blue arrows indicate the location of COI. Left panel, view of top of the head; right panel, lateral view of the head from the left side. [Color figure can be viewed in the online issue, which is available at www.interscience.wiley.com.]

tralateral SM1 for all subjects (n = 8; Table II). The sEMG-MEG maps resembled the MEG-MEG maps, but there were subtle differences (Fig. 6b,c). The coupling between ipsilateral SM1 and sEMG was consistently resolved by the TFCMI method. Such coupling could not be detected by the coherence approach (Table II).

TABLE II. Neural correlates reflected in TFCMI and coherence methods

		MEG-MEG study				sEMG-MEG study			
		cSM1	iSM1	SMA	PM	cSM1	iSM1	SMA	PM
TFCMI	α	8/8[a]	8/8	8/8	8/8				
	β	8/8	8/8	8/8	8/8	8/8	8/8	7/8	8/8
Coherence	α	8/8		2/8	4/8				
	β	8/8	2/8	3/8	6/8	8/8		2/8	4/8

[a] The results are given in a ratio of detection, which indicates the number of subjects against all eight subjects.
cSM1, contralateral primary sensorimotor area; iSM1, ipsilateral primary sensorimotor area; SMA, supplementary motor area; PM, premotor area; contralateral.

Simulation results

Figure 7 shows the simulation result when the SMA-dipole strength is equal to that of the SM1-dipole. The simulated output on SM1 sensor which exhibits the strongest power is shown in Figure 7a. Conventional ECDs, serving as a comparison to TFCMI, were fitted on the synthetic data to estimate the locations of neural generators. The time-point for the ECD fit was chosen at maximal oscillatory amplitude (Fig. 7a; blue line) from which the corresponding simulated topographic pattern is displayed in Figure 7b. Spatial congruence of the simulated SM1-dipole (red) and the estimated SM1-dipole (blue) is displayed in Figure 7c. In Figure 7d, isocontour maps of the synthetic signals at the time point of max SMA-dipole strength are shown in the right column. The synthetic signals from the channel over left SMA are shown in left upper panel, and the left middle and lower panels are the source activity from SM1-dipole and SMA-dipole, respectively. The goodness-of-fit (Gof) for the estimated left-SM1 dipole was 97.2% for Simulation 1 (Table III). In Simulation 2, when both SMA dipole and SM1 dipole have the same strength, the Gof for SM1-dipole and for SMA-dipole were 96.2% and 42.3%, respectively. When the source strength of SMA dipole was half of SM1 dipole, the Gof of SM1 and SMA dipoles decreased to 88.6% and 40%, respectively (Table IV).

Both TFCMI and coherence analysis were performed on the synthetic data (see Fig. 8). In simulation 1 (SM1-dipole only), both TFCMI and coherence maps showed a focal encompassing of SM1, that is, exclusive connectivity to itself only (Fig. 8; upper panel). In simulation 2 (SM1-dipole and SMA-dipole), the time courses of the two dipoles were coherent and had a significant transformed coherence value of 0.957 after averaging 100 simulation trials in source space since they are with similar temporal profile (Fig. 3d) and are stationary across trials. However, after forward modeling, only TFCMI resolved more spatially distributed connections in sensor space, anatomically encompassing the SM1 and SMA, respectively, where the two dipoles were seated whereas the coherence method cannot discern the coupling (coherence = 0.0023) and solely showed connectivity within SM1 (Fig. 8; lower panel).

In addition, we have computed the SNR (=10 log(signal power/noise power)) of the experimental data measured from the sensor above left SM1 for the comparison with the SNR in simulation. The segment of averaged data from −4 to −3.5 s was considered as the noise and that from −2

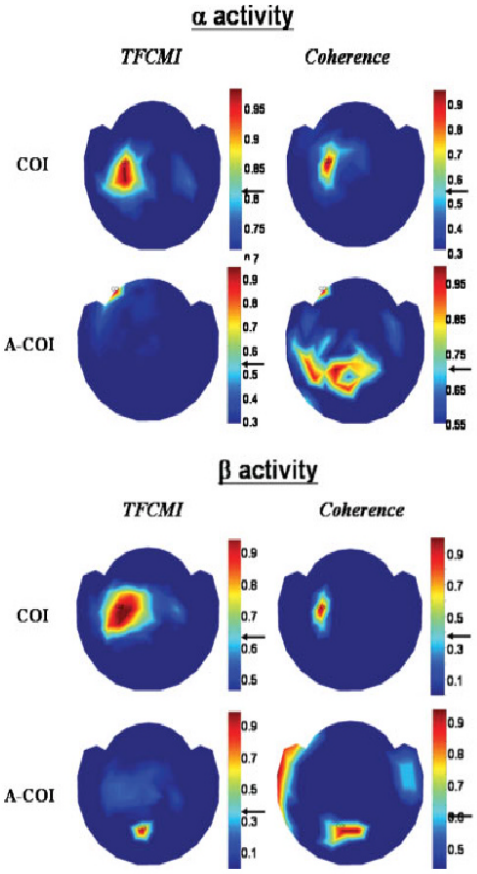

Figure 5.
Influence of reference chosen on TFCMI and coherence analysis with respect to α and β activities. When the task-related COI was properly chosen (upper panel), TFCMI results consistently showed more neural connections involving bilateral sensorimotor areas and the SMA for both α and β activities than coherence analysis. When the A-COIs were chosen as reference (lower panel), the A-COI TFCMI result demonstrated a highly focal encompassing centered at A-COI area (connectivity exclusively to itself), while the A-COI coherence result showed rather dispersed neural connections with A-COI, incongruent with the known anatomy. [Color figure can be viewed in the online issue, which is available at www.interscience.wiley.com.]

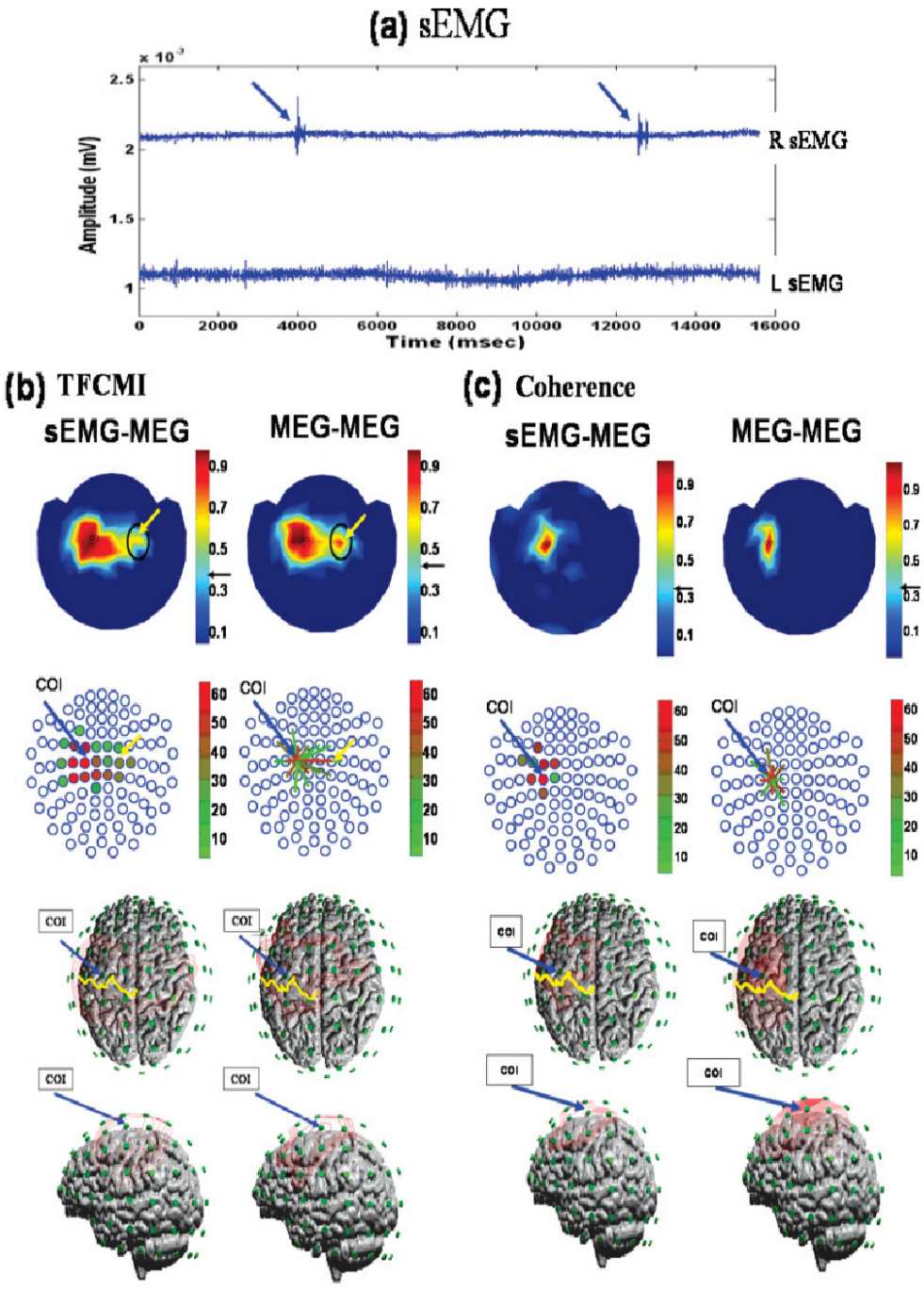
(a) sEMG
x 10^-3
Amplitude (mV)
R sEMG
L sEMG
Time (msec)
(b) TFCMI
sEMG-MEG
MEG-MEG
(c) Coherence
sEMG-MEG
MEG-MEG
COI

Figure 6.

to +2 s was the signal of activity. The averaged SNR in averaged data from 8 subjects was 26.57 + 2.9 dB. In Simulation 2, the minimum SNR for TFCMI method to detect the connection between SM1 and SMA (Table IV) is 21.8 dB, where the simulated signal was a composition generated from hypothetical SM1- and SMA-dipoles with the same dipole strength. In summary, our simulations indicate that the TFCMI method has superior detection specificity compared to the coherence method in low SNR situation.

DISCUSSION

Detection Specificity in Low SNR Data: Computational Simulation

A question central to the discussion of TFCMI approach in the current study is whether TFCMI could detect and resolve spatially distributed connections in low SNR circumstance. In this study, two simulations were conducted to provide the face validation of the TFCMI method in this regard. As a result, the Simulation 1 (SM1 dipole only) shows a focal encompassing of SM1, that is, exclusive connectivity to itself only (Fig. 8; upper panel) and the Simulation 2 demonstrates that TFCMI can decipher spatially distributed connections in low SNR circumstance. It is noteworthy that, though the simulation results show that TFCMI method can resolve the spatially distributed connections in low SNR circumstance, we have not presented an exhaustive simulation to emulate the underlying functional connections during movements. Since the TFCMI method is a pair-wise analysis and the TFCMI results from experimental data may be influenced by some distant but coupled sources fed into the COI and other channels, the interpretation of the TFCMI results should be restricted. Further validation is needed for the TFCMI method to process and represent on the source level instead of the sensor level. Nevertheless, the simulation results demonstrate that TFCMI was capable of discerning noise and showing the neural connectivity between distinct areas, in this case, between SM1 and SMA, with low SNR whereas both the ECD fit and the coherence method were not able to detect (Figs. 7, 8; Table IV).

Robustness of TFCMI Method

TFCMI analysis is resistant to reference selection and efficient in deciphering task-related connections from the irrelevant ones. Proper selection of COI is critical for the study of functional coupling using the coherence method [Gerloff et al., 1998]. Such a prerequisite is also seen in Figure 5 when A-COI was chosen as reference, despite which the coherence method is robust when the reference electrode is correct and the interaction is stationary across trials [David et al., 2004]. On the contrary, the A-COI TFCMI result demonstrated a highly focal encompassing centering at the A-COI area (exclusive connectivity to itself) which was validated by Simulation 1 (Fig. 8; upper panel) where the unconnected-solitary source (chosen as COI) showed no factitious coupling. In addition, when sEMG was used as COI in the between-modality study, the TFCMI showed neurophysiologically and neuoranatomically sEMG-MEG topographies (Fig. 6b, Table II). Moreover, the TFCMI method in broadband analysis performs reliably compared with the conventional mutual information method whose sensitivity is less reliable in broadband and weak coupling signals [David et al., 2004]. Collectively, the data imply that TFCMI can better resolve task-related connections.

Resolving Power Under Nonlinear Interactions

It is well known that the planning and execution of voluntary movement relies upon the integration of premotor and primary motor areas operating in conjunction with sensory and association areas, including SMA and cerebellum. The functional relevance between left and right SM1 in MEG-MEG event-related experiments as disclosed by the TFCMI is congruent with previous imaging studies showing bihemispheric engagement for motoric movement (Table II). [Gerloff et al., 1998; Hsieh et al., 2002; Joliot et al., 1998; Stippich et al., 1998]. The TFCMI also shows consistent engagement of ipsilateral SM1 in the sEMG-MEG event-related experiment (Table II; Fig. 6b). The inconsistent interhemispheric interaction in existing studies using the coherence or partial coherence approach has lead to a debate on bilateral involvement of SM1 for unilateral finger movement control [Andres et al., 1999;

Figure 6.

Ipsilateral SM1 in between- and within-modality TFCMI studies. Individual data set. (a) Right (upper trace) and left (lower trace) hand sEMGs during right finger movement (blue arrows). The left sEMG precluded mirror movement of the left hand during the experiment. (b,c) Results of β activity from TFCMI and coherence, respectively, for between- (sEMG-MEG; left panel) and within-modality (MEG-MEG; right panel) studies. The sEMG-MEG maps (first row) exhibit prominent corticomuscular coupling at contralateral SM1 in both TFCMI and coherence analyses, and resemble MEG-MEG maps. Yellow arrows indicate ipsilateral SM1 encompassing by TFCMI. No such coupling was detected using the coherence method. Second row presents couplings in an alternative manner, with blue circles representing MEG sensor sites. Blue arrows anchor the COI for MEG-MEG analysis, which is also indicated in sEMG-MEG maps only. Coupling strengths are coded in different colors either in the form of solid dots in the sEMG-MEG maps or line links in the MEG-MEG maps. The third (view of the top of the head) and fourth (left lateral view of the head) rows display the isocontour maps for a better appreciation of neuroanatomical correspondence. Yellow curves are the central sulci. [Color figure can be viewed in the online issue, which is available at www.interscience.wiley.com.]

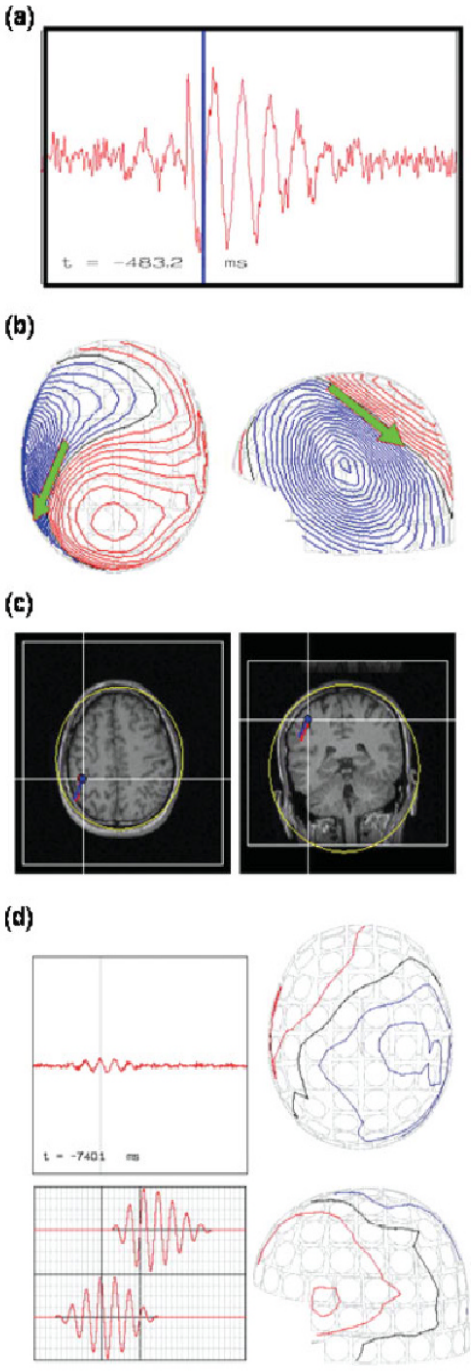

Andrew and Pfurtscheller, 1996, 1999; Gerloff et al., 1998; Manganotti et al., 1998; Mima et al., 2000a]. This inconsistency could also been seen in our coherence results (Table II). However, transcranial magnetic stimulation (TMS) studies have confirmed the role of ipsilateral SM1 in self-paced finger movement tasks [Chen et al., 1997; Rau et al., 2003]. Studies on patients with motor disorders have shown a significant activation of ipsilateral SM1/corticospinal tract as compensatory mechanisms [Caramia et al., 2000; Cuadrado et al., 1999; Jones et al., 1989; Marshall et al., 2000; Ward and Cohen, 2004]. Our TFCMI analytical results are consistent with the known anatomy since 10% of corticospinal fibers have ipsilateral projections [for a review, see Kuypers, 1981] and the ipsilateral influence is integrated with the prevailing contralateral one (also evinced by the preponderant contralateral expression of TFCMI values) for the overall control of movement [de Oliveira, 2002]. Accordingly, it is plausible that the coupling between contra- and ipsi-lateral SMI may be through a nonlinear or nonstationary interaction and could be better unraveled by TFCMI.

Fundamental Differences Between the TFCMI Method and Coherence Method

In this study, the functional connectivity during a self-paced brisk finger movement task was studied. Such a discrete movement paradigm may mandate more cognitive processing than automatic movement paradigm within sub-second inter-movement interval [Lewis and Miall, 2003]. Moreover, the latency of maximal post-movement β rebound exhibits trial-to-trial variability [Lee et al., 2003b]. These suggest that there is inherent nonstationarity in the neural processing. Under the assumption that neural processes are stationary across trials [Lachaux et al., 2002; Nunez et al., 1997], the coherence method measures the linear dependency between signals via normalized spectral

Figure 7.

Poor detection of SMA-dipole by simulation. (a) Synthetic signals from the channel over SM1 as produced by SM1- and SMA-dipoles. (b) Isocontour maps of the synthetic signals and the ECD result of SM1-dipole. The blue bar in (a) indicates snap time for the contour maps. (c) Spatial congruence of the simulated SM1-dipole and the estimated SM1-dipole. The estimated SM1-dipole (in blue, with a very high goodness-of-fit, about 96%) almost coincides with the simulated (in red). (d) Isocontour maps of the synthetic signals at the time point of max SMA-dipole strength (right column). The synthetic signals from the channel over left SMA are shown in left upper panel, and the left middle and lower panels are the source activity from SM1-dipole and SMA-dipole, respectively. The goodness-of-fit for the SMA-dipole was 42.3% (Table IV). The poor Gof for the SMA-dipole was in line with the consensus that the MEG dipole fit for SMA source can be ambiguous due to insufficient SNR. [Color figure can be viewed in the online issue, which is available at www.interscience.wiley.com.]

TABLE III. Simulated-dipole parameters and ECD results for source estimation: Simulation I

		Simulated-dipole parameters		ECD results; SNR = 21.8 dB			
Index		Location	Moment	Location	Moment	Distance[a] (mm)	Gof (%)
SM1-dipole	*x*	35.2	0.42	35.3	0.43		
	y	7.2	0.80	7.2	0.79	1.03	97.2[b]
	z	88.9	0.41	88.3	0.41		

[a] Between the simulated and the estimated location.
[b] 85% Gof.
ECD, equivalent current dipole; SNR, signal-to-noise ratio in source space; Gof, goodness of fit.

covariances, that is, second-order statistics. This second-order method works well for Gaussianly distributed signals but may not for the non-Gaussian ones, as shown in the upper panel of Fig. 1(e). The TFCMI method, on the contrary, utilizes the wavelet transform as the preprocessing procedure to bandpass the signals with better temporal resolution than Fourier transform such that the subtle temporal scenarios within pre-specitifc frequency bands can be properly reserved. Then, based on the joint probability of coincidence occurrence of oscillatory signal power with more accurate temporal resolution, TFCMI computation is not limited to the linearity of spectral modulation across trials. In fact, the use of pdf and joint pdf takes the advantage of high-order statistics to extract the nonlinear coupling that may not be correctly identified using the second-order techniques. Therefore, the combination of wavelet and mutual information substantiate a significant contribution for nonlinear analysis and is a salient feature of the TFCMI method. Such fundamental differences make the TFCMI method more adaptive than coherence method in analyzing complex dynamic data.

The Limitations of and Prospects for the TFCMI Method

Since the cortical oscillatory activity acquired from a MEG sensor cannot be fully attributed to the underlying cortical region, the interpretation of TFCMI results is limited to the sensor space in current study. Further validation, such as simultaneous recording of EEG and fMRI, may serve as a complementary to the TFCMI method. Alternatively, the recording signals from MEG sensors can be the inversely mapped into the source space by using a spatial filter as developed in the dynamic imaging of coherent sources (DICS) method [Gross et al., 2001, 2002, 2003; Ishii et al., 2002]. This will allow the calculation of TFCMI on the source space and subsequently analyze the functional coupling within the brain. Another drawback of the TFCMI method is the low temporal resolution (4 s), since the estimation of probability density function and joint probability density function was based on the histograms of signal amplitudes over a 4-s time window. Various lengths of time window will be used to assess the performance of TFCMI in the future work. Besides, the TFCMI method was not designed to unravel the propagation direction of the electrical activity among brain structures. Once the evident functional coupling on the sensor space was resolved using the TFCMI method, other approaches, such as the direct transfer function (DTF) method, phase synchronization, or the directional index can be employed for the quantification of coupling direction.

CONCLUSIONS

We present a novel method, TFCMI, for the exploration of the neural communication and interaction among distinct brain regions or regions of different neurophysiological modalities. When compared with the coherence

TABLE IV. Simulated-dipole parameters and ECD results for source estimation: Simulation 2

Simulated-dipole parameters				ECD results: SNR = 19.1 (dBSM1-dipole strength:SMA-dipole strength = 1:0.5)				ECD results: SNR = 21.8 (dBSM1-dipole strength:SMA-dipole strength = 1:1)			
Index		Location	Moment	Location	Moment	Distance[a] (mm)	Gof (%)	Location	Moment	Distance[a] (mm)	Gof (%)
SM1-dipole	*x*	35.2	0.42	36.8	0.2809			34.3	0.42	1.15	
	y	7.8	0.80	7.6	0.8827	4.87	88.6[a]	7.2	0.79		96.2[b]
	z	88.9	0.41	84.3	0.3796			89.3	0.42		
SMA-dipole	*x*	3.4	0.54					1.0	0.68	10.71	
	y	20.4	0.58				below 40	10.6	0.71		42.3
	z	87.9	0.60					91.5	0.14		

[a] Between the simulated and the estimated location.
[b] 85% Gof.
ECD, equivalent current dipole; SNR, signal-to-noise ratio in source space; Gof, goodness of fit.

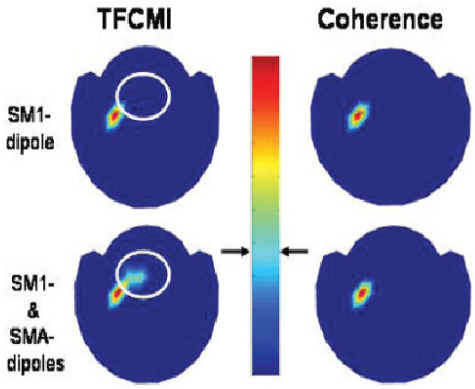

Figure 8.

Detection specificity of TFCMI in low SNR data. Both TFCMI and the coherence method yielded one unambiguous focus in the first simulation (only SM1 dipole, upper panel). In the second simulation (SM1-dipole and SMA-dipole), only the TFCMI resolved more spatially distributed connections in low SNR data, anatomically encompassing the SM1 and SMA, respectively, where the two dipoles were seated (lower panel). The white circle in the lower panel highlights the difference between the TFCMI and coherence results which is the supposed SMA area. The white circle in the upper panel indicates the same SMA area only for comparison with the result in the lower panel. [Color figure can be viewed in the online issue, which is available at www.interscience.wiley.com.]

approach (linear dependency only), the TFCMI method showed better specificity on dependency measurement in broadband analysis, clearer demarcation of event-related regions from nonrelated, and more robustness for between-modality study. Although TFCMI is not a stringently complete "data-driven" approach, it can be considered as a "model-free" approach [Lee et al., 2003a]: a priori knowledge of neuronal architecture at the anatomical level can be heuristic for the analytical penetration of functional organization. The TFCMI method promises a possibility to better unravel the intricate brain functional organizations in the context of oscillation-coded communication. Further work is currently in progress to allow the TFCMI processing and representation on the source level instead of the sensor level.

ACKNOWLEDGMENTS

The authors thank anonymous reviewers for the insightful comments and particularly thank Dr. Li-Fen Chen, Dr. James Kilner, and Professor Karl Friston for valuable suggestions.

REFERENCES

Andres FG, Mima T, Schulman AE, Dichgans J, Hallett M, Gerloff C (1999): Functional coupling of human cortical sensorimotor areas during bimanual skill acquisition. Brain 122 (Part 5):855–870.

Andrew C, Pfurtscheller G (1996): Dependence of coherence measurements on EEG derivation type. Med Biol Eng Comput 34:232–238.

Andrew C, Pfurtscheller G (1999): Lack of bilateral coherence of post-movement central beta oscillations in the human electroencephalogram. Neurosci Lett 273:89–92.

Aoki F, Fetz EE, Shupe L, Lettich E, Ojemann GA (2001): Changes in power and coherence of brain activity in human sensorimotor cortex during performance of visuomotor tasks. Biosystems 63:89–99.

Baker SN, Olivier E, Lemon RN (1997): Coherent oscillations in monkey motor cortex and hand muscle EMG show task-dependent modulation. J Physiol 501 (Part 1):225–241.

Caramia MD, Palmieri MG, Giacomini P, Iani C, Dally L, Silvestrini M (2000): Ipsilateral activation of the unaffected motor cortex in patients with hemiparetic stroke. Clin Neurophysiol 111:1990–1996.

Cardoso de Oliveira S (2002): The neuronal basis of bimanual coordination: recent neurophysiological evidence and functional models. Acta Psychol (Amst) 110:139–159.

Chen DF, Hyland B, Maier V, Palmeri A, Wiesendanger M (1991): Comparison of neural activity in the supplementary motor area and in the primary motor cortex in monkeys. Somatosens Mot Res 8:27–44.

Chen R, Gerloff C, Hallett M, Cohen LG (1997): Involvement of the ipsilateral motor cortex in finger movements of different complexities. Ann Neurol 41:247–254.

Conway BA, Halliday DM, Farmer SF, Shahani U, Maas P, Weir AI, Rosenberg JR (1995): Synchronization between motor cortex and spinal motoneuronal pool during the performance of a maintained motor task in man. J Physiol 489 (Part 3):917–924.

Crone NE, Miglioretti DL, Gordon B, Lesser RP (1998): Functional mapping of human sensorimotor cortex with electrocorticographic spectral analysis. II. Event-related synchronization in the gamma band. Brain 121(Part 12):2301–2315.

Cuadrado ML, Egido JA, Gonzalez-Gutierrez JL, Varela-De-Seijas E (1999): Bihemispheric contribution to motor recovery after stroke: A longitudinal study with transcranial doppler ultrasonography. Cerebrovasc Dis 9:337–344.

David O, Cosmelli D, Friston KJ (2004): Evaluation of different measures of functional connectivity using a neural mass model. Neuroimage 21:659–673.

Erdler M, Beisteiner R, Mayer D, Kaindl T, Edward V, Windischberger C, Lindinger G, Deecke L (2000): Supplementary motor area activation preceding voluntary movement is detectable with a whole-scalp magnetoencephalography system. Neuroimage 11:697–707.

Feige B, Kristeva-Feige R, Rossi S, Pizzella V, Rossini PM (1996): Neuromagnetic study of movement-related changes in rhythmic brain activity. Brain Res 734:252–260.

Fein G, Raz J, Brown FF, Merrin EL (1988): Common reference coherence data are confounded by power and phase effects. Electroencephalogr Clin Neurophysiol 69:581–584.

Fraser AM, Swinney HL (1986): Independent coordinates for strange attractors from mutual information. Phys Rev A 33: 1134–1140.

Friston KJ (1997): Transients, metastability, and neuronal dynamics. Neuroimage 5:164–171.

Gerloff C, Richard J, Hadley J, Schulman AE, Honda M, Hallett M (1998): Functional coupling and regional activation of human cortical motor areas during simple, internally paced and externally paced finger movements. Brain 121 (Part 8):1513–1531.

Gross J, Kujala J, Hamalainen M, Timmermann L, Schnitzler A, Salmelin R (2001): Dynamic imaging of coherent sources: Studying neural interactions in the human brain. Proc Natl Acad Sci USA 98:694–699.

Gross J, Timmermann L, Kujala J, Dirks M, Schmitz F, Salmelin R, Schnitzler A (2002): The neural basis of intermittent motor control in humans. Proc Natl Acad Sci USA 99:2299–2302.

Gross J, Timmermann L, Kujala J, Salmelin R, Schnitzler A (2003): Properties of MEG tomographic maps obtained with spatial filtering. Neuroimage 19:1329–1336.

Grosse P, Cassidy MJ, Brown P (2002): EEG-EMG, MEG-EMG and EMG-EMG frequency analysis: physiological principles and clinical applications. Clin Neurophysiol 113:1523–1531.

Grossmann A, Morlet J (1984): Decomposition of Hardy function into square integrable wavelets of constant shape. SIAM J. Math Anal 15:723–736.

Halliday DM, Conway BA, Farmer SF, Rosenberg JR (1998): Using electroencephalography to study functional coupling between cortical activity and electromyograms during voluntary contractions in humans. Neurosci Lett 241:5–8.

Halliday DM, Rosenberg JR, Amjad AM, Breeze P, Conway BA, Farmer SF (1995): A framework for the analysis of mixed time series/point process data–theory and application to the study of physiological tremor, single motor unit discharges and electromyograms. Prog Biophys Mol Biol 64:237–278.

Hamalainen M, Hari R, Ilmoniemi RJ, Knuutila J, Lounasmaa OV (1993). Magnetoencephalography-theory, instrumentation, and applications to noninvasive studies of the working human brain. Rev Mod Phys 65:413–497.

Hari R, Imada T (1999): Ipsilateral movement-evoked fields reconsidered. Neuroimage 10:582–588.

Hsieh JC, Cheng H, Hsieh HM, Liao KK, Wu YT, Yeh TC, Ho LT. (2002): Loss of interhemispheric inhibition on the ipsilateral primary sensorimotor cortex in patients with brachial plexus injury: fMRI study. Ann Neurol 51:381–385.

Ishii R, Schulz M, Xiang J, Takeda M, Shinosaki K, Stuss DT, et al. (2002): MEG study of long-term cortical reorganization of sensorimotor areas with respect to using chopsticks. Neuroreport 13:2155–2159.

Jasper H, Penfield W (1949): Electrocorticograms in man: Effect of voluntary movement upon the electrical activity of the precentral gyrus. Arch Psychiatry 183:163–173.

Jeong J, Gore JC, Peterson BS (2001): Mutual information analysis of the EEG in patients with Alzheimer's disease. Clin Neurophysiol 112:827–835.

Joliot M, Crivello F, Badier JM, Diallo B, Tzourio N, Mazoyer B (1998): Anatomical congruence of metabolic and electromagnetic activation signals during a self-paced motor task: a combined PET-MEG study. Neuroimage 7:337–351.

Jones RD, Donaldson IM, Parkin PJ (1989): Impairment and recovery of ipsilateral sensory-motor function following unilateral cerebral infarction. Brain 112(Part 1):113–132.

Jung TP, Makeig S, Humphries C, Lee TW, McKeown MJ, Iragui V, et al. (2000): Removing electroencephalographic artifacts by blind source separation. Psychophysiology 37:163–178.

Kilner JM, Baker SN, Salenius S, Jousmaki V, Hari R, Lemon RN (1999). Task-dependent modulation of 15-30 Hz coherence between rectified EMGs from human hand and forearm muscles. J Physiol 516 (Part 2):559–570.

Kornhuber HH, Deecke L (1965): Changes in the brain potential in voluntary movements and passive movements in man: readiness potential and reafferent potentials. Pflugers Arch Gesamte Physiol Menschen Tiere 284:1–17.

Kuypers HGJM (1981):Anatomy of the descending pathways. In: Brooks VB, editor. Handbook of Physiology, Vol. 2. Bethesda, MD: American Physiological Society. pp 597–666.

Lachaux JP, Lutz A, Rudrauf D, Cosmelli D, Le Van Quyen M, Martinerie J, et al. (2002): Estimating the time-course of coherence between single-trial brain signals: an introduction to wavelet coherence. Neurophysiol Clin 32:157–174.

Lang W, Cheyne D, Kristeva R, Beisteiner R, Lindinger G, Deecke L (1991): Three-dimensional localization of preceding voluntary movement. A study of electric and magnetic fields in a patient with infarction of the right supplementary motor area. Exp Brain Res 87:688–695.

Lee L, Harrison LM, Mechelli A (2003a): A report of the functional connectivity workshop, Dusseldorf, 2002. Neuroimage 19:457–465.

Lee PL, Wu YT, Chen LF, Chen YS, Cheng CM, Yeh TC, et al. (2003b): ICA-based spatiotemporal approach for single-trial analysis of postmovement MEG β-synchronization. Neuroimage 20:2010–2030.

Leocani L, Comi G (1999): EEG coherence in pathological conditions. J Clin Neurophysiol 16:548–555.

Leocani L, Toro C, Manganotti P, Zhuang P, Hallett M (1997): Event-related coherence and event-related desynchronization/synchronization in the 10 Hz and 20 Hz EEG during self-paced movements. Electroencephalogr Clin Neurophysiol 104:199–206.

Lewis PA, Miall RC (2003): Distinct systems for automatic and cognitively controlled time measurement: evidence from neuroimaging. Curr Opin Neurobiol 13:250–255.

Lins OG, Picton TW, Berg P, Scherg M (1993): Ocular artifacts in recording EEGs and event-related potentials. II: Source dipoles and source components. Brain Topogr 6:65–78.

Locatelli T, Cursi M, Liberati D, Franceschi M, Comi G (1998): EEG coherence in Alzheimer's disease. Electroencephalogr Clin Neurophysiol 106:229–237.

Lopes da Silva F (1991): Neural mechanisms underlying brain waves: from neural membranes to networks. Electroencephalogr Clin Neurophysiol 79:81–93.

Magnani G, Cursi M, Leocani L, Volonte MA, Comi G (2002): Acute effects of L-dopa on event-related desynchronization in Parkinson's disease. Neurol Sci 23:91–97.

Manganotti P, Gerloff C, Toro C, Katsuta H, Sadato N, Zhuang P, et al. (1998): Task-related coherence and task-related spectral power changes during sequential finger movements. Electroencephalogr Clin Neurophysiol 109:50–62.

Marshall RS, Perera GM, Lazar RM, Krakauer JW, Constantine RC, DeLaPaz RL (2000): Evolution of cortical activation during recovery from corticospinal tract infarction. Stroke 31:656–661.

Mima T, Hallett M (1999): Corticomuscular coherence: a review. J Clin Neurophysiol 16:501–511.

Mima T, Matsuoka T, Hallett M (2000a): Functional coupling of human right and left cortical motor areas demonstrated with partial coherence analysis. Neurosci Lett 287:93–96.

Mima T, Steger J, Schulman AE, Gerloff C, Hallett M (2000b): Electroencephalographic measurement of motor cortex control of muscle activity in humans. Clin Neurophysiol 111:326–337.

Nagamine T, Kajola M, Salmelin R, Shibasaki H, Hari R (1996): Movement-related slow cortical magnetic fields and changes of spontaneous MEG- and EEG-brain rhythms. Electroencephalogr Clin Neurophysiol 99:274–286.

Nunez PL, Srinivasan R, Westdorp AF, Wijesinghe RS, Tucker DM, Silberstein RB, et al. (1997): EEG coherency. I. Statistics, reference electrode, volume conduction, Laplacians, cortical imaging, and interpretation at multiple scales. Electroencephalogr Clin Neurophysiol 103:499–515.

Pfurtscheller G, Andrew C (1999): Event-related changes of band power and coherence: methodology and interpretation. J Clin Neurophysiol 1:512–519.

Pfurtscheller G, Aranibar A (1979): Evaluation of event-related desynchronization (ERD) preceding and following voluntary self-paced movement. Electroencephalogr Clin Neurophysiol 46:138–146.

Pfurtscheller G, Lopes da Silva FH (1999): Event-related EEG/MEG synchronization and desynchronization: basic principles. Clin Neurophysiol 110:1842–1857.

Pfurtscheller G, Stancak A Jr, Neuper C (1996): Post-movement β-synchronization. A correlate of an idling motor area? Electroencephalogr Clin Neurophysiol 98:281–293.

Pfurtscheller G, Zalaudek K, Neuper C (1998): Event-related β-synchronization after wrist, finger and thumb movement. Electroencephalogr Clin Neurophysiol 109:154–160.

Popivanov D, Dushanova J (1999): Non-linear EEG dynamic changes and their probable relation to voluntary movement organization. Neuroreport 10:1397–1401.

Rau C, Plewnia C, Hummel F, Gerloff C (2003): Event-related desynchronization and excitability of the ipsilateral motor cortex during simple self-paced finger movements. Clin Neurophysiol 114:1819–1826.

Rosenberg JR, Amjad AM, Breeze P, Brillinger DR, Halliday DM (1989): The Fourier approach to the identification of functional coupling between neuronal spike trains. Prog Biophys Mol Biol 53:1–31.

Salenius S, Portin K, Kajola M, Salmelin R, Hari R (1997): Cortical control of human motoneuron firing during isometric contraction. J Neurophysiol 77:3401–3405.

Salmelin R, Hari R (1994): Characterization of spontaneous MEG rhythms in healthy adults. Electroencephalogr Clin Neurophysiol 91:237–248.

Schnitzler A, Gross J, Timmermann L (2000): Synchronised oscillations of the human sensorimotor cortex. Acta Neurobiol Exp (Wars) 60:271–287.

Shannon CE. A mathematical theory of communication. Bell Syst Tech J1948; 27:379-426.Also at 28:623-656.

Stippich C, Freitag P, Kassubek J, Soros P, Kamada K, Kober H, et al. (1998): Motor, somatosensory and auditory cortex localization by fMRI and MEG. Neuroreport 9:1953–1957.

Timmermann L, Gross J, Dirks M, Volkmann J, Freund HJ, Schnitzler A (2003): The cerebral oscillatory network of parkinsonian resting tremor. Brain 126:199–212.

Tononi G, Sporns O, Edelman GM (1994): A measure for brain complexity: relating functional segregation and integration in the nervous system. Proc Natl Acad Sci USA 91:5033–5037.

Vorobyov S, Cichocki A (2002): Blind noise reduction for multisensory signals using ICA and subspace filtering, with application to EEG analysis. Biol Cybern 86:293–303.

Ward NS, Cohen LG (2004): Mechanisms underlying recovery of motor function after stroke. Arch Neurol 61:1844–1848.

Whitton JL, Lue F, Moldofsky H (1978): A spectral method for removing eye movement artifacts from the EEG. Electroencephalogr Clin Neurophysiol 44:735–741.

Woestenburg JC, Verbaten MN, Slangen JL (1983): The removal of the eye-movement artifact from the EEG by regression analysis in the frequency domain. Biol Psychol 16:127–147.

Wu YZ, Niddam DM, Chen CC, Liao KK, Cheng CM, Chen LF, Lee PL, Chen SS, Yeh TZ, Hsieh JC (2006): Effects of cognitive demands on postmovement motor cortical deactivation. Neuroreport 17:371–375.

Zaveri HP, Williams WJ, Sackellares JC, Beydoun A, Duckrow RB, Spencer SS (1999): Measuring the coherence of intracranial electroencephalograms. Clin Neurophysiol 110:1717–1725.

♦ Human Brain Mapping 29:265–280 (2008) ♦

Mutual-Information-Based Approach for Neural Connectivity During Self-Paced Finger Lifting Task

Chun-Chuan Chen,[1,4] Jen-Chuen Hsieh,[1,2,3,4] Yu-Zu Wu,[1,3,5] Po-Lei Lee,[1,6] Shyan-Shiou Chen,[1] David M. Niddam,[1,4] Tzu-Chen Yeh,[1,2,7] and Yu-Te Wu[1,2,8]*

[1]*Laboratory of Integrated Brain Research, Department of Medical Research and Education, Taipei Veterans General Hospital, Taipei, Taiwan*
[2]*Institute of Brain Science, National Yang-Ming University, Taipei, Taiwan*
[3]*Institute of Neuroscience, School of Life Science, National Yang-Ming University, Taipei, Taiwan*
[4]*Center for Neuroscience, National Yang-Ming University, Taipei, Taiwan*
[5]*Department of Physical Therapy, Tzu-Chi College of Technology, Hualien, Taiwan*
[6]*Department of Electrical Engineering, Nation Central University, Jhongli, Taiwan*
[7]*Faculty of Medicine, School of Medicine, National Yang-Ming University, Taipei, Taiwan*
[8]*Department of Biomedical Imaging and Radiological Sciences, National Yang-Ming University, Taipei, Taiwan*

Abstract: Frequency-dependent modulation between neuronal assemblies may provide insightful mechanisms of functional organization in the context of neural connectivity. We present a conjoined time-frequency cross mutual information (TFCMI) method to explore the subtle brain neural connectivity by magnetoencephalography (MEG) during a self-paced finger lifting task. Surface electromyogram (sEMG) was obtained from the extensor digitorum communis. Both within-modality (MEG-MEG) and between-modality studies (sEMG-MEG) were conducted. The TFCMI method measures both the linear and nonlinear dependencies of the temporal dynamics of signal power within a pre-specified frequency band. Each single trial of MEG across channels and sEMG signals was transformed into time-frequency domain with use of the Morlet wavelet to obtain better temporal spectral (power) information. As compared to coherence approach (linear dependency only) in broadband analysis, the TFCMI method demonstrated advantages in encompassing detection for the mesial frontocentral cortex and bilateral primary sensorimotor areas, clear demarcation of event- and non-event-related regions, and robustness for sEMG - MEG between-modality study, i.e., corticomuscular communication. We conclude that this novel TFCMI method promises a possibility to better unravel the intricate functional organizations of brain in the context of oscillation-coded communication. *Hum Brain Mapp 29:265–280, 2008.* ©2007 Wiley-Liss, Inc.

Key words: time-frequency cross mutual information; TFCMI; functional connectivity; magnetoencephalography; surface electromyogram; coherence; corticomuscular communication

Contract grant sponsors: Taipei Veterans General Hospital (V96 ERI-005), National Science Council. (96-2752-B-075-001-PAE, 96-2752-B-010-006-PAE, 96-2752-B-010-007-PAE).

*Correspondence to: Yu-Te Wu, Associate Professor, Department of Biomedical Imaging and Radiological Sciences, National Yang-Ming University, No. 155, Li-Nong Street, Section 2, Pei-Tou, Taipei 112, Taiwan, Republic of China. E-mail: ytwu@ym.edu.tw

Received for publication 7 September 2006; Revised 9 January 2007; Accepted 27 January 2007
DOI: 10.1002/hbm.20386
Published online 29 March 2007 in Wiley InterScience (www.interscience.wiley.com).

INTRODUCTION

Several populations of human cortical neurons exhibit intrinsic properties of oscillation (~10 and ~20 Hz) in a resting state, predominantly in the vicinity of the primary sensorimotor and visual and auditory cortices, as recorded non-invasively using electroencephalography (EEG) or magnetoencephalography (MEG) [Jasper and Penfield, 1949; Salmelin and Hari, 1994]. The power of oscillation can be modulated dynamically with respect to event occurrence, either decreasing or increasing, a phenomenon termed event-related desynchronization (ERD) or synchronization (ERS) [Andrew and Pfurtscheller 1999]. In the context of movement, it has been suggested that the dynamics of ERD may reflect action planning and execution, while the dynamics of ERS may connote deactivation or inhibition of neural networks during the recovery phase [Lee et al., 2003b; Pfurtscheller et al., 1996]. According to principles of brain organization, the functional integration describes the global influence, which requires the interactions, such as functional connectivity, between large subsets in the nerve system to be coherent; these frequency-dependent regulations make the brain a complex system [Friston, 1997; Tononi et al., 1994]. Several analysis methods have been developed to characterize neuronal couplings, including ERD/ERS quantifying small scale interactions, the coherence method measuring functional connectivity, and the cross mutual information (CMI) method estimating the statistic dependency between spatially separated areas or large scale interactions [Andrew and Pfurtscheller, 1999; David et al., 2004; Grosse et al., 2002].

Quantitative analysis of ERD and ERS around rolandic areas, typically segregated around 10 and 20 Hz, provides a means to understand the dynamics of neuronal populations and can be applied to address questions in physiology and pathophysiology of the human sensorimotor system [Aoki et al., 2001; Crone et al., 1998; Pfurtscheller et al., 1998]. For example, Magnani et al. [2002] evaluated mu ERD onset time in patients with idiopathic Parkinson's disease before and after L-dopa treatment [Magnani et al., 2002]. They concluded that dispersible L-dopa has acute positive effects to improve motor performance and advance the latency of cortical activation during motor programming. The basis of the ERD analysis employed, however, mainly rests on phenomenological description and does not provide insightful mechanisms in the context of functional connectivity.

The coherence method, an approach commonly used to study oscillatory activity, has been exploited to address functional coupling or interaction, information exchange, and temporal coordination between cortical regions [Gerloff et al., 1998; Leocani et al., 1997; Nagamine et al., 1996]. High coherence indicates potentially neuroanatomic or functional connections between cortical areas underlying the sensors, while decreased coherence may denote the disruption of functional couplings [Fein et al., 1988; Leocani and Comi, 1999]. For example, patients with Alzheimer's disease showed significant decrease of α-activity coherence in temporo-parieto-occipital areas [Locatelli et al., 1998]. Patients with severe cognitive impairments display further decreases in coherence. In addition, the coherence method has been adopted to elucidate the oscillatory communication at around 20 Hz between somatomotor cortices and muscles in surface electromyogram-magnetoencephalography (sEMG-MEG) studies [Salenius et al., 1997]. In sEMG-MEG coherence studies, it has been suggested that the transient synchronization of rhythmic activities between sensorimotor areas and muscles can be crucial for motor command [Kilner et al., 1999]. Timmermann et al. [2003] reported that abnormal synchronization at 4–6 Hz between the contralateral primary motor cortex and forearm muscles in Parkinsonian patients may contribute to resting tremors [Timmermann et al., 2003]. The investigation of functional connectivity promises the potential to assess functional derangement within or between modalities [Schnitzler et al., 2000].

The coherence method, however, can be problematic if the signals are contaminated by noise, or the oscillatory frequency band is not carefully defined [Andrew and Pfurtscheller, 1999; Nunez et al., 1997] despite the newly developed time-domain [Jung et al., 2000; Lins et al., 1993; Vorobyov and Cichocki, 2002] or frequency-domain approaches [Mima et al., 2000a; Whitton et al., 1978; Woestenburg et al., 1983]. Theoretically speaking, the coherence method mainly measures linear dependency and is insufficient for the study of complex and nonlinear brain dynamics [Lopes da Silva, 1991; Popivanov and Dushanova, 1999].

Mutual information (MI), which employs the entropy of high-order statistics to estimate uncertainty, is a statistical measure of both linear and nonlinear dependencies between two time sequences [Shannon, 1948]. The cross mutual information (CMI) method in a time-domain has been developed to quantify and assess the functional impairment of information transmission from one area to another in Alzheimer patients [Jeong et al., 2001]. David et al. [2004] used the neural mass model to evaluate the profiles of different dependency measurements in the analysis of functional connectivity [David et al., 2004]. They pointed out that the time-domain CMI method is not reliable enough in broadband analysis, especially when the coupling between the modeled cortical areas is weak. Moreover, the CMI method only analyzes overall signal changes in time domain. The subtle temporal scenario of power changes within a defined frequency band is unfortunately lost; yet this information can be critical for the understanding of pathophysiology of disease condition.

The present study seeks to develop a conjoined time-frequency analytical method for MEG-MEG and sEMG-MEG measurements based on mutual information [Shannon, 1948] for the investigation of functional connectivity. Each single trial of MEG across channels and sEMG signals was transformed into time-frequency domain using the Morlet wavelet to obtain better temporal spectral (power) information [Grossmann and Morlet, 1984]. Time-frequency maps

were averaged across trials and the resulting maps were subsequently averaged over specific frequency bands to yield temporal profiles of power with improved signal-to-noise ratio (SNR). The averages of time series of power were used to compute the CMI across channels. Since MI is computed-based on any two temporal power sequences within a task-specific frequency band, the proposed method can be termed time-frequency cross mutual information (TFCMI) method. This TFCMI method is then applied to within (MEG-MEG) and between (sEMG-MEG) modalities in a self-paced finger lifting task and the results are discussed based on the simulation and the experimental data.

MATERIALS AND METHODS

Subjects and Task

Eight healthy, right-handed subjects (24–32 years of age, gender balanced) were recruited for this study. All subjects gave written informed consent for the experiment with a protocol approved by the institutional review board. They sat comfortably in a magnetically shielded room with forearms relaxed. Subjects were asked to lift their right index fingers once every 8 s (35–40° extension angle) in a self-pacing manner. The protocol in this study is the standard procedure for the Bereitschafts-potential (BP; in EEG) or readiness field (RF; in MEG), as first reported by Kornhuber and Deecke [1965]. Subjects' left hands rested on a pillow in order to avoid contamination of movement-related vibrations in the MEG measurements [Hari and Imada, 1999]. Movement onset was registered using an optical pad (4-D Neuroimaging®, Helsinki, Finland). A trigger pulse was generated at the beginning of each movement taking the interdiction of the laser light from the optical pad as the index of movement onset (zero time). To prevent blinking, subjects were requested to keep their eyes fixed on a cross mark on the center of a back-projection screen 1 m in front of them.

Data Acquisition and Preprocessing

MEG signals were continuously measured at a 1,000-Hz sampling rate during task performance using a whole-head, 204 planar gradiometers (Vectorview®, Neuromag, Helsinki, Finland). This planar type of gradiometer has the advantage of sensitivity of superficial sources, and is particularly suitable for the sensor level analyzing. The sEMG was simultaneously recorded at a 1,000-Hz sampling rate from the extensor digitorum communis to verify movement. The total number of finger movements was about 100 for all subjects. Some of the data had been published to address the issue about cognitive demands on motor tasks [Wu et al., 2006]. All the sEMG data were rectified before subsequent calculation of TFCMI and coherence analysis. Bipolar horizontal and vertical electro-oculograms (EOG) were obtained using electrodes placed at the bilateral outer canthi and the left eye respectively. At the beginning of each measurement, the positions of three anatomical landmarks (bilateral pre-auricular points and nasion) were measured using a 3D magnetic digitizer (Isotrak 3s1002, Polhemus Navigation Science, Colchester, VT) to define a head coordinate system. Four head position indicators (HPIs) were subsequently defined and tracked by the MEG system to ensure no head movement during each measurement (maximal translation <1.5 cm). Individual MRI (T1-weighted, 3D gradient-echo pulse sequence, TR/TE/TI:88.1/4.12/650 (all ms), 128 × 128 × 128 matrix, FOV = 250 mm) were obtained with a 3.0-T Bruker MedSpec S300 system (Bruker, Kalsrube, Germany).

MEG measurements of 204 channels were recorded continuously and termed as a Total Set. Among them, EOG-free measurements (EOG <600 uV) were extracted as an Accepted Set (approximately at least 100 trials should be collected on-line). All MEG measurements in the Total Set were used to evaluate the robustness of the TFCMI method against physiological noise.

Computation of Time-Frequency Maps Using Morlet Wavelet Transformation

Each trial of MEG and sEMG raw data with 4,000 samples (from −2 to +2 s relative to the movement onset time) was processed using the Morlet wavelet transformation to generate the time-frequency representation of signals (Fig. 1a,b). The time window was defined during this period based on the prominent spectral changes of movement-related activities (Fig. 1d), which is in line with previous study of a self-paced finger flexion task [Feige et al., 1996], where the 20-Hz spectral power depress started at about −2.5 s and a power elevation in β frequency range started at about +0.5 s, with fading out at about +2 s. Let $x_{i,k}(t)$ denote the data from the kth trial of ith channel at time instant t, its Morlet wavelet transformation is given by:

$$W_{x_{i,k}}(t,f) = \int x_{i,k}(\lambda) \cdot \overline{\phi_{t,f}(t-\lambda)}\,d\lambda$$

where $W_{x_{i,k}}(t,f)$ represents the energy density in frequency f of the kth trial of the ith channel at time instant t; $\phi_{t,f}(\lambda) = A \cdot e^{i2\pi f(\lambda - t)} e^{\frac{-(\lambda-t)^2}{2\sigma^2}}$ are the Morlet wavelets; their time spread is defined by $\sigma = \frac{8}{2\pi f}$; $A = (\sigma\sqrt{2})^{-1/2}$ is the normalization factor and $\overline{\phi_{t,f}(\lambda)}$ are the complex conjugates of $\phi_{t,f}(\lambda)$.

Time-frequency maps encompassing the α (8–13 Hz) and β (16–25 Hz) activities were created separately by averaging across trials within each subject (Fig. 1c). (Note that only two channels with β activity are shown on the map). They were displayed topographically with colors representing power (see Fig. 2). In the sEMG-MEG study of corticomuscular coupling, only the time-frequency map of the β activities underwent further analysis. Frequency components from 16 to 25 Hz were chosen, based on previous electromangentophysiological studies of weak and moderate tonic contractions [Baker et al., 1997; Conway

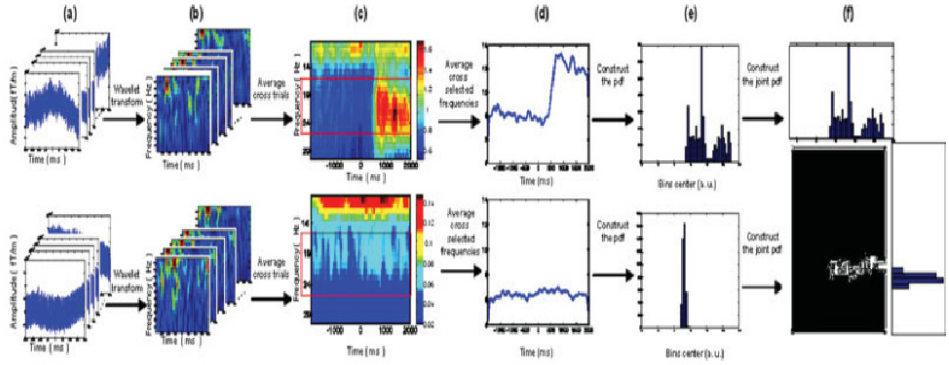

Figure 1.

Schematic diagram of TFCMI computation. Raw MEG measurements from any two planar gradiometers of each trial (a) were processed using the Morlet wavelet transformation to obtain time-frequency maps (b). Colors indicate power amplitude in an arbitrary unit (a.u.). The mean time-frequency map (c) for each channel was created by averaging the individual time-frequency maps across trials. The red rectangle represents the prespecified bandwidth in β band (16–25 Hz). The temporal curves of power changes for each channel (d) were created by averaging over the β band (or α band) in the mean time-frequency map and were used to estimate the probability density function (e) and the joint probability density function (f). [Color figure can be viewed in the online issue, which is available at www.interscience.wiley.com.]

et al., 1995; Halliday et al., 1998; Kilner et al., 1999; Mima and Hallett, 1999; Mima et al., 2000b; Salenius et al., 1997].

Detection of Neural Connectivity Using TFCMI

Power from two averaged time-frequency maps was subsequently separately averaged over selected frequency bands to produce two temporal curves (Fig. 1d). Each curve represents 4,000 samples of a random variable, F_i, at the ith MEG channel. These samples of F_i were used to construct the probability density function (pdf), $p(F_{i,b})$, (Fig. 1e) for the computation of entropy, $H(F_i)$:

$$H(F_i) = -\sum_{b=1}^{64} p(F_{i,b}) \ln p(F_{i,b})$$

where the $b = 1, 2, \ldots, 64$ was the index of sampling bins for the construction of approximated pdf. It is noteworthy that the estimation of pdf and joint pdf from the data histogram is crucial for the computation of mutual information. In order to estimate pdf and joint pdf stably, that is, neither underestimation nor overestimation [Fraser and Swinney, 1986], 64 bins were adopted for 4,000 samples as suggested by Jeong et al. [Jeong et al., 2001].

Entropy is the average amount of information reflecting the measure of uncertainty. Similarly, the joint probability density function (jpdf) between the ith and jth MEG channels can be computed as $p(F_{i,b}, F_{j,b})$ for the estimation of joint entropy, $H(F_i, F_j)$ (Fig. 1f).

$$H(F_i, F_j) = -\sum_{b=1}^{64} p(F_{i,b}, F_{j,b}) \ln p(F_{i,b}, F_{j,b})$$

Then the TFCMI between two random variables F_i and F_j was calculated as follows:

$$\mathrm{TFCMI}(F_i, F_j) = H(F_i) + H(F_j) - H(F_i, F_j) = -\sum_{b=1}^{64} p(F_{i,b}, F_{j,b}) \ln \frac{p(F_{i,b}, F_{j,b})}{p(F_{i,b}) p(F_{j,b})}$$

The TFCMI value is used as an index of functional connectivity. Figure 1 shows the schematic diagram for TFCMI computation.

Determination of the COI

The channel located in the vicinity of the sensorimotor area exhibiting the most prominent β ERD was chosen as the channel of interest (COI) [Pfurtscheller and da Silva, 1999 for the details of β ERD computation; Andrew and Pfurtscheller, 1999; Pfurtscheller and Aranibar, 1979; Pfurtscheller and da Silva, 1999]. TFCMI and coherence were computed between the COI and any other channels. In addition, the COI was replaced by an arbitrary channel (A-COI) unrelated to the motor task to investigate the specificity for regional detection. For the between-modality study, that is, the sEMG-MEG study, the sEMG was used as the COI.

Statistical Threshold

The 95% confidence limit of t-distribution was used as a threshold to determine the regions of significant likelihood associated with the COI in TFCMI and coherence analysis,

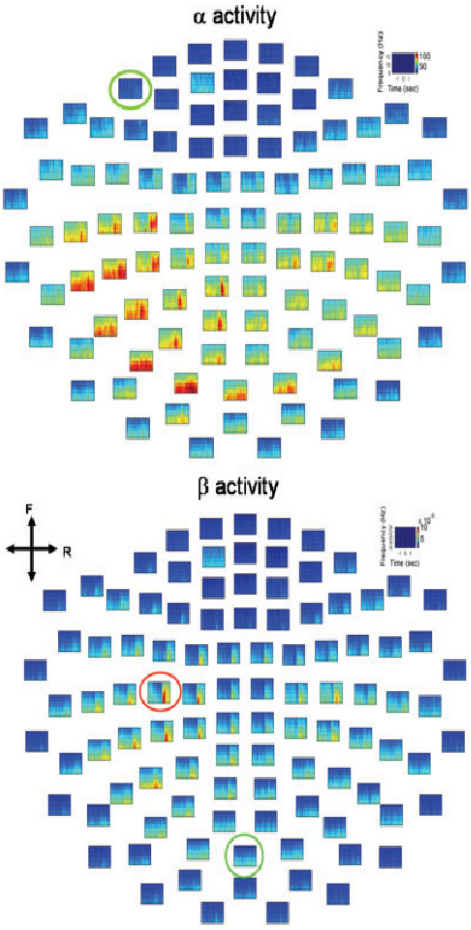

Figure 2.

Mean time-frequency maps of α and β oscillatory activities. The red circle indicates the channel-of-interest (COI) with the strongest β oscillatory activity (lower panel); the chosen COI was also used for analysis of α oscillation. Green circles denote arbitrary COIs (A-COIs), irrelevant to the motor task. Both COI and A-COIs were employed as reference channels in the subsequent analyses (see Figs. 4, 5). Color indicates power amplitude. The maps are shown in top view. F, front; R, right. [Color figure can be viewed in the online issue, which is available at www.interscience.wiley.com.]

respectively. The confidence levels for TFCMI and coherence were computed in different ways fundamentally. For TFCMI method, value of TFCMI between the COI and any other channels was pre-normalized with respect to the maximal value of TFCMI obtained at the COI. Normalized values were between 0 and 1 and were used to construct the t-distribution. The degree of freedom is 1 since we have averaged across trials before TFCMI calculating. In other words, the TFCMI was computed from only one averaged power spectrum. The 95% confidence level was then set at mean +6.314 standard deviation (SD; df = 1, one tailed) to eliminate the bias due to large variation. The conventional coherence method (or magnitude squared coherence) [Zaveri et al., 1999] was also applied to the same data set based on the same COI by using an fast Fourier transform window of 512 points with 256 points overlapping, trial by trial. This allows no overlapping of each epoch signals and makes the spectral resolution (Δf) of this coherence estimate to be 0.25 Hz, the inverse of the epoch length, 1/4 sec ^{1} [Zaveri et al., 1999]. Before averaging across trials, an arc-hyperbolic tangent transform are applied to the coherence values, as described by Rosenberg et al. [1989], so that the coherence values have a normal distribution [Rosenberg et al., 1989]. The significant threshold of 95% confidence limit was then given by mean +1.65SD (df = 100, one tailed) [Halliday et al., 1995]. For the purpose of presentation, coherence values between 0 and 1 were rescaled to the maximal coherence value. Only values of TFCMI and coherence above the significant thresholds were cataloged as significant interactions and were represented topographically as maps with colors indicating the relative coupling level above significance.

Visualization of TFCMI maps

To better visualize the resolved coupled areas of each subject, the TFCMI maps were superimposed on top of each individual cortical surface. The procedure was described in following steps. First, the positions of four HPIs were used to calculate the relative rotation and translation between the sensor coordinate system and the head coordinate system. This allowed the sensor array positions to be transformed into the head coordinate system. Second, three anatomical landmarks (bilateral pre-auricular points and nasion) on individual MRI were identified and aligned with head coordinate. The sensor array positions were subsequently transformed into the MRI coordinate system. Third, the cortex was segmented from each individual MRI and reconstructed using ASA® (A.N.T. software BV, The Netherlands). Fourth, a sphere was fitted to the transformed sensor array positions using the least squares technique and rescaled to make the sensors abut to the reconstructed cortical surface. Finally, the TFCMI results in the form of contour maps were projected onto the transformed sensor arrays overlaid on top of cortical surface.

It should be noted that the correspondence between the position of the MEG gradiometers and the underlying sources cannot be precisely determined without a proper source analysis. Nevertheless, the MEG gradiometer is designed to detect the largest signal right above the current source and suppressing ambient noise, suggesting that the gradiometer with the maximum current flux may ascribe to currents mainly from the directly beneath cortical area and partly from several surrounding cortical regions. In this article, the word "regions," referring to

"regions directly beneath MEG sensors and possibly surrounding regions," is used loosely henceforth for the purpose of simplicity. Though the minor contribution from surrounding regions was not taken into account in this study, it will be exploited on the source space in future work.

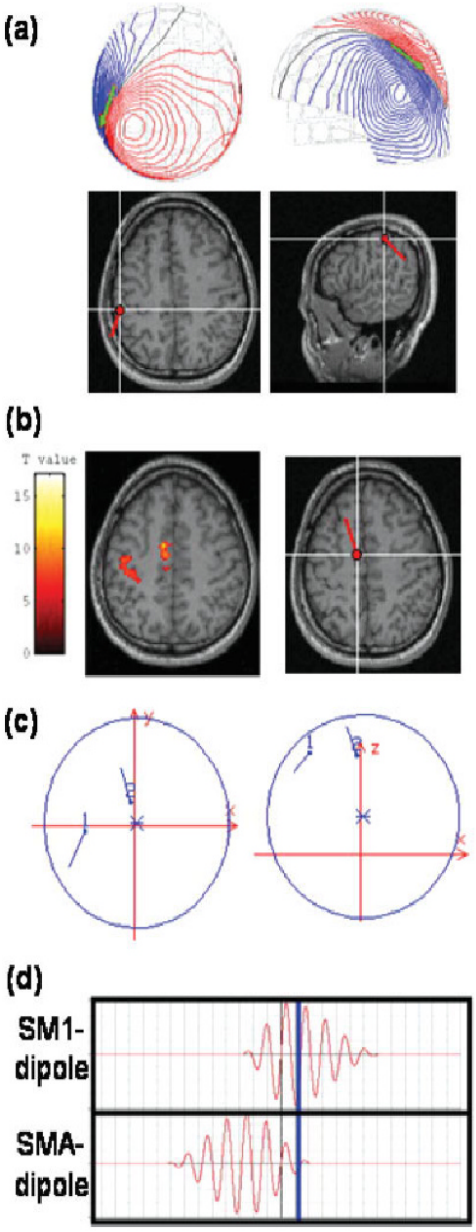

Simulation of Coupling Between Two Regions

Two simulations (Simulation, Neuromag® system software) were conducted to establish the face validation of the TFCMI method in terms of the detection efficacy. Simulation 1 examined the ability of TFCMI to reject false coupling caused by noise when there were no actual coupled sources. Simulation 2 attempted to clarify the detection efficacy of TFCMI with regards to low SNR under the circumstance that the neuromagnetic signals received by planar MEG from the bilateral SMAs can be drastically attenuated due to anatomical architecture [Joliot et al., 1998; Lang et al., 1991].

In Simulation 1, one oscillatory dipole (23 Hz) was placed in the left SM1 (SM1-dipole) of a chosen subject to synthesize magnetic fields on the sensor array. Position and moment of the SM1-dipole were taken from the equivalent current dipole (ECD) fit [Hamalainen et al., 1993] to the movement evoked field I (MEFI) of the specific subject (Fig. 3a). The time point of the fit was 14 ms post movement. In Simulation 2, an additional dipole (23 Hz) (SMA-dipole) was placed at a mesial region in the vicinity of SMA and pointed anteriorly based on the literature [Erdler et al., 2000; Lang et al., 1991]. The anatomical seeding of the SMA-dipole was adopted from the same subject's results in a parallel functional MRI (fMRI) experiment using similar task (repetitive index finger movement; T2*-weighted gradient-echo echo planar imaging sequence, TR/TE/flip angle = 2000/50 ms/90°, 64 × 64 × 20 matrix, FOV = 192 mm) (Fig. 3b). The distance between the SM1- and SMA-dipole was 55.07 mm (Fig. 3c). The oscillating source of the SMA-dipole preceded that of the SM1-dipole by 600 msec (Fig. 3d) [Erdler et al., 2000; Lang et al., 1991]. It is noteworthy that this design aims to emulate the spa-

Figure 3.

SM1- and SMA-dipole allocation in simulation studies. (a) SM1-dipole position and moment. The SM1-dipole placement in the left SM1 was based on the equivalent current dipole (ECD) fit to movement evoked field I. Upper panel displays the isocontour maps of the recorded neuromagnetic signals and the dipole (in green). The SM1-dipole was rendered onto the subject's own MRIs in axial view (lower panel; subject's right hemisphere to the right of the image). Anatomically, this SM1-dipole was located slightly posterior to the contralateral central sulcus. (b) SMA-dipole position and moment. The SMA-dipole was seeded in the left SMA (right panel) close to the midline with coordinates adopted from a parallel fMRI experiment conducted by the same subject (left panel). (c) Spatial relationship between SM1- and SMA-dipoles. Left, axial view; right, sagittal view. (d) Time courses of SM1-dipole (upper panel) and SMA-dipole (lower panel). In this simulation, the time course of the SMA-dipole preceded that of SM1-dipole by 600 m (Erdler et al., 2000; Lang et al., 1991). The blue line denotes the time-point for the ECD fit in the subsequent analysis (see Fig. 7a). [Color figure can be viewed in the online issue, which is available at www.interscience.wiley.com.]

tially distributed connections in low SNR circumstance, rather than to link this simulation to the underlying functional connections during movements. Accordingly, the strength of the SMA-dipole activity used in Simulation 2 was manipulated with a range of 0.5 to 1 times of SM1 dipole to modulate SNR [Chen et al., 1991; Erdler et al., 2000; Joliot et al., 1998]. Random noise was added onto each sensor measurement. Both TFCMI and coherence analysis were performed on the synthetic data. Moreover, conventional ECDs were fitted on the synthetic data to estimate the locations of neural generators, which were used as comparisons to TFCMI results.

RESULTS

Motor Task Performance

All subjects followed the instructions and performed the task well. The average number of trials in Accepted Sets among subjects was 98 epochs. Intervals between successive movements (intermovement interval, IMI) of Accepted Sets among subjects were between 7.968 and 15.162 seconds (mean, 13.124 s) and there was no feedback to cue subjects' movements. EOG ratio (the ratio of EOG sets to Total Sets) varied from 1.9% to 35.29%. Table I shows task performance and compositions of MEG test data for Accepted Set, IMI, EOG trials, Total Set and EOG ratio.

Neural Correlates of Event-Related α and β Oscillatory Activities: Within Modality

The resultant spatial distributions of neural connectivity for α and β activities, respectively, were represented by maps with colors representing the values, that is, the strengths of neural connectivity of α and β activities (Fig. 4a). TFCMI maps, both show strong connectivity within the contralateral sensorimotor region. The strengths of connectivity above threshold (95% confidence limit) can be alternatively displayed using colored lines, linking significant regions and the COI (Fig. 4b). Under the assumption that the gradiometer MEG sensors represent the major cortical oscillatory activity of underlying cortical tissues, contour maps projected on the reconstructed cortical surface reveal the regions coupled with the COI, including the mesial frontocentral cortex (termed the supplementary motor area, SMA, due to the anatomical correspondence; see simulation and discussion), bilateral primary sensorimotor areas (SM1), and contralateral premotor area (PM) (Fig. 4c). Table II lists neural correlates revealed by TFCMI and coherence methods. In MEG-MEG studies, TFCMI results for all subjects ($n = 8$) show encompassing of bilateral SM1s, SMA, and contralateral PM in both α and β activities. The coherence results for β activity show encompassing of bilateral SM1s ($n = 2$), SMA ($n = 3$), and contralateral PM ($n = 6$) in some subjects. For α activity, contralateral SM1 was engaged in all subjects ($n = 8$). Two of the subjects had additional SMA encompassing, and four showed contralateral PM encompassing.

Impact of COI on TFCMI and Coherence Analysis

Figure 5 shows the COI-specific results obtained from TFCMI method and coherence method. The TFCMI method resolved more neural connections than coherence method, such as ipsilateral SM1, when task-related COI was chosen (Fig. 5, upper panel; Table II). When the task-related COI was replaced by an A-COI irrelevant to the motor task, the A-COI TFCMI result demonstrated a highly focal encompassing centered at A-COI area (exclusively within), while the A-COI coherence result showed a rather dispersed neural connection with A-COI, incongruent with the known anatomy (Fig. 5, lower panel).

Between- and Within-Modality Analysis: sEMG-MEG and MEG-MEG

Figure 6 gives analytical results for TFCMI and coherence around beta band (16–25 Hz) for between- and within-modality signals, (sEMG-MEG and MEG-MEG studies) for subject 8. Simultaneous recording of sEMG for both right and left hands precluded mirror movement in the left hand (Fig. 6a). Both TFCMI and coherence results exhibited remarkable corticomuscular coupling over con-

TABLE I. Motor task performance and MEG test data

Subject index	Accepted set	IMI (mean ± SD; ms)	EOG Set	Total set	EOG ratio (%)
1	105	15,162 ± 6,969	27	132	20.45
2	93	14,571 ± 3,612	38	131	29.01
3	104	14,476 ± 3,774	41	145	28.27
4	91	13,867 ± 3,891	16	107	14.95
5	88	13,760 ± 7,589	48	136	35.29
6	103	14,302 ± 7,237	2	105	1.90
7	100	7,968 ± 1,573	8	108	7.40
8	98	14,968 ± 3,807	3	101	2.97
Average	98		22	120	

IMI, inter-movement interval; SD, standard deviation; EOG, electro-oculogram.

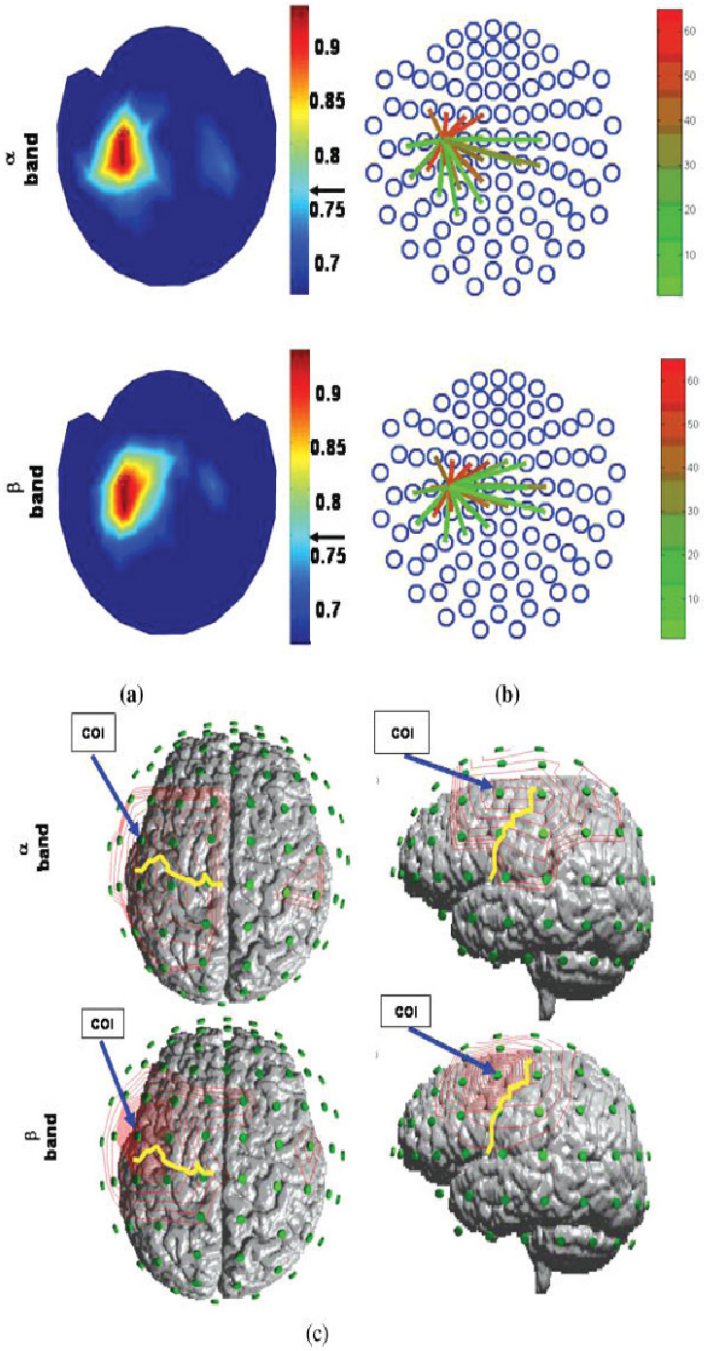

Figure 4.
Event-related α and β oscillatory activities networks (TFCMI). Individual data set. (a) Topographic maps of the spatial distribution of significant TFCMI values between COI and other MEG channels for α and β oscillatory activities. Color indicates the strength of connectivity. The arrows besides the color bar indicate the significant threshold. (b) An alternative display of the strengths of connectivity above the significant threshold. Regions of significant communications with the chosen COI were marked by links emanating from the COI. (c) TFCMI values in contour maps. The maps were projected onto the rescaled sensor array and the individual MRI to better the anatomical visualization of the coupled regions. Areas engaged included SMAs, bilateral SM1s, and contralateral PM. Yellow curves are the central sulcus; blue arrows indicate the location of COI. Left panel, view of top of the head; right panel, lateral view of the head from the left side. [Color figure can be viewed in the online issue, which is available at www.interscience.wiley.com.]

tralateral SM1 for all subjects (n = 8; Table II). The sEMG-MEG maps resembled the MEG-MEG maps, but there were subtle differences (Fig. 6b,c). The coupling between ipsilateral SM1 and sEMG was consistently resolved by the TFCMI method. Such coupling could not be detected by the coherence approach (Table II).

TABLE II. Neural correlates reflected in TFCMI and coherence methods

		MEG-MEG study				sEMG-MEG study			
		cSM1	iSM1	SMA	PM	cSM1	iSM1	SMA	PM
TFCMI	α	8/8[a]	8/8	8/8	8/8				
	β	8/8	8/8	8/8	8/8	8/8	8/8	7/8	8/8
Coherence	α	8/8		2/8	4/8				
	β	8/8	2/8	3/8	6/8	8/8		2/8	4/8

[a] The results are given in a ratio of detection, which indicates the number of subjects against all eight subjects.
cSM1, contralateral primary sensorimotor area; iSM1, ipsilateral primary sensorimotor area; SMA, supplementary motor area; PM, premotor area; contralateral.

Simulation results

Figure 7 shows the simulation result when the SMA-dipole strength is equal to that of the SM1-dipole. The simulated output on SM1 sensor which exhibits the strongest power is shown in Figure 7a. Conventional ECDs, serving as a comparison to TFCMI, were fitted on the synthetic data to estimate the locations of neural generators. The time-point for the ECD fit was chosen at maximal oscillatory amplitude (Fig. 7a; blue line) from which the corresponding simulated topographic pattern is displayed in Figure 7b. Spatial congruence of the simulated SM1-dipole (red) and the estimated SM1-dipole (blue) is displayed in Figure 7c. In Figure 7d, isocontour maps of the synthetic signals at the time point of max SMA-dipole strength are shown in the right column. The synthetic signals from the channel over left SMA are shown in left upper panel, and the left middle and lower panels are the source activity from SM1-dipole and SMA-dipole, respectively. The goodness-of-fit (Gof) for the estimated left-SM1 dipole was 97.2% for Simulation 1 (Table III). In Simulation 2, when both SMA dipole and SM1 dipole have the same strength, the Gof for SM1-dipole and for SMA-dipole were 96.2% and 42.3%, respectively. When the source strength of SMA dipole was half of SM1 dipole, the Gof of SM1 and SMA dipoles decreased to 88.6% and 40%, respectively (Table IV).

Both TFCMI and coherence analysis were performed on the synthetic data (see Fig. 8). In simulation 1 (SM1-dipole only), both TFCMI and coherence maps showed a focal encompassing of SM1, that is, exclusive connectivity to itself only (Fig. 8; upper panel). In simulation 2 (SM1-dipole and SMA-dipole), the time courses of the two dipoles were coherent and had a significant transformed coherence value of 0.957 after averaging 100 simulation trials in source space since they are with similar temporal profile (Fig. 3d) and are stationary across trials. However, after forward modeling, only TFCMI resolved more spatially distributed connections in sensor space, anatomically encompassing the SM1 and SMA, respectively, where the two dipoles were seated whereas the coherence method cannot discern the coupling (coherence = 0.0023) and solely showed connectivity within SM1 (Fig. 8; lower panel).

In addition, we have computed the SNR (=10 log(signal power/noise power)) of the experimental data measured from the sensor above left SM1 for the comparison with the SNR in simulation. The segment of averaged data from −4 to −3.5 s was considered as the noise and that from −2

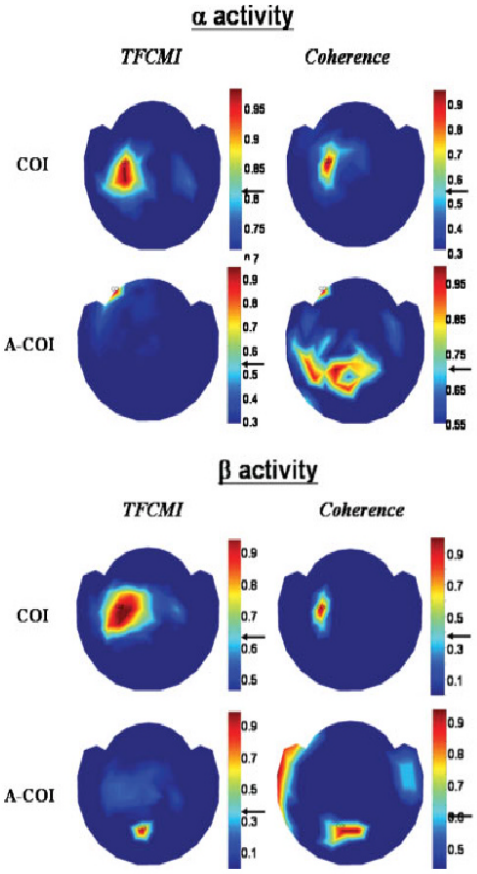

Figure 5.
Influence of reference chosen on TFCMI and coherence analysis with respect to α and β activities. When the task-related COI was properly chosen (upper panel), TFCMI results consistently showed more neural connections involving bilateral sensorimotor areas and the SMA for both α and β activities than coherence analysis. When the A-COIs were chosen as reference (lower panel), the A-COI TFCMI result demonstrated a highly focal encompassing centered at A-COI area (connectivity exclusively to itself), while the A-COI coherence result showed rather dispersed neural connections with A-COI, incongruent with the known anatomy. [Color figure can be viewed in the online issue, which is available at www.interscience.wiley.com.]

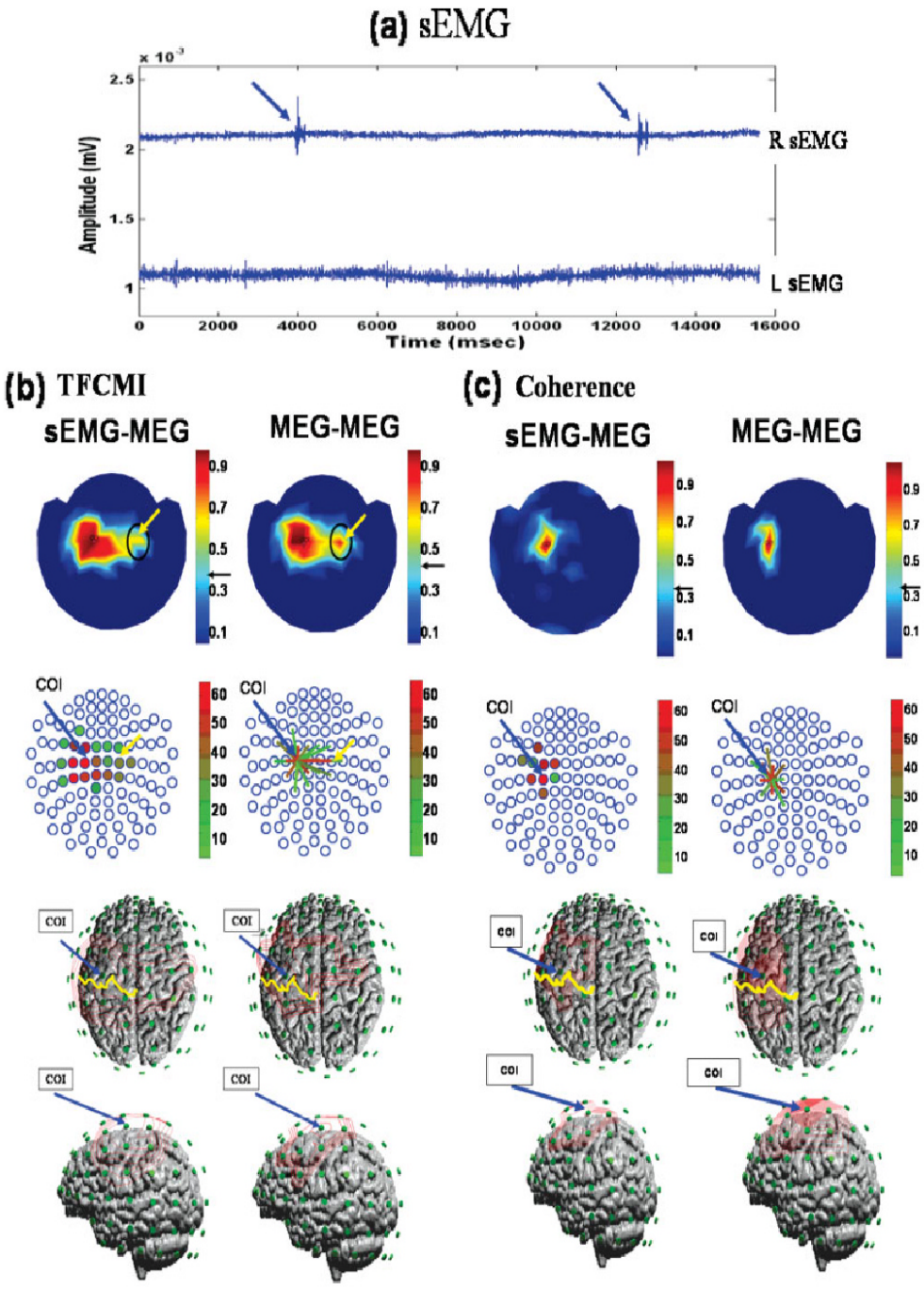
(a) sEMG
x 10^-3
Amplitude (mV)
R sEMG
L sEMG
Time (msec)
(b) TFCMI
sEMG-MEG
MEG-MEG
(c) Coherence
sEMG-MEG
MEG-MEG
COI

Figure 6.

to +2 s was the signal of activity. The averaged SNR in averaged data from 8 subjects was 26.57 + 2.9 dB. In Simulation 2, the minimum SNR for TFCMI method to detect the connection between SM1 and SMA (Table IV) is 21.8 dB, where the simulated signal was a composition generated from hypothetical SM1- and SMA-dipoles with the same dipole strength. In summary, our simulations indicate that the TFCMI method has superior detection specificity compared to the coherence method in low SNR situation.

DISCUSSION

Detection Specificity in Low SNR Data: Computational Simulation

A question central to the discussion of TFCMI approach in the current study is whether TFCMI could detect and resolve spatially distributed connections in low SNR circumstance. In this study, two simulations were conducted to provide the face validation of the TFCMI method in this regard. As a result, the Simulation 1 (SM1 dipole only) shows a focal encompassing of SM1, that is, exclusive connectivity to itself only (Fig. 8; upper panel) and the Simulation 2 demonstrates that TFCMI can decipher spatially distributed connections in low SNR circumstance. It is noteworthy that, though the simulation results show that TFCMI method can resolve the spatially distributed connections in low SNR circumstance, we have not presented an exhaustive simulation to emulate the underlying functional connections during movements. Since the TFCMI method is a pair-wise analysis and the TFCMI results from experimental data may be influenced by some distant but coupled sources fed into the COI and other channels, the interpretation of the TFCMI results should be restricted. Further validation is needed for the TFCMI method to process and represent on the source level instead of the sensor level. Nevertheless, the simulation results demonstrate that TFCMI was capable of discerning noise and showing the neural connectivity between distinct areas, in this case, between SM1 and SMA, with low SNR whereas both the ECD fit and the coherence method were not able to detect (Figs. 7, 8; Table IV).

Robustness of TFCMI Method

TFCMI analysis is resistant to reference selection and efficient in deciphering task-related connections from the irrelevant ones. Proper selection of COI is critical for the study of functional coupling using the coherence method [Gerloff et al., 1998]. Such a prerequisite is also seen in Figure 5 when A-COI was chosen as reference, despite which the coherence method is robust when the reference electrode is correct and the interaction is stationary across trials [David et al., 2004]. On the contrary, the A-COI TFCMI result demonstrated a highly focal encompassing centering at the A-COI area (exclusive connectivity to itself) which was validated by Simulation 1 (Fig. 8; upper panel) where the unconnected-solitary source (chosen as COI) showed no factitious coupling. In addition, when sEMG was used as COI in the between-modality study, the TFCMI showed neurophysiologically and neuoranatomically sEMG-MEG topographies (Fig. 6b, Table II). Moreover, the TFCMI method in broadband analysis performs reliably compared with the conventional mutual information method whose sensitivity is less reliable in broadband and weak coupling signals [David et al., 2004]. Collectively, the data imply that TFCMI can better resolve task-related connections.

Resolving Power Under Nonlinear Interactions

It is well known that the planning and execution of voluntary movement relies upon the integration of premotor and primary motor areas operating in conjunction with sensory and association areas, including SMA and cerebellum. The functional relevance between left and right SM1 in MEG-MEG event-related experiments as disclosed by the TFCMI is congruent with previous imaging studies showing bihemispheric engagement for motoric movement (Table II). [Gerloff et al., 1998; Hsieh et al., 2002; Joliot et al., 1998; Stippich et al., 1998]. The TFCMI also shows consistent engagement of ipsilateral SM1 in the sEMG-MEG event-related experiment (Table II; Fig. 6b). The inconsistent interhemispheric interaction in existing studies using the coherence or partial coherence approach has lead to a debate on bilateral involvement of SM1 for unilateral finger movement control [Andres et al., 1999;

Figure 6.

Ipsilateral SM1 in between- and within-modality TFCMI studies. Individual data set. (a) Right (upper trace) and left (lower trace) hand sEMGs during right finger movement (blue arrows). The left sEMG precluded mirror movement of the left hand during the experiment. (b,c) Results of β activity from TFCMI and coherence, respectively, for between- (sEMG-MEG; left panel) and within-modality (MEG-MEG; right panel) studies. The sEMG-MEG maps (first row) exhibit prominent corticomuscular coupling at contralateral SM1 in both TFCMI and coherence analyses, and resemble MEG-MEG maps. Yellow arrows indicate ipsilateral SM1 encompassing by TFCMI. No such coupling was detected using the coherence method. Second row presents couplings in an alternative manner, with blue circles representing MEG sensor sites. Blue arrows anchor the COI for MEG-MEG analysis, which is also indicated in sEMG-MEG maps only. Coupling strengths are coded in different colors either in the form of solid dots in the sEMG-MEG maps or line links in the MEG-MEG maps. The third (view of the top of the head) and fourth (left lateral view of the head) rows display the isocontour maps for a better appreciation of neuroanatomical correspondence. Yellow curves are the central sulci. [Color figure can be viewed in the online issue, which is available at www.interscience.wiley.com.]

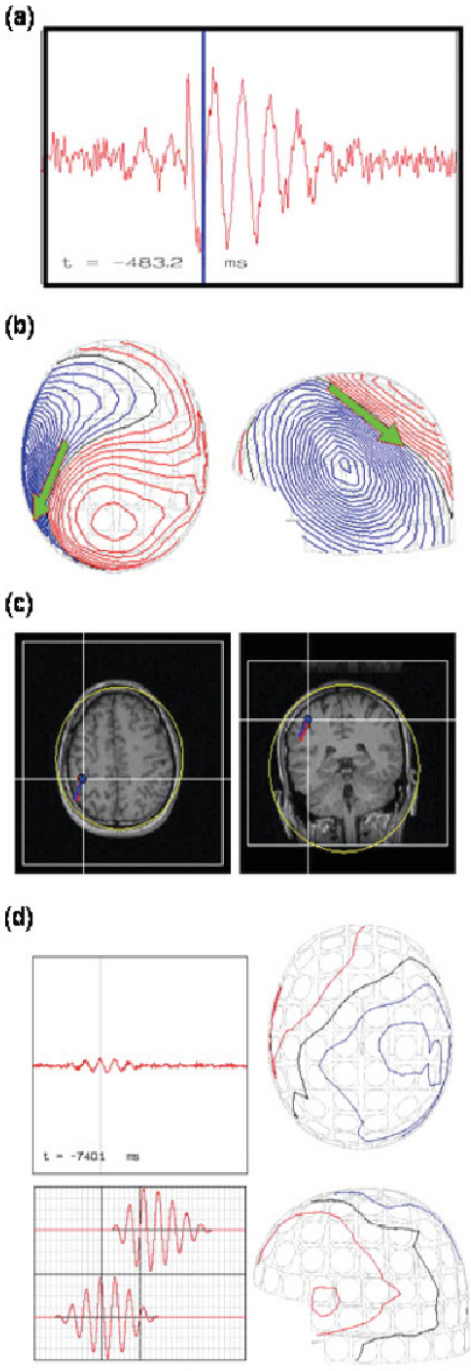

Andrew and Pfurtscheller, 1996, 1999; Gerloff et al., 1998; Manganotti et al., 1998; Mima et al., 2000a]. This inconsistency could also been seen in our coherence results (Table II). However, transcranial magnetic stimulation (TMS) studies have confirmed the role of ipsilateral SM1 in self-paced finger movement tasks [Chen et al., 1997; Rau et al., 2003]. Studies on patients with motor disorders have shown a significant activation of ipsilateral SM1/corticospinal tract as compensatory mechanisms [Caramia et al., 2000; Cuadrado et al., 1999; Jones et al., 1989; Marshall et al., 2000; Ward and Cohen, 2004]. Our TFCMI analytical results are consistent with the known anatomy since 10% of corticospinal fibers have ipsilateral projections [for a review, see Kuypers, 1981] and the ipsilateral influence is integrated with the prevailing contralateral one (also evinced by the preponderant contralateral expression of TFCMI values) for the overall control of movement [de Oliveira, 2002]. Accordingly, it is plausible that the coupling between contra- and ipsi-lateral SMI may be through a nonlinear or nonstationary interaction and could be better unraveled by TFCMI.

Fundamental Differences Between the TFCMI Method and Coherence Method

In this study, the functional connectivity during a self-paced brisk finger movement task was studied. Such a discrete movement paradigm may mandate more cognitive processing than automatic movement paradigm within sub-second inter-movement interval [Lewis and Miall, 2003]. Moreover, the latency of maximal post-movement β rebound exhibits trial-to-trial variability [Lee et al., 2003b]. These suggest that there is inherent nonstationarity in the neural processing. Under the assumption that neural processes are stationary across trials [Lachaux et al., 2002; Nunez et al., 1997], the coherence method measures the linear dependency between signals via normalized spectral

Figure 7.

Poor detection of SMA-dipole by simulation. (a) Synthetic signals from the channel over SM1 as produced by SM1- and SMA-dipoles. (b) Isocontour maps of the synthetic signals and the ECD result of SM1-dipole. The blue bar in (a) indicates snap time for the contour maps. (c) Spatial congruence of the simulated SM1-dipole and the estimated SM1-dipole. The estimated SM1-dipole (in blue, with a very high goodness-of-fit, about 96%) almost coincides with the simulated (in red). (d) Isocontour maps of the synthetic signals at the time point of max SMA-dipole strength (right column). The synthetic signals from the channel over left SMA are shown in left upper panel, and the left middle and lower panels are the source activity from SM1-dipole and SMA-dipole, respectively. The goodness-of-fit for the SMA-dipole was 42.3% (Table IV). The poor Gof for the SMA-dipole was in line with the consensus that the MEG dipole fit for SMA source can be ambiguous due to insufficient SNR. [Color figure can be viewed in the online issue, which is available at www.interscience.wiley.com.]

TABLE III. Simulated-dipole parameters and ECD results for source estimation: Simulation I

		Simulated-dipole parameters		ECD results; SNR = 21.8 dB			
Index		Location	Moment	Location	Moment	Distance[a] (mm)	Gof (%)
SM1-dipole	*x*	35.2	0.42	35.3	0.43		
	y	7.2	0.80	7.2	0.79	1.03	97.2[b]
	z	88.9	0.41	88.3	0.41		

[a] Between the simulated and the estimated location.
[b] 85% Gof.
ECD, equivalent current dipole; SNR, signal-to-noise ratio in source space; Gof, goodness of fit.

covariances, that is, second-order statistics. This second-order method works well for Gaussianly distributed signals but may not for the non-Gaussian ones, as shown in the upper panel of Fig. 1(e). The TFCMI method, on the contrary, utilizes the wavelet transform as the preprocessing procedure to bandpass the signals with better temporal resolution than Fourier transform such that the subtle temporal scenarios within pre-specitifc frequency bands can be properly reserved. Then, based on the joint probability of coincidence occurrence of oscillatory signal power with more accurate temporal resolution, TFCMI computation is not limited to the linearity of spectral modulation across trials. In fact, the use of pdf and joint pdf takes the advantage of high-order statistics to extract the nonlinear coupling that may not be correctly identified using the second-order techniques. Therefore, the combination of wavelet and mutual information substantiate a significant contribution for nonlinear analysis and is a salient feature of the TFCMI method. Such fundamental differences make the TFCMI method more adaptive than coherence method in analyzing complex dynamic data.

The Limitations of and Prospects for the TFCMI Method

Since the cortical oscillatory activity acquired from a MEG sensor cannot be fully attributed to the underlying cortical region, the interpretation of TFCMI results is limited to the sensor space in current study. Further validation, such as simultaneous recording of EEG and fMRI, may serve as a complementary to the TFCMI method. Alternatively, the recording signals from MEG sensors can be the inversely mapped into the source space by using a spatial filter as developed in the dynamic imaging of coherent sources (DICS) method [Gross et al., 2001, 2002, 2003; Ishii et al., 2002]. This will allow the calculation of TFCMI on the source space and subsequently analyze the functional coupling within the brain. Another drawback of the TFCMI method is the low temporal resolution (4 s), since the estimation of probability density function and joint probability density function was based on the histograms of signal amplitudes over a 4-s time window. Various lengths of time window will be used to assess the performance of TFCMI in the future work. Besides, the TFCMI method was not designed to unravel the propagation direction of the electrical activity among brain structures. Once the evident functional coupling on the sensor space was resolved using the TFCMI method, other approaches, such as the direct transfer function (DTF) method, phase synchronization, or the directional index can be employed for the quantification of coupling direction.

CONCLUSIONS

We present a novel method, TFCMI, for the exploration of the neural communication and interaction among distinct brain regions or regions of different neurophysiological modalities. When compared with the coherence

TABLE IV. Simulated-dipole parameters and ECD results for source estimation: Simulation 2

Simulated-dipole parameters				ECD results: SNR = 19.1 (dBSM1-dipole strength:SMA-dipole strength = 1:0.5)				ECD results: SNR = 21.8 (dBSM1-dipole strength:SMA-dipole strength = 1:1)			
Index		Location	Moment	Location	Moment	Distance[a] (mm)	Gof (%)	Location	Moment	Distance[a] (mm)	Gof (%)
SM1-dipole	*x*	35.2	0.42	36.8	0.2809			34.3	0.42	1.15	
	y	7.8	0.80	7.6	0.8827	4.87	88.6[a]	7.2	0.79		96.2[b]
	z	88.9	0.41	84.3	0.3796			89.3	0.42		
SMA-dipole	*x*	3.4	0.54					1.0	0.68	10.71	
	y	20.4	0.58				below 40	10.6	0.71		42.3
	z	87.9	0.60					91.5	0.14		

[a] Between the simulated and the estimated location.
[b] 85% Gof.
ECD, equivalent current dipole; SNR, signal-to-noise ratio in source space; Gof, goodness of fit.

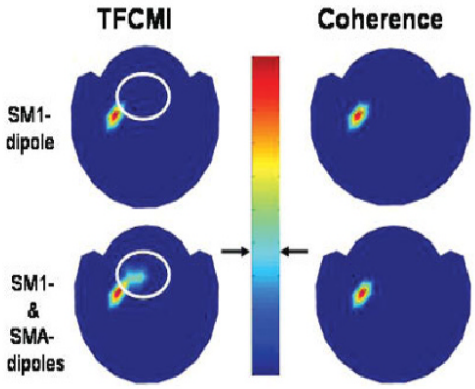

Figure 8.

Detection specificity of TFCMI in low SNR data. Both TFCMI and the coherence method yielded one unambiguous focus in the first simulation (only SM1 dipole, upper panel). In the second simulation (SM1-dipole and SMA-dipole), only the TFCMI resolved more spatially distributed connections in low SNR data, anatomically encompassing the SM1 and SMA, respectively, where the two dipoles were seated (lower panel). The white circle in the lower panel highlights the difference between the TFCMI and coherence results which is the supposed SMA area. The white circle in the upper panel indicates the same SMA area only for comparison with the result in the lower panel. [Color figure can be viewed in the online issue, which is available at www.interscience.wiley.com.]

approach (linear dependency only), the TFCMI method showed better specificity on dependency measurement in broadband analysis, clearer demarcation of event-related regions from nonrelated, and more robustness for between-modality study. Although TFCMI is not a stringently complete "data-driven" approach, it can be considered as a "model-free" approach [Lee et al., 2003a]: a priori knowledge of neuronal architecture at the anatomical level can be heuristic for the analytical penetration of functional organization. The TFCMI method promises a possibility to better unravel the intricate brain functional organizations in the context of oscillation-coded communication. Further work is currently in progress to allow the TFCMI processing and representation on the source level instead of the sensor level.

ACKNOWLEDGMENTS

The authors thank anonymous reviewers for the insightful comments and particularly thank Dr. Li-Fen Chen, Dr. James Kilner, and Professor Karl Friston for valuable suggestions.

REFERENCES

Andres FG, Mima T, Schulman AE, Dichgans J, Hallett M, Gerloff C (1999): Functional coupling of human cortical sensorimotor areas during bimanual skill acquisition. Brain 122 (Part 5):855–870.

Andrew C, Pfurtscheller G (1996): Dependence of coherence measurements on EEG derivation type. Med Biol Eng Comput 34:232–238.

Andrew C, Pfurtscheller G (1999): Lack of bilateral coherence of post-movement central beta oscillations in the human electroencephalogram. Neurosci Lett 273:89–92.

Aoki F, Fetz EE, Shupe L, Lettich E, Ojemann GA (2001): Changes in power and coherence of brain activity in human sensorimotor cortex during performance of visuomotor tasks. Biosystems 63:89–99.

Baker SN, Olivier E, Lemon RN (1997): Coherent oscillations in monkey motor cortex and hand muscle EMG show task-dependent modulation. J Physiol 501 (Part 1):225–241.

Caramia MD, Palmieri MG, Giacomini P, Iani C, Dally L, Silvestrini M (2000): Ipsilateral activation of the unaffected motor cortex in patients with hemiparetic stroke. Clin Neurophysiol 111:1990–1996.

Cardoso de Oliveira S (2002): The neuronal basis of bimanual coordination: recent neurophysiological evidence and functional models. Acta Psychol (Amst) 110:139–159.

Chen DF, Hyland B, Maier V, Palmeri A, Wiesendanger M (1991): Comparison of neural activity in the supplementary motor area and in the primary motor cortex in monkeys. Somatosens Mot Res 8:27–44.

Chen R, Gerloff C, Hallett M, Cohen LG (1997): Involvement of the ipsilateral motor cortex in finger movements of different complexities. Ann Neurol 41:247–254.

Conway BA, Halliday DM, Farmer SF, Shahani U, Maas P, Weir AI, Rosenberg JR (1995): Synchronization between motor cortex and spinal motoneuronal pool during the performance of a maintained motor task in man. J Physiol 489 (Part 3):917–924.

Crone NE, Miglioretti DL, Gordon B, Lesser RP (1998): Functional mapping of human sensorimotor cortex with electrocorticographic spectral analysis. II. Event-related synchronization in the gamma band. Brain 121(Part 12):2301–2315.

Cuadrado ML, Egido JA, Gonzalez-Gutierrez JL, Varela-De-Seijas E (1999): Bihemispheric contribution to motor recovery after stroke: A longitudinal study with transcranial doppler ultrasonography. Cerebrovasc Dis 9:337–344.

David O, Cosmelli D, Friston KJ (2004): Evaluation of different measures of functional connectivity using a neural mass model. Neuroimage 21:659–673.

Erdler M, Beisteiner R, Mayer D, Kaindl T, Edward V, Windischberger C, Lindinger G, Deecke L (2000): Supplementary motor area activation preceding voluntary movement is detectable with a whole-scalp magnetoencephalography system. Neuroimage 11:697–707.

Feige B, Kristeva-Feige R, Rossi S, Pizzella V, Rossini PM (1996): Neuromagnetic study of movement-related changes in rhythmic brain activity. Brain Res 734:252–260.

Fein G, Raz J, Brown FF, Merrin EL (1988): Common reference coherence data are confounded by power and phase effects. Electroencephalogr Clin Neurophysiol 69:581–584.

Fraser AM, Swinney HL (1986): Independent coordinates for strange attractors from mutual information. Phys Rev A 33: 1134–1140.

Friston KJ (1997): Transients, metastability, and neuronal dynamics. Neuroimage 5:164–171.

Gerloff C, Richard J, Hadley J, Schulman AE, Honda M, Hallett M (1998): Functional coupling and regional activation of human cortical motor areas during simple, internally paced and externally paced finger movements. Brain 121 (Part 8):1513–1531.

Gross J, Kujala J, Hamalainen M, Timmermann L, Schnitzler A, Salmelin R (2001): Dynamic imaging of coherent sources: Studying neural interactions in the human brain. Proc Natl Acad Sci USA 98:694–699.

Gross J, Timmermann L, Kujala J, Dirks M, Schmitz F, Salmelin R, Schnitzler A (2002): The neural basis of intermittent motor control in humans. Proc Natl Acad Sci USA 99:2299–2302.

Gross J, Timmermann L, Kujala J, Salmelin R, Schnitzler A (2003): Properties of MEG tomographic maps obtained with spatial filtering. Neuroimage 19:1329–1336.

Grosse P, Cassidy MJ, Brown P (2002): EEG-EMG, MEG-EMG and EMG-EMG frequency analysis: physiological principles and clinical applications. Clin Neurophysiol 113:1523–1531.

Grossmann A, Morlet J (1984): Decomposition of Hardy function into square integrable wavelets of constant shape. SIAM J. Math Anal 15:723–736.

Halliday DM, Conway BA, Farmer SF, Rosenberg JR (1998): Using electroencephalography to study functional coupling between cortical activity and electromyograms during voluntary contractions in humans. Neurosci Lett 241:5–8.

Halliday DM, Rosenberg JR, Amjad AM, Breeze P, Conway BA, Farmer SF (1995): A framework for the analysis of mixed time series/point process data–theory and application to the study of physiological tremor, single motor unit discharges and electromyograms. Prog Biophys Mol Biol 64:237–278.

Hamalainen M, Hari R, Ilmoniemi RJ, Knuutila J, Lounasmaa OV (1993). Magnetoencephalography-theory, instrumentation, and applications to noninvasive studies of the working human brain. Rev Mod Phys 65:413–497.

Hari R, Imada T (1999): Ipsilateral movement-evoked fields reconsidered. Neuroimage 10:582–588.

Hsieh JC, Cheng H, Hsieh HM, Liao KK, Wu YT, Yeh TC, Ho LT. (2002): Loss of interhemispheric inhibition on the ipsilateral primary sensorimotor cortex in patients with brachial plexus injury: fMRI study. Ann Neurol 51:381–385.

Ishii R, Schulz M, Xiang J, Takeda M, Shinosaki K, Stuss DT, et al. (2002): MEG study of long-term cortical reorganization of sensorimotor areas with respect to using chopsticks. Neuroreport 13:2155–2159.

Jasper H, Penfield W (1949): Electrocorticograms in man: Effect of voluntary movement upon the electrical activity of the precentral gyrus. Arch Psychiatry 183:163–173.

Jeong J, Gore JC, Peterson BS (2001): Mutual information analysis of the EEG in patients with Alzheimer's disease. Clin Neurophysiol 112:827–835.

Joliot M, Crivello F, Badier JM, Diallo B, Tzourio N, Mazoyer B (1998): Anatomical congruence of metabolic and electromagnetic activation signals during a self-paced motor task: a combined PET-MEG study. Neuroimage 7:337–351.

Jones RD, Donaldson IM, Parkin PJ (1989): Impairment and recovery of ipsilateral sensory-motor function following unilateral cerebral infarction. Brain 112(Part 1):113–132.

Jung TP, Makeig S, Humphries C, Lee TW, McKeown MJ, Iragui V, et al. (2000): Removing electroencephalographic artifacts by blind source separation. Psychophysiology 37:163–178.

Kilner JM, Baker SN, Salenius S, Jousmaki V, Hari R, Lemon RN (1999). Task-dependent modulation of 15-30 Hz coherence between rectified EMGs from human hand and forearm muscles. J Physiol 516 (Part 2):559–570.

Kornhuber HH, Deecke L (1965): Changes in the brain potential in voluntary movements and passive movements in man: readiness potential and reafferent potentials. Pflugers Arch Gesamte Physiol Menschen Tiere 284:1–17.

Kuypers HGJM (1981):Anatomy of the descending pathways. In: Brooks VB, editor. Handbook of Physiology, Vol. 2. Bethesda, MD: American Physiological Society. pp 597–666.

Lachaux JP, Lutz A, Rudrauf D, Cosmelli D, Le Van Quyen M, Martinerie J, et al. (2002): Estimating the time-course of coherence between single-trial brain signals: an introduction to wavelet coherence. Neurophysiol Clin 32:157–174.

Lang W, Cheyne D, Kristeva R, Beisteiner R, Lindinger G, Deecke L (1991): Three-dimensional localization of preceding voluntary movement. A study of electric and magnetic fields in a patient with infarction of the right supplementary motor area. Exp Brain Res 87:688–695.

Lee L, Harrison LM, Mechelli A (2003a): A report of the functional connectivity workshop, Dusseldorf, 2002. Neuroimage 19:457–465.

Lee PL, Wu YT, Chen LF, Chen YS, Cheng CM, Yeh TC, et al. (2003b): ICA-based spatiotemporal approach for single-trial analysis of postmovement MEG β-synchronization. Neuroimage 20:2010–2030.

Leocani L, Comi G (1999): EEG coherence in pathological conditions. J Clin Neurophysiol 16:548–555.

Leocani L, Toro C, Manganotti P, Zhuang P, Hallett M (1997): Event-related coherence and event-related desynchronization/synchronization in the 10 Hz and 20 Hz EEG during self-paced movements. Electroencephalogr Clin Neurophysiol 104:199–206.

Lewis PA, Miall RC (2003): Distinct systems for automatic and cognitively controlled time measurement: evidence from neuroimaging. Curr Opin Neurobiol 13:250–255.

Lins OG, Picton TW, Berg P, Scherg M (1993): Ocular artifacts in recording EEGs and event-related potentials. II: Source dipoles and source components. Brain Topogr 6:65–78.

Locatelli T, Cursi M, Liberati D, Franceschi M, Comi G (1998): EEG coherence in Alzheimer's disease. Electroencephalogr Clin Neurophysiol 106:229–237.

Lopes da Silva F (1991): Neural mechanisms underlying brain waves: from neural membranes to networks. Electroencephalogr Clin Neurophysiol 79:81–93.

Magnani G, Cursi M, Leocani L, Volonte MA, Comi G (2002): Acute effects of L-dopa on event-related desynchronization in Parkinson's disease. Neurol Sci 23:91–97.

Manganotti P, Gerloff C, Toro C, Katsuta H, Sadato N, Zhuang P, et al. (1998): Task-related coherence and task-related spectral power changes during sequential finger movements. Electroencephalogr Clin Neurophysiol 109:50–62.

Marshall RS, Perera GM, Lazar RM, Krakauer JW, Constantine RC, DeLaPaz RL (2000): Evolution of cortical activation during recovery from corticospinal tract infarction. Stroke 31:656–661.

Mima T, Hallett M (1999): Corticomuscular coherence: a review. J Clin Neurophysiol 16:501–511.

Mima T, Matsuoka T, Hallett M (2000a): Functional coupling of human right and left cortical motor areas demonstrated with partial coherence analysis. Neurosci Lett 287:93–96.

Mima T, Steger J, Schulman AE, Gerloff C, Hallett M (2000b): Electroencephalographic measurement of motor cortex control of muscle activity in humans. Clin Neurophysiol 111:326–337.

Nagamine T, Kajola M, Salmelin R, Shibasaki H, Hari R (1996): Movement-related slow cortical magnetic fields and changes of spontaneous MEG- and EEG-brain rhythms. Electroencephalogr Clin Neurophysiol 99:274–286.

Nunez PL, Srinivasan R, Westdorp AF, Wijesinghe RS, Tucker DM, Silberstein RB, et al. (1997): EEG coherency. I. Statistics, reference electrode, volume conduction, Laplacians, cortical imaging, and interpretation at multiple scales. Electroencephalogr Clin Neurophysiol 103:499–515.

Pfurtscheller G, Andrew C (1999): Event-related changes of band power and coherence: methodology and interpretation. J Clin Neurophysiol 1:512–519.

Pfurtscheller G, Aranibar A (1979): Evaluation of event-related desynchronization (ERD) preceding and following voluntary self-paced movement. Electroencephalogr Clin Neurophysiol 46:138–146.

Pfurtscheller G, Lopes da Silva FH (1999): Event-related EEG/MEG synchronization and desynchronization: basic principles. Clin Neurophysiol 110:1842–1857.

Pfurtscheller G, Stancak A Jr, Neuper C (1996): Post-movement β-synchronization. A correlate of an idling motor area? Electroencephalogr Clin Neurophysiol 98:281–293.

Pfurtscheller G, Zalaudek K, Neuper C (1998): Event-related β-synchronization after wrist, finger and thumb movement. Electroencephalogr Clin Neurophysiol 109:154–160.

Popivanov D, Dushanova J (1999): Non-linear EEG dynamic changes and their probable relation to voluntary movement organization. Neuroreport 10:1397–1401.

Rau C, Plewnia C, Hummel F, Gerloff C (2003): Event-related desynchronization and excitability of the ipsilateral motor cortex during simple self-paced finger movements. Clin Neurophysiol 114:1819–1826.

Rosenberg JR, Amjad AM, Breeze P, Brillinger DR, Halliday DM (1989): The Fourier approach to the identification of functional coupling between neuronal spike trains. Prog Biophys Mol Biol 53:1–31.

Salenius S, Portin K, Kajola M, Salmelin R, Hari R (1997): Cortical control of human motoneuron firing during isometric contraction. J Neurophysiol 77:3401–3405.

Salmelin R, Hari R (1994): Characterization of spontaneous MEG rhythms in healthy adults. Electroencephalogr Clin Neurophysiol 91:237–248.

Schnitzler A, Gross J, Timmermann L (2000): Synchronised oscillations of the human sensorimotor cortex. Acta Neurobiol Exp (Wars) 60:271–287.

Shannon CE. A mathematical theory of communication. Bell Syst Tech J1948; 27:379-426.Also at 28:623-656.

Stippich C, Freitag P, Kassubek J, Soros P, Kamada K, Kober H, et al. (1998): Motor, somatosensory and auditory cortex localization by fMRI and MEG. Neuroreport 9:1953–1957.

Timmermann L, Gross J, Dirks M, Volkmann J, Freund HJ, Schnitzler A (2003): The cerebral oscillatory network of parkinsonian resting tremor. Brain 126:199–212.

Tononi G, Sporns O, Edelman GM (1994): A measure for brain complexity: relating functional segregation and integration in the nervous system. Proc Natl Acad Sci USA 91:5033–5037.

Vorobyov S, Cichocki A (2002): Blind noise reduction for multisensory signals using ICA and subspace filtering, with application to EEG analysis. Biol Cybern 86:293–303.

Ward NS, Cohen LG (2004): Mechanisms underlying recovery of motor function after stroke. Arch Neurol 61:1844–1848.

Whitton JL, Lue F, Moldofsky H (1978): A spectral method for removing eye movement artifacts from the EEG. Electroencephalogr Clin Neurophysiol 44:735–741.

Woestenburg JC, Verbaten MN, Slangen JL (1983): The removal of the eye-movement artifact from the EEG by regression analysis in the frequency domain. Biol Psychol 16:127–147.

Wu YZ, Niddam DM, Chen CC, Liao KK, Cheng CM, Chen LF, Lee PL, Chen SS, Yeh TZ, Hsieh JC (2006): Effects of cognitive demands on postmovement motor cortical deactivation. Neuroreport 17:371–375.

Zaveri HP, Williams WJ, Sackellares JC, Beydoun A, Duckrow RB, Spencer SS (1999): Measuring the coherence of intracranial electroencephalograms. Clin Neurophysiol 110:1717–1725.

Bibliography

Allison T, Ginter H, McCarthy G, Nobre AC, Puce A, Luby M, et al, (1994), Face recognition in human extrastriate cortex, J Neurophysiol; 71: 821-5

Andrew C, Pfurtscheller G (1996), Event-related coherence as a tool for studying dynamic interaction of brain regions, Electroencephalogr Clin Neurophysiol 98: 144-8

Angelucci A, Bressloff PC, (2006),Contribution of feedforward, lateral and feedback connections to the classical receptive field center and extra-classical receptive field surround of primate V1 neurons, Prog Brain Res,;154:93-120,

Angelucci A, Levitt JB, Lund JS, (2002b) Anatomical origins of the classical receptive field and modulatory surround field of single neurons in macaque visual cortical area V1, Prog, Brain Res, 136:373-88

Angelucci A, Levitt JB, Walton EJ, Hupe JM, Bullier J, Lund JS, (2002a) Circuits for local and global signal integration in primary visual cortex, J Neurosci, 22:8633-46

Babiloni C, Bares M, Vecchio F, Brazdil M, Jurak P, Moretti DV (2004), Synchronization of gamma oscillations increases functional connectivity of human hippocampus and inferior-middle temporal cortex during repetitive visuomotor events, Eur J Neurosci ; 19: 3088-98

Babiloni C, Miniussi C, Moretti D, Vecchio F, Salinari S, Frisoni G, (2004) Cortical networks generating movement-related EEG rhythms in Alzheimer's disease: an EEG coherence study, Behav Neurosci ; 118: 698-706,

Baillet S, Garnero LA, (1997), Bayesian approach to introducing anatomo-functional priors in the EEG/MEG inverse problem, IEEE Trans Biomed, Eng, 44: 374-85

Balconi M, Pozzoli U (2008), Event-related oscillations (ERO) and event-related potentials (ERP) in emotional face recognition, Int J Neurosci; 118: 1412-24,

Ballard DH, Hinton GE, Sejnowski TJ (1983) Parallel visual computation, Nature, 306:21-6

Barbeau EJ, Taylor MJ, Regis J, Marquis P, Chauvel P, Liegeois-Chauvel C, (2008), Spatio temporal dynamics of face recognition, Cereb Cortex; 18: 997-1009,

Basar E, Guntekin B, Oniz A (2006), Principles of oscillatory brain dynamics and a treatise of recognition of faces and facial expressions, Prog Brain Res; 159: 43-62,

Bendat JS, (1990), Nonlinear System Analysis and Identification from Random Data, John Wiley and Sons, New York USA

Bernasconi, C, Konig, P, (1999), On the directionality of cortical interactions studied by structural analysis of electrophysiological recordings, Biol, Cybern, 81: 199– 210,

Bitan T, Booth JR, Choy J, Burman DD, Gitelman DR, Mesulam MM,(2005) Shifts of effective connectivity within a language network during rhyming and spelling, J Neurosci,; 25(22):5397-403

Bragin A, Jandó G, Nádasdy Z, Hetke J, Wise K, Buzsáki G, (1995) Gamma (40-100 Hz) oscillation in the hippocampus of the behaving rat, J Neurosci,

15(1 Pt 1):47-60,

Breakspear M, (2002), Nonlinear phase desynchronization in human electroencephalographic data, Hum Brain Mapp 15: 175-98

Breakspear M, Williams LM, Stam CJ,(2004) A novel method for the topographic analysis of neural activity reveals formation and dissolution of 'Dynamic Cell Assemblies', J Comput Neurosci ; 16: 49-68,

Breakspear M, and Terry JR, (2002), Detection and description of non-linear interdependence in normal multichannel human EEG data, Clin, Neurophysiol, 113:735-753,

Bressler S, (1995), Large-scale cortical networks and cognition, Brain Res,Rev, 20: 288-304,

Brodmann K, (1909), Brodmann's 'Localisation in the Cerebral Cortex, London: Smith-Gordon,

Brovelli A, Ding M, Ledberg A, Chen Y, Nakamura R, Bressler SL, (2004), Beta oscillations in a large-scale sensorimotor cortical network: directional influences revealed by Granger causality, Proc, Natl, Acad, Sci, U, S, A, 101: 9849–9854,

Brown P, (2007), Abnormal oscillatory synchronisation in the motor system leads to impaired movement, Curr Opin Neurobiol, 17(6):656-64,

Bruno RM, Simons DJ, (2002) Feedforward mechanisms of excitatory and inhibitory cortical receptive fields, J Neurosci ; 22: 10966-75

Büchel C and Friston KJ, (1997) Modulation of connectivity in visual pathways by attention: Cortical interactions evaluated with structural equation modelling and fMRI, Cerebral Cortex 7:768-778

Bullock TH, Achimowicz JZ, Duckrow RB, Spencer SS, Iragui-Madoz VJ, (1997), Bicoherence of intracranial EEG in sleep, wakefulness and seizures, Electroencephalogr Clin Neurophysiol, 103: 661-78

Buzsaki G, Kaila K, Raichle M,(2007) Inhibition and brain work, Neuron; 56: 771-83

Cabeza R, Anderson ND, Locantore JK, McIntosh AR,(2002a) Aging gracefully: compensatory brain activity in high-performing older adults, Neuroimage; 17: 1394-402,

Cabeza R, Nyberg L,(2000) Imaging cognition II: An empirical review of 275 PET and fMRI studies, J Cogn Neurosci; 12: 1-47,

Cabeza R,(2002b) Hemispheric asymmetry reduction in older adults: the HAROLD model. Psychol Aging; 17: 85-100.

Canolty RT, Edwards E, Dalal SS, Soltani M, Nagarajan SS, Kirsch HE, Berger MS, Barbaro NM, Knight RT, (2006) High gamma power is phase-locked to theta oscillations in human neocortex. Science.313(5793):1626-8.

Chavez M, Martinerie J, Le Van Quyen M, (2003). Statistical assessment of nonlinear causality: application to epileptic EEG signals. J Neurosci Methods; 124: 113-28.

Chance FS, Abbott LF, Reyes AD,(2002) Gain modulation from background synaptic input. Neuron; 35: 773-82

Chawla D, Lumer ED, Friston KJ, (1999) The relationship between synchronization among neuronal populations and their mean activity levels. Neural Comput.15;11(6):1389-411

Chen CC, Kiebel SJ, Friston KJ, (2008) Dynamic causal modelling of induced

responses. Neuroimage ; 41: 1293

Chen CC, Henson RN, Stephan KE, Kilner JM, Friston KJ (2009). Forward and backward connections in the brain: A DCM study of functional asymmetries. Neuroimage; 45: 453-62

Chen CC, Hsieh JC, Wu YZ, Lee PL, Chen SS, Niddam DM, et al, (2008b) Mutual-information-based approach for neural connectivity during self-paced finger lifting task. Hum Brain Mapp; 29: 265-80.

Crone NE, Miglioretti DL, Gordon B, Sieracki JM, Wilson MT, Uematsu S, et al (1998a). Functional mapping of human sensorimotor cortex with electrocorticographic spectral analysis. I. Alpha and beta event-related desynchronization. Brain 121 (Pt 12): 2271-99.

Crone NE, Miglioretti DL, Gordon B, Lesser RP (1998b). Functional mapping of human sensorimotor cortex with electrocorticographic spectral analysis. II. Event-related synchronization in the gamma band. Brain 121 (Pt 12): 2301-15.

Czigler B, Csikos D, Hidasi Z, Anna Gaal Z, Csibri E, Kiss E (2007). Quantitative EEG in early Alzheimer's disease patients - Power spectrum and complexity features. Int J Psychophysiol.

Darling WG, Wolf SL, Butler AJ (2006). Variability of motor potentials evoked by transcranial magnetic stimulation depends on muscle activation. Exp Brain Res; 174: 376-85.

Darvas F, Pantazis D, Kucukaltun-Yildirim E, Leahy RM, (2004), Mapping human brain function with MEG and EEG: methods and validation. NeuroImage 23 Suppl 1: S289-99

David O, Cosmelli D, Friston KJ (2004), Evaluation of different measures of functional connectivity using a neural mass model. Neuroimage; 21: 659-73

David O, Kiebel S, Harrison L, Mattout J, Kilner JM, Friston KJ, (2006a). "Dynamic causal modelling of evoked responses in EEG and MEG". NeuroImage 20 : 1255-1272.

David O, Kilner JM, Friston KJ,(2006b). Mechanisms of evoked and induced responses in MEG/EEG. Neuroimage; 31: 1580-91.

David O, Cosmelli D, Lachaux J-P, Baillet S, Garnero L, Martinerie J. (2003). A theoretical and experimental introduction to the non-invasive study of large-scale neural phase synchronization in human beings. International Journal of Computational Cognition 1: 53-77

David O, Guillemain I, Saillet S, Reyt S, Deransart C, Segebarth C, et al,(2008) Identifying neural drivers with functional MRI: an electrophysiological validation. PLoS Biol; 6: 2683-97

Dayan P, Hinton GE, Neal R, Zemel RS, (1995) The Helmholtz Machine. Neural Computation. 7:1022-1037

Deecke L (1987), Bereitschaftspotential as an indicator of movement preparation in supplementary motor area and motor cortex. Ciba Found Symp ; 132: 231-50.

Deecke L,(1990) Electrophysiological correlates of movement initiation. Rev Neurol (Paris); 146: 612-9.

Dien J, Khoe W, Mangun GR, (2007). Evaluation of PCA and ICA of simulated ERPs: Promax vs, Infomax rotations. Hum Brain Mapp; 28: 742-63.

Dolcos F, Rice HJ, Cabeza R,(2002) Hemispheric asymmetry and aging: right hemisphere decline or asymmetry reduction. Neurosci Biobehav Rev; 26: 819-25.

Dumermuth G, Huber PJ, Kleiner B, Gasser T, (1971), Analysis of interrelations between frequency bands of EEG by means of bispectrum - preliminary study. Electroencephalogr Clin Neurophysiol 31: 137-148

Eaton SA, Salt TE, (1996) Role of N-methyl-D-aspartate and metabotropic glutamate receptors in corticothalamic excitatory postsynaptic potentials in vivo. Neuroscience 73:1-5.

Engel AK, Fries P, Singer W, (2001). Dynamic predictions: oscillations and synchrony in top-down processing. Nat Rev Neurosci 2: 704-716.

Ermentrout GB, Kleinfeld D, (2001), Traveling Electrical Waves in Cortex: Insights from Phase Dynamics and Speculation on a Computational Role. Neuron 29, 33–44,

Ethofer T, Anders S, Erb M, Herbert C, Wiethoff S, Kissler J, Grodd W, Wildgruber D, (2006). Cerebral pathways in processing of affective prosody: a dynamic causal modeling study. NeuroImage.; 30(2):580-7,

Faber ES, Sah P (2003) Calcium-activated potassium channels: multiple contributions to neuronal function. Neuroscientist 9:181-194

Fairhall SL, Ishai A, (2007) Effective connectivity within the distributed cortical network for face perception. Cereb Cortex.; 17(10):2400-6

Fan J, Hof PR, Guise KG, Fossella JA, Posner MI, (2007), The Functional Integration of the Anterior Cingulate Cortex during Conflict Processing. Cereb Cortex. Jul 25;

Farmer SF, Gibbs J, Halliday DM, Harrison LM, James LM, Mayston MJ, et al, Changes in EMG coherence between long and short thumb abductor muscles during human development. J Physiol 2007; 579: 389-402.

Felleman DJ and Van Essen DC (1991) Distributed hierarchical processing in the primate cerebral cortex. Cerebral Cortex 1:1-47

Fliess M, Lamnabhi M and Lamnabhi-Lagarrigue F (1983). An algebraic approach to nonlinear functional expansions. IEEE Transactions on Circuits and Systems 30:554-570

Fox K, Sato H, Daw N (1989) The location and function of NMDA receptors in cat and kitten visual cortex. J Neurosci 9:2443–2454.

Fox K, Sato H, Daw N (1990) The effect of varying stimulus intensity on NMDA receptor activity in cat visual cortex. J Neurophysiol 64:1413–1428.

Friston KJ, Ungerleider LG, Jezzard P, Turner R, (1995), Characterizing modulatory interactions between V1 and V2 in human cortex with fMRI. Human Brain Mapping; 2:211-224,

Friston KJ, (1997a) Another neural code? Neuroimage; 5: 213-20,

Friston KJ, (1997b),Transients, metastability, and neuronal dynamics, Neuroimage 5: 164-71

Friston K, Phillips J, Chawla D, Buchel C (1999), Revealing interactions among brain systems with nonlinear PCA, Hum Brain Mapp; 8: 92-7,

Friston K, Phillips J, Chawla D, Buchel C (2000), Nonlinear PCA: characterizing interactions between modes of brain activity. Philos Trans R Soc Lond B Biol Sci ; 355: 135-46,

Friston KJ, (2000), The Labile Brain I: Neuronal Transients and nonlinear

coupling. Phil, Trans, R, Soc, (Lond,) 355:215-236

Friston KJ,(2001). Brain function, nonlinear coupling, and neuronal transients. Neuroscientist; 7(5):406-18

Friston KJ, (2003a), Learning and inference in the brain. Neural Networks; 16:1325-1352

Friston KJ, Harrison L, Penny W, (2003b) Dynamic causal modeling. NeuroImage 19:1273-302

Friston K,(2005) A theory of cortical responses. Philos Trans R Soc Lond B Biol Sci.; 360(1456):815-36

Friston K, Kilner J, Harrison L,(2006). A free energy principle for the brain. J Physiol Paris.;100(1-3):70-87.

Friston K, Mattout J, Trujillo-Barreto N, Ashburner J, Penny W, (2007). Variational free energy and the Laplace approximation. NeuroImage.; 34(1):220-34.

Friston K, Harrison L, Daunizeau J, Kiebel S, Phillips C, Trujillo-Barreto N, Henson R, Flandin G, Mattout J, (2008). Multiple sparse priors for the M/EEG inverse problem. NeuroImage.;39(3):1104-20

Friston K, (2009), Causal modelling and brain connectivity in functional magnetic resonance imaging. PLoS Biol ; 7: e33

Garrido MI, Kilner JM, Kiebel SJ, Friston KJ, (2007a). Evoked brain responses are generated by feedback loops. Proc Natl Acad Sci U S A ; 104: 20961-6,

Garrido MI, Kilner JM, Kiebel SJ, Stephan KE, Friston KJ, (2007b). Dynamic causal modelling of evoked potentials: a reproducibility study.

Neuroimage; 36: 571-580.

Garrido MI, Kilner JM, Kiebel SJ, Friston KJ (2009). Dynamic causal modelling of the response to frequency deviants. J Neurophysiol

Gazzaley A, Clapp W, Kelley J, McEvoy K, Knight RT, D'Esposito M, (2008) Age-related top-down suppression deficit in the early stages of cortical visual memory processing. Proc Natl Acad Sci U S A ; 105: 13122-6.

Gentet LJ, Ulrich D, (2004). Electrophysiological characterization of synaptic connections between layer VI cortical cells and neurons of the nucleus reticularis thalami in juvenile rats. Eur J Neurosci. 19(3):625-33.

Gerloff C, Andres FG, (2002). Bimanual coordination and interhemispheric interaction. Acta Psychol (Amst) 110: 161-86.

Gerloff C, Richard J, Hadley J, Schulman A, Honda M, Hallett M (1998), Functional coupling and regional activation of human cortical motor areas during simple, internally paced and externally paced finger movements. Brain 121 (Pt 8): 1513-31.

Girard P, Bullier J, (1989). Visual activity in area V2 during reversible inactivation of area 17 in the macaque monkey. J Neurophysiol. 62:1287-1301.

Granger CWJ, (1969), Investigating causal relations by econometric models and cross-spectral methods. Econometrica 37: 424–438.

Granger CWJ, (1980). Testing for causality: a personal viewpoint. J. Econ. Dyn. Control 2: 329–352.

Gray CM, Konig P, Engel AK, Singer W (1989). Oscillatory responses in cat visual cortex exhibit inter-columnar synchronization which reflects

global stimulus properties. Nature 338: 334-337

Grol MJ, Majdandzic J, Stephan KE, Verhagen L, Dijkerman HC, Bekkering H, Verstraten FA, Toni I (1998). Parieto-frontal connectivity during visually guided grasping. J. Neurosci. 27:11877-11887.

Gross J, Kujala J, Hamalainen M, Timmermann L, Schnitzler A, Salmelin R (2001). Dynamic imaging of coherent sources: Studying neural interactions in the human brain. Proc Natl Acad Sci U S A 98: 694-9.

Grosse P, Cassidy MJ, Brown P (2002). EEG-EMG, MEG-EMG and EMG-EMG frequency analysis: physiological principles and clinical applications. Clin Neurophysiol ; 113: 1523-31.

Gruss M, Braun K (2004). Age- and region-specific imbalances of basal amino acids and monoamine metabolism in limbic regions of female Fmr1 knock-out mice. Neurochem Int ; 45: 81-8.

Guderian S, Duzel E, (2005). Induced theta oscillations mediate large-scale synchrony with mediotemporal areas during recollection in humans. Hippocampus 15: 901-12.

Guntekin B, Basar E (2007). Emotional face expressions are differentiated with brain oscillations. Int J Psychophysiol; 64: 91-100.

Haaland KY, Harrington DL, Knight RT (2000). Neural representations of skilled movement. Brain 123 (Pt 11): 2306-13.

Hamalainen MS (1992), Magnetoencephalography: a tool for functional brain imaging. Brain Topogr; 5: 95-102

Haxby JV, Hoffman EA, Gobbini MI (2000). The distributed human neural system for face perception. Trends Cogn Sci ; 4: 223-233.

Hershey T, Revilla FJ, Wernle AR, McGee-Minnich L, Antenor JV, Videen TO, et al,(2003) Cortical and subcortical blood flow effects of subthalamic nucleus stimulation in PD. Neurology; 61: 816-21.

Helmholtz H (1860/1962) Handbuch der physiologischen optik. (English trans., Southall JPC. Ed.) Vol. 3, New York: Dover.

Henson RN, Goshen-Gottstein Y, Ganel T, Otten LJ, Quayle A, Rugg MD (2003), Electrophysiological and haemodynamic correlates of face perception. recognition and priming. Cereb Cortex 13: 793-805.

Henson RN, Mattout J, Singh KD, Barnes GR, Hillebrand A, Friston K,(2007). Population-level inferences for distributed MEG source localization under multiple constraints: application to face-evoked fields. NeuroImage.; 38(3):422-38

Hilgetag CC, O'Neill MA, and Young MP, (2000). Hierarchical organisation of macaque and cat cortical sensory systems explored with a novel network processor. Philos Trans R Soc. Lond B Biol. Sci 355:71-89

Hirsch JA, Martinez LM, Alonso JM, Desai K, Pillai C, Pierre C, (2002), Synaptic physiology of the flow of information in the cat's visual cortex in vivo. J Physiol. 540(Pt 1):335-50.

Hupe JM, James AC, Payne BR Lomber SG, Girard P and Bullier J, (1998). Cortical feedback improves discrimination between figure and background by V1, V2 and V3 neurons. Nature. 394:784-7

Itier RJ, Herdman, AT, (2006). Inversion and contrast-reversal effects on face processing assessed by MEG. Brain Res. 1115(1): 108-20.

James LM, Halliday DM, Stephens JA, Farmer SF (2008). On the development of

human corticospinal oscillations: age-related changes in EEG-EMG coherence and cumulant. Eur J Neurosci ; 27: 3369-79.

Jansen BH, Rit VG, (1995), Electroencephalogram and visual evoked potential generation in a mathematical model of coupled cortical columns. Biological Cybernetics 73:357-366,

Jeffrey CS, Chamoun NG, (1994). An introduction to bispectral analysis for the electroencephalogram. J. Clin. Monit.; 10 : 392–404

Jensen O, Colgin LL (2007), Cross-frequency coupling between neuronal oscillations. Trends Cogn Sci 11: 267-9.

Jung TP, Makeig S, Humphries C, Lee TW, McKeown MJ, Iragui V(2000a) . et al. Removing electroencephalographic artifacts by blind source separation. Psychophysiology ; 37: 163-78.

Jung TP, Makeig S, Westerfield M, Townsend J, Courchesne E, Sejnowski TJ (2000b). Removal of eye activity artifacts from visual event-related potentials in normal and clinical subjects. Clin Neurophysiol; 111: 1745-58.

Jung TP, Makeig S, Westerfield M, Townsend J, Courchesne E, Sejnowski TJ, (2001) Analysis and visualization of single-trial event-related potentials. Hum Brain Mapp ; 14: 166-85

Kahana MJ, Caplan JB, Sekuler R, Madsen JR (1999).Using intracranial recordings to study theta Response to J. O'Keefe and N. Burgess (1999). Trends Cogn Sci 3: 406-407.

Kaiser J, Lutzenberger W (2003). Induced gamma-band activity and human brain function. Neuroscientist ; 9: 475-84.

Kandel ER,(2000) Principles of neural science

Kanwisher N, Yovel G, (2006). The fusiform face area: a cortical region specialized for the perception of faces. Philos Trans R Soc Lond B Biol Sci. 361: 2109-28.

Karni A, Meyer G, Jezzard P, Adams MM, Turner R, Ungerleider LG, (1995). Functional MRI evidence for adult motor cortex plasticity during motor skill learning. Nature 377: 155-8.

Kawato M Hayakawa H and Inui T (1993) A forward-inverse optics model of reciprocal connections between visual cortical areas. Network. 4:415-422

Keller I, Heckhausen H (1990), Readiness potentials preceding spontaneous motor acts: voluntary vs. involuntary control. Electroencephalogr Clin Neurophysiol; 76: 351-61.

Kelly JB, Zhang H (2002) Contribution of AMPA and NMDA receptors to excitatory responses in the inferior colliculus. Hear. Res. 168:35– 42.

Kersten D, Mamassian P and Yuille A (2004) Object perception as Bayesian inference. Annu. Rev. Psychol. 55:271-304

Kiebel SJ, David O, Friston, KJ, (2006). Dynamic causal modelling of evoked responses in EEG/MEG with lead field parameterization. NeuroImage 30 (4) :1273-1284

Kiebel SJ, Daunizeau J, Phillips C, Friston KJ, (2008). Variational Bayesian inversion of the equivalent current dipole model in EEG/MEG. NeuroImage 39(2):728-41

Kilner JM, Baker SN, Salenius S, Hari R, Lemon RN (2000). Human cortical

muscle coherence is directly related to specific motor parameters. J Neurosci 2000; 20: 8838-45.

Kilner JM, Alonso-Alonso M, Fisher R, Lemon RN,(2002). Modulation of synchrony between single motor units during precision grip tasks in humans. J Physiol. 541: 937-48.

Kilner JM, Salenius S, Baker SN, Jackson A, Hari R, Lemon RN,(2003). Task-dependent modulations of cortical oscillatory activity in human subjects during a bimanual precision grip task. Neuroimage 18: 67-73.

Kilner J, Paulignan Y, Boussaoud D (2004). Functional connectivity during real vs imagined visuomotor tasks: an EEG study. Neuroreport 15: 637-42

Kilner JM, Mattout J, Henson R, Friston KJ, (2005).Hemodynamic correlates of EEG: a heuristic. Neuroimage 2005; 28: 280-6.

Klopp J, Halgren E, Marinkovic K, Nenov V, (1999). Face-selective spectral changes in the human fusiform gyrus. Clin Neurophysiol ; 110: 676-82.

Klopp J, Marinkovic K, Chauvel P, Nenov V, Halgren E,(2000). Early widespread cortical distribution of coherent fusiform face selective activity. Hum Brain Mapp; 11: 286-93

Kloppel S, van Eimeren T, Glauche V, Vongerichten A, Munchau A, Frackowiak RS, et al (2007). The effect of handedness on cortical motor activation during simple bilateral movements. Neuroimage 34: 274-80.

Kopell N, Ermentrout GB, Whittington MA, Traub RD (2000). Gamma rhythms and beta rhythms have different synchronization properties. Proc Natl Acad Sci U S A; 97: 1867-72.

Kopell N, Ermentrout GB, (1986). Symmetry and phaselocking in chains of

weakly coupled oscillators. Comm. Pure Appl. Math, 39: 623–660.

Kotini A, Anninos P (2002). Detection of non-linearity in schizophrenic patients using magnetoencephalography. Brain Topogr 15: 107-13.

Kuramoto Y, (1984). Chemical Oscillations, Waves and Turbulence. New York: Springer Verlag.

Lachaux JP, Rodriguez E, Martinerie J, Varela FJ (1999). Measuring phase synchrony in brain signals. Hum Brain Mapp. 8: 194-208

Lamme VA, Supèr H, Spekreijse H,(1998). Feedforward, horizontal, and feedback processing in the visual cortex. Curr Opin Neurobiol.; 8(4):529-35.

Lamme VA, Roelfsema PR,(2000) The distinct modes of vision offered by feedforward and recurrent processing. Trends Neurosci.: 23(11):571-9.

Larkum ME, Senn W, Luscher HR (2004) Top-down dendritic input increases the gain of layer 5 pyramidal neurons. Cereb. Cortex 14:1059 –1070

Lee KH, Williams LM, Breakspear M, Gordon E,(2003). Synchronous gamma activity: a review and contribution to an integrative neuroscience model of schizophrenia. Brain Res Brain Res Rev. 41: 57-78.

Leocani L, Toro C, Manganotti P, Zhuang P, Hallett M (1997). Event-related coherence and event-related desynchronization/synchronization in the 10 Hz and 20 Hz EEG during self-paced movements. Electroencephalogr Clin Neurophysiol 104: 199-206.

Levy R, Ashby P, Hutchison WD, Lang AE, Lozano AM, Dostrovsky JO (2002). Dependence of subthalamic nucleus oscillations on movement and dopamine in Parkinson's disease. Brain 125(Pt 6):1196-209.

Lisman J, Idiart M, (1995). Storage of 7±2 short term memories in oscillatory

subcycles. Science; 267 :1512–1515

London M, Häusser M,(2005), Dendritic computation. Annu Rev Neurosci. ;28:503-32

MacKay DM, (1956). The epistemological problem for automata, In Automata Studies. (eds, Shannon CE, and McCarthy J). Princeton. NJ. Princeton University Press. pp 235-251

Makeig S, Debener S, Onton J, Delorme A,(2004) Mining event-related brain dynamics. Trends Cogn Sci ; 8: 204-10.

Makeig S, Westerfield M, Jung TP, Enghoff S, Townsend J, Courchesne E,(2002). Dynamic brain sources of visual evoked responses. Science; 295: 690-4.

Manganotti P, Gerloff C, Toro C, Katsuta H, Sadato N, Zhuang P(1998) Task-related coherence and task-related spectral power changes during sequential finger movements. Electroencephalogr Clin Neurophysiol; 109: 50-62.

Marceglia S, Foffani G, Bianchi AM, Baselli G, Tamma F, Egidi M, et al (2006). Dopamine-dependent non-linear correlation between subthalamic rhythms in Parkinson's disease. J Physiol. 15;571(Pt 3):579-91.

Mattay VS, Fera F, Tessitore A, Hariri AR, Das S, Callicott JH,(2002) Neurophysiological correlates of age-related changes in human motor function. Neurology; 58: 630-5.

Mattout J, Phillips C, Penny WD, Rugg MD, Friston KJ, (2006). MEG source localization under multiple constraints: an extended Bayesian framework. Neuroimage 30: 753-67.

Mattout J, Henson RN, Friston KJ, (2007). Canonical Source Reconstruction for

MEG. Computational Intelligence and Neuroscience; 1:17-27

Maunsell JH, and van Essen DC, (1983). The connections of the middle temporal visual area (MT) and their relationship to a cortical hierarchy in the macaque monkey. J. Neurosci. 3:2563-86

Mechelli A, Price CJ, Noppeney U, Friston KJ,(2003). A dynamic causal modeling study on category effects: bottom-up or top-down mediation? J Cogn Neurosci.;15(7):925-34

Metherate R, Cox CL, Ashe JH (1992) Cellular bases of neocortical activation: modulation of neural oscillations by the nucleus basalis and endogenous acetylcholine. J Neurosci 12:4701-4711.

Michel CM, Murray MM, Lantz G, Gonzalez S, Spinelli L, Grave de Peralta R, (2004). EEG source imaging. Clin Neurophysiol; 115: 2195-222

Mima T, Hallett M (1999). Corticomuscular coherence: a review. J Clin Neurophysiol ; 16: 501-11.

Moon TK, Stirling WC, (2000). Mathematical Methods and algorithms for signal processing: Prentice-Hall.

Moran RJ, Stephan KE, Kiebel SJ, Rombach N, O'Connor WT, Murphy KJ, Reilly RB, Friston KJ (2008) Bayesian estimation of synaptic physiology from the spectral responses of neural masses. NeuroImage 42: 272-284.

Moran RJ, Stephan KE, Seidenbecher T, Pape HC, Dolan RJ, Friston KJ, (2009) Dynamic causal models of steady-state responses. Neuroimage; 44: 796-811

Moran RJ, Kiebel SJ, Stephan KE, Reilly RB, Daunizeau J, Friston KJ, (2007). A Neural Mass Model of spectral responses in electrophysiology.

Neuroimage. 37: 706-20

Mormann F, Fell J, Axmacher N, Weber B, Lehnertz K, Elger C, (2005). Phase/amplitude reset and theta–gamma interaction in the human medial temporal lobe during a continuous word recognition memory task. Hippocampus 15 : 890–900.

Morrison JH, Hof PR,(2002) Selective vulnerability of corticocortical and hippocampal circuits in aging and Alzheimer's disease. Prog Brain Res; 136: 467-86.

Muller GR, Neuper C, Rupp R, Keinrath C, Gerner HJ, Pfurtscheller G,(2003) Event-related beta EEG changes during wrist movements induced by functional electrical stimulation of forearm muscles in man. Neurosci Lett ; 340: 143-7.

Muller-Putz GR, Zimmermann D, Graimann B, Nestinger K, Korisek G, Pfurtscheller G,(2007) Event-related beta EEG-changes during passive and attempted foot movements in paraplegic patients. Brain Res; 1137: 84-91.

Mumford D (1992). On the computational architecture of the neocortex. II, The role of cortico-cortical loops. Biol. Cybern 66:241-51

Murphy PC and Sillito AM (1987). Corticofugal feedback influences the generation of length tuning in the visual pathway. Nature. 329:727-9

Naccarato M, Calautti C, Jones PS, Day DJ, Carpenter TA, Baron JC, (2006). Does healthy aging affect the hemispheric activation balance during paced index-to-thumb opposition task? An fMRI study. Neuroimage. 32: 1250-6

Neuper C, Pfurtscheller G,(2001) Event-related dynamics of cortical rhythms: frequency-specific features and functional correlates. Int J Psychophysiol; 43: 41-58.

Niedermeyer E, Lopes da Silva FH, (1999). Electroencephalography, Basic pricipals, clinical applications and related fields. London: Williams & Wikins

Nunez PL, Srinivasan R, Westdorp AF, Wijesinghe RS, Tucker DM, Silberstein RB, Cadusch PJ(1997). EEG coherency, I: Statistics, reference electrode, volume conduction, Laplacians, cortical imaging, and interpretation at multiple scales. Electroencephalogr. Clin. Neurophysiol. 103: 499-515.

Oberman LM, Hubbard EM, McCleery JP, Altschuler EL, Ramachandran VS, Pineda JA,(2005) EEG evidence for mirror neuron dysfunction in autism spectrum disorders. Brain Res Cogn Brain Res; 24: 190-8.

Ohara S, Ikeda A, Kunieda T, Yazawa S, Baba K, Nagamine T,(2000) Movement-related change of electrocorticographic activity in human supplementary motor area proper. Brain; 123 (Pt 6): 1203-15.

Oishi N, Mima T, Ishii K, Bushara KO, Hiraoka T, Ueki Y (2007) Neural correlates of regional EEG power change. Neuroimage; 36: 1301-12.

Okun M, Lampl I,(2008) Instantaneous correlation of excitation and inhibition during ongoing and sensory-evoked activities. Nat Neurosci ; 11: 535-7

Omlor W, Patino L, Hepp-Reymond MC, Kristeva R (2007). Gamma-range corticomuscular coherence during dynamic force output. Neuroimage 34(3):1191-8

Osipova D, Mazaheri A, Jensen O, (2007) Gamma power is phase-locked to

posterior alpha activity. Proceedings of the 13th annual meeting of the organization for human brain mapping Chicago. June 10–14.

Ozgoren M, Basar-Eroglu C, Basar E, (2005)Beta oscillations in face recognition. Int J Psychophysiol ; 55: 51-9.

Page TL, Einstein M, Duan H, He Y, Flores T, Rolshud D,(2002). Morphological alterations in neurons forming corticocortical projections in the neocortex of aged Patas monkeys. Neurosci Lett ; 317: 37-41.

Palva S, Palva JM, (2007) New vistas for alpha-frequency band oscillations. Trends Neurosci 30 (4) :150–158

Palva JM, Palva S, Kaila, K, (2005). Phase Synchrony among Neuronal Oscillations in the Human Cortex. J. Neurosci; 25:3962-3972

Pantev C, (1995). Evoked and induced gamma-band activity of the human cortex. Brain Topogr; 7: 321-30.

Patino L, Chakarov V, Schulte-Monting J, Hepp-Reymond MC, Kristeva R, (2006). Oscillatory cortical activity during a motor task in a deafferented patient. Neurosci Lett; 401: 214-8.

Patino L, Omlor W, Chakarov V, Hepp-Reymond MC, Kristeva R, (2008) Absence of gamma-range corticomuscular coherence during dynamic force in a deafferented patient. J Neurophysiol; 99: 1906-16.

Pearl J, (1998) Graphs, causality, and structural equation models. Sociological Methods and Research 27 : 226–284

Penny WD, Duzel E, Miller KJ, Ojemann JG, (2008).Testing for nested oscillation. J Neurosci Methods; 174: 50-61

Penny WD, Kiebel SJ, Kilner JM, Rugg MD (2002). Event-related brain dynamics.

Trends Neurosci ; 25: 387-9.

Penny WD, Stephan KE, Mechelli A & Friston KJ (2004a) Comparing dynamic causal models. NeuroImage 22: 1157-1172.

Penny WD, Stephan KE, Mechelli A, Friston KJ (2004b). Modelling functional integration: a comparison of structural equation and dynamic causal models. Neuroimage ; 23 Suppl 1: S264-74

Pereda E, Quiroga RQ, Bhattacharya J,(2005). Nonlinear multivariate analysis of neurophysiological signals. Prog Neurobiol; 77:1-37

Pezard L, Jech R, Ruzicka E,(2001) Investigation of non-linear properties of multichannel EEG in the early stages of Parkinson's disease. Clin Neurophysiol; 112: 38-45

Pfurtscheller G, Andrew C (1999). Event-Related changes of band power and coherence: methodology and interpretation. J Clin Neurophysiol 16: 512-9

Pfurtscheller G, Graimann B, Huggins JE, Levine SP, Schuh LA,(2003) Spatiotemporal patterns of beta desynchronization and gamma synchronization in corticographic data during self-paced movement. Clin Neurophysiol; 114: 1226-36.

Pfurtscheller G, Lopes da Silva FH, (1999). Event-related EEG/MEG synchronization and desynchronization: basic principles. Clin Neurophysiol; 110: 1842-57.

Pfurtscheller G, Zalaudek K, Neuper C,(1998) Event-related beta synchronization after wrist, finger and thumb movement. Electroencephalogr Clin Neurophysiol 1998; 109: 154-60.

Pfurtscheller G, (1992), Event-related synchronization (ERS): an electrophysiological correlate of cortical areas at rest. Electroencephalogr Clin Neurophysiol ; 83: 62-9.

Pfurtscheller G,(2003) Induced oscillations in the alpha band: functional meaning. Epilepsia; 44 Suppl 12: 2-8.

Pikovsky A, Rosenblum M, Kurths J, (2001). Synchronization, A universal concept in nonlinear sciences. Cambridge University Press. Cambridge.

Pilgreen KL, Nunez PL, editor(1995) Neocortical dynamics and human EEG rhythms. Oxford: Oxford University Press

Pollok B, Gross J, Schnitzler A (2006). Asymmetry of interhemispheric interaction in left-handed subjects. Exp Brain Res 175: 268-75

Praamstra P, Stegeman DF, Horstink MW, Brunia CH, Cools AR,(1995) Movement-related potentials preceding voluntary movement are modulated by the mode of movement selection. Exp Brain Res; 103: 429-39.

Priestley MB, (1988). Non-linear and non-stationary time series analysis London: Academic Press.

Priori A, Ardolino G, Marceglia S, Mrakic-Sposta S, Locatelli M, Tamma F (2006). Low-frequency subthalamic oscillations increase after deep brain stimulation in Parkinson's disease. Brain Res Bull; 71: 149-54.

Priori A, Foffani G, Pesenti A, Tamma F, Bianchi AM, Pellegrini M, et al (2004). Rhythm-specific pharmacological modulation of subthalamic activity in Parkinson's disease. Exp Neurol; 189(2):369-79.

Quian Quiroga R, Kraskov A, Kreuz T, Grassberger P, (2002). Performance of

different synchronization measures in real data: a case study on electroencephalographic signals. Phys. Rev. E 65: 041903

Raethjen J, Govindan RB, Kopper F, Muthuraman M, Deuschl G, (2007).Cortical involvement in the generation of essential tremor. J Neurophysiol; 97: 3219-28

Raethjen J, Govindan RB, Kopper F, Muthuraman M, Deuschl G,(2007) Cortical involvement in the generation of essential tremor. J Neurophysiol; 97: 3219-28.

Rao RP, Ballard DH, (1999) Predictive coding in the visual cortex: A functional interpretation of some extra-classical receptive field effects. Nature Neuroscience 2:79-87

Rao RP (1999). An optimal estimation approach to visual perception and learning. Vision Res; 39:1963-89

Rau C, Plewnia C, Hummel F, Gerloff C,(2003) Event-related desynchronization and excitability of the ipsilateral motor cortex during simple self-paced finger movements. Clin Neurophysiol; 114: 1819-26.

Rektor I, Sochurkova D, Bockova M (2006). Intracerebral ERD/ERS in voluntary movement and in cognitive visuomotor task. Prog Brain Res; 159: 311-30.

Rivadulla C, Martinez LM, Varela C, Cudeiro J, (2002). Completing the corticofugal loop: a visual role for the corticogeniculate type 1 metabotropic glutamate receptor. J. Neurosci; 22:2956-62

Robinson PA, Rennie CJ, Rowe DL, O'Connor SC, Wright JJ, Gordon E(2003). Neurophysical modeling of brain dynamics. Neuropsychopharmacology;

28 Suppl 1: S74-9.

Rockland KS, Pandya DN (1979). Laminar origins and terminations of cortical connections of the occipital lobe in the rhesus monkey. Brain Res 179: 3-20.

Rockland KS, and Pandya DN, (1979) Laminar origins and terminations of cortical connections of the occipital lobe in the rhesus monkey. Brain Res. ; 179:3-20

Rodriguez E, George N, Lachaux JP, Martinerie J, Renault B, Varela FJ (1999) Perception's shadow: long-distance synchronization of human brain activity. Nature 397: 430-3

Roelfsema NM, Cobben JM. The EEC syndrome: a literature study. Clin Dysmorphol 1996; 5: 115-27.

Roelfsema PR, Engel AK, Konig P, Singer W. Visuomotor integration is associated with zero time-lag synchronization among cortical areas. Nature 1997; 385: 157-61

Rosenblum M, Pikovsky A, Kurths J,(1996). Phase synchronization of chaotic oscillators. Phys.Rev.Lett. 76: 1804-1807.

Rosenstein MT, Collins JJ, De Luca CJ, (1994). Reconstruction expansion as a geometry-based framework for choosing proper delay times. Physica D; 73:82-98.

Rosier AM, Arckens L, Orban GA, Vandesande F (1993) Laminar distribution of NMDA receptors in cat and monkey visual cortex visualized by [3H]-MK-801 binding. J. Comp. Neurol; 335:369-380.

Rossini PM, Rossi S, Babiloni C, Polich J,(2007) Clinical neurophysiology of

aging brain: from normal aging to neurodegeneration. Prog Neurobiol; 83: 375-400.

Rossion B, Caldara R, Seghier M, Schuller AM, Lazeyras F, Mayer E,(2003). A network of occipito-temporal face-sensitive areas besides the right middle fusiform gyrus is necessary for normal face processing. Brain; 126: 2381-95

Roulston MS, (1999). Estimating the errors on measured entropy and mutual information. Physica D 125: 285-294.

Rowe DL, Robinson PA, Gordon E, (2005). Stimulant drug action in attention deficit hyperactivity disorder (ADHD): inference of neurophysiological mechanisms via quantitative modelling. Clin Neurophysiol; 116(2):324-35.

Rowe JB, Siebner H, Filipovic SR, Cordivari C, Gerschlager W, Rothwell J (2006a). Aging is associated with contrasting changes in local and distant cortical connectivity in the human motor system. Neuroimage ; 32: 747-60.

Rowe WB, Kar S, Meaney MJ, Quirion R, (2006b) Neurotensin receptor levels as a function of brain aging and cognitive performance in the Morris water maze task in the rat. Peptides; 27: 2415-23.

Rulkov NF, Sushchik MM, Tsimring LS, Abarbanel HD, (1995). Generalized synchronization of chaos in directionally coupled chaotic systems. Phys. Rev. E ;51: 980-994.

Salin P-A and Bullier J (1995) Corticocortical connections in the visual system: Structure and function. Psychol. Bull. 75:107-154

Salmelin R, Hari R, (1994)Characterization of spontaneous MEG rhythms in healthy adults. Electroencephalogr Clin Neurophysiol; 91: 237-48.

Salt TE, (2002) Glutamate receptor functions in sensory relay in the thalamus. Philos Trans R Soc Lond B Biol Sci 357:1759-1766.

Sandell JH and Schiller PH, (1982). Effect of cooling area 18 on striate cortex cells in the squirrel monkey. J. Neurophysiol. ; 48:38-48

Sarter M, Bruno JP (2004). Developmental origins of the age-related decline in cortical cholinergic function and associated cognitive abilities. Neurobiol Aging; 25: 1127-39.

Schack B, Vath N, Petsche H, Geissler HG, Moller E,(2002). Phase-coupling of theta-gamma EEG rhythms during short-term memory processing. Int J Psychophysiol; 44: 143-63

Schack B, Vath N, Petsche H, Geissler H, Moller E, (2002)Phase-coupling of theta–gamma EEG rhythms during short-term memory processing. Int J Psychophysiol.; 44 : 143–163

Schiff SJ, So P, Chang T, Burke RE, Sauer T, (1996). Detecting dynamical interdependence and generalized synchrony through mutual prediction in a neural ensemble. Phys. Rev. E ; 54: 6708-6724.

Schiller J, Schiller Y, (2001) NMDA receptor-mediated dendritic spikes and coincident signal amplification. Curr Opin Neurobiol. 11(3):343-8.

Schwartz M, Bennett WR, Stein, S, (1995) communication systems and techniques: Wileys-IEEE press

Serrien D, Orth M, Evans A, Lees A, Brown P (2005). Motor inhibition in patients with Gilles de la Tourette syndrome: functional activation patterns as

revealed by EEG coherence. Brain 128: 116-25.

Sherman SM, and Guillery RW, (1998). On the actions that one nerve cell can have on another: distinguishing "drivers" from "modulators". Proc Natl Acad Sci USA 95:7121-6

Shibasaki H, Hallett M, (2006).What is the Bereitschaftspotential? Clin Neurophysiol; 117: 2341-56

Shils JL, Litt M, Skolnick BE, Stecker MM (1996). Bispectral analysis of visual interactions in humans. Electroencephalogr Clin Neurophysiol 98: 113-125

Shils JL, Litt M, Skolnick BE, Stecker MM (1996), Bispectral analysis of visual interactions in humans, Electroencephalogr, Clin, Neurophysiol; 98: 113–125.

Shipp S, (2005). The importance of being agranular: a comparative account of visual and motor cortex. Philos Trans R Soc Lond B Biol Sci 360(1456):797-814

Singer W (1999). Neuronal synchrony: a versatile code for the definition of relations? Neuron 24: 49-65

Singer W, Gray CM (1995). Visual feature integration and the temporal correlation hypothesis. Annu Rev Neurosci 18: 555-86.

Singh KD, Barnes GR, Hillebrand A, Forde EM, Williams AL, (2002). Task-related changes in cortical synchronization are spatially coincident with the hemodynamic response, NeuroImage 16(1):103-14,

Singh KD. Barnes GR. Hillebrand A. (2003). Group imaging of task-related changes in cortical synchronisation using nonparametric permutation

testing. Neuroimage; 19: 1589-601.

Smith CD, Umberger GH, Manning EL, Slevin JT, Wekstein DR, Schmitt FA (1999) Critical decline in fine motor hand movements in human aging. Neurology; 53: 1458-61.

Soltesz I, Deschênes M, (1993) Low- and high-frequency membrane potential oscillations during theta activity in CA1 and CA3 pyramidal neurons of the rat hippocampus under ketamine-xylazine anesthesia. J Neurophysiol. 70(1):97-116.

Stark H, (1994) Probability, random processes, and estimation theory for engineers: Prentice-Hall.

Stephan KE, Kasper L, Harrison LM, Daunizeau J, Den Ouden HEM, Breakspear M, Friston KJ (2008) Nonlinear dynamic causal models for fMRI. NeuroImage, 42: 649-62.

Stephan KE, Penny WD, Daunizeau J, Moran RJ, Friston KJ,(2009) Bayesian model selection for group studies. Neuroimage, in press

Stephan KE, Marshall JC, Penny WD, Friston KJ, Fink GR (2007a) Inter-hemispheric integration of visual processing during task-driven lateralization. J. Neurosci. 27: 3512-3522.

Stephan KE, Weiskopf N, Drysdale PM, Robinson PA, Friston KJ (2007b) Comparing hemodynamic models with DCM. NeuroImage 38: 387-401.

Summerfield C, Egner T, Greene M, Koechlin E, Mangels J, Hirsch J (2006) Predictive codes for forthcoming perception in the frontal cortex. Science 314:1311-1314.

Sun QQ,(2007) The missing piece in the 'use it or lose it' puzzle: is inhibition regulated by

activity or does it act on its own accord? Rev Neurosci ; 18: 295-310

Sohal VS, Huguenard JR, (2005) Inhibitory coupling specifically generates emergent gamma oscillations in diverse cell types. Proc Natl Acad Sci U S A ; 102: 18638-43

Swartz BE, Goldensohn ES (1998). Timeline of the history of EEG and associated fields. Electroencephalogr Clin Neurophysiol; 106: 173-6.

Talairach J, and Tournoux P,(1988) "Co-planar Stereotaxic Atlas of the Human Brain: 3-Dimensional Proportional System - an Approach to Cerebral Imaging". Thieme Medical Publishers. New York, NY

Talelli P, Ewas A, Waddingham W, Rothwell JC, Ward NS (2008), Neural correlates of age-related changes in cortical neurophysiology. NeuroImage 40: 1772-81.

Tallon-Baudry C, Bertrand O (1999). Oscillatory gamma activity in humans and its role in object representation. Trends Cogn Sci 3: 151-162.

Tallon-Baudry C, Bertrand O, Delpuech C, Permier J, (1997). Oscillatory gamma-band (30-70 Hz) activity induced by a visual search task in humans. J Neurosci; 17: 722-34.

Tallon-Baudry C, Bertrand O,(1999) Oscillatory gamma activity in humans and its role in object representation. Trends Cogn Sci ; 3: 151-162.

Tass P, Rosenblum MG, Weule J, Kurths J, Pikovsky A, Volkmann J, Schnitzler A, Freund H-J (1998). Detection of n:m phase locking from noisy data: application to magnetoencephalography. Phys Rev Lett 81: 3291-3294

Thut G, Miniussi C,(2009) New insights into rhythmic brain activity from TMS-EEG studies. Trends Cogn Sci ; 13: 182-9.

Tiitinen H, Sinkkonen J, Reinikainen K, Alho K, Lavikainen J, Naatanen R,(1993). Selective attention enhances the auditory 40-Hz transient response in humans. Nature; 364: 59-60.

Toro C, Cox C, Friehs G, Ojakangas C, Maxwell R, Gates JR(1994). 8-12 Hz rhythmic oscillations in human motor cortex during two-dimensional arm movements: evidence for representation of kinematic parameters. Electroencephalogr Clin Neurophysiol; 93: 390-403.

Ulloa ER, Pineda JA,(2007) Recognition of point-light biological motion: mu rhythms and mirror neuron activity. Behav Brain Res; 183: 188-94

Vanhatalo S, Palva J, Holmes M, Miller J, Voipio J, Kaila K, (2004), Infraslow oscillations modulate excitability and interictal epileptic activity in the human cortex during sleep. Proc Natl Acad Sci USA; 101 (14):5053–5057

Varela F, Lachaux JP, Rodriguez E, Martinerie J (2001). The brainweb: phase synchronization and large-scale integration. Nat Rev Neurosci 2: 229-39.

von Stein A, Chiang C, Konig P,(2000a) Top-down processing mediated by interareal synchronization. Proc Natl Acad Sci U S A ; 97: 14748-53.

von Stein A, Sarnthein J (2000b). Different frequencies for different scales of cortical integration: from local gamma to long range alpha/theta synchronization. Int J Psychophysiol; 38: 301-13.

Ward NS, Frackowiak RS, (2003). Age-related changes in the neural correlates of motor performance. Brain 126: 873–888

Ward NS, Cohen LG (2004a), Mechanisms underlying recovery of motor function after stroke. Arch Neurol 61: 1844-8.

Ward NS (2004b). Functional reorganization of the cerebral motor system after stroke. Curr Opin Neurol 2004; 17: 725-30.

Ward NS (2005). Neural plasticity and recovery of function. Prog Brain Res; 150: 527-35.

Ward NS (2006a). Compensatory mechanisms in the aging motor system. Ageing Res Rev; 5: 239-54.

Ward NS,(2006b) The neural substrates of motor recovery after focal damage to the central nervous system. Arch Phys Med Rehabil; 87: S30-5.

Ward NS, Swayne OB, Newton JM (2008). Age-dependent changes in the neural correlates of force modulation: an fMRI study. Neurobiol Aging 29: 1434-46.

Ward NS, Swayne OB, Newton JM,(2008) Age-dependent changes in the neural correlates of force modulation: an fMRI study. Neurobiol Aging; 29: 1434-46

Wehr M, Zador AM,(2003) Balanced inhibition underlies tuning and sharpens spike timing in auditory cortex. Nature; 426: 442-6

Wheaton LA, Carpenter M, Mizelle JC, Forrester L,(2008) Preparatory band specific premotor cortical activity differentiates upper and lower extremity movement. Exp Brain Res ; 184: 121-6.

White JA, Banks MI, Pearce RA, Kopell NJ. Networks of interneurons with fast and slow gamma-aminobutyric acid type A (GABAA) kinetics provide substrate for mixed gamma-theta rhythm. Proc Natl Acad Sci U S A 2000; 97: 8128-33

Winston JS, Henson RN, Fine-Goulden MR, Dolan RJ (2004). fMRI-adaptation

reveals dissociable neural representations of identity and expression in face perception. J Neurophysiol 2004; 92: 1830-9

Wright JJ, Liley DT, (1994). A millimetric-scale simulation of electrocortical wave dynamics based on anatomical estimates of cortical synaptic density. Computation in Neural Systems; 5(2):191-202.

Wright JJ, Robinson PA, Rennie CJ, Gordon E, Bourke PD, Chapman CL (2001). Toward an integrated continuum model of cerebral dynamics: the cerebral rhythms, synchronous oscillation and cortical stability. Biosystems; 63: 71-88.

Yamawaki N, Stanford IM, Hall SD, Woodhall GL (2008). Pharmacologically induced and stimulus evoked rhythmic neuronal oscillatory activity in the primary motor cortex in vitro. Neuroscience 151: 386-95

Zeki S and Shipp S (1988). The functional logic of cortical connections. Nature 335:311-317